UNIVERSITY OF
LIVERPOOL

Enhanced Signal Area Estimation for Spectrum-Aware Systems based on Image Processing Techniques

A Thesis Submitted to the
Department of Electrical Engineering and Electronics
of the University of Liverpool
in accordance with the requirements for the Degree of

DOCTOR OF PHILOSOPHY

MOHAMMED M. ALAMMAR

June 2023

Thesis Supervisor: Dr. MIGUEL LÓPEZ-BENÍTEZ

Abstract

In many practical application scenarios, radio communication signals are very frequently represented as spectrograms, which represent the received signal strength measured at multiple discrete time instants and frequency points within a specific time interval and frequency band, respectively. Radio spectrograms have been used for time-frequency signal analysis in spectrum-aware systems for many purposes. An important aspect in the processing of radio spectrograms is the region that each individual radio transmission or signal component occupies in the time-frequency domain within the spectrogram, which in this research is referred to as Signal Area (SA). The concept of SA precisely determines the occupied bandwidth and the start/end times of each individual radio transmission. The capability to obtain this information accurately from a radio spectrogram can be useful in many practical applications, including spectrum surveillance (both for enforcement of spectrum regulations and gathering of signal intelligence in military applications), radio signal interception and identification, electronic warfare and radio environment spectral awareness (for instance, in databases for spectrum sharing systems). Consequently, the process of Signal Area Estimation (SAE), which entails determining the subsets of spectrogram points that belong to one or more SAs, is an important function is spectrum-aware wireless communication systems.

The interest of this research is on how to accurately determine the SAs present in a radio spectrogram obtained from empirical spectrum measurements based on the application of techniques from the field of image processing. Image processing techniques can be employed to this end by treating spectrograms as images, where each time-frequency point in the spectrogram is seen as an image pixel. This point of view converts the problem of SAE in a noisy spectrogram into the problem of recognising rectangular shapes in a noisy image, for which several image processing techniques can be employed. The unique characteristics of the SAE problem in radio spectrograms require a tailored research study. In this context, the main aim of this thesis is to explore the feasibility of using image processing techniques to enhance the accuracy of SAE, and to propose novel SAE methods based on image processing techniques. To this end, a broad range of relevant techniques from the field of image processing are explored, including morphologic operations, edge detection and flood fill techniques, the Hough transform along with other heuristic methods and solutions based on deep learning techniques for the processing of images. The proposed methods are evaluated both with software simulations and using an experimental hardware platform specifically built to this end. The obtained simulation and experimental results show that the methods proposed in this thesis can provide significant accuracy improvements compared to other SAE methods in the existing literature.

Acknowledgements

Contents

List of Figures

List of Tables

List of Abbreviations

5G	Fifth Generation
AI	Artificial Intelligence
ANN	Artificial Neural Network
API	Application Programming Interfaces
ASIC	Application-Specific Integrated Circuit
CFAR	Constant False Alarm Rate
CNN	Convolution Neural Network
COR	Channel Occupancy Rate
CR	Cognitive Radio
CSD	Cyclic Spectral Density
CSDR	Constant Signal Detection Rate
CT-SA	Contour Tracing Signal Area
DC	Duty Cycle
DL	Deep Learning
DOG	Difference of Gaussian
DOH	Determinant of Hessian
DSA	Dynamic Spectrum Access
DSP	Digital Signal Processor
ED	Energy Detection
eMBB	Enhanced Mobile Broadband
FBO	Frequency Band Occupancy
FCC	Federal Communications Commission
FCO	Frequency Channel Occupancy
FFT	Fast Fourier Transform
HT	Hough Transform
IoT	Internet of Things
IOU	Intersection over Union
ITU	International Telecommunication Union
LAN	Local Area Network
LOG	Laplacian of Gaussian
LOG	Laplacian of Gaussian
LSA	Licensed Shared Access
LSTM	Long-Short Term Memory
MA	Minesweeper Algorithm
MAC	Medium Access Control

ML	Machine Learning
MLP	Multi-Layer Perceptron
mMTC	Massive Machine Type Communications
MO	Morphological Operation
MSE	Mean Squared Error
MSER	Minimum Sensing Error Rate
PU	Primary User
REM	Radio Environment Map
RNN	Recurrent Neural Network
SA	Signal Area
SAE	Signal Area Estimation
SAS	Spectrum Awareness System
SE	Structuring Element
SNR	Signal-to-Noise Ratio
SRO	Spectrum Resource Occupancy
SoC	System-on-Chip
SSA	Simple Signal Area
STFT	Short-Term Fourier Transform
SU	Secondary User
SUD	Spectrum Usage Detection
TECCL	Transmission Encapsulation based on the Connected Component Labelling
TOA	Time of Arrival
URLLC	Ultra Reliable and Low Latency Communications
WS	White Space

Chapter 1

Introduction

1.1 Background

The influence of wireless systems transcends borders and geographies, and nearly all parts of the world rely on this technology to achieve several purposes. In today's age, wireless systems are critical to many applications, and they are particularly indispensable to modern-day communication systems. What was once an extension of the public switched telephone network is today a crucial part of nearly all aspects of societies and economies [1].

The history of wireless networks ranges back several decades, before the industrial age, when people relied on the transmission of information over long distances using fairly crude methods, such as smoke signals and flare signals. Elevated stations were built for observation of these signals, which were eventually replaced by the world's first telegraph network in 1838. A few decades later, the world's first telephone was invented and this led to the invention of the first radio network in 1971. Finally, in 1985, the development of wireless networks was formally commissioned by the Federal Communications Commission (FCC) in the United States and a series of innovations since then have led to the wireless network systems of today [2].

In the past, wireless networks were used to primarily relay data for voice communication, but this has rapidly evolved to enable sharing of different multimedia across these networks. As such, wireless systems are increasingly expected to exhibit much higher data transmission rates, with constantly improving signal quality. This has called for significant investment into the wireless networks infrastructure as the popularity of such systems has soared [3].

The vision for wireless communication, in particular, was motivated by the enhanced connectivity it allows to individuals to reach out to each other over long distances using small devices such as mobile phones and laptops. The advent of wireless communication systems propagated a need for such electronic gadgets to harness the power of wireless networks, and this has not only allowed people to connect with each other, but also enabled large businesses to flourish.

At present, there are various forms of wireless communication systems in use, the most popular ones of which are wireless Local Area Networks (LANs), wide area wireless data services, broadband wireless access, and satellite networks. Wireless LANs provide high speed data to users within a small range, whereas wide area wireless

services can provide data to users over a large geography. Broadband enables the provision of data to users between fixed access points, and satellite networks enable the broadcasting of data over very large geographic areas usually beyond easy reach of terrestrial networks [2]. Today's cellular deployments are moving towards the Fifth Generation (5G) technology, which relies on medium and high-band spectrum (mmWave bands) to provide coverage over shorter distances by means of a dense network of base stations. This approach enables not only a more effective provision of Enhanced Mobile Broadband (eMBB) services but also supports new service types such as Ultra Reliable and Low Latency Communications (URLLC) and Massive Machine Type Communications (mMTC) for the Internet of Things (IoT) [4].

It can be difficult to visualise the technologies and resources at play within wireless systems, and it is crucial to understand their importance in allowing these networks to operate smoothly. Perhaps the most critical of these resources is spectrum. Spectrum refers to frequency bands and electromagnetic radiation that travels over long distances as *signals* to enable connectivity. While the electromagnetic spectrum encompasses wide ranges of frequencies, spectrum frequencies are classified into the *radio waves* region that normally ranges between 20 kHz to 300 GHz (though some networks may utilise other frequencies outside this range). It is thus clear that wireless communication networks can utilise different ranges of spectrum frequencies, and these are normally classified as low, medium, and high-band frequencies.

Low-band spectrum is normally considered to be below 3 GHz and, as the name suggests, lower frequencies allow the signal to travel longer distances with low disruption. Medium-band spectrum lies between 3 – 24 GHz and it provides a mixture of both low and high-spectrum, encompassing the benefits and drawbacks of each. High-band spectrum lies above 24 GHz and, owing to high frequencies, the signal travels very short distances though it has very high capacity due to the larger amount of bandwidth available at high frequencies. Predictably, most modern-day telecommunication systems operate in the low-band spectrum to enable signal transmission over longer distances.

At present, the 'radio' range within the electromagnetic spectrum is heavily relied upon by industries within private and public sectors, encompassing communication networks spanning across land, air and sea. The importance of such networks to enable inter-connectivity within society is evident, but there is an equally important need to manage these systems. Spectrum is a limited resource, and much work has been dedicated towards spectrum management in order to develop optimal and efficient spectrum allocation methods that aim to maximise the efficiency of the exploitation of this resource [5].

A key issue associated with the radio frequency wireless spectrum is the strict regulation that has historically been in place, whereby a spectrum with a specific bandwidth is allocated to a specific wireless system for it exclusive usage. This approach was motivated by concerns surrounding interference issues among multiple users relying on the same wireless spectrum. This traditional spectrum regulation approach has effectively controlled interference between wireless communication systems but has at the same time given birth to the so-called issue of *spectrum scarcity*. As wireless systems have become more and more popular, the majority of the available spectrum regarded as desirable for wireless communications (i.e., low- to mid-frequency bands)

has been allocated all over the world, which has led to spectrum scarcity (i.e., less spectrum available for use by new systems and technologies). While new systems can in principle be deployed over high-frequency bands, this approach is far from ideal given the unfavourable propagation characteristics of high frequencies and the higher cost of the technology required to operate there. Low- to -mid-frequency bands, therefore, remain the most appealing bands for both legacy and new wireless communication systems. In recent years, research has suggested that most of the allocated spectrum is not fully utilised, which calls for better allocation of spectrum in accordance with anticipated usage in order to maintain sustainable development of wireless systems [1].

1.2   Spectrum Sharing

The issue of spectrum scarcity is addressed through spectrum sharing, which refers to the ability to share the same spectrum between two or more spectrum users, and this can be done in various ways including sharing between users, sharing between users and operators, as well as sharing between operators. As such, spectrum sharing techniques are broadly grouped into two categories: open sharing and hierarchical access. In open sharing, unconstrained sharing between networks is permitted without any restrictions, which is why this model is also known as the free sharing model. In hierarchical access, networks are divided into primary and secondary networks and each can access the spectrum without affecting the other, which concerns primary users (PUs) and secondary users (SUs), with SUs monitoring and accessing the spectrum whenever and wherever it is not being used by PUs, who have priority to exploit the spectrum [6].

Spectrum sharing entails optimising the spectrum for use and reuse in a manner that prevents interference across services. The traditional spectrum sharing technique involved assigning different frequency bands to different services. Separation was based on four axes: frequency, space, time and signal. This model minimised interference by mandating the testing of new communication equipment. As demand sored, new sharing models were introduced, notably: use of administrative methods, secondary market arrangements such as leasing and spectrum trading, and incentivising the use of efficient technologies such as low-power radios. On a national level, modern sharing approaches include allotment plans (includes frequency and spatial sharing), license time terms and standards (includes time sharing and coding sharing). For example, the International Telecommunication Union (ITU) provides a Licensed Shared Access sharing standard which is a regulatory approach that sets out a sharing framework and rules for a limited number of licensees.

Another classification of spectrum sharing considers three groups: interweave spectrum sharing, overlay spectrum sharing and underlay spectrum sharing. For interweave spectrum sharing, the allocation of spectrum is reliant upon 'holes' within the spectrum. These are voids that remain unused by users, and they are dynamic in that they shift in time and place. Using the activity patterns of users on the spectrum, these voids are detected and communicated to other parts of the system so that they may be shared [6].

In underlay spectrum sharing, the principle of knowledge of interference due to users is relied upon to allow primary and secondary systems to transmit information.

Here, a specific acceptable threshold is defined for both primary and secondary users, above which transmission is not allowed. Here, the secondary systems are aware of channel strengths of the primary system and below the set limit, the SUs can transmit in tandem with the PUs [6]. For the case of overlay systems, the secondary systems are aware of the primary system's channel gains and messages, so the SU can transmit simultaneously with the PU and interferences between the two can be offset using each other's power [6].

Another classification of spectrum sharing approaches considers dynamic spectrum sharing and cooperative spectrum sharing. In dynamic spectrum sharing, SUs are able to identify opportunities to utilise routes and transmit data through these. At present, dynamic spectrum sharing is plagued by issues of interference management which limit its usage, and given its early stages of development, this is an impressive spectrum sharing approach that applies advanced technologies to utilisation of spectrum. Given the dynamic nature of this system, it constantly unitises spectrum by considering available time slots and geographical locations, thereby enabling users to utilise specific pieces of spectrum at specific times and in specific spaces.

Considering cooperative spectrum sharing, this model leverages spatial diversity to limit interference issues and spectrum scarcity. In cooperative spectrum sharing applications, users are bound to fixed locations and the network topology is also fixed. The network functions by promoting a 'cooperation region' between PUs and SUs which enables spectrum to be shared between the primary and secondary systems. However, for cooperative spectrum sharing, special attention must be paid to outage probabilities which remain constant and do not decrease as is the case with dynamic sharing [6].

In recent years, another spectrum sharing approach has been studied: Geo-location based spectrum sharing. As the name suggests, this technique relies on a Geo-location spectrum database in order to log the spectrum usage data for PUs. Examples of logged data include the location, frequency band, and time the user was active, amongst others. When spectrum is required by the SU, they consult this database to inquire for spectrum access. An available spectrum band is found and allocated to the SU, without causing interference to the PU. This approach is fairly simple compared to other spectrum sharing techniques and it reduces the complexity altogether. The fact that a database is maintained ensures that relevant consultation is always done by users to ensure there is no interference for PUs or SUs. These advantages have led to popularity of Geo-location based spectrum sharing in recent years [7].

Considering the aforementioned spectrum sharing classifications, it is evident that technologies have evolved – spectrum issues, too, have evolved and newer classifications are continually developed in an effort to mitigate spectrum scarcity and interference issues, among others. The aforementioned spectrum sharing classifications are not exhaustive, and are intended to provide a general overview of the subject matter.

1.3   Cognitive Radio

One of the most popular principles to effectively implement spectrum sharing is Cognitive Radio (CR). CR is based on a hierarchical spectrum access principle (as discussed in Section 1.2) where a network of Primary Users (PUs) have a licence for exclusive access to the spectrum while a network of Secondary Users (SUs) without a spectrum

licence monitor the PU spectrum with the aim to find temporarily unused holes of spectrum (in the space, time or frequency domains) and then exploit them as long as the PUs do not require the use of such spectrum. In order to implement spectrum sharing following this principle, several functions are required in the CR system, which are briefly discussed below.

Firstly, the *spectrum awareness* function of CR is in charge of obtaining information about the surrounding radio environment in order to detect unused spectrum holes in the space, time or frequency domains that are suitable for SU transmissions. Spectrum awareness information can be acquired by directly monitoring the spectrum occupancy and use in order to detect any PU signals that may be potentially present/absent (i.e., spectrum sensing), but can also be obtained by means of other techniques such as geolocation databases or PU beacon signals if available.

Secondly, the *spectrum selection* function of CR is needed to decide which of the detected spectrum holes or spectrum opportunities are most suitable to perform the SU transmission. This involves two steps, namely spectrum analysis (in order to characterise the detected spectrum holes in terms of some relevant performance metrics or parameters such as bandwidth, interference, emission limits, frequency, etc.) and spectrum decision (in order to implement a method to effectively select the spectrum hole that has the greatest potential to meet the requirements of the SUs.)

Thirdly, the *spectrum sharing* function of CR is in charge of providing a fair spectrum access to the coexisting SUs of the same network by coordinating the access to the available spectrum holes similar to a medium access control protocol (i.e., horizontal spectrum sharing) while at the same time ensuring that no interference is caused to the PUs (i.e., vertical spectrum sharing). Notice that the term used to refer to this third component of the CR principle is the same used to refer to the ability to share spectrum between different spectrum users (discussed in Section 1.2), however in each case this term is employed with different a connotation and should not be confused.

Fourthly, the *spectrum mobility* function of CR is in charge of ensuring that the SUs vacate the spectrum as soon as a PU transmission is detected in order to avoid harmful interference. This function is also known as spectrum handover.

The main contribution of this thesis is related to the spectrum awareness function as it enables any spectrum-aware system to obtain information about the surrounding radio environment. Spectrum awareness is discussed below in more detail.

1.4   Spectrum Awareness

As telecommunication organisations and systems implement spectrum sharing to mitigate the spectrum scarcity problem, there is an urging need for increased awareness in radio frequency usage. Spectrum awareness is gaining traction in the field of communication. This is the feature of radio equipment that automatically detects a network through spectrum sensing (also referred to as signal detection) algorithms and determines the extent to which spectrum is being used in the surrounding environment. Spectrum awareness is an essential aspect of wireless communication technology and a key enabler of the spectrum sharing concept. Wireless communication systems can obtain spectrum awareness information by monitoring the spectrum usage in the frequency and time domains and representing this information as a time-frequency
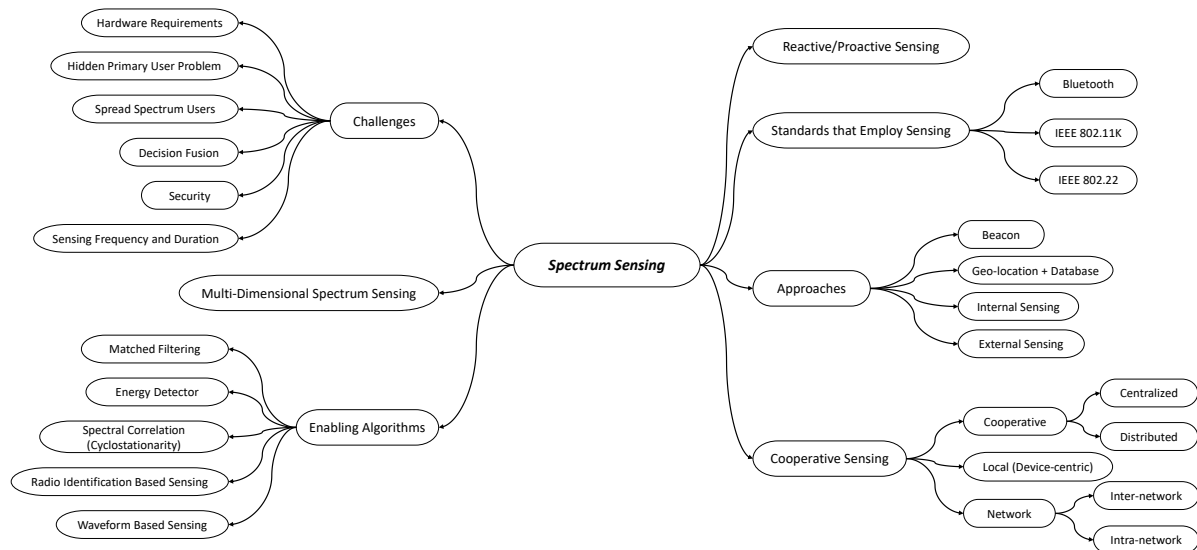
Figure 1.1: Relevant aspects of spectrum sensing.

matrix, which is also known as *spectrogram*. Various spectrum awareness techniques have been classified in the literature, and emerging ones are also highlighted.

In general, spectrum awareness techniques are grouped into passive and active awareness. For the former, SUs are able to receive and use spectrum awareness information from outside the secondary system (i.e., they use the PU's spectrum information). In active awareness, SUs are able to sense their environment and modify transmission based upon the measurements obtained. Active awareness may be performed through both cooperative or non-cooperative methods [8].

Spectrum awareness techniques are also classified according to the response time and topology of the system. Response times can be rapid or slow, and topologies can be distributed or centralised. Passive approaches are usually slow whereas active approaches are mostly classified as rapid. In distributed systems, nodes are locally aware of the spectrum and this approach is favourable for cases where spectrum sensing is not viable. In contrast, centralised systems strictly regulate the spectrum usage and they may be favourable in cases where chaotic situations must be avoided [8].

Perhaps the most important of these in establishing CR is spectrum sensing. Spectrum sensing or detection represents the first step in spectrum sharing. Fig. 1.1 provides a general summary of the spectrum sensing concept with an indication of the major issues concerned, including spectrum sensing principles, types and challenges, among other relevant aspects [9]. This function serves to improve spectrum utilization through identification of unused spectrum as well as to limit interference of unlicensed users with licensed users. Spectrum sensing aims to decide between two hypotheses, H_0 and H_1. These techniques are classified into primary transmitter detection and interference temperature concept. Primary transmitter detection can be further classified into energy detection, matched filter detection and feature detection. Key issues surrounding spectrum sensing remain the restricted sensing ability of CRs, interferences measurement, and spectrum sensing in multi-user environments [8].

Several authors have developed different categories for spectrum sensing techniques. A popular classification is into direct and indirect methods; the direct method relies upon a frequency domain approach whereas the indirect method relies upon a time domain approach. Another classification of spectrum sensing methods is into model-based parametric method and periodogram-based non-parametric method. Yet another type of spectrum sensing classification is according to the application. Spectrum sensing in cases where spectrum opportunities must be detected is divided into primary transmitter detection and cooperative detection. Primary transmitter detection incorporates detection of PUs based upon the signal received. Cooperative detection relies on spectrum signals detected through cooperation of users [10].

Spectrum sensing approaches are not able to guarantee quality of service in most practical cases, which calls for database approaches, particularly for satellite communications. Owing to this, as well as many other difficulties associated with spectrum sensing, databases are a popular method used for spectrum awareness. This is partly owed to the fact that databases guarantee better protection to users. The basic operating principle of the database methodology is that SUs are unable to access spectrum until the database allows it, and the database conducts prior checks to ensure the spectrum is available.

The most general database approach relies upon spectrum measurements to obtain data such as occupancy information including very precise geographic location. The database also contains information regarding spectrum regulations, and these data are relayed to SUs in order to ensure adherence to standards, for example, maximum allowed transmission power. When the database receives a request from SUs, it checks against standards such as interference tolerance of receivers and informs SUs regarding the available spectrum to use in their location. Availability of frequency is also essential here. Databases enable the use of historical data to predict future spectrum use [8].

One common strategy for radio awareness is energy detector method. Here, a network is detected through measuring noise variance for correlation with predefined thresholds. Another method is waveform-based sensing. This approach entails detecting fixed patterns in wireless systems such as spreading sequence, preambles and pilot signals. The cyclostationarity-based sensing method monitors periodicities in the received signal using cyclic spectral density (CSD). Radio identification-based sensing focuses on examining the transmission technology by considering its spectrum characteristics. Spectrum database can also be utilised as they provide information related to communication equipment's location, spectrum use, coverage and so forth.

There are many approaches for spectrum databases. One example is the radio environment map (REM), which is a centralised database including information about device locations, spectrum use and interference levels, amongst others. Another example is licensed shared access (LSA) whereby spectrum sharing is propagated on a licensed basis. Spectrum sharing in LSA may be static or dynamic, and the later often contains CR technologies. In general, spectrum databases are used to account for both short-term and long-term usage of spectrum at specific frequency bands, and data stored here can be used to achieve many purposes in spectrum allocation. For example, occupancy patterns in various bands can be modelled, and relationships between different bands can also be studied [8]. As a consequence, there is need for the adoption of effective spectrum management approaches among primary and secondary

users. According to research findings by the Federal Communications Commission (FCC), a spectrum's utilization rate in regards to time and frequency ranges between 15 and 85 percent [11]. This implies that there is always whitespace (WS), which is an unused portion of a spectrum. To improve the utilization rate, several approaches have been proposed including the adoption of a dynamic spectrum access (DSA) [11], [12]. This approach provides the ability for an unlicensed user (secondary user) to use a spectrum owned by another user (primary user) on the condition that the usage by the former does not result in harmful interference to the latter's services. However, SUs need to possess the ability to detect WS accurately. For instance, in a CR environment, which is an important technology in wireless communication, the utilization rate of a PU's networks is enhanced by the incorporation of intelligent transmitters that automatically alter their transmitting parameters based on the detection and utilization of "white holes" – unused radio resources in frequency, time, and space domains [13]. Effectively, a network that is equipped with CR capabilities exhibits improved utilization rate as it allows SUs to opportunistically gain access to a licensed band whenever the primary use is unavailable. In such a situation, spectrum sensing is crucially appropriate, since it can recognize instantaneous changes in the state of spectrum utilization.

One of the preferred approaches to accurate prediction of spectrum utilization is statistical methods. The use of statistics is based on the determination parameters such as frequency channel occupancy (FCO), frequency band occupancy (FBO), spectrum resource occupancy (SRO), and others [12], [14]. These parameters provide a statistical reference point in regards to spectrum utilization by PU as they represent the usage rate in spectrum sensing. One of the most common statistical approaches to spectrum sensing is duty cycle (DC) or channel occupancy rate (COR), which utilizes detectors such as the energy detector, waveform detector, and cyclostationary-based detectors [14]. Studies on the effectiveness of statistical approaches have demonstrated that these approaches could be utilised to not only achieve sophisticated spectral management, but also channel selection and MAC protocol design for enhanced spectrum efficiency.

The requirements of spectrum sensing are often challenging. Some of the notable challenges in spectrum sensing in DSA include high accuracy, low latency, low computational cost [12]. In an attempt to solve these challenges, new approaches such as smart spectrum access have been studied. In smart spectrum access, the characteristics of spectrum utilization by PU are estimated based on spectrum measurements that are based on a priori statistical information. These measurements can be used to enhance the performance of spectrum sensing and DSA-based wireless networks. However, as asserted by Mizuchii et al [12], [13], [14], an increase in efficiency of spectrum usage measurement could be achieved by using a two-layer smart spectrum access implementation. In this approach, the first layer is a DSA-based spectrum sharing platform and the second layer is a spectrum awareness system (SAS) that is dedicated on the acquisition of a priori information. However, despite lower costs in the implementation of statistical information estimation, the level of complexity associated with SAS implementation in regards to spectrum area estimation is high due to the framework's larger area of coverage, which demands for a significant number of spatially deployed sensors. This assertion has resulted in the adoption of several methods of estimating spectrum utilization.

1.5 Signal Area Estimation

1.5.1 Concept Overview

Wireless communication signals are often represented in the time-frequency domain by means of spectrograms, which show the time evolution of the power spectral density of a signal or set of signals present in a frequency band. In many practical applications spectrograms are processed to extract relevant signal information such as the received signal strength, carrier frequency, occupied bandwidth, spectral mask and transmission pattern. Among the many signal parameters that can be extracted from a spectrogram, the interest of this research is on accurately determining the time-frequency region occupied by each radio transmission or signal component within a spectrogram, which has been referred to in the literature as Signal Area (SA). By definition, an SA is a rectangularly-shaped cluster of spectrogram points where a transmitted signal component is present. Each of such points or elements of the spectrogram corresponds to a measured time slot and frequency bin in the time and frequency domains, respectively. The dimensions of each SA within a spectrogram indicate the bandwidth occupied by each radio transmission as well as its start and end times. Thus, the SA precisely determines the occupied bandwidth and start/end times of each radio transmission. The ability to accurately extract this information from a spectrogram can be useful in many practical scenarios such as spectrum surveillance for enforcement of spectrum regulations or gathering of signal intelligence in military applications, signal interception and identification, electronic warfare and radio environment spectral awareness (e.g., databases for spectrum sharing).

It is worth noting that, as stated above, this work assumes a rectangularly-shaped SA model. Such assumption should be valid for the vast majority of signals found in wireless communication technologies. On the one hand, for transmitters that operate at a constant carrier frequency and with a constant signal bandwidth, the SAs generated by them will be perfectly rectangular. This includes the majority of wireless communication systems. On the other hand, however, some wireless technologies will not operate at a constant carrier frequency and/or with a constant signal bandwidth and, as a result, the resulting SA in a spectrogram will not be perfectly rectangular. Some examples of this case include analogue signals based on frequency modulation (where the carrier frequency is constant but the signal bandwidth is variable) and wireless systems based on frequency hopping (where the signal bandwidth is usually constant but the carrier frequency changes over time according to a predefined hopping pattern). Chirped spread spectrum signals such as those generated by LoRa systems represent another example of such kind. Even in these cases the rectangular SA model considered in this work is still useful for the purpose of SAE. This is because wireless systems that do not operate at a constant carrier frequency and/or with a constant signal bandwidth fall into one of two possible categories, namely one where the frequency variability of the signal is limited within a certain minimum and maximum frequency (e.g., frequency modulated signals and LoRa signals) or another category where the signal can be decomposed into a number of signal subcomponents, each of which can be accurately represented by a rectangular SA (e.g., frequency hopping signals). These observations motivate the consideration of a rectangular SA model for the purpose of SAE. Notice that this is a common assumption in many other works in the literature.
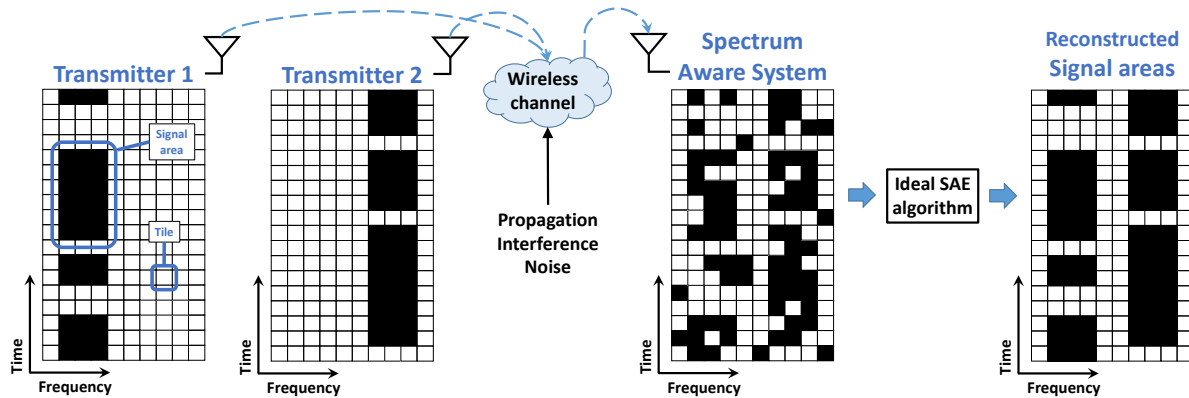
Figure 1.2: Illustration of the concept of Signal Area (SA) and system model for Signal Area Estimation (SAE).

One of the merits of Signal Area Estimation (SAE) in wireless communication is that it helps spectrum awareness systems (SAS) to allocate spectrum to users in an efficient way. For instance, the introduction of DSA has helped secondary users (SU) be assigned the spectrum without interfering with the primary users (PU). Additionally, paid users' utilised spectrum leaves significant white space (WS), which can be assigned to secondary users. It is necessary to have spectrum usage detection (SUD) methods that can attain high accuracy, low cost, and low latency to achieve a smart spectrum assignment to the SU. The idea of SUD can be useful in other application scenarios such as compliance verification and enforcement of spectrum regulations, and network planning and optimisation. Thus, there is a need to implement techniques that ensure high performance in SAS. In this context, SAE is an essential process in SAS.

SAE methods are applied to spectrum readings based on two-dimensional time-frequency grids of spectrum data. The time-frequency grids consist of clustered tiles where each element reflects the signal presence state in the corresponding time and frequency point. In power spectrograms, each tile represents a continuous-domain power value, which can be mapped to a discrete-domain occupied/empty state by using an appropriate decision threshold [15]. This binary time-frequency grid provides the fundamental data required for SAE and is the input information that most SAE methods need, based on which they will attempt to estimate as accurately as possible rectangularly-shaped regions containing adjacent tiles in the occupied state. Each of such regions is referred to as a Signal Area (SA) and it univocally identifies the occupied bandwidth and duration of each radio transmission. Notice that, by definition, most wireless communication signals should produce a rectangularly-shaped SA – or a set of rectangular SAs in the case of certain particular signal formats (e.g., frequency hopping signals). However, due to the degradation introduced by the presence of noise and the radio propagation channel, the SAs present in the spectrogram observed at the radio receiver will not necessarily have a perfectly rectangular solid shape. The purpose of SAE methods is to attempt to decide the dimensions of each SA in a spectrogram as accurately as possible and reconstruct the original rectangular SAs produced by the transmitter activity based on the imperfect/degraded version observed at the receiver. The concept and considered system model are illustrated in Fig. 1.2.

10

The process of determining the right SA begins with sampling the spectrum and generating the observed power levels for each time slot and frequency bin (i.e., each tile) [16]. The process then involves the use of a threshold to check the power levels, producing a binary matrix that indicates whether every tile is deemed to be in the idle or busy state, referring, respectively, to the absence or presence of a signal component in that tile. The binarization of power spectrograms is aimed at simplifying the process of SAE, given that, by definition, a SA represents a hard boundary between a region of the spectrogram where a signal is present and another region where it is not. Attempting SAE directly on a power spectrogram, rather than a binary spectrogram, would therefore increase the complexity of this task. Thus, the resulting binary matrix becomes the input to the SAE algorithm, which extracts the set or sets of tiles in rectangular clusters for which it detects one or more SAs. The process, however, is not trivial since the spectrum data observed by the monitoring spectrum-aware system is a degraded version of the transmitted signals after having suffered impairments introduced by radio propagation, the receiver's own noise and other external sources of unwanted noise and interference (e.g., out-of-band transmissions, ambient noise or man-made noise) [17–22]. The process of performing SAE encounters similar challenges to that of spectrum sensing or signal detection, given that SAE methods rely on the output of spectrum sensing techniques, making them equally vulnerable to missed detections and false alarms [11]. Missed detections occur when the signal detection method employed detects occupied tiles as idle, while false alarms occur when idle tiles are deemed busy, with the two errors affecting the actual shape of the observed SAs and degrading the performance of SAE schemes. The occurrence of sensing errors for individual tiles is the major challenge in the use of SAE techniques [23].

Despite the close relation between spectrum sensing (or signal detection) methods and SAE methods, it is worth noting that the ultimate purpose of SAE methods is different from that of signal detection techniques. Signal detection techniques are aimed at accurately detecting the instantaneous presence of a signal in a certain frequency band and therefore it is important to produce an accurate detection in every time-frequency tile. However, on the other hand, SAE is concerned with an accurate estimation of the overall SA but certainly pays minimal attention to the accuracy of individual tiles as long as the overall SA can be estimated accurately. This is because the aim of SAE methods is to establish the time-frequency region occupied by each SA rather than the instantaneous signal presence in each time-frequency point of the spectrum. Moreover, signal detection methods are usually aimed at providing real-time decisions on the instantaneous (current) spectrum occupancy state and this information is normally used for short-term decisions (i.e., transmit or vacate the channel immediately), while SAE methods are usually not envisaged to be applied in real-time (which would certainly be not possible due to the time span needed to capture the amount of data required to complete a spectrogram). SAE methods are typically employed for offline processing of spectrum occupancy data and its characterisation in a longer-term. The information obtained from SAE is typically useful for optimizing spectrum and radio resource management in the longer-term. Therefore, in SAE the focus is on determining the spectrum occupancy pattern of spectrum users in the time-frequency domains and in a medium to long term. SAE methods rely on the output of signal detection methods but have a different purpose and objective.

1.5.2 Existing Signal Area Estimation Methods

Several methods have been proposed in the literature to estimate accurately the SAs present in a radio spectrogram based on the (degraded) signal power data observed at the receiver [11, 12, 24–33]. Some popular methods include fast Fourier transform-based energy detection (ED-FFT) [33], Contour-Tracing (CT-SA) algorithms [31], and the so-called Simple Signal Area (SSA) algorithm proposed in [11, 12, 32]. From the existing literature on SAE, the most common approach that many authors have exploited is ED-FFT [33] owing to its simplicity and low computational cost. This approach simply determines the state of every tile (busy or idle) in the time-frequency domain using tile-by-tile ED-FFT [34]. While simple and convenient, ED-FFT methods produce no rectangular estimation of the SA in the spectrum and therefore tend to be more inaccurate. Nevertheless, ED-FFT can be used (and will be used in this research) as a reference baseline for comparison with other existing and newly proposed SAE methods. A more sophisticated approach is the Transmission Encapsulation based on the Connected Component Labelling (TECCL) method proposed in [31], which performs clustering based on connected component labelling [35] and estimates the SA of each cluster as its extreme dimensions (bounding box). This method can be implemented using standard Contour-Tracing (CT-SA) techniques [36] (see [12] for instance), which is the approach adopted in this research. A more powerful and accurate SAE method is the SSA algorithm proposed in [11, 12, 32], which is a sophisticated method of estimating the SA in the time-frequency domain in a series of steps. The steps in SSA include raster scan to detect the first corner of a potential SA, horizontal scan to evaluate the width of the SA, a coarse estimation of the SA height and finally a fine height estimation procedure to determine the approximate total dimensions of the SA. Some variants to reduce the impact of false alarms are proposed in [11, 32, 33].

1.6 Image Processing for Signal Area Estimation

Digital image processing refers to the use of computers to process digital images through algorithms in order to achieve several specific objectives, which can include improving certain aspects of a digital image, extracting meaningful information, or generating reports and data for further analysis. This methodology involves the use of computerised algorithms in order to derive meaningful information from input images. The analysis of images is a necessity and has found many application in different disciplines, including wireless communication systems. Image processing is a well-developed field where many advanced and sophisticated tools have been proposed to detect shapes in noisy images, which are potentially well-suited to the SAE problem.

There exist some studies on the application of image processing techniques to resolve certain problems in wireless communication systems. Some examples that can be related to this research include the study presented in [37], where a grid concept similar to the concept of SA is considered. According to [37], shape recognition approaches can be used in detecting the presence or absence of a new shape within a defined database. In this case, the authors focus on the estimation of false alarm estimates in the implementation of a shape recognition algorithm. Specifically, the illustrated method assigns the right matching threshold by defining the number of false alarms,

which could lead to either the acceptance or rejection of image features based on the threshold of shape matching. Another related example includes the study presented in [38], where power spectrum maps are used as a tool to estimate the presence of a PU's signal across a defined geographical area. Images of power maps are used to determine the distribution strength of a signal besides determining the spectrum utilization in a defined region. In this case, the power spectrum map is considered as an image representation of the spectrum. Based on this approach, a model of power spectrum estimation is proposed. The setup includes several receiving SUs and transmitting PUs that are spatially distributed in the region under investigation. To improve on the accuracy levels, the receiver SUs are uniformly spaced. In their conclusion, the authors illustrate how image processing techniques can be used to accurately estimate the presence of a PU's signal across a defined geographical area.

Despite some earlier applications of image processing techniques to certain research problems in wireless communication systems, to the best of the author's knowledge there is no rigorous study that has systematically investigated the application of image processing techniques to the problem of SAE in spectrum-aware communication systems. The problem of estimating a solid SA in a time-frequency matrix of degraded power values and their corresponding binary one/zero observations is equivalent to the problem of recognition of patterns in an noisy image (in this case, rectangularly shaped solid areas). The use of image processing methods to the problem of SAE is motivated by the fact that the problem of estimating a SA in a noisy spectrogram is similar to the problem or recognising a rectangle in a noisy image. Image processing techniques can be employed to this end by treating the spectrogram of power values as a greyscale image or its binary version as a black-and-white image, where each spectrogram time-frequency point represents an image pixel (the latter case is considered in this research). Therefore, by interpreting each radio spectrogram point (indicating a binary occupied/empty state) as a pixel in a binary (black-and-white) image, spectrograms can be seen as images, which enables the application of several powerful image processing techniques to the problem of SAE, concretely, the estimation of solid rectangular shapes degraded by the presence of noise and radio propagation impairments. The problem of SAE then becomes the problem of detecting a rectangular shape in a binary noisy image. This innovative point of view opens a new perspective for interdisciplinary research where a broad range of powerful tools from the field of image processing can be exploited for SAE in spectrum-aware wireless communication systems. Image processing is a well-developed field where many advanced and sophisticated tools have been proposed to detect shapes in noisy images, which are potentially well-suited to the SAE problem considered in this work. Therefore, this new point of view enables the application of a rich body of knowledge from the field of image processing to the SAE problem.

Concretely, the interest of this research is in exploring the feasibility of using image processing techniques to enhance the accuracy of SAE, and to propose novel SAE methods based on image processing techniques. To this end, a broad range of relevant techniques from the field of image processing will be explored, including morphologic operations, edge detection and flood fill techniques, the Hough transform along with other heuristic methods as well as solutions based on deep learning techniques for the processing of images. These are all different techniques employed in image processing

to process, detect or enhance certain aspects of a digital image. Their application to problem of SAE will be investigated in this thesis. In some cases, the considered image processing technique will be directly applied to a binary spectrogram to determine to what extent this can improve the recognisability of SAs present in the spectrogram along with the corresponding optimum configuration of the particular technique's parameters. In other cases, different algorithms will be envisaged based on or inspired by the considered image processing technique and the binary spectrogram will be processed as an image accordingly. Each chapter of the thesis will consider one specific image processing technique and will apply one of these approaches to develop a suitable SAE method based on such image processing technique. A brief introduction of the main image processing techniques that will be investigated in this thesis in the context of SAE is provided in the subsequent paragraphs below.

One of the types of image processing techniques relied upon in this research are those embraced by the concept of mathematical morphology, which is a set theory and collection of non-linear operations and techniques that provide an approach to digital image processing based on geometrical structures (i.e., morphological image processing is related to the shape or morphology of features in an image). Depending on the type of operation, specific features of the objects in an image, such as shape and size, can be given consideration. The morphological image processing approach is used in the identification of the characteristics and properties of an image by removing irrelevant background information. The background is considered to be noisy and is eliminated to allow a clearer analysis of the object under study depending on its morphology. After the elimination of the background, the process then involves an analysis of the morphology.

Another two well-known techniques from the field of image processing, namely edge detection and flood fill, are of interest in this research. Edge detection is an image processing technique used to find edges of objects or boundaries between two regions within an image. The main objective of edge detection is to determine the most likely boundaries of potential objects in the noisy image. Once these boundaries are determined, a flood fill algorithm can be employed to fill the space within the detects edges in order to produce solid objects (i.e., such as SAs in a radio spectrogram).

In addition, the Hough Transform (HT) is a feature extraction technique in image processing whose purpose is to identify imperfect instances of objects in an image. The HT originated from the basic need to detect certain shapes inside arbitrary images corrupted by noise and other artefacts and is well suited to detect rectangular shapes such as those arising from SAs in radio spectrograms.

Overall, SAE remains to date an essential area of exploration in wireless communication systems. Despite having received some attention, it remains a largely unexplored research topic in spectrum-aware systems. Moreover, the suitability of image processing techniques in the particular field of SAE has not been investigated so far, which motivates the research presented in this thesis.

1.7 Motivation and Objectives

Today, most wireless communication systems rely on radio frequency spectrum to relay data, and there are many aspects of the spectrum that must be accounted for

to ensure seamless inter-connectivity for users, the most important of which include spectrum scarcity, spectrum awareness and spectrum management. While these problems have persisted for nearly as long as modern wireless communication systems themselves, certain recent technologies propose spectrum sharing approaches to try to allocate spectrum between licensed and unlicensed users, and the key here is to identify and allot unused spectrum to users. Spectrum awareness information is critical to resolving such issues, and it is also widely used in many other application scenarios such as compliance verification and enforcement of spectrum regulations as well as network planning and optimisation.

Relevant spectrum awareness information can be extracted from radio spectrograms by means of SAE methods. Despite having received some attention, overall, SAE remains to date a largely unexplored research topic in spectrum-aware systems and an essential area of exploration in wireless communication systems. Moreover, most existing SAE methods are heuristic in nature. In this context, this thesis aims to explore the applicability and suitability of image processing techniques to the detection and estimation of SA in empirical spectrum data sets in the context of wireless communication systems. Despite some earlier applications of image processing techniques to certain research problems in wireless communication systems, there is no rigorous study that has systematically investigated the application of image processing techniques to the problem of SAE in spectrum-aware communication systems. The suitability of image processing techniques in other areas of wireless communications has received some previous attention, however it remains unexplored in the particular field of SAE, where their applicability has not been investigated so far, and this motivates the research presented in this thesis. This thesis therefore aims to fill this gap by investigating the feasibility of using image processing techniques to enhance the accuracy of SAE. The main objective is to demonstrate that SAE methods can benefit from the application of image processing principles by proposing novel SAE methods based on image processing techniques. To this end, a broad range of relevant techniques from the field of image processing will be explored, including morphologic operations, edge detection and flood fill techniques, the Hough transform along with other heuristic methods as well as solutions based on deep learning techniques for the processing of images. Based on this approach, this research will be able to demonstrate that it is practical to utilise several algorithms from image processing to improve the accuracy of spectrum SAE estimation. The novel methods that arise from this research can be useful for the development of spectrum-aware systems in practical spectrum sharing scenarios. Such methods can provide relevant information to the research community in the development of spectrum usage models and assist policy makers to define adequate DSA policies for improving the exploitation of underutilised spectrum resources.

1.8   Thesis Contributions and Organisation

Leveraging on the lessons learned from previous studies carried out so far and the broad body of knowledge from the field of image processing, the research carried out in this thesis provides multiple contributions, each of them presented in a separate chapter. Fig. 1.3 shows the organisation of this thesis. The contributions presented in each chapter are as follows:
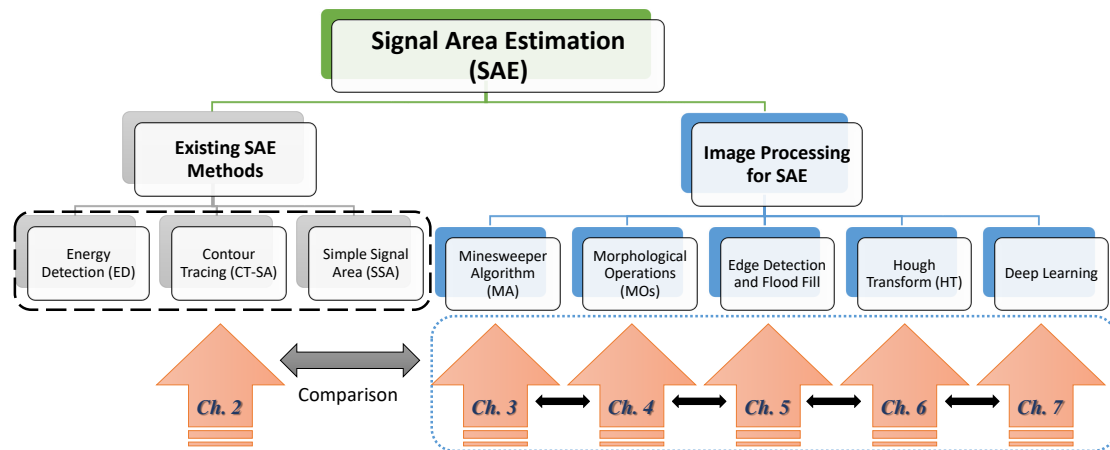
Figure 1.3: Illustration of the structure of this thesis.

- Chapter 2 presents a comparative study of the performance of existing SAE methods under different configuration parameters. This study fills the gap due to the lack of comparative research to show how the configuration of such methods affects their relative performance. Relevant configuration parameters that have been considered in previous studies include the energy decision threshold used to convert continuous-domain power values to discrete spectrograms and the frequency/time resolution of spectrum measurements. The impact of the decision threshold and the frequency/time resolution on the impact of SAE methods is investigated under various operational conditions, and the most appropriate configuration for SAE methods is determined. This study provides useful insights into the optimum design and configuration of SAE methods that will be useful for the aspects researched in subsequent chapters.

- Chapter 3 proposes a novel SAE technique based on a minesweeper algorithm (MA), which can be seen as a kind of morphological operation and therefore as a first attempt to apply image processing principles to SAE. The proposed method processes each tile in the time-frequency matrix (spectrogram) where the SA is to be detected to determine the most likely state (busy/idle) based on the number of busy tiles around it. Two variants are explored, one where the number of busy tiles around a central tile is compared to a threshold to decide the central tile state and a more complex approach where the actual pattern of idle/busy states around the central tile (and not only the number of busy tiles) is taken into account to make the final decision. The proposed method can be employed both as a standalone SAE method as well as a pre/post-processing technique for other SAE methods (to correct sensing errors or errors introduced by the other method itself). When used as a standalone SAE method it can provide similar or even

slightly better accuracy than other methods at a much lower computational cost. However, the best performance improvement is actually obtained when used as a pre/post-processing technique in combination with other existing methods (such as CT-SA and SSA), without increasing significantly the total computation cost. The proposed MA method has a low complexity and therefore does not increase significantly the computational cost of existing SAE methods while providing noticeable accuracy improvements when combined with them.

- Chapter 4 provides an exhaustive analysis of the impact of the main morphological operations (MOs) on the accuracy of SAE. By means of simulations, the result of applying different MOs to SAE are investigated under a broad range of con- figuration parameters. The analysis is conducted over a representative range of Signal-to-Noise ratio (SNR) conditions typically found in wireless communication systems. In such analysis, the performance of MOs is explored when used both as a standalone SAE method and along with other existing SAE methods from the literature (as pre/post-processing stages). Based on the outcomes of this study, a suitable MO-based SAE method is formulated, which employs MOs as pre/post-processing techniques to other existing SAE methods. The proposed approach is shown to provide significant accuracy improvements in the detected SAs (with respect to the case where the other SAE methods are used without the aid of MOs) and without having a noticeable impact on the overall computational cost (even reducing it in some cases).

- Chapter 5 provides an exhaustive analysis on the suitability of common edge detection techniques to the problem of SAE, including gradient-based methods, the Laplacian of Gaussian method, and the Canny method. Edge detection is used to find the most likely edges of SAs. Once these boundaries are determined, a flood fill algorithm is employed to fill the space within the detects edges in order to produce solid objects (i.e., final detected SAs). By means of simulations, the consequence of applying different edge detectors to SAE is investigated under a broad range of configuration parameters for each edge detector. In such analysis, the accuracy of edge detection plus flood fill is explored when used both as a standalone SAE method and as a pre/post-processing stage combined with other existing SAE methods from the literature. Based on the outcomes, the optimum configuration for each detector achieving the highest observed accuracy is deter- mined and a suitable SAE strategy is formulated for each edge detection method. The proposed approach is shown to provide significant accuracy improvements in the detected SAs at low SNR (with respect to the case where the other SAE methods are used alone) and without having a significant impact on the overall computational cost.

- Chapter 6 explores the usability of the Hough transform (HT) in the context of SAE and proposes two approaches that exploit the HT to estimate SAs in a spectrogram. The main interest of the proposed methods, and a distinguishing feature with respect to most other methods proposed in the literature, is their ability to automatically extract the parameters of each SA (i.e., the coordinates of the vertical and horizontal lines containing each SA). Most of the previously

proposed SAE methods produce enhanced spectrograms where the present SAs can be appreciated more accurately, however have not typically been designed to automatically provide the coordinates and dimensions of each SA. On the other hand, the HT-based methods proposed in this chapter can provide not only an enhanced spectrogram but also the coordinates and dimensions for each of the SAs detected in such spectrogram. This feature can be extremely useful in the automatic processing of radio spectrograms, for instance in the context of autonomous spectrum-aware wireless and mobile communication systems.

- Chapter 7 proposes a novel approach for SAE based on the use of widely known and well-developed deep learning techniques, aimed at addressing the limitations of existing methods proposed in the literature, which include one or more of the following issues: are based on heuristic principles, involve a number of configuration parameters that need to be tunned individually for each operation scenario, offer a poor performance when the SNR is low, or are unable to extract automatically the coordinates of each SA present in a spectrogram. The performance of the proposed method combined with some of the image processing techniques investigated in previous chapters is also investigated. As demonstrated by both simulation and experimental results, a key feature of the proposed method is the improvement in the SAE accuracy compared to other existing methods (in particular in the low SNR regime) and the capability to extract the location of the detected SAs automatically (which is useful for automatic spectrogram processing is autonomous spectrum-aware wireless systems).

Finally, Chapter 8 summarises the main findings of the research presented in this thesis and provides several suggestions for future work.

1.9   List of Publications

The contributions presented in this thesis have resulted in a number of publications in international journals and conferences, which are listed below.

Journals

[J.1] **M. M. Alammar** and M. López-Benítez, "Enhanced Signal Area Estimation Based on Edge Detection and Flood Fill," in *IEEE Access*, vol.10, pp. 47179–47194, Apr 28, 2022.

[J.2] **M. M. Alammar** and M. López-Benítez, "Signal Area Estimation based on Deep Learning," Physical Communication, vol. 59, pp. 1-17, August 2023.

[J.3] **M. M. Alammar**, M. López-Benítez, J. J. Lehtomäki and K. Umebayashi, "Enhanced Signal Area Estimation in Radio-Communication Spectrograms based on Morphological Image Processing," *submitted (under review)*.

[J.4] M. López-Benítez and **M. M. Alammar**, "Accurate Automatic Extraction of Signal Components from Noisy Radio Spectrograms," in *IEEE Transactions on Cognitive Communications and Networking*, vol.8, no.4 pp.1604–1617, Sep 12, 2022.

International conferences

[C.1] **M. M. Alammar** and M. López-Benítez, "Evaluation of the Impact of Thresholding and Frequency/Time Resolution on Signal Area Estimation Methods," in Proceedings of the *IEEE 93rd Vehicular Technology Conference (VTC 2021-Spring), in the 7th IEEE International Workshop on Smart Spectrum (IWSS 2021)*, Helsinki, Finland, April 25, 2021.

[C.2] **M. M. Alammar** and M. López-Benítez, "A Minesweeper Algorithm for Improved Signal Area Estimation in Spectrum Aware Systems," in Proceedings of the *28th IEEE International Conference on Telecommunications (ICT 2021)*, London, UK, June 1-3, 2021.

[C.3] **M. M. Alammar**, M. López-Benítez and Janne J. Lehtomäki, "Automatic Extraction of Signal Areas from Radio Spectrograms Based on the Hough Transform," in Proceedings of the *the 23rd IEEE International Symposium on a World of Wireless, Mobile and Multimedia Networks (WoWMoM 2022)*, Belfast, UK, June 14-17, 2022.

Chapter 2

Evaluation of the Impact of Thresholding and Frequency/Time Resolution on Signal Area Estimation Methods

2.1 Introduction

Spectrum awareness is an essential aspect of wireless communication technology. Wireless communication systems can obtain spectrum awareness information by monitoring the spectrum usage in the frequency and time domains and representing this information as a time-frequency matrix. In many practical cases, it is useful to determine the subsets of elements of such matrix where a signal is present (i.e., the signal area). Several signal area (SA) estimation methods with varying performance have been proposed in the literature. However, there is a lack of comparative research that shows how the configuration of such methods affects their relative performance. In this context, this chapter investigates the impact of two essential configuration aspects for any signal area estimation (SAE) method, namely the threshold used to decide whether each element of the time/frequency grid contains a signal component or just noise, and the frequency/time resolution of the measurements carried out to obtain such data matrix. Several popular threshold decision criteria and a broad range of measurement resolutions are investigated, showing that these two particular aspects play a key role in the optimum configuration and performance of SAE methods. Several useful findings and design guidelines are provided as well.

SAE is an essential process that entails determining the subsets of elements of a time-frequency matrix where a signal is present (i.e., the signal area). Several SAE methods with varying performance have been proposed in the literature. According to [12], spectrum usage detection processes include Fast Fourier transform (FFT), Energy detection (ED), and SAE methods. Since FFT and ED have been researched in [34] and the best methods proposed, the focus of this chapter shall be on SAE. Research done by [11] shows that the application of SAE methods has enabled the reduction of cost and attainment of high accuracy. However, the challenges affecting

the techniques include practical limitations and inaccuracies such as false alarms and missed detections [12]. This chapter shall concentrate on a comparative study of the performance of SAE methods under different configuration parameters and will cover the gap due to the lack of comparative research to show how the configuration of such methods affects their relative performance.

SAs can be detected based on several methods. The methods include ED techniques such as the Fourier transform energy detection or the simple signal area estimation (SSA) algorithm described in [11, 12, 32]. Besides, the contour tracing SA (CT-SA) estimation algorithm [31] can be applied. The three methods have been proposed in previous studies [33]. However, there is no comparative study to evaluate the performance of the three methods under different configuration parameters. Such a comparative study would aid in establishing the most appropriate SAE method and provide useful insights into the optimum design and configuration of SAE methods in practical deployments.

Configuration parameters that have been proposed in previous studies include varying the threshold for energy decisions and the frequency/time resolution of spectrum measurements [11, 16]. Threshold selection is affected by calculations such as the Time of Arrival (TOA) and the signal to noise ratio (SNR). Besides, a study in [33] has proposed a method of a threshold estimation technique that accounts for SNR, intending to adapt a normalized threshold [39]. However, frequency/time resolution depends on other parameters that shall be discussed in this chapter. Thus, this chapter entails an evaluation of the impact of these parameters and their corresponding significance in SAE techniques. The results of this chapter have been published in [40].

The main contributions of this study include:

- A comparative study on the three main methods of SAE that have been proposed in the literature, including ED, CT-SA and SSA.

- Evaluation of the impact of the threshold selection method on the performance of SAE methods under various operational parameters.

- Evaluation of the impact of frequency/time resolution on the estimated SA under various operational parameters.

- Establishment of the most appropriate configuration for SAE methods and gaining of some useful insights into the optimum design and configuration of SAE methods.

The rest of this chapter is organised as follows. First, Section 2.2 provides a formal description of the SAE problem considered in this work and an overview of the main SAE methods proposed to the date. Section 2.3 describes the methodology employed in this work to assess and compare the performance of the considered SAE methods under several parameter configurations and operation conditions. The obtained results are analysed and discussed in Section 2.4. Finally, Section 2.5 summarises the chapter.

2.2   Signal Area Estimation

2.2.1   Problem Description and Formulation

SAE emanates from spectrum measurements, which are based on two-dimensional time/frequency grids. The grids are composed of tiles where every element of the grid corresponds to a single time/frequency tile [16]. When a set of contiguous adjacent tiles are detected as occupied by a signal, a rectangular shaped area is detected, which is referred to as the SA. In this case, the detection distinguishes between two types of tile sets, namely H_0 (not occupied) and H_1 (occupied). The concept of SA refers to a rectangular set of tiles observed in the occupied (H_1) state. The problem of detecting a SA has some similarity to the classical problem of signal detection or spectrum sensing, however there are important differences. First, the focus is not on deciding the instantaneous busy/idle state of a channel but on knowing how spectrum is exploited by its users in order to understand their usage patterns in the time and frequency domains. As a result, an accurate detection of the H_0/H_1 state of every individual tile is in general irrelevant as long as the whole detected SA (i.e., set of tiles) is an accurate representation of the original time/frequency grid actually occupied by the signal (even though some of the individual tiles may be incorrect). Moreover, the detection of H_0/H_1 states in real time is not relevant in SAE (as it is in spectrum sensing) since this information is usually not useful in the short term but in the longer term in order to optimise spectrum and radio resource management decisions or, if it is the case, for spectrum regulatory purposes, network optimisation or any other application scenario where this information may be useful. However, SAE methods rely on spectrum sensing decisions and as such are affected by the same two types of errors in the signal detection process, namely missed detections (busy tiles detected as idle) and false alarms (idle tiles detected as busy) [11]. These two errors will affect the particular shapes of the estimated SAs and therefore the performance of the employed SAE methods.

The performance of SA is determined by several parameters, which can affect the accuracy and performance. Applying SA will involve sampling the spectrum into a set of observed power levels in the frequency and time domains [16]. The outcome is a set of power levels corresponding to each frequency and time bin or tile in the grid. Then, the power levels are compared to a predefined threshold value, which produces a binary matrix indicating the H_0 or H_1 states of every tile. This binary matrix of busy/idle tiles is the input information provided to the SAE method in order to extract the rectangular sets of tiles where one or more SAs are detected in the time/frequency grid. Notice that SAE methods are expected to identify perfectly rectangular sets of busy tiles in the time/frequency grid, which can be a challenging task given the corruption introduced by sensing errors in individual tiles.

The process of SAE is affected by the employed energy decision threshold as well as the time/frequency resolutions of the data grid. In this case, the resolution in the time domain can be adjusted by modifying the sensing period while the resolution in the frequency domain can be adjusted by modifying the employed FFT size [33]. Therefore, threshold selection and resolution are the main parameters that affect the performance and accuracy of SAE techniques and these constitute the focus of this chapter.

2.2.2 Threshold Selection Methods

The performance of threshold selection can be quantified based on the probability of false alarm (P_{fa}) and the probability of detection (P_d) as shown below [34]:

$$P_d(\lambda) = \mathcal{Q}\left(\frac{\frac{\lambda}{\sigma_w^2} - \mathcal{N}(1+\gamma)}{\sqrt{\mathcal{N}}(1+\gamma)}\right) \tag{2.1}$$

$$P_{fa}(\lambda) = \mathcal{Q}\left(\frac{\frac{\lambda}{\sigma_w^2} - \mathcal{N}}{\sqrt{\mathcal{N}}}\right) \tag{2.2}$$

where λ represents the threshold, σ_w^2 is the noise power, $\mathcal{N}$ is the number of signal samples, γ is the SNR and $\mathcal{Q}(\cdot)$ is the Gaussian tail probability Q-function [41].

The threshold selection methods most commonly considered in the literature are based on providing either a Constant False Alarm Rate (CFAR), a Constant Signal Detection Rate (CSDR), or a Minimum Sensing Error Rate (MSER). These methods have been studied comparatively in [34] in the context of evaluating the channel occupancy in cognitive radio. All three methods will be considered in this chapter in the context of SAE. A brief description of each threshold selection method is presented below.

Constant False Alarm Rate (CFAR)

The CFAR method is based on a target probability of false alarm value (P_{fa}^*). In this case, equation (2.2) is solved for the desired false alarm probability to obtain the optimum threshold λ^* as shown below:

$$\lambda^* = \left(\mathcal{Q}^{-1}(P_{fa}^*)\sqrt{\mathcal{N}} + \mathcal{N}\right)\sigma_w^2 \tag{2.3}$$

Notice that this method only requires noise power (σ_w^2) to be estimated in order to calculate the optimum threshold.

Constant Signal Detection Rate (CSDR)

The CSDR method entails selecting the decision threshold so that a certain target probability of detection (P_d^*) can be attained. In this case, solving (2.1) leads to the result below:

$$\lambda^* = \left(\mathcal{Q}^{-1}(P_d^*)\sqrt{\mathcal{N}} + \mathcal{N}\right)(1+\gamma)\sigma_w^2 \tag{2.4}$$

This method requires not only the noise power (σ_w^2) but also the SNR $\gamma = \sigma_x^2/\sigma_w^2$ to be estimated.

Minimum Sensing Error Rate (MSER)

The MSER method relies on the sensing error function below:

$$P_e(\lambda) = P_{fa}(\lambda) + P_{md}(\lambda) \tag{2.5}$$

and selects the decision threshold so as to minimise such sensing error function:

$$\lambda^* = \arg\min_{\lambda} P_e(\lambda) \tag{2.6}$$

Thus, the optimum threshold can be calculated by solving $dP_e(\lambda)/d\lambda = 0$ for λ and is given by:

$$\lambda^* = \left(1 + \sqrt{1 + \frac{2}{\mathcal{N}} \frac{(\gamma + 2)}{\gamma} \ln(1 + \gamma)}\right) \frac{\gamma + 1}{\gamma + 2} \mathcal{N} \sigma_w^2 \tag{2.7}$$

Thus, the MSER method also requires both SNR and noise power to be estimated in order to calculate the threshold.

2.2.3 Signal Area Estimation Methods

Three different approaches for SAE are considered in this work. The first one is a simple tile-by-tile ED, where the individual idle/busy state of each tile in the time/frequency grid is determined by comparing the power level of each tile to a predefined decision threshold. By definition, the ED method outputs a tile-by-tile result where no rectangular SAs in the spectrum are estimated and therefore it cannot be considered a true SAE method. Nevertheless, ED will be used in this work as a reference baseline or benchmark for comparison with other existing SAE methods (i.e., methods that can provide rectangular estimations of each SA detected in a radio spectrogram). The CT-SA estimation method proposed in [31] is also considered, where a rectangular SA is estimated based on contour tracing techniques. Essentially, CT-SA attempts to estimate each SA by determining a bounding box that includes all the relevant points or tiles that are believed to belong to the SA. This approach, however, is susceptible to noise since false alarms around the true SA points may lead to larger (and therefore inaccurate) estimated SAs. Finally, the SSA estimation method described in [11, 12, 32] is also included in this study. The latter is a more sophisticated method that estimates every SA present in the time/frequency grid by following several steps. First, a tile-by-tile raster scan is performed to find the first corner of a prospective SA (isolated busy points are assumed to be false alarms and are therefore discarded, while busy points surrounded by other busy points are considered as potential corner points and considered for further analysis in the subsequent step). Then, using a unit-width window with height Δt, a horizontal scan is performed to estimate the width of the SA. Such width is estimated by comparing the number of busy points observed within the window to an appropriately set threshold. When the scan detects an insufficient number of busy points it is assumed that the SA edge has been exceeded; the scan then stops and the corresponding SA width is determined. Afterwards, a coarse estimation of the SA height is carried out with a window with the same width as estimated for the SA (in the previous step) and height ΔT. This coarse estimation detects the approximated height of the SA by using a similar principle as in the previous step to detect the width. Finally, a fine height estimation is performed using a unit-height window (instead of using height ΔT) to provide an accurate estimation of the height of the SA, thus completing the accurate estimation of both width and height of the detected SA. The details of this method can be found in [32].
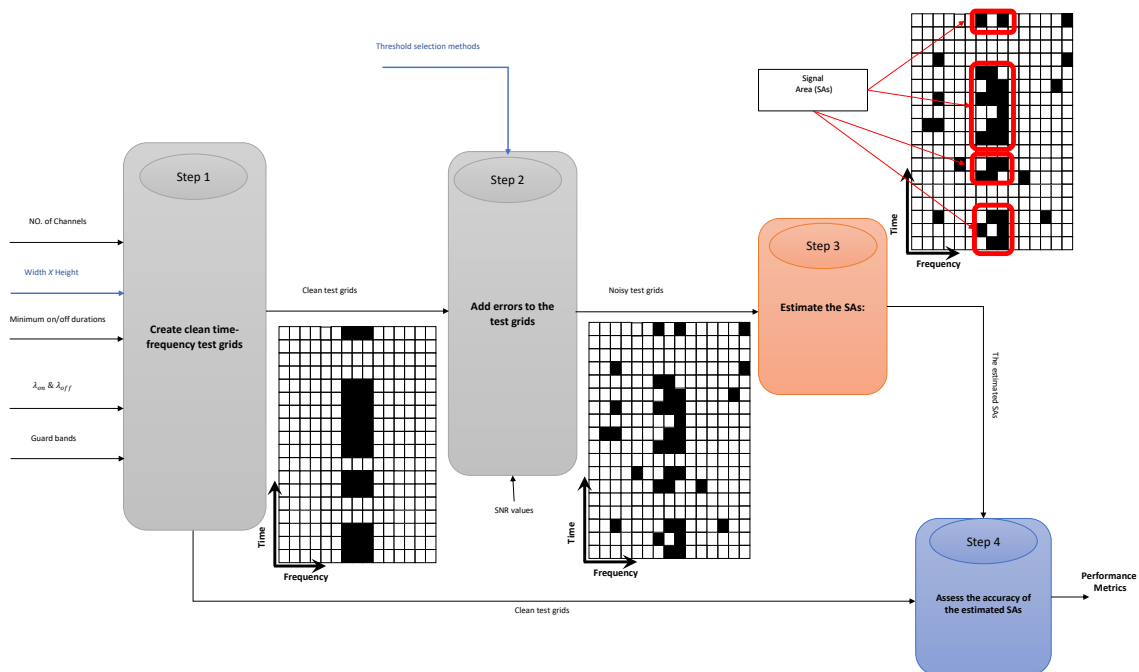
Figure 2.1: The flow diagram of the methodology.

2.3   Evaluation Methodology

2.3.1   Simulation Procedure

This experimental study adopts the use of simulation to test SAE techniques. Given that no software simulator available in the literature is well-suited for the purposes of the research carried out in this research, an in-home simulator was developed from the scratch in Matlab. The design approach adopted in the development of the simulation code is frequency and radio technology agnostic, meaning that no specific details or characteristics of a particular frequency band or radio technology have been considered and, as a result, the simulator is general enough for any spectrum scenario. The spectrograms involved in the simulation are based on synthetic spectrum occupancy data generated from various appropriate models. In the simulation, the generated time-frequency matrices (refered to as test grids) include channelized SAs that have occupancy statuses generated randomly through clearly defined constraints and are corrupted through the addition of random noise and interference before being fed to the evaluated SAE methods, which will operate under different configuration parameters. Finally, the signal area shall be detected based on the three considered methods, namely ED, CT-SA, and SSA. The process takes place in four distinct steps, namely time-frequency test grid creation, corruption of test grids, estimation of SAs, and assessment of the accuracy of the estimated SAs, as illustrated in Fig. 2.1. These steps are discussed in more detail below.

Step 1. Creation of the time-frequency test grids

A rectangular time/frequency grid is randomly generated based on a predefined resolution level. The width (the number of elements in the horizontal dimension) of the test grid is determined by the considered frequency resolution, while its height (the number of elements in the vertical dimension) is determined by the considered time resolution. Notice that in this thesis specific frequency or time units are not provided; instead, spectrograms are represented in terms of the number of points in each of these two dimensions (the actual mapping of these spectrogram points to a practical spectrogram would depend on the considered time and frequency resolutions of the power spectrum sampling process, which is beyond the scope of this research.) Three resolution categories are considered, with several resolution levels (in number of tiles for each dimension): low resolution (10×5, 20×10 and 50×25), medium resolution (100×50, 200×100 and 500×250), and high resolution (1000×500, 2000×1000 and 5000×2500). The resolutions of the test grids are specified in the format horizontal × vertical resolutions in the number of tiles.

   Channelised signal areas are then generated in the test grid based on specified transmission constraints. In this case, a known number of channels is set in the frequency domain and a set of ON/OFF transmissions randomly drawn from exponential distributions with rate parameters $\lambda_{on} = \lambda_{off} = 0.5$ points^{-1} (since transmission durations are generated in terms of the number of spectrogram points, the rate parameter of the corresponding exponential distribution has units of points^{-1}) and minimum on/off durations of 10 and 5 points, respectively. The total frequency span of the spectrogram is divided into three channels with equal bandwidth (1/3 of the spectrogram width with 5% reserved for guardbands). However, for simplicity and clarity of graphical representation, only the central channel is assumed to carry actual data traffic[1]. These test grids represent the original transmission pattern of the target transmitter(s) before the signal(s) pass(es) through the wireless channel and are degraded by propagation and internal/external noise/interference. Fig. 2.2a shows a simple example with five transmitters/channels in the test grid, where the resolutions of the test grid is 200×100 tiles and the minimum on/off durations are 20 and 10 points, respectively.

Step 2. Addition of signal detection errors to the test grid

This step involves the addition of errors to the clean test grids generated in Step 1. The errors are added in such a manner that they affect both the idle tiles (false alarms) and busy tiles (signal missed detections). In specific, idle (busy) tiles can randomly change to busy (idle) state with a certain probability of false alarm P_{fa} (probability of missed detection $1-P_d$). These probabilities are calculated assuming that the measured power samples are converted to binary idle/busy states according to one of the three considered threshold selection methods described in Section 2.2.2. For a detailed performance evaluation, an SNR range from –20 dB to +5 dB was considered and simulations were repeated for each individual SNR value within that range in 1-dB

---

[1]Notice that this choice is made simply for visual clarity in the graphical representation of the spectrograms and does not imply any assumption or any prior knowledge of the frequency extent of the signals to be measured. In this work, no prior information is assumed to be known about the time/frequency extent of the signals that may be present in a spectrogram.
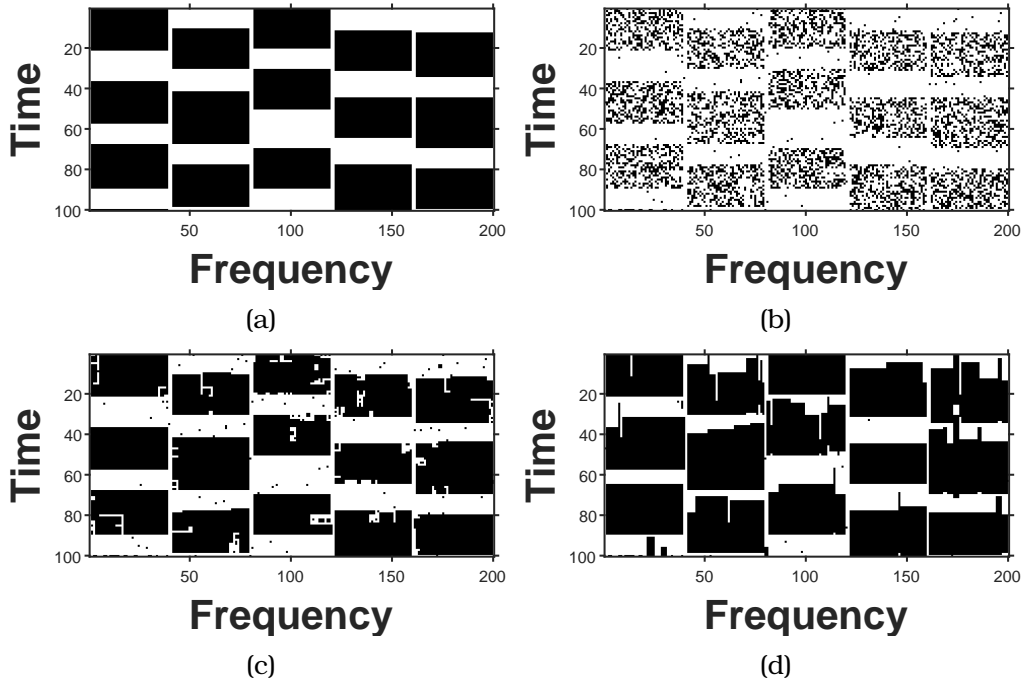
Figure 2.2: An example of a randomly generated test grid with the resolution 200×100: (a) Clean time/frequency test grid, (b) Time/frequency test grid with noise, (c) SA estimated by the CT-SA method, (d) SA estimated by the SSA method.

increments. Fig. 2.2b shows as an example the test grid of Fig. 2.2a as detected when the decision threshold is set based on the CFAR method with a decision threshold calculated for $P_{fa} = 0.01$ and a receiving SNR of –7 dB, at which $P_d \approx 0.39$.

Step 3. Application of the considered SAE method

This step involves the application of one of the SAE methods described in Section 2.2.3 to the (corrupted) noisy test grids obtained in Step 2 in order to estimate the SAs present in the clean test grid. Examples of the SA estimated by CT-SA and SSA methods based on the test grid of Fig. 2.2b are shown in Figs. 2.2c and 2.2d, respectively. In this work, the SSA detection masks were adjusted according to [32, eqs. (3)–(4)], while the values for the sensitivity thresholds were taken from [32]. This choice performs well but may not necessarily lead to a fine tuning of the SSA performance with the particular spectrum dataset employed in this study (an optimization approach is discussed in [32], which is beyond the scope of this work).

Step 4. Assessment of the accuracy of the estimated SAs

This step involves the verification of the accuracy of the estimated SA obtained from Step 3. It is performed through a comparison between each original clean test grid generated in Step 1 and the corresponding test grid obtained in Step 3. The accuracy is evaluated based on several performance metrics, which are explained below.

2.3.2 Performance Metrics

The probabilities of detection and false alarm are commonly used to assess the performance of signal detection methods. However, these metrics are of little use in the context of SAE since the focus is not the accuracy of the detection on every individual tile of the time/frequency signal grid but on the set of SA present, which are the result of some reconstruction processes where subsets of tiles are associated and recognised together as a SA. The analysis of these two probabilities individually does not provide a complete characterisation of the efficacy of the reconstruction implemented in a SAE method. Therefore, these probabilities will not be considered individually. Instead, other metrics that account for the combined impact of these metrics will be considered.

The accuracy of the studied SAE methods is assessed in this chapter by means of two performance metrics. First, a simple Accuracy (ACC) metric is used defined as the percentage of tiles (in either state, idle or busy) that are correctly detected in their real state, which can be obtained as the sum of true positive and true negative detection rates. The limitation of such accuracy metric is that the number of tiles in one state may outnumber those in the other state, thereby introducing a bias in the value of the metric. Thus, the preferred metric used here is the F1 score, which takes into consideration the possible imbalance between the number of tiles in idle and busy states in the original test grid. The F1 score is defined as:

$$F1 = \frac{2 \times TP}{2 \times TP + FP + FN},$$ (2.8)

where TP, FP and FN represent the number of true positive, false positive and false negative detections, respectively [42]. As opposed to the accuracy metric, whose range of values is affected by the ratio of idle/busy tiles in the original test grid, the F1 score always ranges within the interval [0,1] and therefore is a more fair and useful metric when there is an imbalance in the amount of idle/busy tiles in the original image, which is usually the case in most practical contexts.

The computation time of each SAE method is also evaluated in this chapter. This measure is important because it affects the overall performance of the SAE method when it is practically implemented. The broad heterogeneity of SAE methods available in the literature and the inherent characteristics of the principles on which they rely makes it difficult to adopt a common definition of computational complexity that is applicable to all possible cases and enables a fair comparison among different SAE methods. This problem is resolved by assessing and comparing the computational cost or complexity of different methods by means of the computation time, measured as the time required to execute each SAE method in an actual processor. This is a common approach widely used in other SAE studies and is also employed in this work (see Appendix A for a more detailed discussion).

2.4 Results

The results obtained for various thresholding and resolution simulations shall be discussed in this section. Simulation results are based on 100 different randomly generated test grids. For the SSA method, the parameters are configured as recommended in [12]. Common simulation parameter setting is shown in Table 2.1.

Table 2.1: Simulation parameters

Create clean test grids		Add noise to the test grids		The SSA Method	
number of channels	5	SNR	from -20 dB to 5 dB	Δt	min(min_on,min_off)
min_on	width/10	$\mathscr{N}$	100	ΔT	min(min_on,min_off/2)
min_off	min_on/2			γ_{step2}	0.1
λ_{on}	0.5			γ_{step3}	0.15
λ_{off}	0.5				
guard bands	0.05				

2.4.1   Impact of the Decision Threshold

Fig. 2.3 shows the value of the Accuracy (ACC) metric as a function of the SNR for the considered SAE methods (ED, CT-SA and SSA) when different threshold selection methods are employed (CFAR, CSDR and MSER). The results in Fig. 2.3 were obtained for a grid with a resolution of 100×50 tiles. As it can be appreciated in Fig. 2.3, the accuracy of the detected SA degrades as the SNR decreases, however several combinations of SAE and threshold selection methods show different sensitivity to a reduction in the experienced SNR. The results shown in Fig. 2.3 indicate that the criterion employed to select the decision threshold has a more significant impact on the resulting accuracy of the estimated SA than the particular SAE method itself. As matter of fact, it can be noticed that selecting the decision threshold according to the CSDR method leads to the worst accuracy in the estimated SA, while selecting the threshold according to the CFAR method leads to the best observed accuracy, for all the considered SAE methods. The use of different SAE methods obviously has an impact on the resulting estimation accuracy, however the criterion used to select the decision threshold has a more significant impact as shown in Fig. 2.3. This can be explained by the fact that SAE methods attempt to detect rectangular SA in the time/frequency grid based on the idle/busy states obtained after applying the selected decision threshold. An inappropriately set decision threshold will lead to a larger number of errors in the detected idle/busy state for each tile in the time/frequency grid and this will make it more difficult for the SAE method to correctly identify the existing SAs in the provided grid. Based on the results shown in Fig. 2.3, it can be concluded that the CFAR method provides the best performance for the three SAE methods. Notice that the CFAR method only needs the noise power to be known in order to set the decision threshold (as opposed to the CSDR and MSER methods, which also need the signal power or SNR to be accurately known) and this simplifies the practical implementation in real scenarios. Moreover, it can be noticed that the best accuracy over the whole range of SNR values is in general provided by the SSA method proposed in [32] when the decision threshold is set according to the CFAR method.

Fig. 2.4 shows the computation time as a function of the SNR for each considered SAE method (ED, CT-SA and SSA) and threshold selection method (CFAR, CSDR and MSER)[2]. It can be observed that the lowest computation time is for ED, which is the

---

[2]Notice that the computation time in some cases increases slightly around intermediate values of the SNR. This is because in this region it is more challenging to distinguish clearly the presence/absence of a signal component, thus requiring slightly higher computation times for some methods and configurations.
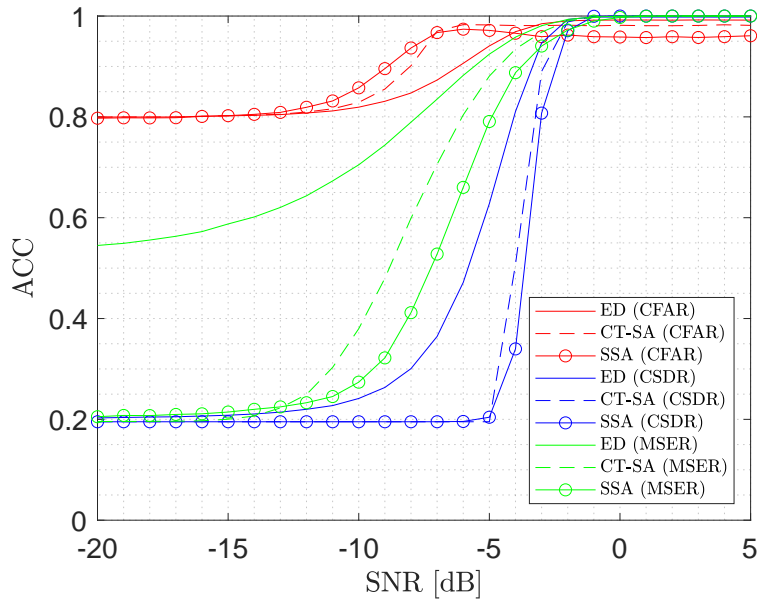
Figure 2.3: Accuracy (ACC) as a function of the SNR for the different SAE methods (ED, CT-SA, SSA) combined with different threshold selection methods (CFAR, CSDR, MSER).

simplest SAE method since it does not attempt to reconstruct any rectangular SAs and simply provides the idle/busy state of every tile. Consequently, its computation time is also constant with the SNR since the number of calculations performed by ED (i.e., comparing the power levels to a threshold for each tile) is constant regardless of the experienced SNR. On the other hand, for the CT-SA and SSA methods, the computation times are higher since these methods perform further processing of the tiles in the time/frequency grid in order to reconstruct rectangular SAs. In the case of the CT-SA method, the computation time increases as the SNR decreases as a result of the presence of more errors in the idle/busy states of the tiles at lower SNR, which makes it more difficult to correctly detect the SAs and requires a more computationally expensive processing for the CT-SA method. This is also corroborated by the computation time of the CT-SA method for the different threshold selection methods; notice that the threshold selection methods that provide a better accuracy for the CT-SA method in Fig. 2.3 also require a lower computation time, since less errors in the idle/busy state of the tiles in the grid means that the CT-SA can reconstruct the SAs not only more accurately (as shown in Fig. 2.3) but also more efficiently (as shown in Fig. 2.4). Compared to the ED and CT-SA methods, the SSA method provides an intermediate computation time that shows the interesting property of remaining approximately constant over the whole range of SNR values. This is because the SSA method systematically applies the scanning process described in Section 2.2.3, whose number of calculations does not depend on the presence of errors in the idle/busy state of the tiles in the grid (more errors will decrease the accuracy of the SSA method as shown in Fig. 2.3 but will not affect the set of computations required by the method, as shown in Fig. 2.4). This observation for the SSA method is also corroborated by the fact that the computation time of the SSA method is not significantly affected by the
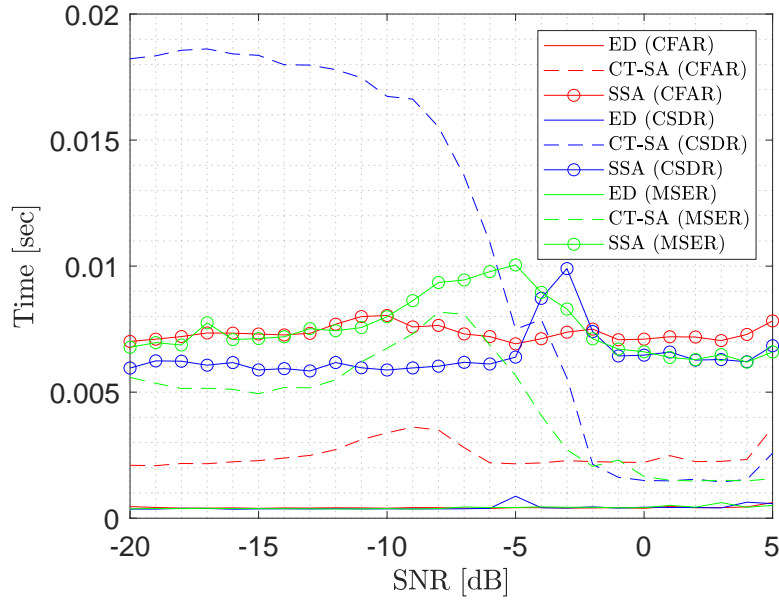
Figure 2.4: Computation time as a function of the SNR for the different SAE methods (ED, CT-SA, SSA) combined with different threshold selection methods (CFAR, CSDR, MSER).

criterion used to select the decision threshold as it can be observed in Fig. 2.4.

Taking into account the results shown in Figs. 2.3 and 2.4, the following two observations can be made. When the SNR is sufficiently high, ED is the preferred approach since it is straightforward to distinguish idle tiles from busy tiles with a very high level of accuracy (even with different values of the decision threshold) and a simple ED approach can provide a (virtually) perfect SA detection (regardless of the employed decision threshold) at the lowest computational cost. When the SNR is moderate to low, the presence of errors in the idle/busy states of the tiles will require some form of more sophisticated processing to detect the SAs and in this case the SSA method provides overall the best trade-off between accuracy and computational cost over the whole range of SNR.

2.4.2 Impact of the Time/Frequency Resolution

The analysis presented above showed that the best accuracy for each SAE method is obtained when the decision threshold is selected according to the CFAR method. This threshold selection method will be assumed in this section (and in future chapters as well) for all the SAE methods in order to investigate the impact of the time/frequency resolution on the accuracy of each SAE method.

Fig. 2.5 shows the performance of the accuracy (ACC) metric as a function of the SNR and the frequency/time resolution (in number of tiles for each dimension) of the signal grid. Fig. 2.6 shows the counterpart of Fig. 2.5 for the F1 score.

For the ED and CT-SA methods, it can be observed in both figures that the main factor affecting the accuracy of the estimated SA is the SNR. Concretely, as the SNR decreases, the accuracy for the ED and CT-SA methods degrades, as expected, and
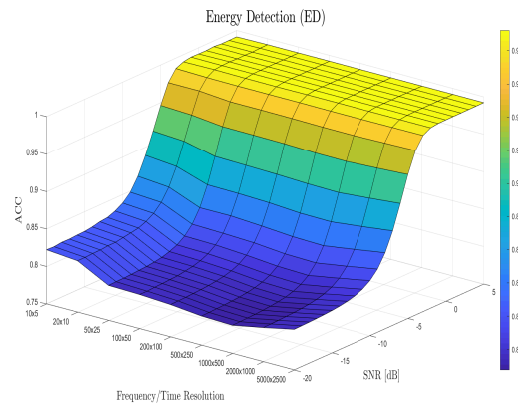
(a)
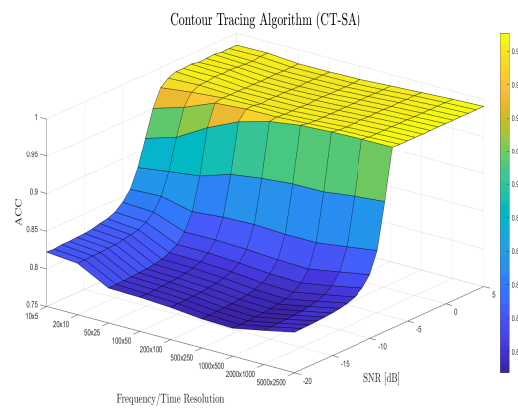
(b)
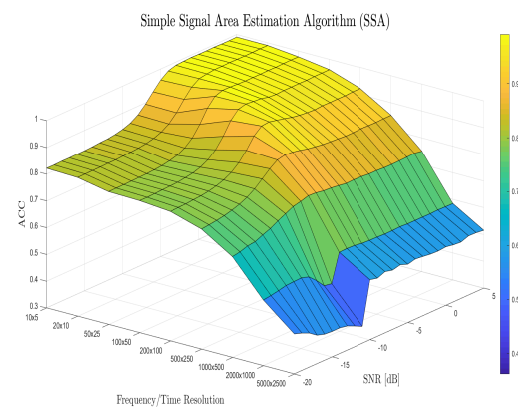
(c)

Figure 2.5: Accuracy (ACC) as a function of the SNR and the time/frequency resolution for the considered SAE methods: (a) ED, (b) CT-SA, and (C) SSA.
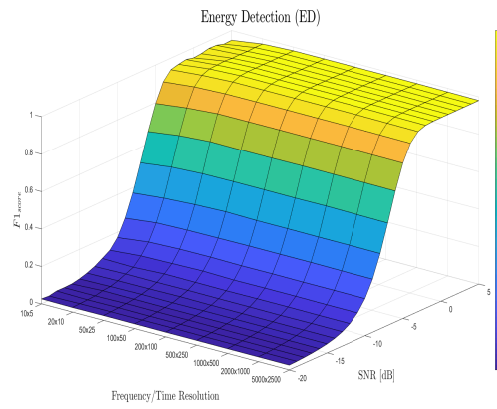
(a)
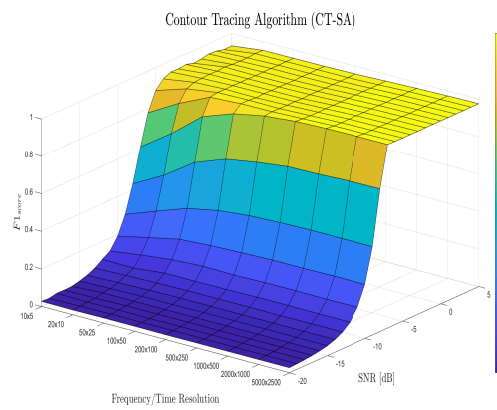
(b)
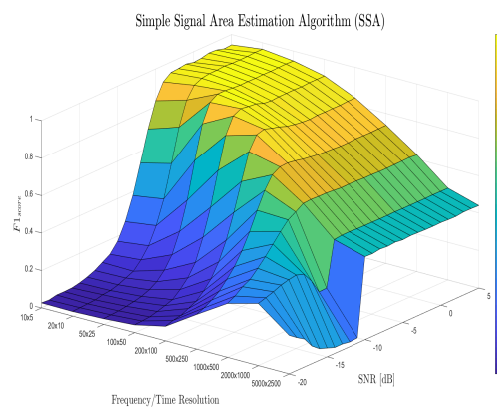
(c)

Figure 2.6: F1 score as a function of the SNR and the time/frequency resolution for the considered SAE methods: (a) ED, (b) CT-SA, and (C) SSA.

modifying the time/frequency resolution in these two methods does not have a significant impact on the resulting accuracy. The results shown in Fig. 2.5 in terms of the ACC parameter suggest that choosing a lower resolution might slightly improve the accuracy, however the improvement observed in Fig. 2.5 by choosing a lower resolution would be marginal. In the case of the ED and CT-SA methods, where the accuracy remains unaffected by the employed grid resolution, the time/frequency resolution should be decided based on the computational cost and a low resolution may be preferred.

For the SSA method, it can be observed that the accuracy of the estimated SA is affected not only by the SNR but also by the employed grid resolution. A reduction in the experienced SNR will also degrade the accuracy. However, in this case, and in contrast with the ED and CT-SA methods, it is possible to compensate for the degraded detection performance of the SSA method when the SNR decreases by increasing the frequency/time resolution. When a low grid resolution is used with the SSA method, it can be noticed that the SAE accuracy will be very close to 100% when the SNR is sufficiently high and will start to degrade when the SNR decreases below about -5 dB. For lower SNR values, it is possible to improve the accuracy by increasing the grid resolution. However, one can use this strategy with the SSA method to a limited extent since simply increasing the grid resolution will not always be able to keep an accuracy close to 100%, in particular if the SNR is very low. Moreover, increasing the resolution beyond certain point will not provide an accuracy improvement and, in fact, if the resolution is too high the accuracy of the SSA method will be significantly degraded, even at high SNR (this can be explained by the fact that a higher grid resolution means a higher number of tiles within the same SA and this will increase the probability that the scanning and recognition method used by the SSA method will fall into errors by its own nature). It is interesting to note that, for the SSA method, exists an optimum time/frequency resolution for each SNR value, which provides an additional degree of freedom in the configuration and optimisation of this method compared to the ED and CT-SA methods, where the variation of the grid resolution has no significant effect.

2.5 Summary

This chapter has presented a comparative study on the impact of thresholding and resolution on SAE methods. The investigated SA methods include ED, CT-SA, and SSA. These methods were investigated under threshold selection methods that include CFAR, CSDR and MSER. The performance under different time/frequency resolutions was studied as well. The obtained results indicate that the three considered SAE methods achieve their best accuracy when the decision threshold is selected according to the CFAR method (i.e., set for a fixed probability of false alarm), which also has the practical advantage that it only requires the noise power (and not the signal power or SNR) to be known. The best accuracy over the whole range of SNR values is provided by the SSA method with a decision threshold set based on the CFAR criterion. It has also been observed that the accuracy of the ED and CT-SA methods is mainly affected by the SNR and remains unaffected by the employed grid resolution. However, in the case of the SSA method, the accuracy is also affected by the grid resolution. Interestingly, for the SSA method, a degradation in the accuracy of the estimated SA

as a result of a reduced SNR can be compensated (at least to some extent) by selecting the optimum grid resolution for each SNR value, which provides an additional degree of freedom in the configuration and optimisation of the SSA method. Based on the results obtained in this study, the SSA method with a CFAR threshold and an optimum SNR-dependent grid resolution is the preferred approach for SAE in spectrum-aware systems and applications.

Chapter 3

Minesweeper Algorithm for Signal Area Estimation

3.1   Introduction

In this chapter, a novel SAE technique based on a minesweeper algorithm (MA) is proposed to improve the performance of existing SAE methods. The proposed method processes each tile in the time-frequency matrix where the SA is to be detected to determine the most likely state (busy/idle) based on the number of busy tiles around it (this approach can be seen as a simple morphological operation, which will be investigated in more detail in Chapter 4). Two variants are explored, one where the number of busy tiles around a central tile is compared to a threshold to decide the central tile state and a more complex approach where the actual pattern of idle/busy states around the central tile (and not only the number of busy tiles) is taken into account to make the final decision. Moreover, the proposed method can be employed in two ways: as a standalone SAE technique and also as a pre/post-processing technique in combination with other signal area estimation methods in order to correct signal detection errors before applying the other estimation method (pre-processing) and/or errors introduced by the other estimation method itself (post-processing). The performance of the proposed minesweeper algorithm in both application approaches is evaluated by means of software simulations and corroborated with experimental results obtained with a hardware prototype specifically used to this end. The impact of the number of iterations of the MA method (i.e., whether any additional performance improvements can be obtained by successively applying the proposed method multiples times) is also investigated. Part of the results presented in this chapter have been published in [43].

The rest of this chapter is organised into four sections. First, Section 3.2 presents the MA-based SAE method proposed in this chapter. Section 3.3 describes the current study's methodological framework for assessing the performance of the proposed MA under various parameter configurations and operational conditions. The analysed research findings are presented and discussed in Section 3.4. Lastly, Section 3.5 summarises and concludes the chapter.

37
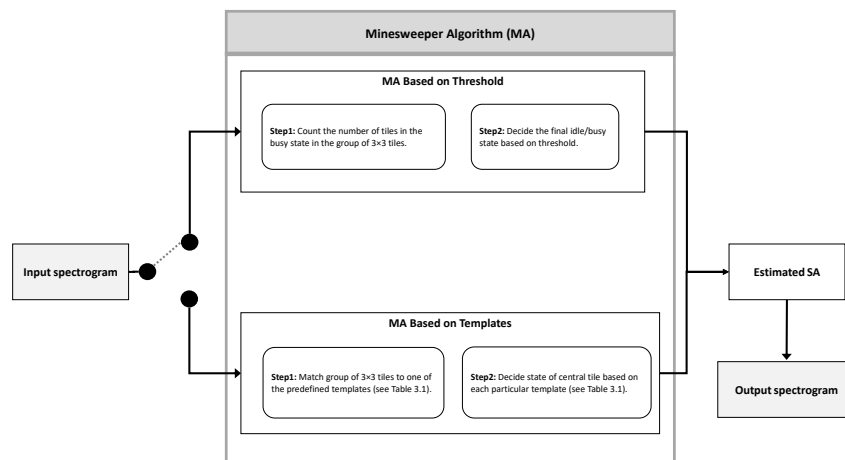
Figure 3.1: Signal processing flow of the input spectrogram according to the proposed Minesweeper Algorithm framework.

3.2   Proposed Minesweeper Algorithm

A flowchart summarising the signal processing flow of the input spectrogram according to the proposed Minesweeper Algorithm framework is illustrated in Fig. 3.1.

3.2.1   Minesweeper Algorithm Based on Threshold

As mentioned earlier, the performance of existing SAE methods can be severely degraded by the presence of signal detection errors (false alarms and missed detections). For instance, false alarms can lead the SSA method to detect SAs where they do not exist, which motivated the false alarm cancellation variant FC-SSA proposed in [11]. In many cases these errors are uncorrelated and occur in isolated random tiles rather than in clusters of tiles (e.g., false alarms are uncorrelated as they are typically caused by increased noise, which is essentially an uncorrelated random process). As a result, many false alarms tend to occur in isolated (busy) tiles surrounded by several idle tiles while many missed detections tend to occur in isolated (idle) tiles surrounded by several busy tiles. Therefore, the state of neighbouring tiles can be used as an indication to infer the potential occurrence of errors in certain tiles and take corrective actions. This is the main principle exploited by the proposed MA method.

The proposed MA method follows a two-step process. The first step entails assigning to every tile in the time/frequency grid a number that equals the number of tiles in the busy state observed in the group of 3×3 tiles composed by the tile under evaluation and the eight neighbouring tiles immediately surrounding such tile as illustrated in Figure 3.2. Notice that the state of the tile under evaluation (i.e., the central tile in the set of 3×3 tiles) is also counted. This counting procedure is similar to that of the popular *minesweeper* game [44], after which the proposed method is named. The second step decides the final idle/busy state of every tile in the time/frequency grid by comparing the number assigned to each tile in the first step to a threshold. Tiles whose values are equal to or greater than the threshold are decided to be in the busy
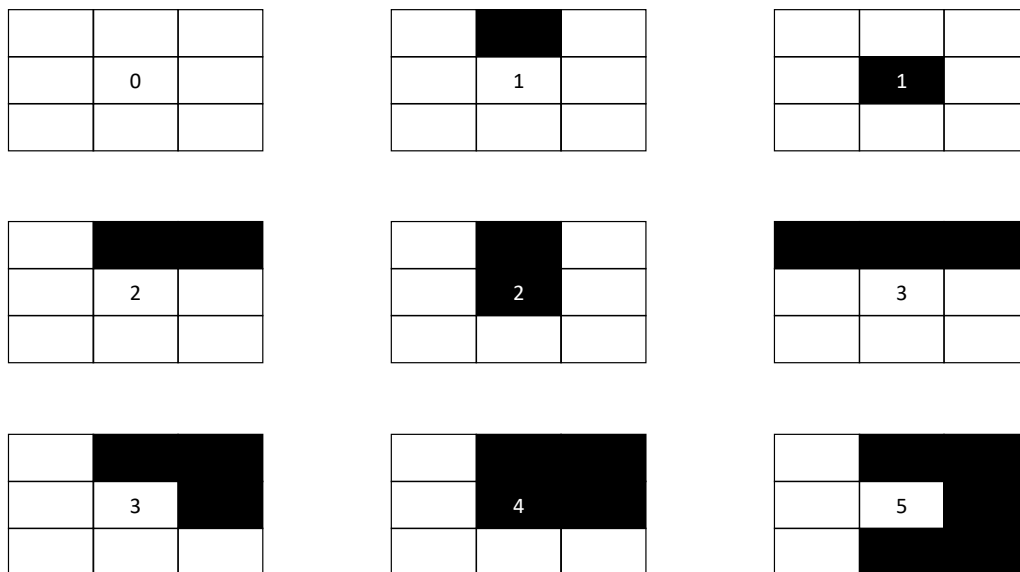
Figure 3.2: An example of a tile and its eight surrounding neighbours.

state, while those with lower values are decided to be in the idle state. By following this procedure, the final state of every tile is decided based on its own state and the state of the neighbouring tiles. With a properly set threshold, this method should be able to correct false alarms and missed detections while leaving most of the other tiles detected in the correct state unchanged.

3.2.2 Minesweeper Algorithm Based on Templates

In addition to the algorithm based on thresholds described above, a different formulation can be made based on an exhaustive analysis of all possible combinations of 0, 1, 2, . . . , 9 busy tiles in a set of 3×3 tiles and the corresponding most likely idle/busy state applicable to each case. Here, instead of simply comparing the value of the central tile to a threshold to make the final decision on the state of each tile, the actual pattern of idle/busy tiles around the central tile is analysed (not only the total number of busy tiles) and the most likely output is determined accordingly based on a logical reasoning. This requires all the possible patterns or templates to be analysed beforehand and the corresponding central tile state to be determined. This is shown in Table 3.1, showing all possible cases when the number of busy tiles ranges from 0 to 9 along with the decided busy/idle states.
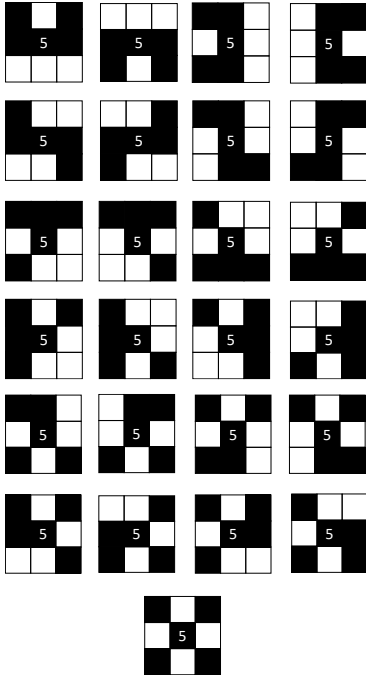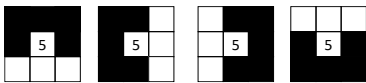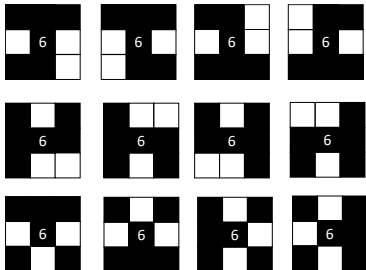
The final decision on the state of the central tile is made based on each particular template and such decision can lead to three possible cases. The first case, which corresponds to the IDLE column of the table, includes all the templates where the central tile was originally in the idle state but is observed in a busy state as a result of a false alarm and the other tiles around the central tile correspond to true busy tiles

in the edges/corners of a true SA. The second case, which corresponds to the BUSY column of the table, includes all the templates where the central tile was originally in the busy state but is observed in an idle state as a result of a missed detection and the other tiles around the central tile correspond to true busy tiles in the edges/corners of a true SA. The third case includes templates whose pattern does not provide enough information to distinguish any of the two other patterns (i.e., it could be both a false alarm or a missed detection depending on the region of a SA that is assumed) and therefore the action taken in this case is to leave the central tile unchanged, in the same state it is observed. Table 3.1 shows that when the number of busy tiles observed around the central tile is 0, 1 or 2, in all cases this is likely to correspond to a lack of signal components or to one or two false alarms (since all the resulting patterns would not match any region of a rectangular SA in any case) and as a result the central tile is decided to be in idle state in all cases. When the number of busy tiles is equal to or greater than 3, there can be some templates that suggest that the central tile was originally in the idle or busy state and in this case the action is evident (change the central tile to its likely idle/busy original state). However, other possible templates that can be observed either do not provide enough information to reach a logical conclusion on the original state of the central tile or provide a pattern where changing the state of the central tile only does not produce a valid pattern that can be matched to any region of a SA, often because there is likely at least one more wrong tile that should be changed as well, but it is not the central tile. Implementing this (i.e., changing two or more tiles at a time) would be too complex and subject to many possible interpretations of the observed template and possible errors that occurred (false alarms and/or missed detections). The decision in such a case is to follow the principle of not changing a tile unless there is a clear certainty that it will produce a valid pattern and that valid pattern is unique, so the final decision in this case is to leave the central tile unchanged, in the same state as observed, even though it likely is not in its correct state.

Notice that this variant based on templates, similar to the variant based on one or two threshodls, can also be applied both as a standalone SAE method directly applied to the idle/busy outcomes of ED as well as a pre- and/or post-processing method for existing SAE methods (e.g., CT-SA and SSA) in order to correct spectrum sensing errors before applying a SAE method (pre-processing) and/or errors introduced by the SAE method itself (post-processing). All these cases will be analysed.

Table 3.1: Summary of Minesweeper Algorithm based templates.

Value	Central tile decided		Left unchanged
	IDLE	**BUSY**	
0, 1, 2	Always	N/A	N/A
3			Any other case
4		N/A	Any other case

Table 3.1 – *Continued from previous page*

5			Any other case
6		N/A	Any other case
7		N/A	Any other case
8	N/A		Any other case
9	N/A		N/A

3.3   Evaluation Methodology

The performance of the proposed MA method in its several variants, both as a standalone SAE method and as a pre/post-processing method for other SAE methods, was evaluated by simulations following the evaluation methodology presented in Chapter 2, with some specific configurations. In addition to this, hardware experiments were carried out to corroborate the simulation results. This section presents the key aspects of both evaluations.

3.3.1   Simulation Procedure

The simulation procedure followed in this chapter is similar to the one presented in Chapter 2 and it will not be repeated here (see Section 2.3 for details). The main differences and specific aspects considered in this chapter are summarised below.

For each simulation, a set of 100 random test grids is generated with a resolution of 50×100 tiles, which can be considered of medium size [40]. The horizontal dimension of 100 tiles corresponds to the number of frequency bins, with the vertical dimension of 50 tiles determined through the time resolution. When introducing signal detection errors in Step 2 of the simulation procedure, the error probabilities are calculated assuming that the measured power samples are converted to binary idle/busy states by means of an ED technique with a threshold calculated to provide a Constant False Alarm Rate (CFAR) of $P_{fa} = 0.01$ according to equation 2.2. Thus, an SNR-dependent probability of detection P_d is obtained as given by equation 2.1. The rest of configuration parameters and aspects of the simulation procedure are as described in Section 2.3.

When evaluating SAE, one of the SAE methods described in Section 2.2.3 and/or one or more of the MA variants described in Section 3.2 are considered. When MA variants are applied, these are used either as a standalone SAE method or in combination with the CT-SA and SSA algorithms as pre/post-processing techniques (i.e., only before, only after, or both before and after). It is worth noting that the performance of SSA is sensitive to its configuration parameters. In this work, the SSA detection masks were adjusted according to [32, eqs. (3)–(4)], while the values for the sensitivity thresholds were taken from [32]. This choice performs well but may not necessarily lead to a fine tuning of the SSA performance with the particular spectrum dataset employed in this study (an optimization approach is discussed in [32], which is beyond the scope of this work).

3.3.2   Experimental Platform

The obtained simulation results were validated against experimental results obtained with the hardware platform shown in Fig. 3.3, which is composed of a Signal Hound VSG25A vector signal generator (acting as the signal transmitter), a short coaxial cable along with a 20 dB attenuator (acting as the transmission channel), and a Tektronix RSA306B real-time spectrum analyser (acting as the signal receiver or spectrum monitoring system). To prevent transmission interference from nearby electronic devices, a wired connection is used. The transmitter and receiver are connected via USB to the same computer, where a Matlab control program is executed to coordinate the operation of both transmitter and receiver to ensure that the data were correctly synchronised for
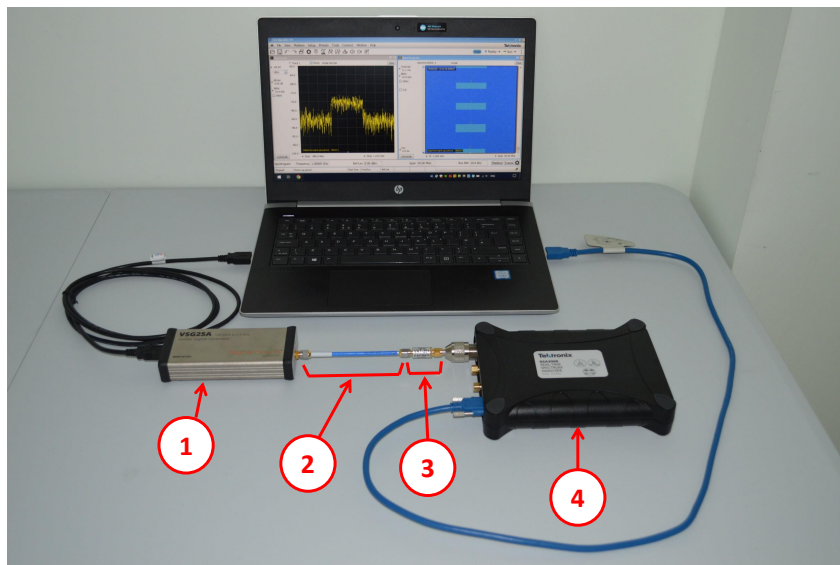
Figure 3.3: Experimental platform used in this work: (1) vector signal generator, (2) coaxial cable, (3) attenuator, and (4) spectrum analyzer.

subsequent comparison later on. The control program is implemented using Matlab's Instrument Control Toolbox along with the libraries and Application Programming Interfaces (APIs) provided by the manufacturers of the vector signal generator and the spectrum analyser.

The settings of the experimental platform were configured to closely reflect the simulation environment. A multi-tone signal was generated at the transmitter with an OFDM-like spectral shape generated by 1001 unmodulated tones with random phase spaced at 10 kHz around a central frequency of 1 GHz, with a total signal bandwidth of 10 MHz. The centre frequency of the receiver was also configured to 1 GHz with a frequency span of 30 MHz (i.e., signal bandwidth was 1/3 of the frequency span). The relation between the transmission power configured at the signal generator and the SNR observed at the spectrum analyser was carefully calibrated to enable a fair comparison between simulation and experimental results.

3.4   Results

To illustrate the benefits of the proposed MA approach, Fig. 3.4 shows an example of a random test grid. The SAs estimated by CT-SA and SSA, with and without the MA method (before, after, and before & after) based on the test grid of Fig. 3.4 are shown in Figs. 3.5 and 3.6 (for single threshold value of $\gamma_{threshold} = 2$ busy tiles). As it can be appreciated, the application of the MA method removes most false alarms and fills several gaps created in the SAs by missed detections. A more detailed assessment is presented below.
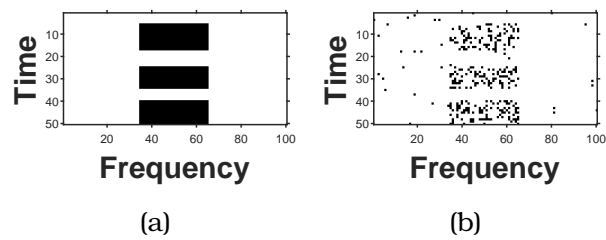
Figure 3.4: Example of a randomly generated time/frequency test grid: (a) Clean test grid, (b) Test grid with noise (SNR = −8 dB).
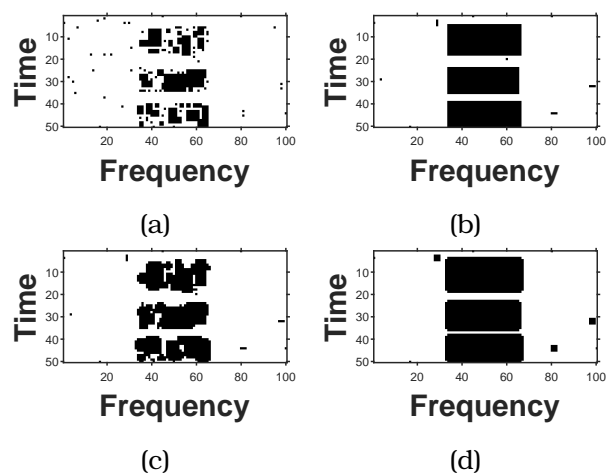
Figure 3.5: An example of SAs estimated by (a) the CT-SA method, (b) MA method before CT-SA, (c) MA method after CT-SA, (d) MA method before & after CT-SA [SNR = −8 dB, $\gamma_{threshold} = 2$].
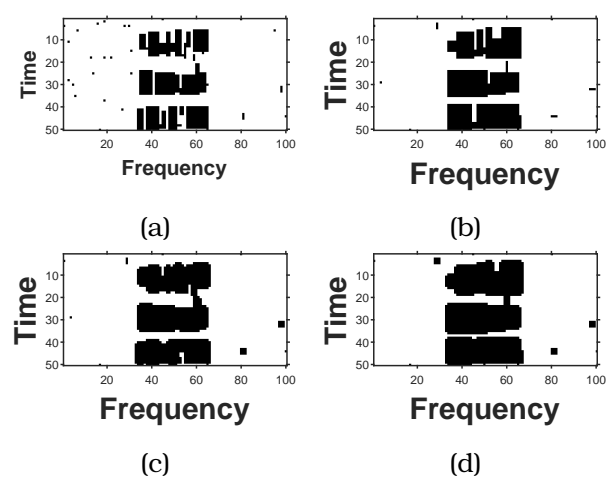
Figure 3.6: An example of SAs estimated by (a) the SSA method, (b) MA method before SSA, (c) MA method after SSA, (d) MA method before & after SSA [SNR = −8 dB, $\gamma_{threshold} = 2$].
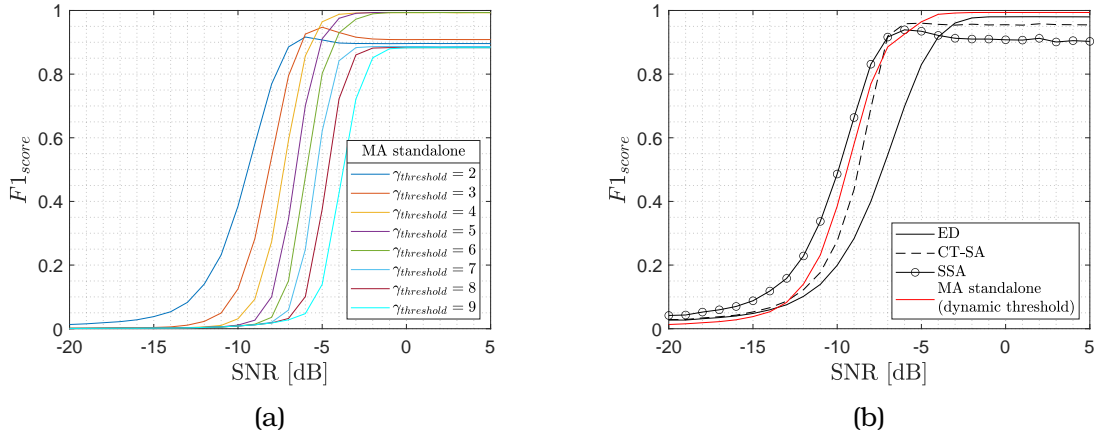
Figure 3.7: F1 score as a function of the SNR for the different SAE methods (ED, CT-SA, SSA) and the standalone MA method with: (a) static threshold, and (b) dynamic threshold.

3.4.1   Minesweeper Algorithm Based on Threshold

1) MA as Standalone SAE Method

The proposed MA method can be employed as a standalone SAE method directly applied to the ED outcomes only. The performance for different thresholds is illustrated in Fig. 3.7a. These results indicate that no single value of the threshold can provide the best performance over the whole range of SNR values. This outcome suggests that a dynamic threshold approach that nominates the best threshold for each SNR could improve the method's performance. Such dynamic approach can be defined by selecting for each SNR value the threshold that provides the best accuracy. According to Fig. 3.7a, a threshold value of 2, 3 and 4 should be used for SNR values in the ranges SNR < –6 dB, SNR ∈ [–6, –5] dB, and SNR > –5 dB, respectively. As shown in Fig. 3.7b, this dynamic MA approach clearly outperforms ED as a SAE technique over the whole range of SNR values and CT-SA over most of the SNR range (with the exception of the range from –7 dB to –5 dB, where the accuracy is slightly lower). When compared to the SSA method, the standalone MA method performs worse below –6 dB and better above –6 dB. As mentioned earlier, false alarms can lead the SSA method to detect SAs where they do not exist (this problem has been addressed in other works such as [11], which are out of the scope of this work and therefore not considered here). At high SNR values (above –5 dB), the proposed MA method as a standalone SAE technique can provide improved F1 scores, reaching values close to 100% (the only method to achieve this accuracy).

When compared to the CT-SA and SSA methods, the standalone MA method has a lower computational cost (see Fig. 3.8) due to the more straightforward processing, which leads to computation times similar to that of a simple ED strategy regardless of the threshold employed for MA. Thus, the MA technique with an SNR-based dynamic threshold can deliver a performance better than CT-SA and comparable to SSA (and better at high SNR values) at a lower computational cost.
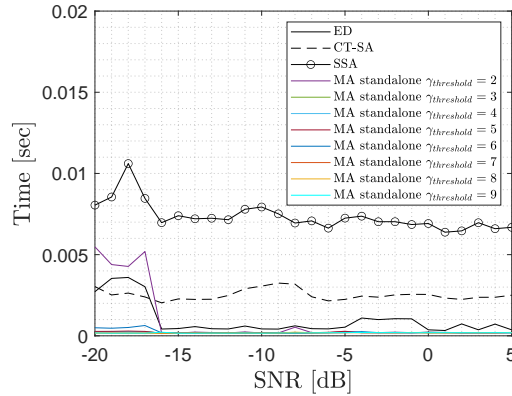
Figure 3.8: Computation time as a function of the SNR for the different SAE methods (ED, CT-SA, SSA) and the proposed MA method as a standalone SAE technique.
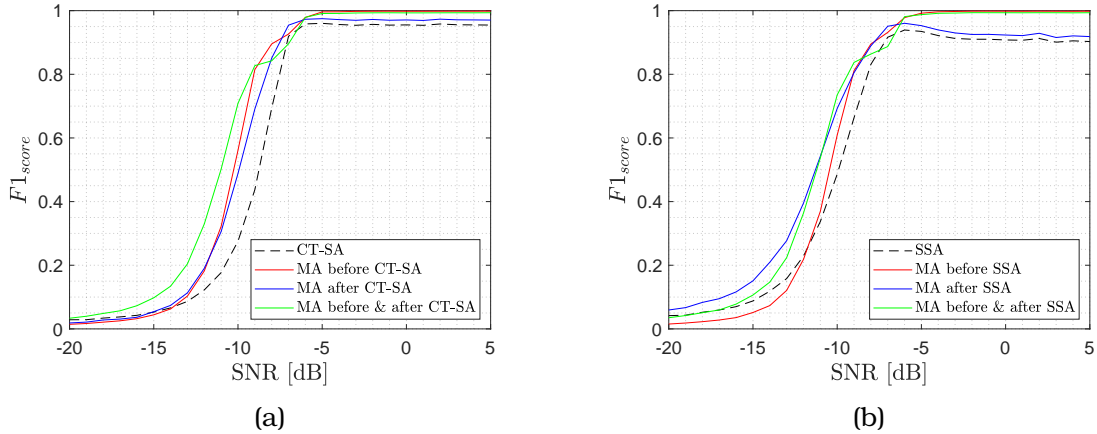
Figure 3.9: F1 score as a function of the SNR for different combinations of the proposed MA method and: (a) CT-SA, (b) SSA.

2) **MA as Pre/Post-Processing for Other SAE Methods**

The proposed MA method can also be employed as a pre/post-processing technique for other SAE methods such as CT-SA and SSA. In this case, the MA method is combined with an existing SAE method to correct sensing errors before applying another SAE method (pre-processing) and/or errors introduced by the other SAE method itself (post-processing). Fig. 3.9 shows the performance of CT-SA and SSA as standalone SAE methods and combined with the proposed MA method as a pre/post-processing technique. In general, applying the MA method before the other SAE method results in a slightly better accuracy than using it afterwards. However, with some exceptions, the highest improvement is in general achieved by employing the proposed MA mechanism both before and after the SAE method.

The results shown in Fig. 3.10 indicate that the total computational time of the CT-SA and SSA methods is not significantly affected regardless of whether the proposed MA method is applied. This can be explained by the fact that the MA
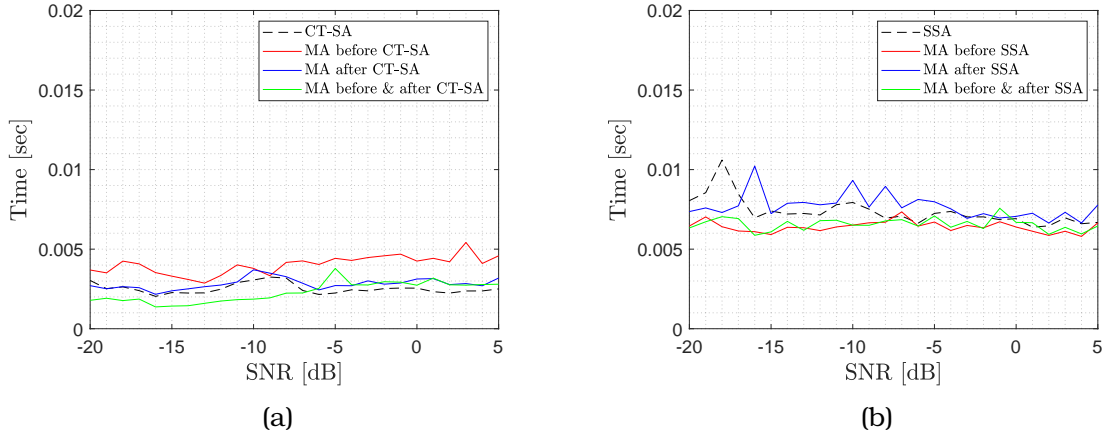
Figure 3.10: Computation time as a function of the SNR for different combinations of the MA method and: (a) CT-SA, (b) SSA.

method is based on a straightforward and much simpler process than CT-SA and SSA and therefore its contribution to the total computation time is very low compared to that of the CT-SA and SSA methods. Consequently, the introduction of the MA method as a pre/post-processing technique does not affect significantly the total computational time of the other SAE methods. Interestingly, it can be seen that, in some cases, the MA mechanism can in fact reduce the total computational time. This phenomenon may be due to the MA method's potential to eliminate some errors in the original signal grid, thus simplifying the other SAE methods' reconstruction procedure and therefore reducing the total computation time. This explanation seems to hold true mostly in the region of low SNR values as it can be appreciated in Fig. 3.10.

3.4.2   Minesweeper Algorithm Based on Templates

1) MA as Standalone SAE Method

The proposed MA method based on templates can be employed as a standalone SAE method directly applied to the ED outcomes only. Figure 3.11 shows the performance of the proposed MA method based on templates as a standalone SAE method, which is also compared to the proposed MA method based on threshold as well as the reference SAE methods from the literature. As appreciated, the performance of the standalone MA method based on templates perfectly matches the performance of ED over the whole range of SNR values. This fact indicates that this version of the MA method does not introduce any changes to the input spectrogram, in other words, the output of the ED procedure used to convert the received power levels to binary idle/busy states is not altered by the MA method based on templates. This can be due to a very low occurrence of matches between the considered templates and the actual spectrograms obtained at the output of the ED procedure. The number of times that a coincidence is found between one of the templates shown in Table 3.1 and any region of the binary spectrogram
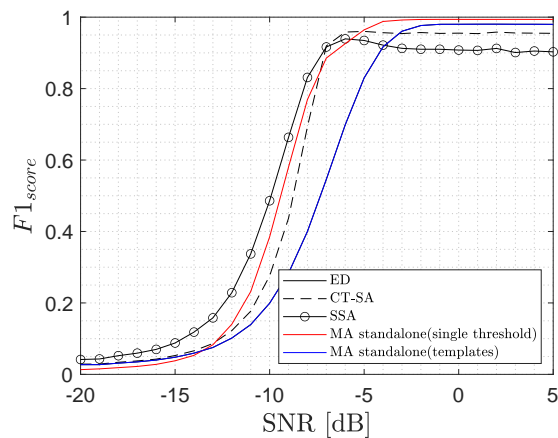
Figure 3.11: F1 score as a function of the SNR for the different SAE methods (ED, CT-SA, SSA), the MA-based on templates as a standalone method and the MA method based on threshold.
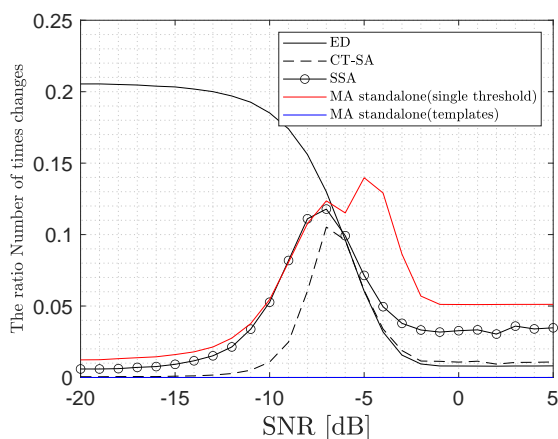
Figure 3.12: Comparison of the ED, CT-SA, SSA performance, and the MA method based both on templates and on threshold.

produced by the ED procedure, and that coincidence also results in a change of the state of the central tile, is not significant enough to result in a relevant difference between the spectograms at the input and output of the proposed MA method based on templates. This is corroborated by Fig. 3.12, which shows the fraction of tiles whose state is changed by the application of different SAE methods. Notice that all methods introduce a significant number of changes in the state of the spectrogram tiles, except the MA method based on templates, whose ratio of change is nearly zero. As a result, this version of the MA method virtually has no effect on the output of ED and its performance is the same.

2) MA as Pre/Post-Processing for Other SAE Methods

The proposed MA method based on templates can also be employed as a pre/post-processing technique for other SAE methods such as CT-SA and SSA. The results shown in Fig. 3.13 show the performance of the CT-SA and SSA methods used
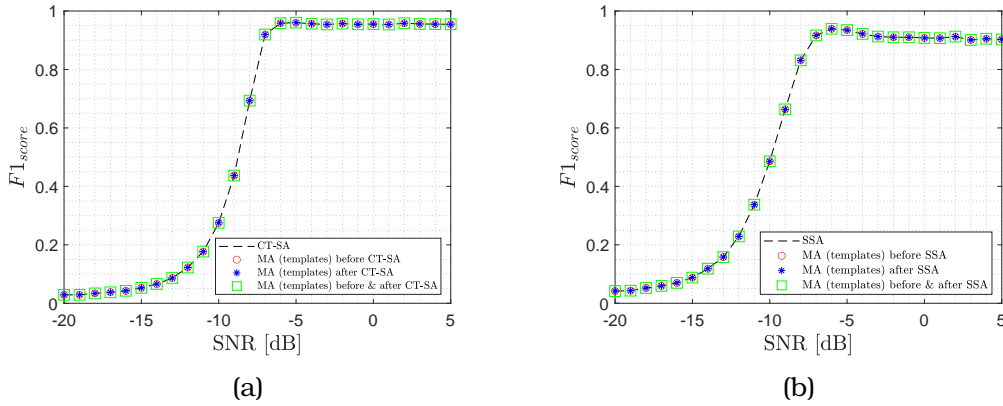
Figure 3.13: F1 score as a function of the SNR for different combinations of the MA-based on templates and: (a) CT-SA, (b) SSA.

as standalone SAE methods and also combined with the proposed MA method based on templates used as a pre/post-processing technique. As it can be seen, the obtained accuracy is the same in all cases, which is a natural consequence of the observation made above about the null impact of applying the MA method based on templates. Since this version of the MA method does not introduce a significant number of changes in the input spectogram, its application has not significant effect and as a result the performance of the CT-SA and SSA methods is the same, regardless of whether the MA method based on templates is applied or not. In conclusion, the application of the MA method based on templates provides not benefit or noticeable difference compared to the case where it is not applied. Therefore, this variant of the proposed MA method has no interest.

3.4.3   Impact of the Number of Iterations

In the previous sections, the performance of the proposed MA method has been investigated assuming that it is applied only once. This section investigates the impact of repeating the proposed MA method several times when it is applied. The impact of several iterations is quantified and shown numerically.

1) MA as Standalone SAE Method

Figure 3.14 shows the F1 score as a function of the SNR for the different SAE reference methods (ED, CT-SA, SSA) and for the proposed MA method based on threshold operating as a standalone SAE method. In this case, the proposed MA method is iterated one, three and five consecutive times when it is applied. These results indicate that there is no significant performance improvement associated with increasing the number of iterations at high SNR, which suggests that only one iteration is enough to achieve a good performance in the region of high SNR. On the other hand, at low SNR, the results indicate that increasing the number of iterations enhances the F1 score and therefore the estimation accuracy. However, this is only an artefact resulting from a magnifying effect of false alarms when the method is iterated several times. This will be shown more clearly next.
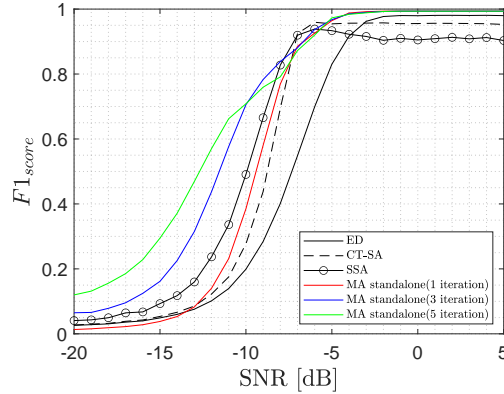
Figure 3.14: F1 score as a function of the SNR for the different SAE methods (ED, CT-SA, SSA) and the standalone MA based on threshold with one, three and five iterations.

2) **MA as Pre/Post-Processing for Other SAE Methods**

Figure 3.15 shows the obtained results when the proposed MA method is iterated five consecutive times and used as a pre/post-processing stage for the CT-SA and SSA methods. In this case, increasing the number of iterations from one to five results in a higher F1 score over most of the whole SNR range, which in principle suggests an improved SAE accuracy. However, as pointed out above, this is an artefact resulting from magnifying the presence of false alarms as a result of applying the proposed MA method several times. This effect is illustrated and more clearly appreciated in Figs. 3.16 and 3.17 for the CT-SA and SSA methods, respectively, at an SNR value of –15 dB. At such low SNR, most of the original SAs will not be detectable and as a result the output is composed of small fragments and some random false alarms. However, if the proposed MA method is iterated in that case, this process will add some additional busy tiles around those that are present, which continue to add further new busy tiles around as more iterations are repeated, thus magnifying the effect of false alarms and vestigial SA fragments. The outcomes are large busy sets of tiles around false alarms where there are no true SAs or around vestigial fragments of SAs. Coincidentally, these enlarged fragments and false alarms will increase the percentage of match with the original SAs, thus leading to a higher value of the F1 score, however this is just mere coincidence and not the result of a more accurate SAE estimation. Therefore, based on these results, it can be concluded that there is no real benefit in increasing the number of iterations and only one iteration should be used when applying the proposed MA method. This not only will provide the accuracy that the method is able to achieve in practice but will also do so at the minimal required computational cost.

3.4.4   **Experimental Validation**

So far, the results provided have been acquired using software simulations. Although simulations are a convenient and efficient way to investigate the performance of the SAE approaches considered in this study under a wide range of operating conditions,
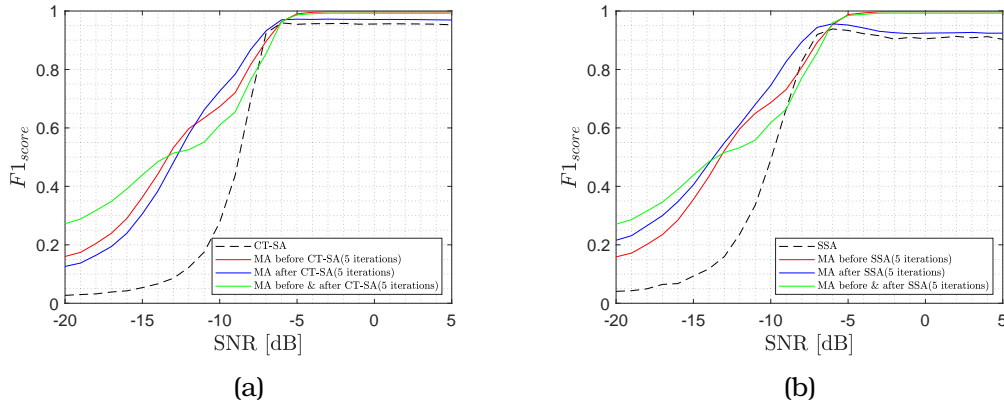
Figure 3.15: F1 score as a function of the SNR for different combinations of the proposed MA based on single threshold with five iterations as pre/post-processing for: (a) CT-SA, (b) SSA.

experimental validation is required to provide a more convincing case demonstrating the potential benefits that the proposed MA method can bring in a practical system implementation. Fig. 3.18 validates the performance of the proposed MA-based SAE method by comparing the performance forecasted by simulations with the actual performance obtained based on experimental data collected with the experimental setup presented in Section 3.3.2. As it can be observed, simulation and experimental results match very closely over the whole range of SNR values. The results shown in Fig. 3.18 indicate that the use of MA with existing methods (i.e. CT-SA and SSA) can actually improve the performance of existing SAE methods significantly when implemented in practical systems.

3.5 Summary

A minesweeper-based algorithm has been proposed in this chapter as an effective approach for improved SAE. Two variants have been proposed, one based on a simple thresholding principle and a more sophisticated one based on the matching of some templates/patterns with the input spectrogram. The obtained results have shown that the second variant does not produce significant alterations to the input spectrogram and therefore its application provides no benefit. However, the first proposed variant based on thresholding can provide noticeable performance improvements at a low computational cost. The impact of introducing several iterations has also been investigated, showing that a single iteration is enough to provide the achievable performance improvement without introducing unnecessarily increased computational cost.

The proposed method can be employed both as a standalone SAE method as well as a pre/post-processing technique for other SAE methods (to correct sensing errors or errors introduced by the other method itself). When used as a standalone SAE method it can provide similar or even slightly better accuracy than other methods at a much lower computational cost. However, the best performance improvement is actually obtained when used as a pre/post-processing technique in combination with other existing methods (such as CT-SA and SSA), without increasing significantly the

Figure 3.16: An example of SAs estimated using MA method before & after CT-SA (SNR = −15 dB, $\gamma_{threshold} = 2$): (a) original/clean image, (b) 1 iteration, (c) 3 iterations, (d) 5 iterations.
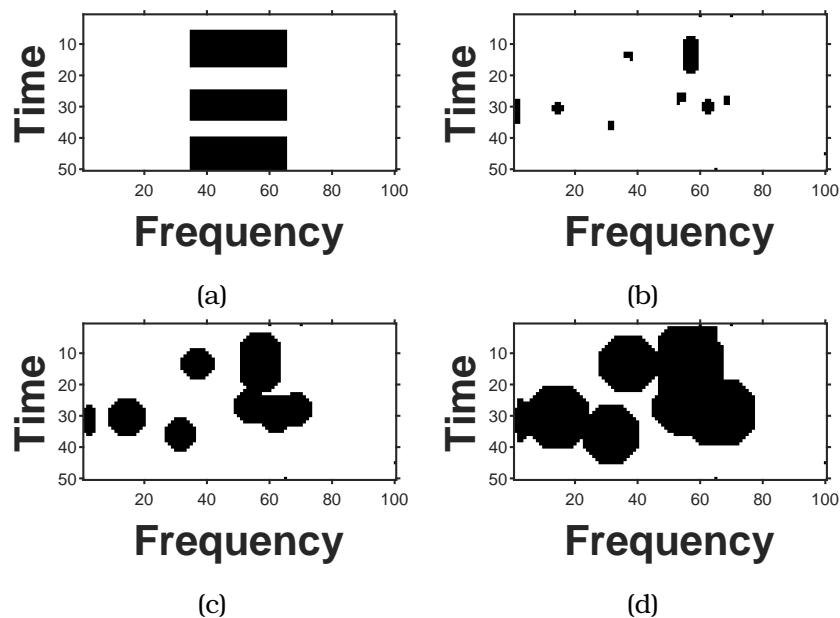
Figure 3.17: An example of SAs estimated using MA method before & after SSA (SNR = −15 dB, $\gamma_{threshold} = 2$): (a) original/clean image, (b) 1 iteration, (c) 3 iterations, (d) 5 iterations.
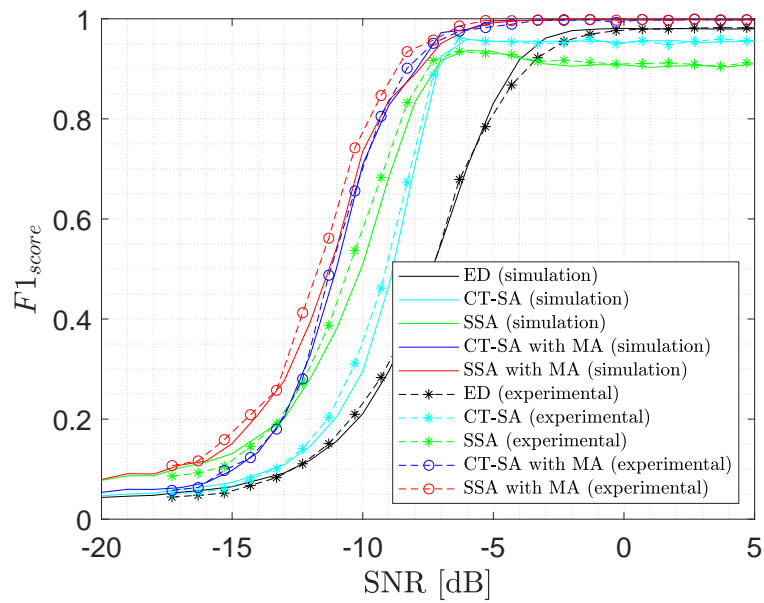
Figure 3.18: Experimental validation of the proposed method.

total computation cost. The proposed MA method has a low complexity and therefore does not increase significantly the computational cost of existing SAE methods while providing noticeable accuracy improvements when combined with them.

Chapter 4

Signal Area Estimation based on Morphological Image Processing

4.1 Introduction

This chapter considers a novel approach where Morphological Operations (MOs) [45] from the field of Image Processing are utilized to improve the detection accuracy of the estimated SA. The use of MOs in SAE is motivated by the fact that the problem of estimating a SA in a time-frequency matrix of observed power samples (obtained from spectrum measurements) is similar to the problem of recognition of patterns in an image (in this case, rectangularly shaped areas). Image processing techniques can be utilized to identify shapes after separating them from their background. This principle can be applied in SAE by taking the entire time-frequency matrix of power samples and converting it into a binary matrix of idle/busy states (by comparing each power sample to a properly set decision threshold). The binary matrix of zero/one elements (where each element represents the detected idle/busy state of that element) can be seen as an image where each element of the time-frequency matrix is considered as a black/white pixel. The problem of SAE then becomes the problem of detecting a rectangular shape in a binary noisy image. This point of view opens an entirely new line of research where the utility of many powerful tools from the field of Image Processing in the context of SAE can be explored. Image Processing is a well developed field where many advanced and sophisticated tools have been proposed to detect shapes in noisy images. Such tools are potentially well-suited to the SAE problem considered in this thesis and their applicability in this context is the focus of the research presented in this chapter. The interest of this work is in exploring the feasibility of using MOs to enhance the accuracy and performance of SAE.

There have been a few attempts in the literature to utilise or explore the utility of MOs in the processing of spectrum power measurements. In [46], a technique for automatically estimating the noise floor spectrum in the presence of signals (i.e., without requiring spectrum noise-only measurements) is proposed based on mathematical morphology. The work reported in [47] and references therein proposes an algorithm based on morphological image processing and statistical analysis to automatically select a suitable energy detection threshold based on power spectrum measurements where radio-frequency signals are present as well. The applicability of mathematical

morphology to the Short-Term Fourier Transform (STFT) is explored in [48], with a special focus on the detection of radar signals. A related STFT-based approach is proposed in [49] to extract features from frequency-hopping signals (hopping carrier frequency, hop timing and hop rate) based on MOs. A morphological algorithm is proposed in [50] for radio-frequency interference detection (in the context of astronomy rather than radio communications). However, to the best of the author' knowledge, this is the first attempt in the literature to apply morphological image processing techniques to improve the accuracy and performance of SAE.

The contribution of this work is many-fold. First, it provides an exhaustive analysis of the impact of the main MOs on the accuracy of SAE. By means of simulations, the result of applying different MOs to SAE are investigated under a broad range of configuration parameters for the MOs. The analysis is conducted over a representative range of Signal-to-Noise ratio (SNR) conditions typically found in wireless communication systems. In such analysis, the performance of MOs is explored when used both as a standalone SAE method and along with other existing SAE methods from the literature (as pre/post-processing stages). Based on the outcomes of this study, a suitable MO-based SAE method is formulated, which employs MOs as pre/post-processing techniques to other existing SAE methods. The proposed approach is shown to provide significant accuracy improvements in the detected SAs (with respect to the case where the other SAE methods are used without the aid of MOs) and without having a noticeable impact on the overall computational cost (even reducing it in some cases). The performance results obtained by simulations are corroborated with experimental results obtained with a hardware prototype specifically used to this end.

The rest of this chapter is organised as follows. First, Section 4.2 details the principle of image processing MOs through an exposition of its use in image processing applications and its relevance to the proposed SAE approach. The analysed research findings from the conduction of the simulations are presented and discussed under Section 4.3, where a new MO-based SAE method is proposed based on the observed performance of MOs. Lastly, Section 4.4 summarises and concludes the chapter.

4.2   Morphological Image Processing
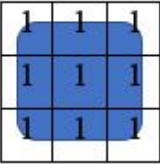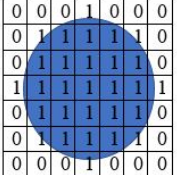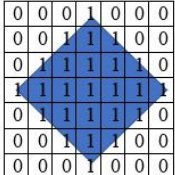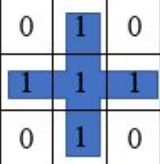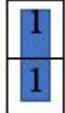
This section provides an overview of the main concepts from the field of image processing used in this chapter and shows some examples of how MOs affect the process of SAE.

4.2.1   Overview

Image processing refers to the procedure of extracting meaningful information from an object to generate reports and data for further analysis [51]. The analysis of images is a necessity in different disciplines, including engineering. Thus, there is a need for accuracy in the image processing technique that is adopted for a specific function or operation [52].

Mathematical morphology is a set theory and collection of non-linear operations and techniques that provide an approach to digital image processing based on geometrical structures (i.e., morphological image processing is related to the shape or morphology of features in an image). Depending on the type of operation, specific features of the

Table 4.1: Typical SE shapes for MOs.

Square	Disk or Circle	Diamond	Cross	Horizontal rectangle	Vertical rectangle
1 1 1 1 1 1 1 1 1	0 0 0 1 0 0 0 0 1 1 1 1 1 0 0 1 1 1 1 1 0 1 1 1 1 1 1 1 0 1 1 1 1 1 0 0 1 1 1 1 1 0 0 0 0 1 0 0 0	0 0 0 1 0 0 0 0 0 1 1 1 0 0 0 1 1 1 1 1 0 1 1 1 1 1 1 1 0 1 1 1 1 1 0 0 0 1 1 1 0 0 0 0 0 1 0 0 0	0 1 0 1 1 1 0 1 0	1 1	1 1

objects in an image, such as shape and size, can be given consideration. The morphological image processing approach is used in the identification of the characteristics and properties of an image by removing irrelevant background information [53]. The background is considered to be noisy and is eliminated to allow a more clear analysis of the object under study depending on its morphology. After the elimination of the background, the process then involves an analysis of the morphology.

4.2.2 Structuring Element

Morphological techniques probe an image with a small template referred to as the Structuring Element (SE). The SE is a small binary image (smaller than the processed image) represented as a small matrix of pixels, each with a value of zero or one. The SE is defined by three main configuration parameters, namely: (i) the shape, which is usually a discrete representation of a continuous shape and is defined by the specific pattern of ones and zeros; (ii) the size, which is specified by the SE's matrix dimensions; and (iii) the origin, which identifies the pixel on which the SE is superposed when probing the image. In general, the origin of the SE can be located anywhere (including outside the SE), however it is usually one of its pixels, most commonly the one lying at the geometrical centre of the SE (which is the case considered in this work). Table 4.1 shows some examples of typical shapes for the SE commonly used in MO-based image processing.

It is worth noting that, while the origin can be freely chosen for any SE, the shape and size are not always completely independent configuration parameters. For instance, Table 4.1 shows that for an SE size of 7 × 7 pixels the disk/circle and diamond shapes are almost identical (only 4 out of the 49 pixels differ between both SEs); for a 5 × 5 SE, both shapes would be completely identical, and for a 3 × 3 SE the disk/circle and the diamond would both converge to a cross.

Establishing the shapes and sizes of an SE is predominantly an experiential procedure. However, the universal designation of a SE relies on the graphic figures and patterns that one sets out to extricate from the image data [54]. Since the SE is a shape used to probe or interact with a given image to draw conclusions on how this shape fits or hits the shapes in the input image, one usually sets a way of differentiating objects (or parts of objects) from others according to their shape or spatial orientation

by choosing a particular SE accordingly [51]. Therefore, when the target is to identify rectangular SAs in the image data, it seems reasonable to select a SE with a squared or rectangular shape rather than SEs in the shapes of disks, diamonds or circles, for instance. The impact of the SE shape and size on the accuracy of MO-based SAE will be analysed and discussed in more detail in Section 4.3.

4.2.3 Morphological Operations

A MO is conceptually defined by moving the SE over the binary image to be modified in such a way that it is eventually centred over every image pixel (based on the defined SE's origin), where a local logical operation is performed. The SE is moved across all possible locations in the image and is compared with the corresponding neighbourhood of pixels. Some operations test whether the SE *fits* within the neighbourhood, while others test whether the SE *hits* or intersects the neighbourhood. Based on the outcome of the applied MO, the pixel at the origin of the SE is assigned a value according to the associated logical operation. Therefore, in a MO the value of each picture element (pixel) in the output image is dependent on a collation of the analogous image at the input with its bordering (i.e., each pixel in the original image is adjusted based on the value of other pixels in its neighbourhood) [54]. For every input image, MOs produce an output image of matching dimensions and proportions. A MO on a binary input image (as it is the case in the context of SAE) creates a new binary image in which each pixel has a non-zero value only if the logical test is true at that location in the input image.

This work investigates the SAE accuracy of the four main basic and most commonly used MOs, namely *erosion*, *dilation*, *opening* and *closing*. It is worth noting that the interest and focus of this work is not on image processing techniques themselves but on their application and the potential benefits they can bring to the SAE problem. Therefore, this work focuses on the main existing MOs; other MOs that can be constituted as sequential combinations of these main MOs and/or by combining (adding/subtracting) their output with the original image (such as the adjunct of a binary image or the convergence of two or more binary images [51]) are out of the scope of this work. For the objectives of this work, the four main MOs are sufficient as it will be shown in Section 4.3. A description of the considered MOs is provided below. The description is supported by an illustrative example depicted in Fig. 4.1, which shows the original transmission pattern at a transmitter with one single transmitter/channel in the test grid (Fig. 4.1a), how such transmission pattern is observed at the receiver after the application of ED with a decision threshold calculated for $P_{fa} = 0.01$ and a receiving SNR of -7 dB, at which $P_d \approx 0.39$ (Fig. 4.1b), and how the observed test grid at the receiver is affected by the application of the four considered MOs, namely erosion (Fig. 4.1c), dilation (Fig. 4.1d), opening (Fig. 4.1e) and closing (Fig. 4.1f).

1. **Erosion:** The erosion of an input image I by a SE S (denoted $I \ominus S$) produces a new image $I_{new} = I \ominus S$ with ones at all the locations (x, y) at which that SE S fits the input image I. In other words, $I_{new}(x, y) = 1$ if S fits I at (x, y) and 0 otherwise, repeating for every pixel coordinate (x, y). The SE S is said to fit I at location (x, y) when the SE's origin is placed at (x, y) and all the SE's ones are matched by corresponding ones in the same positions of the input image I. In a binary image
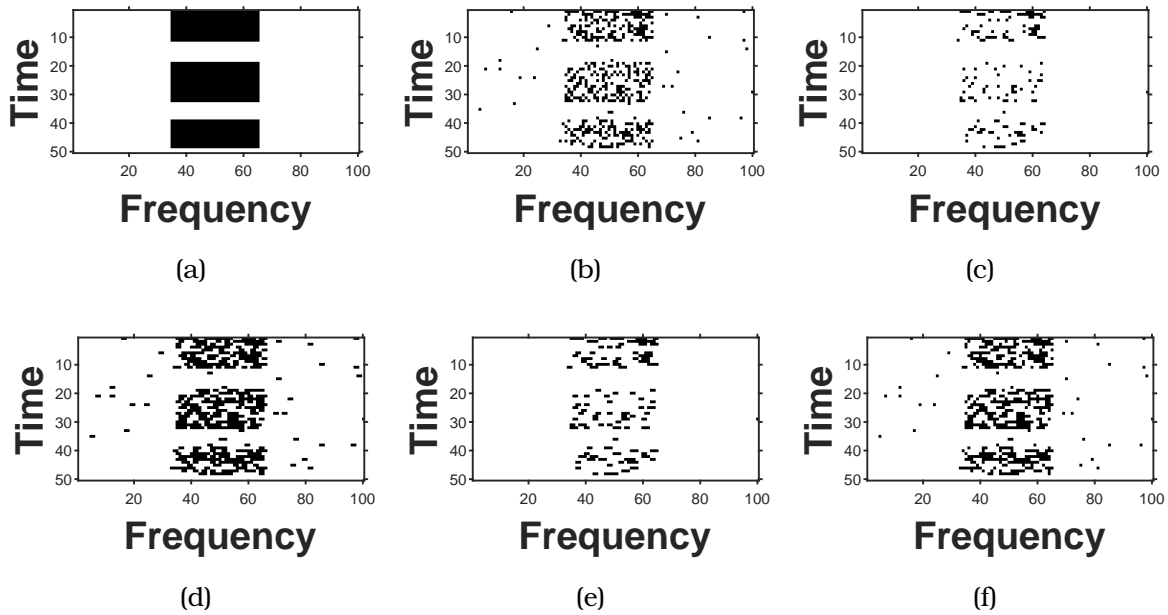
Figure 4.1: Several versions of the same time/frequency grid with a resolution of 100×50: (a) Original generated by transmitter, (b) Observed at receiver after ED (with threshold set for $P_{fa} = 1\%$) at SNR = −7 dB ($P_d \approx 0.39$), (c) Eroded at the receiver with a 1×2 rectangular SE, (d) Dilated at the receiver with a 1×2 rectangular SE, (e) Opened at the receiver with a 1×2 rectangular SE, (f) Closed at the receiver with a 1×2 rectangular SE.

(as it is the case in SAE), a pixel is set to one only if all the neighbouring pixels (as defined by the SE) have the value one, and set to zero if any of the neighbouring pixels (as defined by the SE) have the value zero. Morphological erosion removes *islands* and small objects in the input image, so that only substantive objects remain, and makes gaps between different regions become more pronounced. However it also reduces the size of regions of interest. An example of the impact of erosion on SAE is shown in Fig. 4.1c, which shows how the test grid of Fig. 4.1b is observed after the application of the erosion operation and how only substantive objects remain, thus making gaps between different regions become more pronounced.

2. **Dilation:** The dilation of an input image I by a SE S (denoted $I \oplus S$) produces a new image $I_{new} = I \oplus S$ with ones at all the locations (x, y) at which that SE S hits the input image I. In other words, $I_{new}(x, y) = 1$ if S hits I at (x, y) and 0 otherwise, repeating for every pixel coordinate (x, y). The SE S is said to hit I at location (x, y) when the SE's origin is placed at (x, y) and at least one of the SE's ones is matched by a corresponding one in the same position of the input image I. In a binary image (as it is the case in SAE), a pixel is set to one if any of the neighbouring pixels (as defined by the SE) have the value one, and set to zero if all the neighbouring pixels (as defined by the SE) have the value zero. Morphological dilation has the opposite effect to erosion: adds more pixels to the boundaries of existing regions, making objects more visible and reducing gaps between them. An example of the impact of morphological dilation on SAE is shown in Fig. 4.1d.

3. **Opening:** The opening of an input image I by a SE S (denoted $I \circ S = (I \ominus S) \oplus S$) is attained by first eroding and then dilating an image using the same SE for both operations. With morphological opening, any regions that survive the erosion are (almost) restored to their original size by the subsequent dilation. The visual result of morphological opening is that larger objects joined by thin lines of adjacent pixels are *disconnected*, thus opening up gaps between such objects, hence its name. Morphological opening can remove small entities from an image while conserving the dimensions and proportions of larger objects almost unaltered. Noteworthy, opening is an idempotent operation, meaning that once an image has been opened, subsequent morphological openings using the same SE will have no further effect on that image (i.e., $(I \circ S) \circ S = I \circ S$). An example of morphological opening in SAE is shown in Fig. 4.1e.

4. **Closing:** The closing of an input image I by a SE S (denoted $I \bullet S = (I \oplus S) \ominus S$) is attained by first dilating and then eroding an image using the same SE for both operations (this sequence is the inverse of the morphological opening). Morphological closing enlarges an image and then corrodes the expanded image, with the visual effect being the repletion of gaps in the image. Closing is also an idempotent operation, therefore once an image has been closed, subsequent morphological closings using the same SE will have no further effect on that image (i.e., $(I \bullet S) \bullet S = I \bullet S$). An example of morphological closing in SAE is shown in Fig. 4.1f.

4.2.4 Application of Morphological Operations to SAE

The simplest form of SAE is based on ED, which converts a time-frequency matrix of continuous power samples obtained from measurements into a binary matrix with zero/one (idle/busy) elements. This conversion is achieved by comparing the input power samples to a properly set decision threshold [40]. Other methods specifically envisaged for SAE (such as CT-SA and SSA) take as an input a binary matrix (already obtained as the output of ED such as Fig. 4.1b) and produce as the final output another binary matrix with a (hopefully) more accurate identification of the desired SAs. Fig. 4.2 shows an example of the outputs generated by the CT-SA and SSA algorithms when the input is as shown in Fig. 4.1b. MOs could be applied in this context as another SAE method, which also takes and produces binary matrices as illustrated in Fig. 4.3; in this case, the output matrix is the result of executing MOs on the input matrix, which can help identify existing SAs according to the shape and spatial orientation of the employed SE [55]. However, as observed in Figs. 4.1c–4.1f, MOs by themselves do not seem to provide an estimation of the true SAs (shown in Fig. 4.1a) as accurate as those provided by methods specifically designed for SAE such as CT-SA and SSA (depicted in Fig. 4.2). On the other hand, Fig. 4.2 also shows that existing SAE methods from the literature are imperfect and certain gaps and other imperfections in the estimated SAs could be handled and fixed by means of MOs. This suggests that a combination of existing SAE methods and MOs could provide an improved accuracy in the estimated SAs. To gain an adequate understanding on how MOs can help improve the performance of SAE, two application scenarios are investigated in this chapter: (i) a first scenario where MOs are applied as a standalone
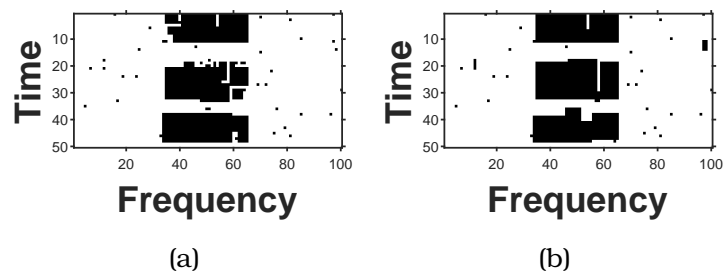
Figure 4.2: Outputs generated by: (a) CT-SA algorithm, and (b) SSA algorithm, when the input is as shown in Fig. 4.1b.
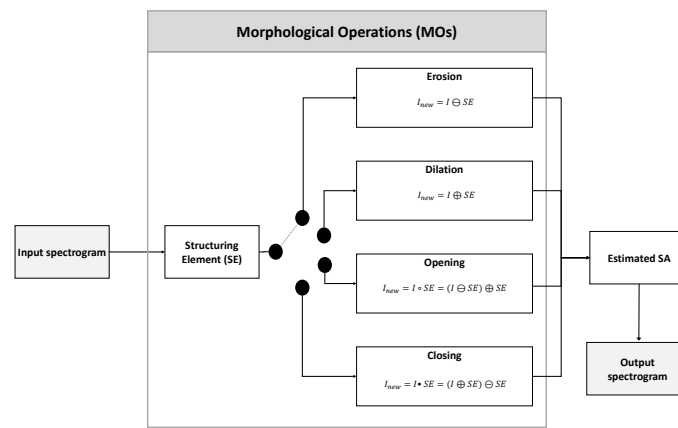
Figure 4.3: Signal processing flow of the input spectrogram according to the proposed MOs framework.

SAE method that takes as an input the binary matrix produced by the application of ED (Fig. 4.1b) and produces its own final output (Figs. 4.1c–4.1f); (ii) a second scenario where MOs are applied in combination with other existing SAE methods (such as CT-SA and SSA) as a pre/post-processing technique, where MOs can be applied only before, only after, or both before and after the other SAE method. The study of both scenarios will provide insights into how to best formulate a suitable MO-based SAE method.

4.3   Performance Analysis and Proposed Methods

The evaluation methodology followed in this chapter is identical to the one presented in Chapter 3 (please refer to Section 3.3 for details).

4.3.1   Performance of MOs in SAE

The first investigated aspect is the impact of the SE's shape. To this end, a maximum reference size of 3 × 3 pixels is selected for all shapes for a fair comparison. For this maximum size, several shapes are defined (square, horizontal and vertical rectangle
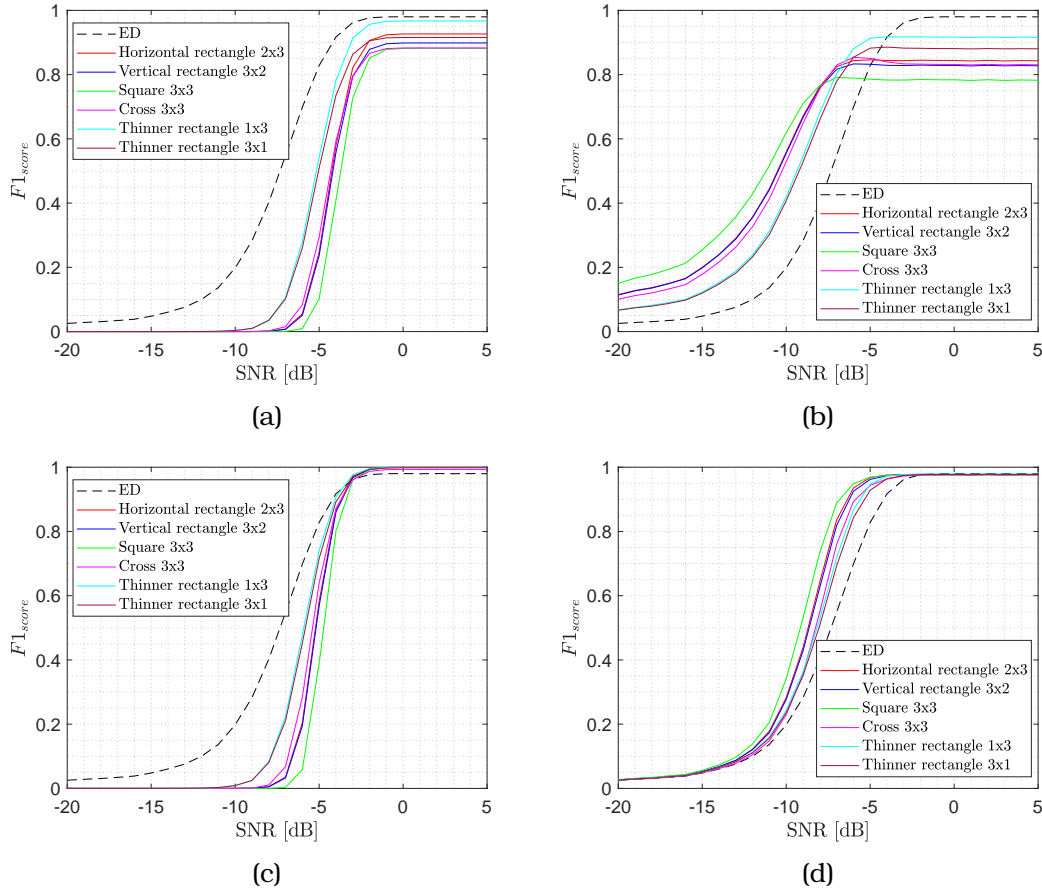
Figure 4.4: F1 scores with different shapes of SE for MOs as standalone SAE: (a) erosion, (b) dilation, (c) opening, (d) closing.

both in thick and thin formats, diamond, cross, and disk/circle[1]) and their performance is evaluated when the four MOs are applied as a standalone SAE method. The results are shown in Fig. 4.4, including ED as a reference (which corresponds to the case where no MO is applied). The simulation results reveal that the SEs of different shapes have different impacts on the estimation accuracy of the SA through the processes of erosion, dilation, opening and closing. Moreover, Fig. 4.4 also provides some insights into how each MO affects the detection of SAs. Concretely, it can be noticed in Fig. 4.4a that erosion results in an overall accuracy degradation over the whole SNR range, regardless of the employed SE shape. This can be explained by the aggressive removal effect of small objects that erosion has on the processed image. This effect could be beneficial to remove false alarms, but unfortunately also removes portions of the actual SA when it has been degraded by the radio transmission process. The overall net effect, as it can be appreciated, is a general accuracy degradation (with respect to the case where erosion is not applied, which is the ED curve). On the other hand, dilation has

---

[1]Notice that for a 3×3 SE the shapes of disk/circle, diamond and cross lead to the same SE template, i.e., a 3×3 cross (see Table 4.1). Therefore, results shown in this chapter for the cross SE are also representative of the performance for the disk/circle and diamond SEs in this case.

a different effect depending on the considered SNR range as shown in Fig. 4.4b. At high SNR, dilation has a degrading effect, which can be explained by its expanding effect on small objects; this effect does not provide a more accurate detection of the actual SA, which is already easy to detect at high SNR, however augments the sizes of regions resulting from false alarms, thus degrading the overall accuracy at high SNR. However, dilation can be helpful at low SNR: it still augments the size of regions resulting from false alarms but also helps filling gaps in the distorted original SA, thus resulting in a more accurate SA detection. The overall net effect is favourable in this case. The square SE provides here the best accuracy improvement at low SNR, followed by the thick rectangular (3×2 and 2×3) SE shapes. This is in agreement with the intuitive notion that the SE shape should be selected in accordance with the geometric shapes that are attempting to be detected from the input image [55]. Fig. 4.4c shows that morphological opening has in general a similar effect as erosion, however with a noticeable accuracy improvement at high SNR. This is because the initial erosion step of the morphological opening removes small objects both resulting from false alarms and found inside the original SA, however the subsequent dilation step fills the gaps opened within the original SA so that the net effect of morphological opening at high SNR is an effective reduction of the incidence of false alarms, without significant degradation of the original SA, and hence an overall accuracy improvement. In this case, the particular shape employed for the morphological opening at high SNR is not relevant as all them provide a similar level of accuracy very close to one. Finally, Fig. 4.4d shows that morphological closing provides an improved level of accuracy over the whole SNR range with respect to ED alone for all SE shapes, again with the best accuracies achieved by the square and thick rectangular SE shapes (3×2 and 2×3). However, when compared to the other MOs, closing the image by itself does not outperform dilation at low SNR nor opening at high SNR. This observation suggests that a suitable choice for MOs is indeed dilation at low SNR (with square SEs) and opening at high SNR (in principle with any SE shape, however a square SE could also be chosen here for simplicity).

To determine the impact of the SE size, F1 scores were calculated for different SE sizes using the best performing combinations of SE shapes as discussed above, namely square and both horizontal/vertical rectangular SE shapes. The obtained results are shown in Figs. 4.5 and 4.6 for the two MOs with potential to improve the SAE accuracy at low and high SNR, respectively (i.e., dilation and opening). The considered SE size categories are as follows: extra small (2×2 square, 1×2 horizontal rectangle, 2×1 vertical rectangle), small (3×3 square, 2×3 horizontal rectangle, 3×2 vertical rectangle), medium (6×6 square, 2×6 horizontal rectangle, 6×2 vertical rectangle) and large (9×9 square, 4×9 horizontal rectangle, 9×4 vertical rectangle). These size categories should not be interpreted in absolute sense but in relation to the overall image size (e.g., the large size category represents in this case 9% and 18% of the horizontal and vertical image dimensions, respectively). Fig. 4.5 shows that the SE size has a significant impact on the performance of morphological dilation. In particular, looking at the region of low SNR (where the morphological dilation is of interest), one can see that the selected SE size should increase as the SNR decreases. For very low SNR (around –20 dB), a large SE size gives a higher F1 score, while for moderately low SNR (just below 0 dB), small or extra small SE sizes give a better F1 score. On the other hand, Fig. 4.6
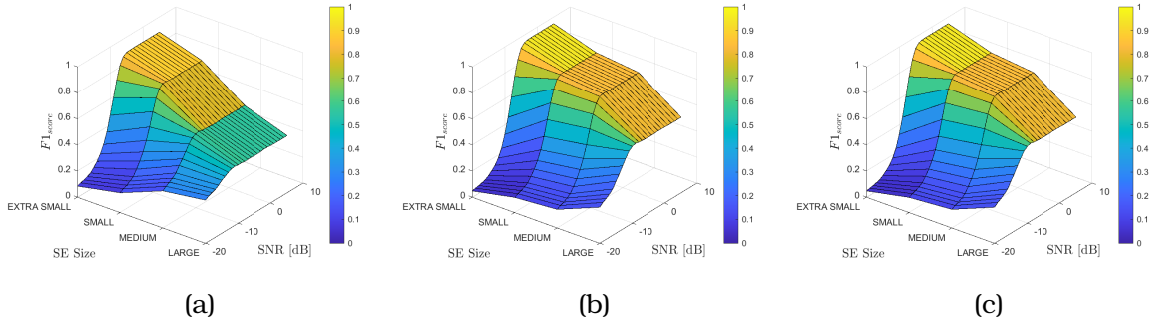
Figure 4.5: F1 score for dilation with different SE sizes and shapes: (a) square, (b) horizontal rectangle, (c) vertical rectangle.
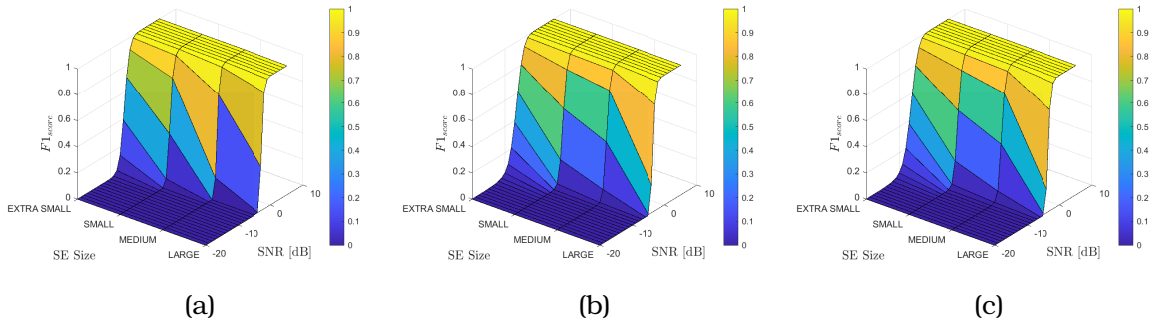
Figure 4.6: F1 score for opening with different SE sizes and shapes: (a) square, (b) horizontal rectangle, (c) vertical rectangle.

shows that the accuracy of morphological opening does not change significantly when the selected SE size varies and it remains close to one at high SNR for all SE sizes.

To further explore the impact of the SE size in these two MOs, some additional results are provided in Figs. 4.7, 4.8 and 4.9 when the original SAs are as shown in Fig. 4.1a. First, Fig. 4.7 shows the output of dilation at an SNR of –7 dB using a horizontal rectangular SE shape, which according to Fig. 4.4b is the SE shape that provides the best accuracy at that SNR. Moreover, Fig. 4.8 shows the output of dilation at a lower SNR of –10 dB using in this case a squared SE shape, which according to Fig. 4.4b is the SE shape that provides the best accuracy at this other SNR. The discussion above concluded from Fig. 4.5 that when applying dilation in the low SNR regime, the SE size should increase at lower SNRs. However, observing the examples of Figs. 4.7 and 4.8 one can see that selecting large SE sizes does not really lead to a useful SAE, even though the numeric value of the F1 score may be higher in some cases. At such very low SNR values (such as –10 dB in Fig. 4.8), an accurate estimation of the SA is not feasible regardless of the selected SE size. However, at slightly higher SNR values (such as –7 dB in Fig. 4.7, only 3 dB more) selecting an extra small SE can provide a reasonable SAE accuracy, which becomes evident by comparing Figs. 4.1a and 4.7a. Therefore, when applying a morphological dilation at low SNR values, the selected SE size should remain at a small or extra small size; this may not lead to a useful SAE at very low SNR (which may not be feasible anyway) but will provide significant accuracy improvements at moderately low SNR values. Since the selected SE size does not have
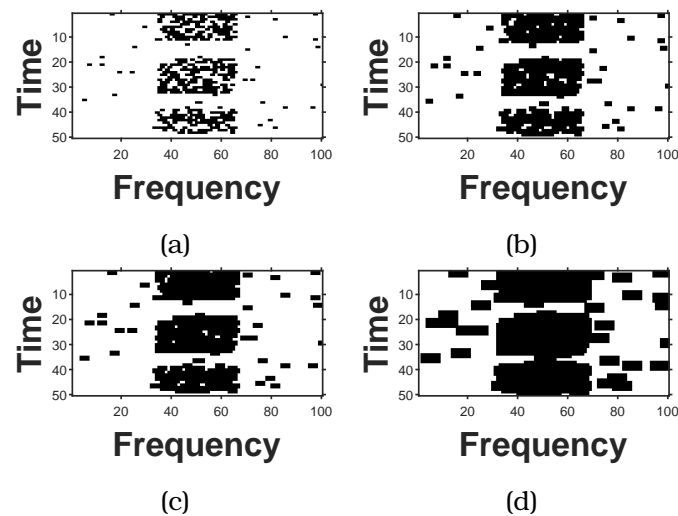
Figure 4.7: Dilation at SNR = –7 dB using a horizontal rectangular SE for the SAs shown in Fig. 4.1a: (a) extra small, (b) small, (c) medium and (d) large.
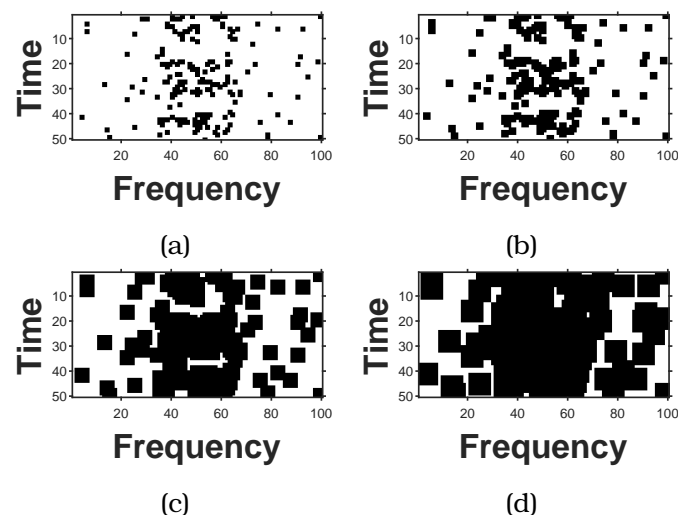
Figure 4.8: Dilation at SNR = –10 dB using a squared SE for the SAs shown in Fig. 4.1a: (a) extra small, (b) small, (c) medium and (d) large.

a significant impact on the resulting accuracy when applying morphological opening at high SNR (as observed in Fig. 4.6 and confirmed by Fig. 4.9) the same SE size selected for dilation at low SNR may also be employed for opening at high SNR.

The results presented so far correspond to MOs applied as standalone SAE methods. Simulations were also conducted to evaluate the four MOs when applied as pre/post-processing to the CT-SA and SSA methods. For comparison purposes, Fig. 4.10 shows the performance of the four MOs as standalone SAE methods while Figs. 4.11 and 4.12 show the counterparts for the combination of MOs with the CT-SA and SSA methods, respectively. An extra small (1×2) horizontal rectangular SE has been selected in this example for illustration purposes, however similar observations and conclusions are
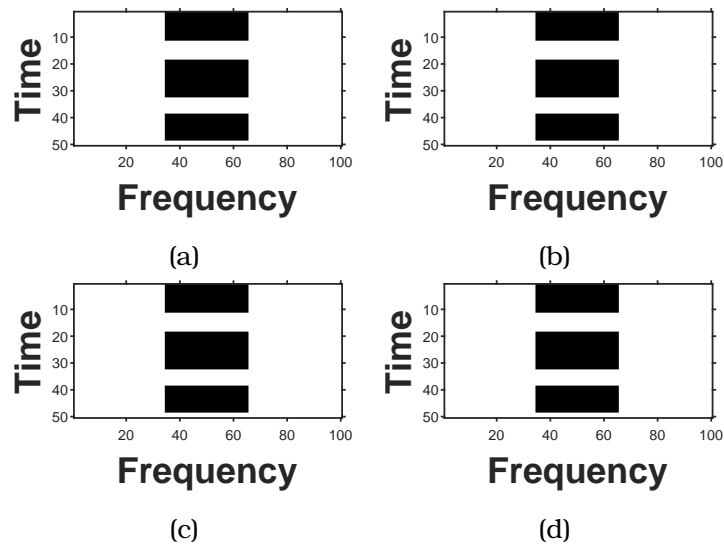
Figure 4.9: Opening at SNR = +5 dB using a squared SE for the SAs shown in Fig. 4.1a: (a) extra small, (b) small, (c) medium and (d) large.
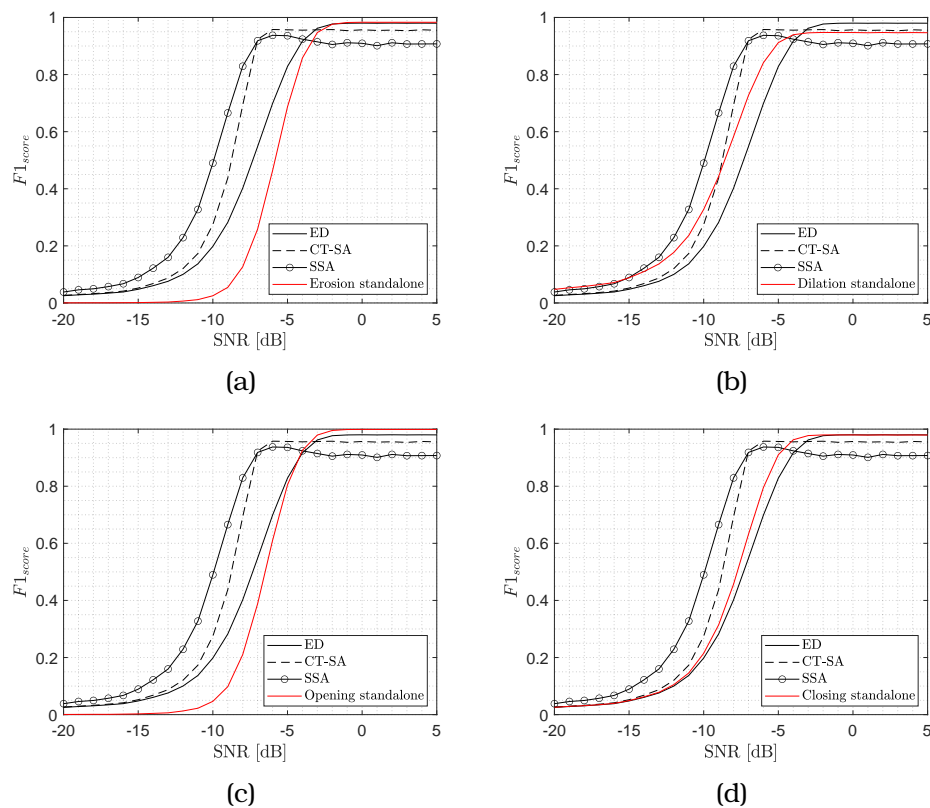
Figure 4.10: MOs as standalone SAE methods: (a) erosion, (b) dilation, (c) opening, and (d) closing.

(a)

(b)

(c)

(d)
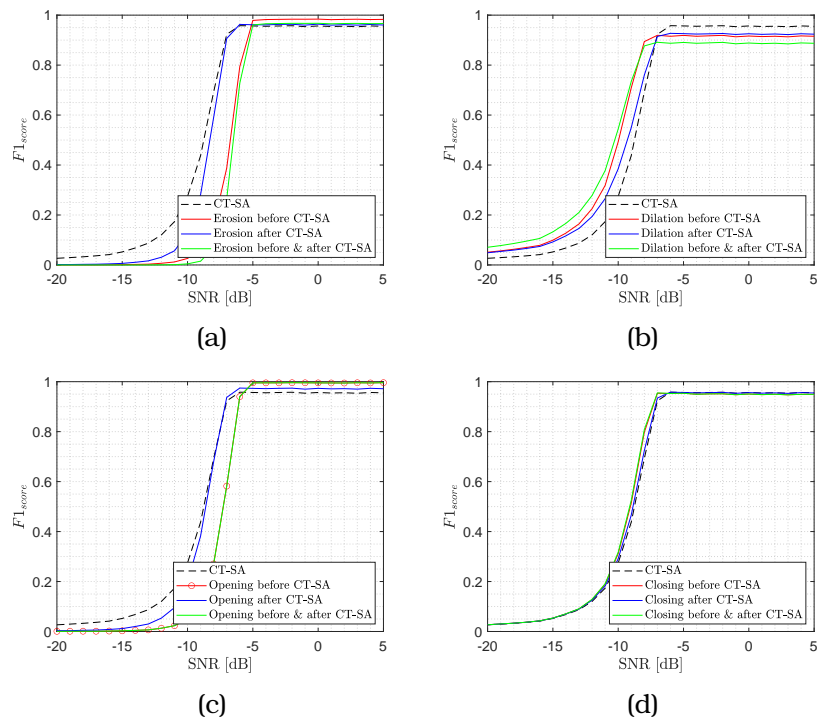
Figure 4.11: MOs as pre/post-processing to CT-SA: (a) erosion, (b) dilation, (c) opening, and (d) closing.

(a)

(b)

(c)

(d)
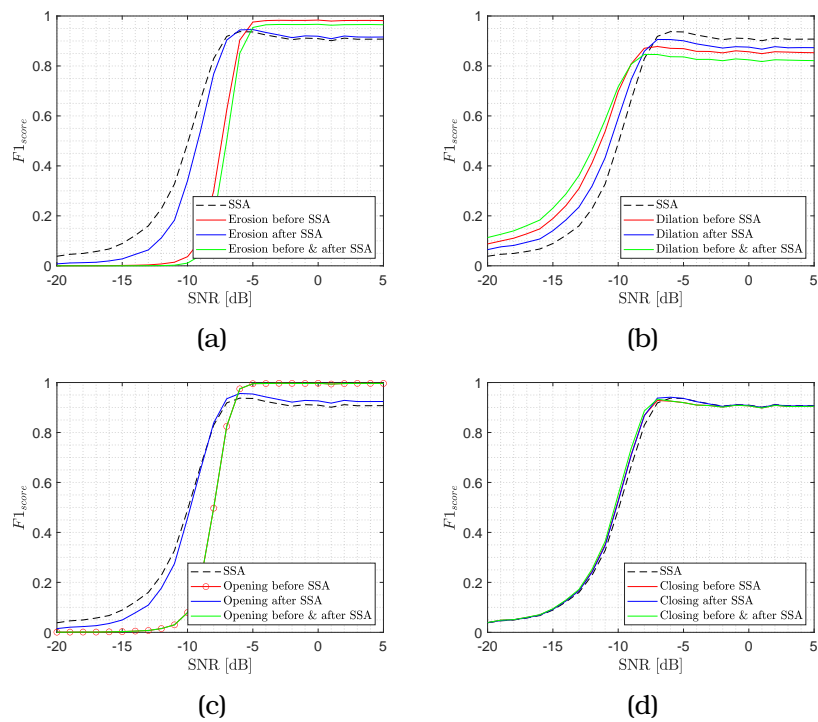
Figure 4.12: MOs as pre/post-processing to SSA: (a) erosion, (b) dilation, (c) opening, and (d) closing.

obtained for horizontal vertical and square SEs. Fig. 4.10 shows that MOs, when executed as standalone SAE methods, may be able to improve the ED accuracy in certain SNR regions but, in general, are unable to outperform or simply provide a comparable accuracy when compared against other methods specifically designed for SAE such as CT-SA and SSA. Therefore, MOs by themselves cannot be used as a standalone SAE method. Nevertheless, Figs. 4.11 and 4.12 demonstrate that MOs can improve the performance of other existing SAE methods when employed as pre/post-processing techniques. It can be noticed that, in line with previous observations, erosion tends to have a degrading effect on the SAE accuracy, dilation tends to improve the accuracy in the lower SNR range (with higher improvements when applied both as a pre- and post-processing stage), opening improves the accuracy in the higher SNR range (in this case it is enough when used as a pre-processing stage only[2]), and closing has no significant impact on the final resulting accuracy. These observations can be exploited to formulate an MO-based SAE method as discussed below.

4.3.2 Proposed SAE Method Based on MOs

The results presented above have indicated that the MOs yield the best results when used as pre/post-processing steps along with other existing SAE techniques such as CT-SA and SSA. However, it has also been shown that no single MO can help improve the accuracy over the whole range of SNR values. In fact, certain combinations of MOs at different SNR values provide better accuracy than others. Taking this observation into account, a suitable MO-based SAE method can be formulated by selecting the best combination of MO and pre/post-processing application for each SNR range. Concretely, it has been shown that at low SNR dilation before and after CT-SA or SSA provides the best accuracy (with a 2×2 square SE), while at high SNR the best accuracy is obtained with opening before CT-SA or SSA (with any shape for the SE). Dilation and opening both help in the morphological filtering process, which can be used to extract the useful SA from the noisy input [56, 57]. Based on these observations, a simple approach would be to set an SNR threshold such that any SNR value below (above) the threshold is considered to be low (high) SNR and the appropriate MO is applied. However, it can be shown that there exists a certain region of intermediate SNR values (between the so called regions of low and high SNR) where the optimum MO and pre/post-processing application may not be any of those observed at low or high SNR. This motivates a more flexible version of the method that distinguishes between low, intermediate and high SNR ranges and selects the best MO for each. Accordingly, and based on the results presented above, the proposed MO-based SAE method is formulated as follows:

- *Low SNR regime* (SNR $\leq$ SNR$_{th}^{L}$): Perform morphological dilation with an extra small squared SE both before and after the employed SAE method.

- *Intermediate SNR regime* (SNR$_{th}^{L}$ < SNR $\leq$ SNR$_{th}^{H}$): Perform morphological opening with an extra small rectangular SE only after the employed SAE method.

---

[2]Note that in Figs. 4.11c and 4.12c the curves for pre-processing only overlap the curves for both pre/post-processing.

- *High SNR regime* (SNR > SNR_{th}^{H}): Perform morphological opening only before the employed SAE method with an extra small SE of any appropriate shape (e.g., squared or rectangular).

The parameters SNR_{th}^{L} and SNR_{th}^{H} are thresholds that delimit the regions of low, intermediate and high SNR and therefore where each MO provides the best accuracy. To determine the optimum thresholds, F1 scores were calculated for threshold values between –10 dB and –5 dB (where the low-to-high SNR transition occurs). The exhaustive search concluded that $\mathrm{SNR}_{th}^{L} \approx -8$ dB and $\mathrm{SNR}_{th}^{H} \approx -5$ dB yield the best accuracy.

The formulation of the proposed algorithm is supported by the obtained simulation results and can be justified as follows. First, at low SNR one can expect a higher number of missed detections. Such missed detections will likely leave a reduced number of busy pixels where a SA was originally present, thus making those few busy pixels the only remaining vestige of the SA that was originally present in that region. Therefore, one can maximise the probability of detecting as much of the SA in that region as possible by following an aggressive detection approach where the presence of a single busy pixel in the neighbourhood of the SE is enough to set the pixel in the centre of the SE as busy. This can explain why a dilation is the most convenient morphological operation at low SNR values (below a properly set threshold). Moreover, due to the difficulty of detecting signal components at low SNR, the greatest benefits can be obtained by dilating the image both before and after the employed SAE method; recall that morphological dilation makes objects more visible and fills in small holes/gaps in the image, thus making SA detection easier for other SAE methods if applied beforehand (pre-processing) and making the SAs (or their portions) detected by the other SAE methods further visible if applied also afterwards (post-processing). On the other hand, at high SNR the dilation operation should also enhance the detection accuracy by filling in gaps within SAs degraded by missed detections. However, the main problem of morphological dilation under high SNR conditions is that the filling of these gaps does not compensate the amplification of false alarms, which are made more visible as a result of the dilation. For this reason, under high SNR it is more convenient to perform first a morphological erosion (in order to remove as many false alarms as possible) followed by a morphological dilation (to safely fill in gaps within degraded SAs once false alarms have been removed). This can explain why opening is the most convenient morphological operation at high SNR (above a properly set threshold). Moreover, due to the relatively easiness to detect signal components at high SNR, it is enough to perform this operation only before applying the other SAE method (results show that it could be applied afterwards as well but this does not provide any accuracy improvements while increases slightly the computational cost). Similarly, at intermediate SNR morphological opening is still the most convenient choice, however in this case performed only after the employed SAE method.

The results shown in Fig. 4.13 provide supporting evidence for the discussion above, showing that the proposed MO-based SAE approach provides the best overall accuracy over the whole SNR range. The accuracy obtained in the transition area of intermediate SNR values is marginally above that of the original SAE methods without any MOs and comparable to that of the original SAE methods with the MA technique proposed in [43]. However, the application of carefully selected and properly configured MOs can provide significant accuracy improvements both at low and high SNR. In

the low SNR region, the accuracy improvement (as quantified by the F1 score) can be as large as 40% (for CT-SA with and without MOs at –10 dB), while in the high SNR region the proposed method achieves a perfect accuracy of 100% (the only method that achieves this level of accuracy at high SNR). It can also be noted that CT-SA and SSA tend to have a noticeably different performance when applied without MOs, but become more similar when MOs are introduced (the same observation applies to the introduction of the MA method). The performance of SSA with MOs tends to be slightly better than that of CT-SA with MOs (in particular at low SNR), which is obtained at the expense of a greater computational cost as shown in Fig. 4.14 resulting from the more complex algorithm associated with the SSA method. Interestingly, it can be noted that the introduction of MOs in the SAE process not only leads to significant accuracy improvements for both CT-SA and SSA as shown in Fig. 4.13 but in some cases can even do so at a lower computational cost as shown in Fig. 4.14. This can be explained by the benefits of using adequate MOs in SAE: these operations, when used properly, can reduce false alarms and fill gaps within the original SAs resulting from missed detections, which facilitates and simplifies the task of detecting SAs for both CT-SA and SSA. As a result, the CT-SA and SSA methods can detect the SAs more accurately and do so at a similar or even lower computational cost, because the enhancements introduced by the application of MOs beforehand reduces the number of computations required by both SAE methods (this is particularly true at high SNR). Therefore, it can be concluded that the proposed MO-based SAE method can help existing SAE methods provide a significantly more accurate estimation of the existing SA without increasing the computational cost and, in some cases, even reducing the associated computational workload.

Finally, Fig. 4.15 validates the performance of the proposed MO-based SAE method by comparing the performance forecasted by simulations with the actual performance obtained based on experimental data collected with the experimental setup presented in Section 3.3.2. As it can be observed, simulation and experimental results match very closely over the whole range of SNR values, except perhaps for SNR values slightly below the low SNR switching threshold, SNR_{th}^{L}, where a maximum deviation between simulation and experimental results of around 1 dB is observed over a short SNR interval. In this SNR region, the actual experimental performance is indeed slightly better than predicted by the simulations. The results shown in Fig. 4.15 indicate that the use of MOs can actually improve the performance of existing SAE methods significantly when implemented in practical systems.

4.4   Summary

This chapter has explored the applicability of MOs from the field of image processing in the context of SAE, analysing their individual impacts when applied both as standalone SAE methods and as pre/post-processing techniques to other existing SAE methods (such as CT-SA and SSA). The obtained results have demonstrated that MOs can provide significant accuracy improvements in the accuracy of the detected SAs in the latter case. The application of carefully selected and properly configured MOs for each SNR regime can provide significant accuracy improvements both at low SNR (with gains of up to 40%) and high SNR (reaching 100% accuracy levels). These operations,
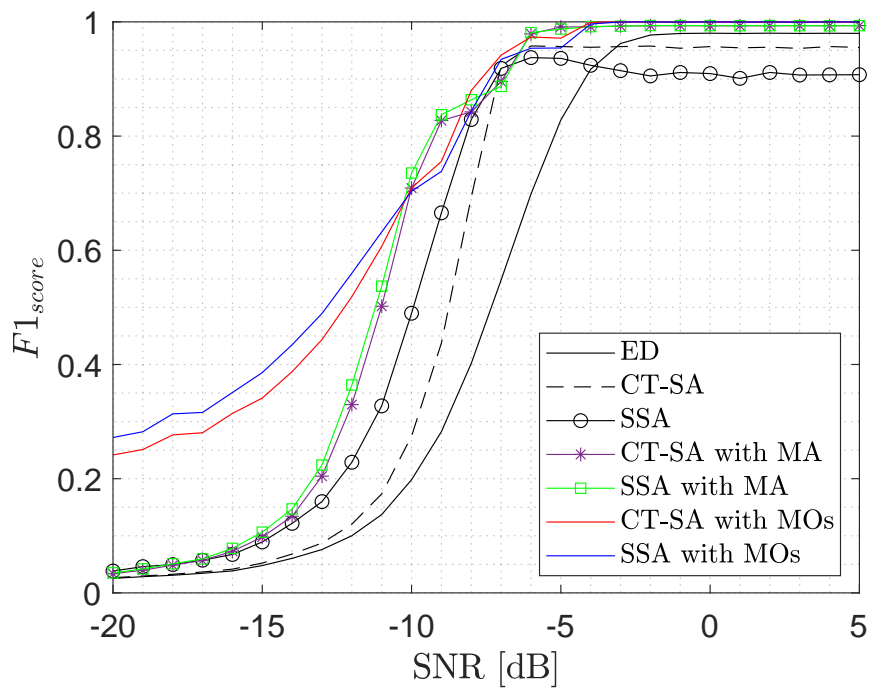
Figure 4.13: F1 score of the proposed MO-based SAE method.
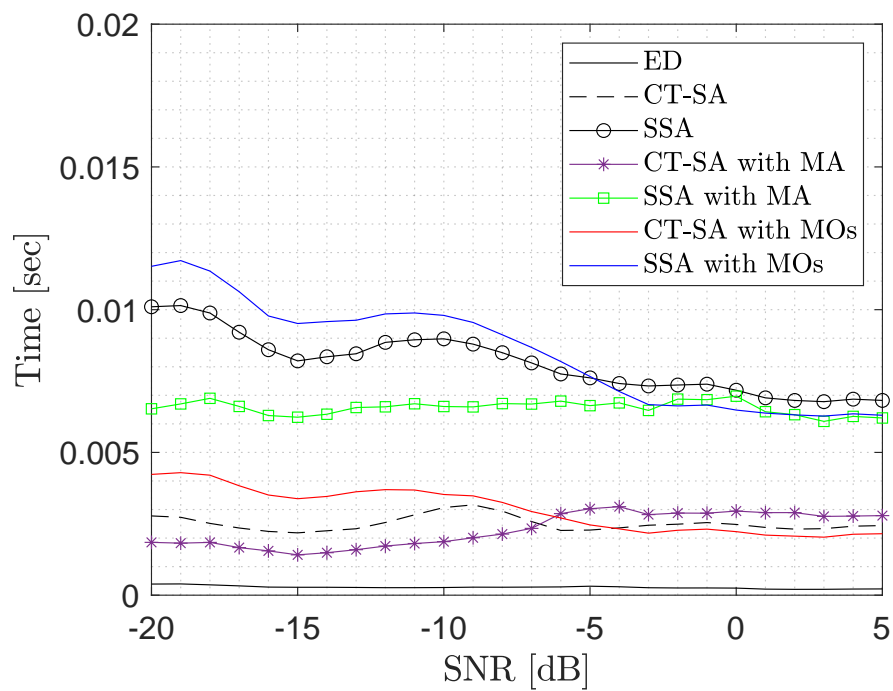
Figure 4.14: Computation time of the proposed MO-based SAE method.
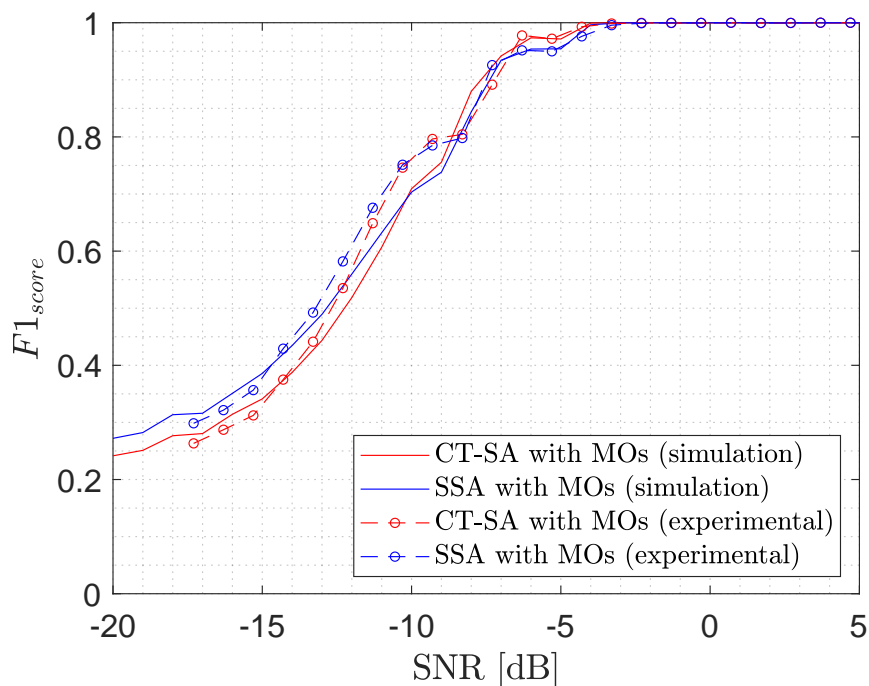
Figure 4.15: Experimental validation of the proposed method.

when used properly, can reduce false alarms and fill gaps within the original SAs, which facilitates and simplifies the task of detecting SAs for both CT-SA and SSA. As a result, the proposed MO-based SAE method can help existing SAE methods provide a significantly more accurate estimation of the existing SAs without increasing, and in some cases even reducing, their computational cost.

Chapter 5

Signal Area Estimation based on Edge Detection and Flood Fill

5.1 Introduction

Several Signal Area Estimation (SAE) methods have been proposed [11, 12, 24–33, 43], which provide different trade-offs between SAE accuracy and computational complexity. This chapter explores a new approach for SAE by treating spectrograms as images, where each spectrogram point is seen as an image pixel, and applying two well-known techniques from the field of image processing, namely edge detection and flood fill. Edge detection is first employed to identify the edges of potential SAs and flood fill is then used to fill the area inside the estimated edges in order to produce a more accurate estimation of the SAs present in a spectrogram. Three methods commonly used for edge detection are considered (gradient magnitude, Laplacian of Gaussian and Canny) and their suitability as SAE methods is explored, both as standalone SAE techniques and combined with other existing SAE methods from the literature as a pre/post-processing stage. The performance of the proposed approach is evaluated with extensive software simulations and corroborated with hardware experiments. It is observed that this approach in general has limited utility when used standalone but can provide significant accuracy improvements in the low SNR regime when used as a pre- and/or post-processing stage to other existing SAE methods. The overall effect is an improvement of their sensitivity and an extension of their SNR range of operation.

While the edge detection and flood fill techniques are well-known and commonly used in image processing, computer vision and other related fields, they are barely known and exploited in the wireless communications community. There have been some previous attempts in the literature to apply edge detection techniques to spectrograms, however mostly for automatic tonal detection and recognition of marine mammal sound patterns in the field of bioacoustics [58–61]. The signal formats and the motivations for applying edge detection techniques in such problem are very different from those in SAE scenarios. To the best of the author' knowledge, this is the first study in the literature that explores the applicability of edge detection techniques to the problem of SAE in spectrograms for wireless communication signals.

This chapter makes a number of contributions. First, it provides an exhaustive analysis on the suitability of common edge detection techniques to the problem of SAE.

73

By means of simulations, the consequence of applying different edge detectors to SAE is investigated under a broad range of configuration parameters for each edge detector. The analysis is conducted over a representative range of Signal-to-Noise ratio (SNR) conditions typically found in wireless communication systems. In such analysis, the accuracy of edge detection plus flood fill is explored when used both as a standalone SAE method and as a pre/post-processing stage combined with other existing SAE methods from the literature. Based on the outcomes, the optimum configuration for each detector achieving the highest observed accuracy is determined and a suitable SAE strategy is formulated for each edge detection method. The proposed approach is shown to provide significant accuracy improvements in the detected SAs at low SNR (with respect to the case where the other SAE methods are used alone) and without having a significant impact on the overall computational cost.

The remainder of this chapter is structured as follows. First, Section 5.2 provides an overview of the fundamentals of the edge detection and flood fill techniques from image processing. The performance of the proposed strategy based on various edge detection techniques is then explored in Section 5.3, where the most convenient SAE approach is formulated as well. Finally, Section 5.4 summarises this chapter.

5.2   Overview of the Edge Detection and Flood Fill

The main idea behind the strategy proposed in this chapter for SAE is based on two fundamental steps, namely edge detection and flood fill. The main objective of the edge detection step is to determine the most likely boundaries of potential SAs in the received time/frequency spectrum data grid. Once these boundaries are determined, a flood fill algorithm is in charge of filling the space within the detected edges in order to produce solid SAs. The problems of edge detection and flood filling have been extensively investigated for several decades and the available literature is abundant [62]. This section provides an overview of the main strategies for edge detection and flood fill with a special focus on those aspects that are relevant to the problem of SAE.

5.2.1   Edge Detection

Edge detection is an image processing technique used to find edges of objects or boundaries between two regions within an image. In image processing jargon, an edge is essentially a curve of connected pixels that follows a path of rapid change in image intensity; as such, it can be found by looking for places in the image where there is a rapid change or abrupt discontinuity in the intensity levels. A relatively simple technique to detect discontinuities in the intensity level is by looking for regions of the image where the magnitude of the first-order derivative of the intensity is greater than a properly set threshold. Since digital images are two-dimensional matrices of pixels, the two-dimensional gradient is employed:

$$\nabla f = \frac{\partial f}{\partial x}\mathbf{i} + \frac{\partial f}{\partial y}\mathbf{j} = (G_x * f)\mathbf{i} + (G_y * f)\mathbf{j} \qquad (5.1)$$

where $\partial f / \partial x$ and $\partial f / \partial y$ are the first-order partial derivatives of a digital image $f(x, y)$ at every location (x, y) in the horizontal and vertical directions[1], respectively, while G_x and G_y are first-order discrete differentiation operators used to estimate the intensity gradients in each direction (the symbol $*$ denotes two-dimensional convolution). Since the gradient ∇f points in the direction of maximum rate of change of image f at location (x, y), its magnitude $\|\nabla f\|$ gives the maximum rate of increase of $f(x, y)$ per unit distance in that direction. The result therefore represents how abruptly the image intensity changes at every point, thus giving an indication of how likely that part of the image belongs to an edge and how that edge is likely to be oriented. This implies that the magnitude of the gradient vector will be zero in areas of constant intensity and will find local maxima where edges are present. By comparing the magnitude of the gradient vector to an adequate threshold, the set of pixels belonging to edges can be extracted from an image. Concretely, a pixel will belong to an edge ($\mathcal{H}_1$) if the gradient magnitude is greater than the selected threshold λ, and will be assumed not to belong ($\mathcal{H}_0$) otherwise[2]:

$$\|\nabla f\| = \sqrt{\left(G_x * f\right)^2 + \left(G_y * f\right)^2} \underset{\mathcal{H}_0}{\overset{\mathcal{H}_1}{\gtrless}} \lambda \tag{5.2}$$

The two-dimensional gradient is obtained by computing the first-order partial derivatives $\partial f / \partial x$ and $\partial f / \partial y$ at every pixel location (x, y). This is accomplished by convolving the input image f with a predefined small squared sub-image usually called *filter*, *mask* or *convolution kernel*. This is a linear spatial filtering process whereby the filter mask is moved through every pixel of the input image and at each point the filter response is calculated as the sum of the products between each of the filter coefficients and the intensity levels of the corresponding image pixels within the region encompassed by the mask. Mathematically, the result of this convolution/filtering process is a discrete approximation to the gradient of the image intensity. As it can be seen from (5.1), two filter masks G_x and G_y are used, one to estimate the intensity gradient in each orthogonal direction. The magnitude of the intensity gradient at every image point is then obtained as shown in (5.2).

The filter coefficients are calculated so as to approximate the response of the first-order derivative (gradient) in the desired direction (hence, the filter masks G_x and G_y are also referred to as *gradient operators*). Several methods have been proposed in the literature to calculate these coefficients. Table 5.1 shows the gradient operators proposed by Prewitt [64], Sobel [65, 66], Scharr [67] and Kroon [68]. Notice that in all masks the coefficients sum to zero, thus indicating a zero response in areas of constant intensity (i.e., where edges are not present) as expected of a gradient/derivative operator. Prewitt masks are the simplest differentiation filters, while Sobel masks have a slightly superior noise suppression performance [63, p.579]. Both Prewitt and Sobel masks provide in general a low level of isotropicity or rotational invariance (i.e., ability not to bias any directions in images, providing an equally sensitive response in all directions),

---

[1]In image processing the horizontal axis coordinate increases positively left-to-right while the vertical axis coordinate increases positively top-to-bottom (instead of bottom-to-top as in the common Cartesian coordinate system).

[2]As discussed in [63], the computational burden required by the calculation of squares and square roots can be removed by approximating $\|\nabla f\| \approx \left|G_x * f\right| + \left|G_y * f\right|$. The resulting filters will not be isotropic (invariant to rotation) in general but this is not an issue with filters specifically designed to detect horizontal and vertical edges as the ones considered in this work.

Table 5.1: Common gradient operators for edge detection.

	G_x	G_y
Prewitt	$\begin{bmatrix} 1 & 0 & -1 \\ 1 & 0 & -1 \\ 1 & 0 & -1 \end{bmatrix}$	$\begin{bmatrix} 1 & 1 & 1 \\ 0 & 0 & 0 \\ -1 & -1 & -1 \end{bmatrix}$
Sobel	$\begin{bmatrix} 1 & 0 & -1 \\ 2 & 0 & -2 \\ 1 & 0 & -1 \end{bmatrix}$	$\begin{bmatrix} 1 & 2 & 1 \\ 0 & 0 & 0 \\ -1 & -2 & -1 \end{bmatrix}$
Scharr	$\begin{bmatrix} 3 & 0 & -3 \\ 10 & 0 & -10 \\ 3 & 0 & -3 \end{bmatrix}$	$\begin{bmatrix} 3 & 10 & 3 \\ 0 & 0 & 0 \\ -3 & -10 & -3 \end{bmatrix}$
Kroon	$\begin{bmatrix} 17 & 0 & -17 \\ 61 & 0 & -61 \\ 17 & 0 & -17 \end{bmatrix}$	$\begin{bmatrix} 17 & 61 & 17 \\ 0 & 0 & 0 \\ -17 & -61 & -17 \end{bmatrix}$

which has motivated the proposal of other gradient operators by Scharr and Kroon as well as alternative filter designs [69–71]. All filter masks shown in Table 5.1 have in common that they are specifically designed to be sensitive to horizontal and vertical edges (which can be intuitively inferred from the symmetric design around central rows and columns of zeros). This property is of particular interest in this work since SAs are precisely delimited by horizontal and vertical edges. Other filter masks such as those proposed by Roberts [72], Kayyali [73] or Kirsch [74] are designed to be sensitive to diagonal edges and are not considered in this work. Filter masks are strictly defined as 3×3 templates even though some ad hoc methods have been proposed to generate larger kernels for higher dimensions by expansion [75] or dilation [76, 77].

An alternative strategy to the gradient-magnitude edge detection methods discussed above is to calculate the second-order derivative of the intensity and look for its zero-crossings to detect edges. Since digital images are two-dimensional matrices of pixels, the two-dimensional Laplacian is employed:

$$\nabla^2 f = \frac{\partial^2 f}{\partial x^2} + \frac{\partial^2 f}{\partial y^2} = L * f \tag{5.3}$$

where $\partial^2 f/\partial x^2$ and $\partial^2 f/\partial y^2$ are the second-order partial derivatives of a digital image $f(x, y)$ at every location (x, y) in the horizontal and vertical directions, respectively, and L is a discretely sampled version of the Laplacian operator (the symbol $*$ denotes

two-dimensional convolution). Since the Laplacian is usually unacceptably sensitive to noise, the input image is first processed with a smoothing Gaussian filter whose response is typically of the form [63]:

$$h(r) = \exp\left(-\frac{r^2}{2\sigma^2}\right) \tag{5.4}$$

where $r^2 = x^2 + y^2$ and σ is the filter's standard deviation, which determines the level of *smoothing* or *blurring* in the filtered image. The Laplacian operator is then applied to the noise-filtered result, which is equivalent to filter the original input image with a Laplacian of Gaussian (LoG) filter:

$$\nabla^2 h(r) = \left[\frac{r^2 - 2\sigma^2}{\sigma^4}\right] \exp\left(-\frac{r^2}{2\sigma^2}\right) \tag{5.5}$$

Thus, the input image is convolved with a discretely sampled version of the filter in (5.5), whose size $n \times n$ is usually selected based on the filter's standard deviation as $n = 2\lceil 3\sigma \rceil + 1$ (this ensures that the filter dimensions are large enough to include three standard deviations around the mean, which accounts for 99.73% of the Gaussian filter response). The zero-crossings of the resulting output can be exploited to extract edges from the input image. As opposed to the gradient-magnitude methods discussed above, the LoG method is not specifically sensitive to edges with a particular orientation.

A third popular strategy for edge detection is the method proposed by Canny [78]. The formulation of this method starts with the aim of finding an optimum filter that addresses the three main issues of edge detection (error rate, localisation and uniqueness of the filter response). Such optimum filter is approximated by the first derivative of a Gaussian filter. Based on this finding, the Canny method undertakes the following steps [62, sect. 2.4]: i) a Gaussian filter is applied to smooth the input image and remove noise; ii) the intensity gradient of the filtered image is found in order to perform a minimum cut-off (non-maximum) suppression of gradient magnitudes, or lower bound thresholding, as an edge thinning technique so that spurious responses of the filter are eliminated and multi-pixel wide *ridges* are thinned down to single pixel width; iii) final edges are determined according to a process of edge tracking by hysteresis based on double thresholding. This last step is the most significant difference between the Canny and other edge detection methods. A high threshold λ_{high} for low edge sensitivity (typically set at around 0.7 times the maximum intensity level) is used to detect pixels belonging to strong edges, while a low threshold λ_{low} for high edge sensitivity (typically selected as $\lambda_{low} \approx 0.3 \lambda_{high}$) is used to decide on weak edges. Pixels whose intensity gradient magnitude is greater (lower) than λ_{high} (λ_{low}) are selected (discarded). Pixels whose intensity gradient magnitude lies within the interval $[\lambda_{low}, \lambda_{high}]$ are included in the output only if they are connected/adjacent to strong edges (whose intensity gradient is above λ_{high}), otherwise they are assumed to be noise or spurious responses and therefore discarded. Similar to the LoG method, the Canny method is not particularly sensitive to edges with a certain orientation. The Canny method requires three parameters, namely the standard deviation of the Gaussian filter (σ) and the pair of thresholds ($\lambda_{low}, \lambda_{high}$).

5.2.2   Flood Fill

While edge detection is the key technique employed in this work to detect SAs, it is unable by itself to produce solid SAs as it will only identify their most likely edges/boundaries. To solve this problem, a flood fill algorithm is applied immediately after the edge detection step in order to fill the empty space within the detected edges and thus produce solid SAs.

The traditional flood-fill algorithm spreads throughout the image based on the connectivity of the pixels. Two connectivity types are usually defined: the first connectivity type considers that two pixels are connected if their edges touch (in this case each pixel will be connected to a maximum of four neighbouring pixels that are adjacent in the horizontal and/or vertical directions) while the second connectivity type deems two pixels as connected if their edges or corners touch (in this other case each pixel will be connected to a maximum of eight neighbouring pixels that are adjacent in the horizontal, vertical and/or diagonal directions).

The algorithm starts at a random zero-valued (idle state) pixel within the boundaries of the detected edges and recursively reverts the state of other connected zero pixels (from zero to one, i.e., busy or occupied state) until all branches of the recursive process reach a location where all the connected pixels are one. At that point, the connected region of idle-state pixels within the boundaries of the detected edges will be filled and a solid SA will be produced. This recursive process can be used to *fill holes*, i.e., areas of connected idle/zero pixels surrounded by busy/one pixels (belonging to edges). The flood fill method used in this work is based on the morphological reconstruction algorithm described in [79, pp. 173-174].

A common issue that can degrade the performance of the flood fill step is the presence of SAs (or parts thereof) in contact with the border of the image (time/frequency data grid). This typically occurs when a transmission starts before or ends after the time-frequency data are captured, thus leading to SAs that are clipped in one of their sides by the bottom or top borders of the image, respectively. Clipping by the left or right borders of the image can also occur when the measurement bandwidth of the receiver is not large enough to fully embrace the bandwidth of the signals being monitored. Edge detection methods do not identify image borders as edges and the lack of *edge pixels* in one of the sides of a clipped SA affects the ability of the flood fill step to correctly fill the space within the SA. This problem is resolved by adding two rows of padding edge pixels to the top and bottom borders of the image (and possibly two columns to the left and right borders as well) to help the flood fill step complete its task. Once the flood fill step is completed, these padding edge pixels are removed and the image is restored to its original dimensions.

5.2.3   Application of Edge Detection and Flood Fill to SAE

A flowchart summarising the signal processing flow of the input spectrogram according to the proposed edge detection plus flood fill framework is illustrated in Fig. 5.1. The main motivation for the application of edge detection and flood fill as a SAE method lies on the ability of edge detection techniques to detect edges of objects (SAs in this case) even when they are partly degraded and the ability of flood fill techniques to fill holes within objects. Edge detection techniques have some tolerance to edge irregularities
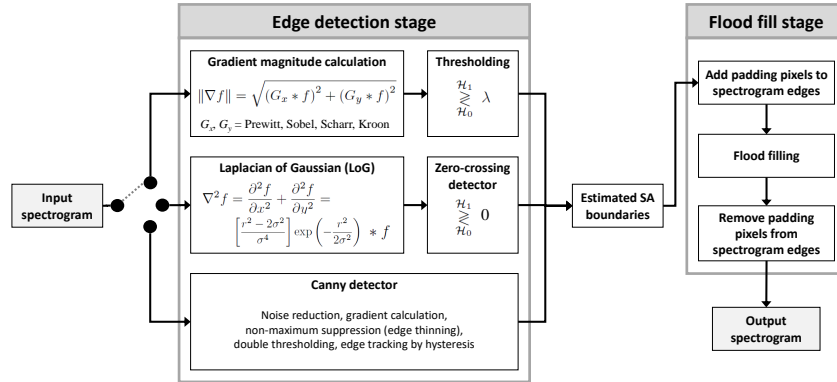
Figure 5.1: Signal processing flow of the input spectrogram according to the proposed edge detection plus flood fill framework.

caused by *noise* (i.e., missed detections and false alarms in the context of SAE). Some methods, such as the Canny method, can even reconnect fragments of edges that have been disconnected due to noise degradation. Moreover, flood fill techniques can fill gaps within SAs resulting from missing SA points due to signal missed detections under low SNR conditions. Therefore, edge detection seems a reasonable way to identify the boundaries of SAs and potentially close them when they are not perfectly closed, while flood fill can be used to fill the area within the detected edges in order to produce a solid SA that otherwise might not be detected so accurately. These observations motivate this work to explore the performance of the edge detection and flood fill operations as a SAE method.

To gain an adequate understanding on whether and how these two image processing techniques can help improve the performance of SAE, two application scenarios are investigated in this work: (i) a first scenario where the proposed approach is applied as a standalone SAE method that takes as an input the binary matrix produced by the application of ED and produces its own final output, similar to how other SAE techniques such as CT-SA or SSA would be applied; (ii) a second scenario where the proposed approach is applied in combination with other existing SAE methods such as CT-SA and SSA as a pre/post-processing technique, where it can be applied only before, only after, or both before and after the other SAE method. The study of both scenarios will provide insights into how to best formulate a suitable SAE method based on edge detection and flood fill.

5.3   Performance Analysis and Proposed Methods

This section presents simulation and experimental results for the performance of edge detection methods (with flood fill) as SAE methods. The evaluation methodology followed in this chapter is identical to the one presented in Chapter 3 (please refer to Section 3.3 for details). First, the performance of each edge detection strategy is explored for various parameter configurations; based on the obtained results, the optimum configuration is selected and a suitable SAE strategy is proposed for each edge detection method. This is carried out for the three edge detection methods considered

(a) Prewitt (SNR = +5 dB)   (b) Sobel (SNR = +5 dB)   (c) Scharr (SNR = +5 dB)   (d) Kroon (SNR = +5 dB)

(e) Prewitt (SNR = –5 dB)   (f) Sobel (SNR = –5 dB)   (g) Scharr (SNR = –5 dB)   (h) Kroon (SNR = –5 dB)
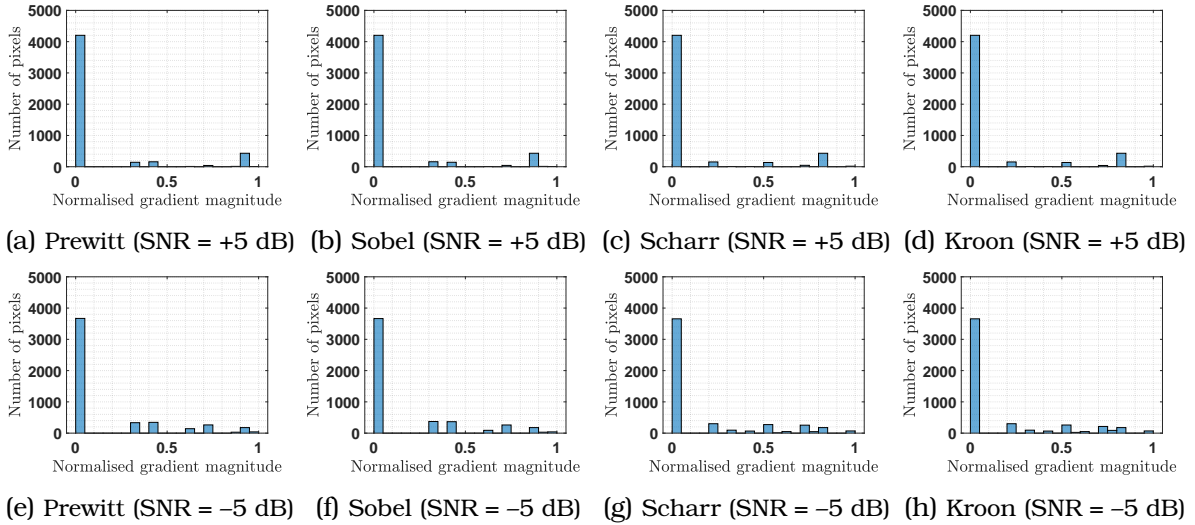
Figure 5.2: Sample histograms of the gradient magnitudes $\|\nabla f\|$ (normalised to $[0,1]$) obtained after filtering the same image of time/frequency data with the gradient operators shown in Table 5.1. Results are shown for high SNR (+5 dB, top) and low SNR (–5 dB, bottom).

in this work (gradient-magnitude, LoG and Canny). Subsequently, the performances of the best configuration for each strategy are compared and analysed to determine the extent to which the SAE approaches explored in this work can improve the accuracy of the detected SAs. The evaluation methodology followed in this study is identical to the one employed in Chapter 3 (see Section 3.3).

5.3.1 Analysis of Gradient-Magnitude Methods

The main configuration parameter of gradient-magnitude methods is the edge detection threshold λ used in (5.2) to extract the edge pixels. To help select suitable thresholds, Fig. 5.2 shows some sample histograms of the gradient magnitude values $\|\nabla f\|$ obtained after filtering the same image of received time/frequency data with the gradient operators shown in Table 5.1. The results are shown for high SNR (+5 dB) and low SNR (–5 dB) at the receiver and the gradient magnitudes are normalised to the interval $[0,1]$. As it can be appreciated, the Prewitt/Sobel masks have similar performance and so does the Scharr/Kroon pair (this can be explained by the fact that the masks in each pair follow similar design principles and this work deals with binary black-and-white images where only horizontal and vertical edges are present). Most pixels have an intensity gradient magnitude of zero (corresponding to the image background) that can be easily separated with a threshold $\lambda = 0.1$ at both low and high SNR. As inferred from the histograms for the high SNR scenario, strong edge pixels are found at levels above $\lambda = 0.8$, which is the second most frequent level. Other gradient magnitude levels between 0.1 and 0.8 are due to either weak edge pixels (mostly found in the corners of SAs), spurious responses of the edge detection filter or false alarms. For the low SNR scenario, gradient magnitude values are slightly more uniformly distributed as a result of a more frequent presence of weak edges and spurious filter responses. Based on these histograms, a set of thresholds $\lambda \in \{0.1, 0.8\}$ is selected for a more detailed study.
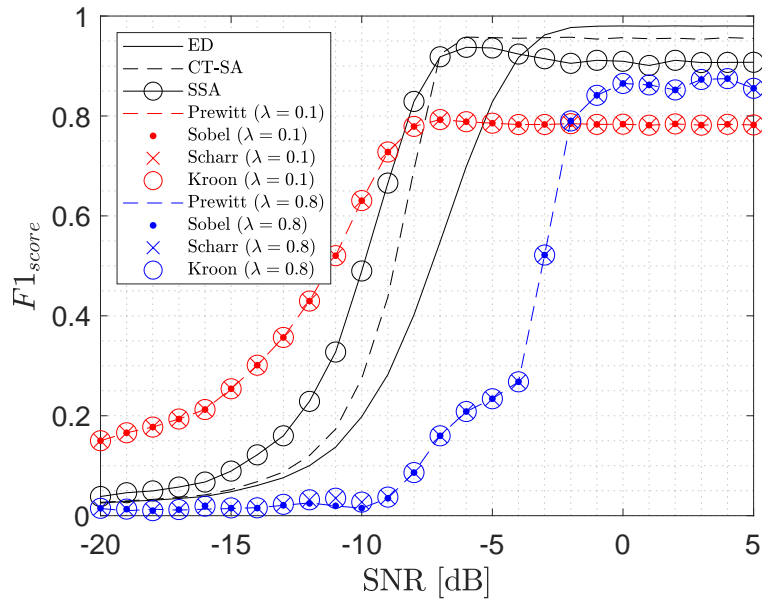
Figure 5.3: Performance of different gradient operators and decision thresholds for gradient-magnitude edge detection methods.

Fig. 5.3 shows the performance of gradient-magnitude edge detection methods (for the four gradient operators of Table 5.1) as a function of the SNR for the two thresholds selected above. These results correspond to the case where these gradient-magnitude edge detectors are used as standalone SAE methods (i.e., only applied to the output of ED without any combination with CT-SA or SSA). The performance of ED alone is included for comparison and the reference SAE methods (CT-SA and SSA) are included as well for completeness. First, it is worth noting that all four gradient operators lead to a largely similar performance in terms of F1 score. This can be explained by the fact that the different design criteria on which these masks rely do not result in any practical difference in the case of the SAE problem considered in this work. Recall that all masks are aimed at approximating the gradient operator, with Prewitt being the simplest one. The Sobel mask is designed to improve the noise suppression characteristics of the Prewitt mask, however noisy pixels in the case of binary (black-and-white) images are more localised and likely less frequent than in continuous (grayscale) images, so in practice there is no apparent difference. Moreover, the Scharr and Kroon filters are designed to improve the isotropicity (rotational invariance) of the Sobel mask, which is irrelevant when the edges of interest are either horizontal or vertical, for which all masks seem to be equally sensitive. Based on these observations, the Prewitt mask (the simplest one) suffices for gradient-magnitude SAE.

Fig. 5.3 also shows the impact of the threshold for the two extreme cases $\lambda = 0.1$ and $\lambda = 0.8$. The curves for these two thresholds give an indication of the worst/best performance that can be attained with gradient-magnitude methods at every SNR. As one may expect, better accuracy is obtained with a more restrictive threshold ($\lambda = 0.8$) at high SNR (to filter weak edges and rely on strong edges) and with a more permissive threshold ($\lambda = 0.1$) at low SNR (to increase sensitivity). However, some counter-intuitive

trends are observed in Fig. 5.3 when the performance of gradient-magnitude edge detectors is compared to the reference SAE methods (ED, CT-SA and SSA). On the one hand, one would expect that edge detection should be a relatively easy task at high SNR and therefore the gradient-magnitude methods should work relatively well, however they exhibit a significant loss of accuracy in this SNR regime with respect to the reference methods. On the other hand, one may also expect edge detection to fail at low SNR due to degraded signal quality, however edge detection based SAE outperforms the reference methods in the low SNR regime. To gain insights into the operation of SAE based on edge detection and explain this trend, Fig. 5.4 shows some examples of the time/frequency grid (image) observed at different stages of the SAE process based on edge detection.

At high SNR, the image observed after ED (Fig. 5.4a) is an accurate reproduction of the true SAs, except for the presence of some false alarms. After the edge detection step (Fig. 5.4c), the boundaries of the SAs are correctly identified, however the detected edges lie on the outer sides of the SAs and the subsequent flood fill operation (Fig. 5.4e) produces a set of final SAs that are slightly larger than the original SAs (this can be noticed in the narrower gaps between SAs in Fig. 5.4e than in Fig. 5.4a). This magnifying effect is observed not only in the true SAs but in the false alarms as well, whose dimensions are also larger in Fig. 5.4e than in Fig. 5.4a. This explains the lower accuracy attained by the gradient-magnitude edge detectors at high SNR. Several techniques could be applied to remedy this degrading effect. For instance, a noise removal step (by morphological erosion or Gaussian filtering) could be introduced to reduce false alarms before the actual edge detection. Moreover, the above mentioned magnifying effect on the true SAs could be reduced by using edge thinning techniques or increasing the image resolution so that the number of edge pixels represents a lower proportion of the total number of image pixels (and hence the pixel-by-pixel calculated F1 score improves). However, this is unlikely to provide better performance than ED and therefore the increased computational cost would not be justified. This suggests that gradient-magnitude edge detectors may not be useful for SAE at high SNR.

At low SNR, the image observed after ED (Fig. 5.4b) shows a high level of degradation where the presence and dimensions of any potential SAs are unrecognisable. The edge detection step (Fig. 5.4d) followed by the subsequent flood fill step (Fig. 5.4f) also have a magnifying effect, both for false alarms (which depend on the noise power only and are therefore independent of the SNR) and true signal components. However, in this case, this is beneficial for SA detection since the small signal components or portions of true SAs observed in Fig. 5.4b are interpreted as separate SAs, and each of these signal components is thus magnified. This somehow helps to fill empty spaces between the vestiges of true SAs, which makes the presence of SAs more visible as it can be clearly appreciated by comparing Figs. 5.4b and 5.4f. The final output obtained at low SNR in Fig. 5.4f may not be useful in applications where the number, location and dimensions of the present SAs need to be known accurately, however it clearly shows the presence of a signal and its approximated bandwidth and such information can be useful in signals intelligence (e.g., signal interception) and similar applications.

The discussion above leads to the conclusion that, in the context of SAE, the interest of gradient-magnitude edge detection lies in the low SNR regime. At low SNR, Fig. 5.3 indicates that the best performance is obtained by using any gradient

(a) Received (5 dB SNR)

(b) Received (–10 dB SNR)

(c) Edge detection (5 dB SNR)

(d) Edge detection (–10 dB SNR)

(e) Edge det. & flood fill (5 dB)

(f) Edge det. & flood fill (–10 dB)
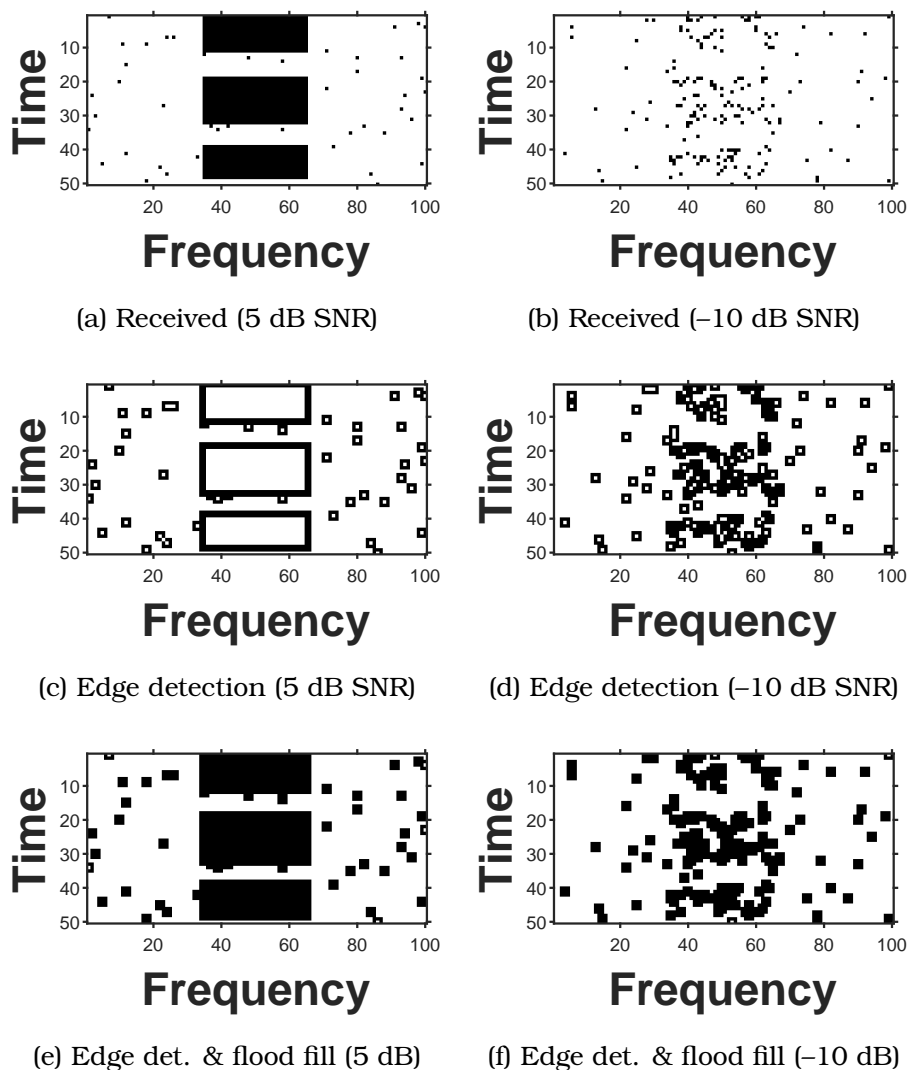
Figure 5.4: Sample images (time/frequency grids) observed at different stages of the SAE process based on gradient-magnitude edge detectors: after ED thresholding (top), after edge detection (middle), and final result after edge detection plus flood fill (bottom). Examples are shown for high SNR (5 dB, left) and low SNR (–10 dB, right). Results correspond to a Prewitt mask and a threshold $\lambda = 0.1$.

operator (e.g., Prewitt for simplicity) and a threshold $\lambda = 0.1$. Compared to most practical edge detection application scenarios, this threshold value may seem quite low and permissive; essentially, any pixel with a gradient magnitude above zero (i.e., any pixel that is not part of the image background, see Fig. 5.2) is considered an edge pixel. However, recall that the images processed in the context of this work are binary black-and-white images composed of zeros (background) and ones (SAs); thus, at low SNR any pixel whose gradient magnitude is above zero is either a false alarm (which will typically occur with low probability depending on the selected ED threshold, e.g. 0.01 in this work) or an edge pixel. Such low threshold value thus yields an improved sensitivity to edge pixels that helps deliver a better performance at low SNR.

The results discussed so far correspond to the application of gradient-magnitude edge detectors as standalone SAE methods (i.e., applied directly to the output of ED as the final SAE stage). These methods can also be applied in combination with other SAE methods (such as CT-SA and SSA) as a pre/post-processing technique. The F1 score performance in this case is illustrated in Figs. 5.5 and 5.6 when combined with the CT-SA and SSA methods, respectively. As noticed, the performance observed in both figures is quite similar. Moreover, the optimum SAE procedure depends on the particular SNR experienced at the monitoring receiver. Based on these results, a suitable SAE method based on gradient-magnitude edge detection can be formulated:

- If $SNR \leq \gamma_l$, perform edge detection before and after the other SAE method.

- If $\gamma_l < SNR \leq \gamma_m$, perform edge detection only before the other SAE method.

- If $\gamma_m < SNR \leq \gamma_h$, perform edge detection only after the other SAE method.

- If $SNR > \gamma_h$, apply the other SAE method alone (without edge detection).

In this formulation, *the other SAE method* refers to CT-SA, SSA or any other suitable SAE algorithm and (γ_l, γ_m, γ_h) is a set of low, medium and high SNR switching thresholds, respectively, that determine the best operation to perform within each SNR range. The optimum values for these thresholds can be obtained from Figs. 5.5 and 5.6 as the crossing points between curves such that the resulting F1 score is the envelope of all the individual curves. This SAE approach provides the best accuracy that can be attained with the help of gradient-magnitude edge detectors for every SNR value, which, as shown in Figs. 5.5 and 5.6, can provide significant accuracy improvements in the low SNR regime (with respect to the use of the other SAE method alone, e.g. up to 40% for CT-SA at –10 dB SNR). This is illustrated with some sample images in Fig. 5.7 for the CT-SA method operating at an SNR of –10 dB (similar trends and conclusions are observed for SSA). The outcome of ED at such low SNR (Fig. 5.4b) does not seem to provide any clear indication that a signal is present. The application of CT-SA alone (Fig. 5.7a) seems to provide some hint that a signal may be present, however in an unclear manner and without enough detail to estimate basic signal properties such as its bandwidth. However, the introduction of edge detection as a pre/post-processing step (Figs. 5.7b–5.7d) provides a clear indication that a signal is present as well as sufficient detail for a rough estimation of its bandwidth. As stated earlier, the output in this case does not provide sufficient detail to obtain accurate information about the number, location and dimensions of the present SAs (such as in Fig. 5.4a under high SNR conditions) but can be very useful in the context of signals intelligence (e.g., for signal interception) and other similar application scenarios.

Comparing Fig. 5.3 with Figs. 5.5 and 5.6 it can be observed that gradient-magnitude edge detectors perform better when combined with other SAE methods (based on the dynamic SNR-switching approach described above) than when used standalone. This is true for the whole range of SNR values where the use of gradient-magnitude detectors is beneficial (i.e., at low SNR). Therefore, the optimum configuration for gradient-magnitude edge detection methods is achieved when combined with other SAE methods according to the three SNR switching thresholds (γ_l, γ_m, γ_h) as discussed above.
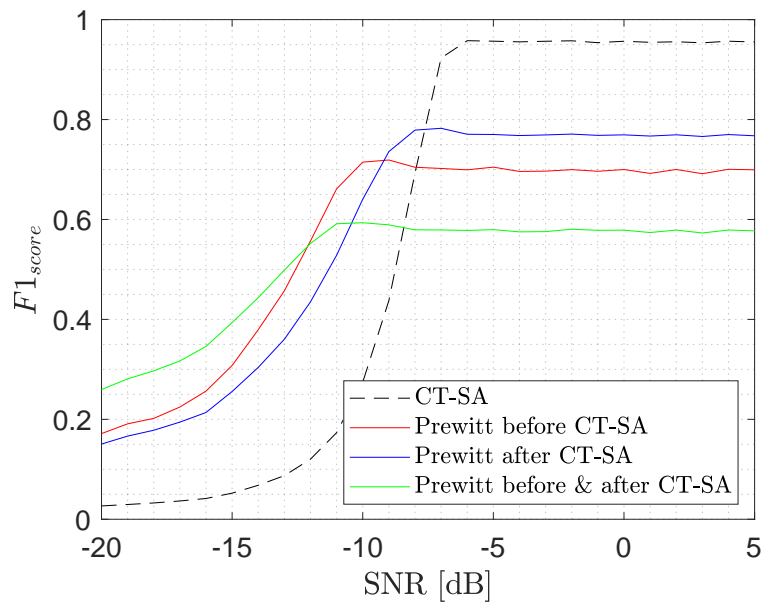
Figure 5.5: Performance of SAE based on CT-SA combined with gradient-magnitude edge detection (Prewitt mask, $\lambda = 0.1$) as a pre/post-processing technique.
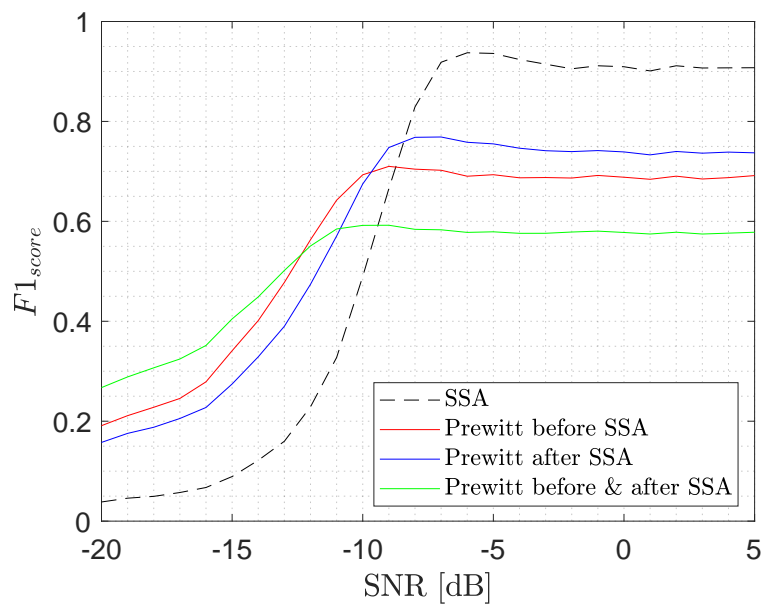
Figure 5.6: Performance of SAE based on SSA combined with gradient-magnitude edge detection (Prewitt mask, $\lambda = 0.1$) as a pre/post-processing technique.

(a) CT-SA alone

(b) Edge det. before CT-SA

(c) Edge det. after CT-SA

(d) Edge det. before+after CT-SA
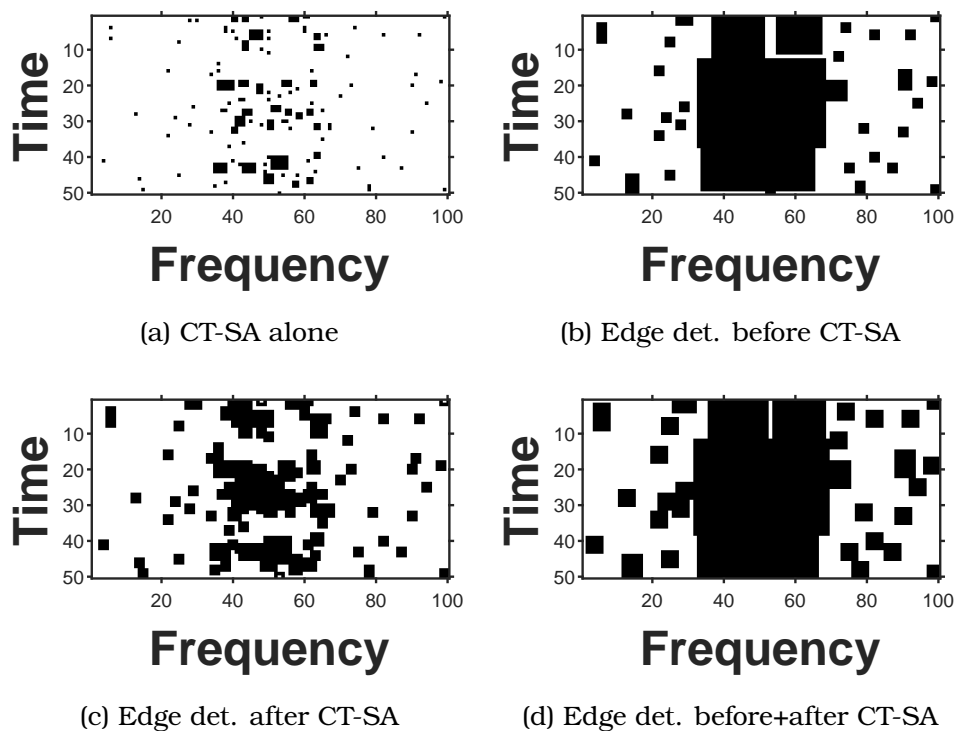
Figure 5.7: Sample images (time/frequency grids) observed for SAE based on CT-SA combined with gradient-magnitude edge detection (Prewitt mask, $\lambda = 0.1$) as pre/post-processing stage (–10 dB SNR).

5.3.2 Analysis of the Laplacian of Gaussian Method

Fig. 5.8 shows the performance of the LoG edge detector as a function of the SNR for selected values of the Gaussian filter's standard deviation (parameter σ) when used as a standalone SAE method. The performance of ED alone is included for comparison and the reference SAE methods (CT-SA and SSA) are included as well for completeness. Similar to the case of gradient-magnitude methods, the accuracy is degraded in the high SNR regime and improved at low SNR, for the same reasons explained in Section 5.3.1. The extent to which the accuracy is improved or degraded in each SNR range depends on the filter's standard deviation. Interestingly, the optimum value of σ that yields the best attainable accuracy decreases with the experienced SNR. This can be explained based on the filter's averaging/blurring effect for different σ values. At high SNR, the present SAs are clearly visible and therefore easily detectable; any averaging/blurring process can only degrade the current image quality and therefore reduce the accuracy of the edge detection process. For this reason, at high SNR the optimum choice is a low standard deviation as this will have a low averaging/blurring effect. In the example of Fig. 5.8 this corresponds to $\sigma = 0.5$ (the lowest considered value), which has no effect on the filtered signal and is equivalent to skip the edge detection plus flood fill step altogether. As the SNR decreases, parts of the true SA will start to disappear as a result of a lower detection probability, thus making them look more similar to background areas of the image (with no signal components) and
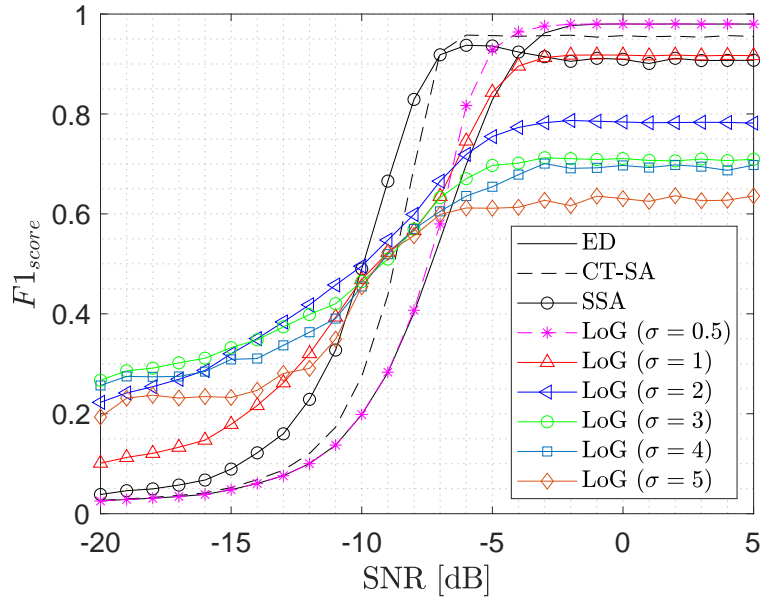
Figure 5.8: Performance of the LoG edge detector as a standalone SAE method for different values of the filter's standard deviation.

therefore affecting the filter's ability to respond to the presence of edges. This can be overcome by increasing the filter's standard deviation (i.e., the filter's width) so that more neighbouring pixels are included in the averaging process, which will increase the probability of a detectable response at the output of the LoG filter when an edge is present. This explains why the optimum value of σ that yields the best attainable accuracy increases when the experienced SNR decreases (in the example of Fig. 5.8, the optimum choice is $\sigma = 0.5$ down to –6.5 dB, at which point $\sigma = 1$ yields a similar accuracy, then $\sigma = 2$ from –6.5 dB down to –14 dB, and finally $\sigma = 3$ for lower SNR values).

The performance of the LoG edge detector when used as a pre/post-processing technique for other SAE methods is illustrated in Fig. 5.9 for the CT-SA method (the counterpart figure for the SSA method is omitted as it is highly similar). Most of the observations for the LoG edge detector as a standalone SAE method that were discussed above are also valid when used as a pre/post-processing stage. It is worth noting from Fig 5.9 that, in the SNR range where the use of the LoG method is beneficial (i.e., in the region of lower SNR), the best accuracy is obtained when used as a pre-processing technique (i.e., only before the other SAE method is applied). Applying the LoG method as a post-processing stage leads to a lower accuracy and indeed degrades the accuracy obtained when also applied as a pre-processing stage. This indicates that the magnifying effect of the LoG edge detection plus flood fill step makes it easier for other SAE methods to detect the presence of SAs more accurately. Similar to the standalone scenario, in this case the optimum σ increases as the experienced SNR decreases, which is illustrated in Fig. 5.10 when CT-SA is employed as the main SAE method (similar results are obtained for SSA). Comparing Figs. 5.8 and 5.10, and assuming that the optimum σ for each experienced SNR is selected, one can

(a) $\sigma = 0.5$

(b) $\sigma = 1$

(c) $\sigma = 2$

(d) $\sigma = 3$

Figure 5.9: Performance of SAE based on CT-SA combined with LoG edge detection as a pre/post-processing technique for several values of filter's standard deviation (parameter σ).

see that a better accuracy can be obtained when the LoG edge detector is combined with another SAE method as a pre-processing stage (similar to what was observed for gradient-methods in Section 5.3.1) and therefore this is the preferred configuration.

An important aspect in the configuration of the LoG method is how the value of σ should be selected for each experienced SNR so that the resulting SAE accuracy is maximised. To answer this question, extensive simulations were run for SNR values in the range from –20 dB to –5 dB (notice in Fig. 5.10 that for SNR values above –5 dB the best choice is to skip the LoG edge detection step, as discussed earlier). For each simulated SNR, values of σ in the range from 0.5 to 5.0 in increments of 0.1 were tested and the resulting SAE accuracy was calculated in terms of the F1 score. The results of this simulation are shown in Fig. 5.11. These results can be further processed to find out the optimum σ that maximises the F1 score for each SNR (σ_{opt}), which is shown in Fig. 5.12. The stair shape of the simulation results (labelled as *optimum*) in Fig. 5.12 suggests that only a small finite set of σ values is enough to optimise the accuracy over the whole SNR range of interest, except for SNR values below –15 dB where a more
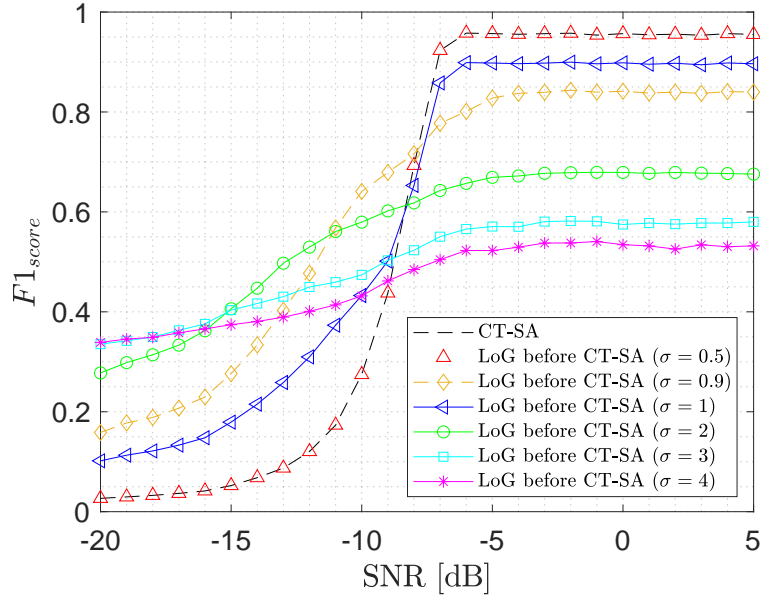
Figure 5.10: Performance of SAE based on CT-SA combined with LoG edge detection as a pre-processing technique only for several values of the filter's standard deviation (parameter σ).

diverse range of σ_{opt} is observed. However, it can be noted in Fig. 5.11 that for SNR below –15 dB the optimum F1 score is observed in a rather flat region and therefore its value is not very sensitive to small variations of σ. In particular, values of σ in the interval [3, 3.5] give very similar F1 score for SNR below –15 dB, therefore replacing the true σ_{opt} with σ =3 for SNR below –15 dB will not have a noticeable impact on the resulting accuracy. This is labelled as *near-optimum* in Fig. 5.12. The advantage of this approach is that a small set of values $\sigma \in \{0.75, 1.1, 1.4, 2.1, 3.0\}$ represents the entire domain of σ_{opt} over the whole SNR range of interest as shown in Fig. 5.12. The SNR switching thresholds can be readily obtained from the same figure.

The simulation results in Fig. 5.12 can be fitted to a Gaussian model of the form:

$$\sigma_{\text{opt}} \approx \sum_{n=1}^{N} a_n \exp\left(-\left[\frac{x - b_n}{c_n}\right]^2\right) \tag{5.6}$$

with the fitting coefficients shown in Tables 5.2 and 5.3 for the *optimum* and *near-optimum* results, respectively. This mathematical approximation may be useful both in practical implementations and analytical studies.

In summary, the optimum configuration for the LoG edge detector as a SAE method is as follows. At low SNR, the best accuracy is obtained when combined with another SAE method as a pre-processing step, adjusting the filter standard deviation according to the experienced SNR as shown in Fig. 5.12 or alternatively according to the model in (5.6) with the fitting coefficients shown in Table 5.3. At high SNR (above –5 dB according to Figs. 5.10 and 5.12) the best accuracy is obtained by using only the other SAE method (i.e., without edge detection).
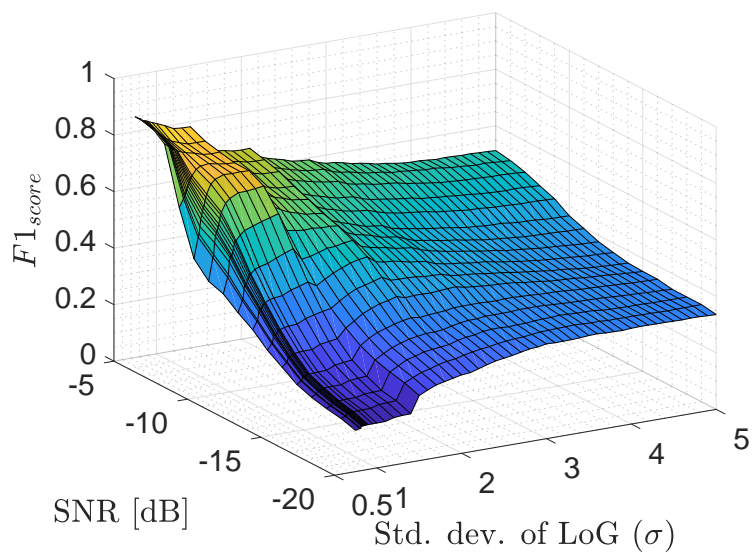
Figure 5.11: Performance of SAE based on CT-SA combined with LoG edge detection as a pre-processing technique as a function of the experienced SNR and the filter's standard deviation (parameter σ).
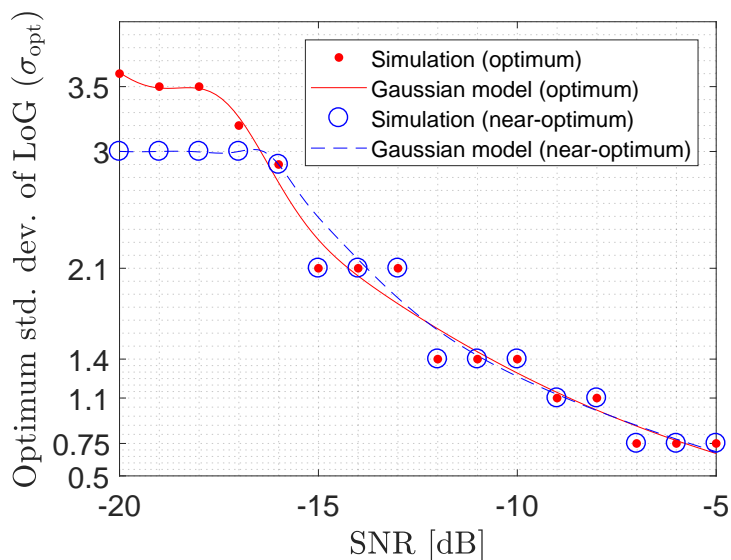
Figure 5.12: Optimum value of the LoG filter's standard deviation as a function of the experienced SNR (based on Fig. 5.11).

5.3.3 Analysis of the Canny Method

The Canny method has three configuration parameters: the standard deviation of the Gaussian filter (σ) and the pair of thresholds for weak and strong edge pixels ($\lambda_{low}, \lambda_{high}$). To find a suitable parameter configuration for SAE, histograms of the gradient magnitude similar to those shown in Fig. 5.2 were calculated for standard

Table 5.2: Fitting coefficients of the model in (5.6) for the *optimum* simulation results of Fig. 5.12.

Parameter	Value	95% confidence interval
x	SNR [dB]	N/A
N	2	N/A
a_1	8.428	(–11.99, 28.85)
b_1	–41	(–88.32, 6.311)
c_1	22.64	(2.588, 42.69)
a_2	0.5554	(0.1586, 0.9522)
b_2	–17.39	(–18.32, –16.46)
c_2	1.636	(–0.0176, 3.29)
RMSE of fit	0.1597	N/A

Table 5.3: Fitting coefficients of the model in (5.6) for the *near-optimum* simulation results of Fig. 5.12.

Parameter	Value	95% confidence interval
x	(SNR [dB] + 12.5) / 4.761	N/A
N	3	N/A
a_1	0.1703	(–0.7789, 1.12)
b_1	–0.7968	(–1.818, 0.2247)
c_1	0.1616	(–2.096, 2.419)
a_2	0.6097	(–0.5327, 1.752)
b_2	–0.8657	(–2.02, 0.2885)
c_2	0.6896	(–1.463, 2.843)
a_3	3.589	(–3.644, 10.82)
b_3	–3.593	(–12.56, 5.369)
c_3	4.019	(–1.455, 9.493)
RMSE of fit	0.1772	N/A

deviation values within the interval $\sigma \in [0.5, 10]$ and for SNR values within the interval [–20 dB, 5 dB]. Details of the figures are not shown due to the amount of space this would require, however the main findings are summarised here. Compared to Fig. 5.2, the histograms obtained in this case showed a larger proportion of gradient magnitude values in the lower bottom of the range. Recall that the Canny method applies in its first step a Gaussian filter before calculating the gradient magnitude and applying the thresholds (see Section 5.2.1). This Gaussian filtering step has a blurring effect that de-emphasises sharp gradient changes in the image, thus resulting
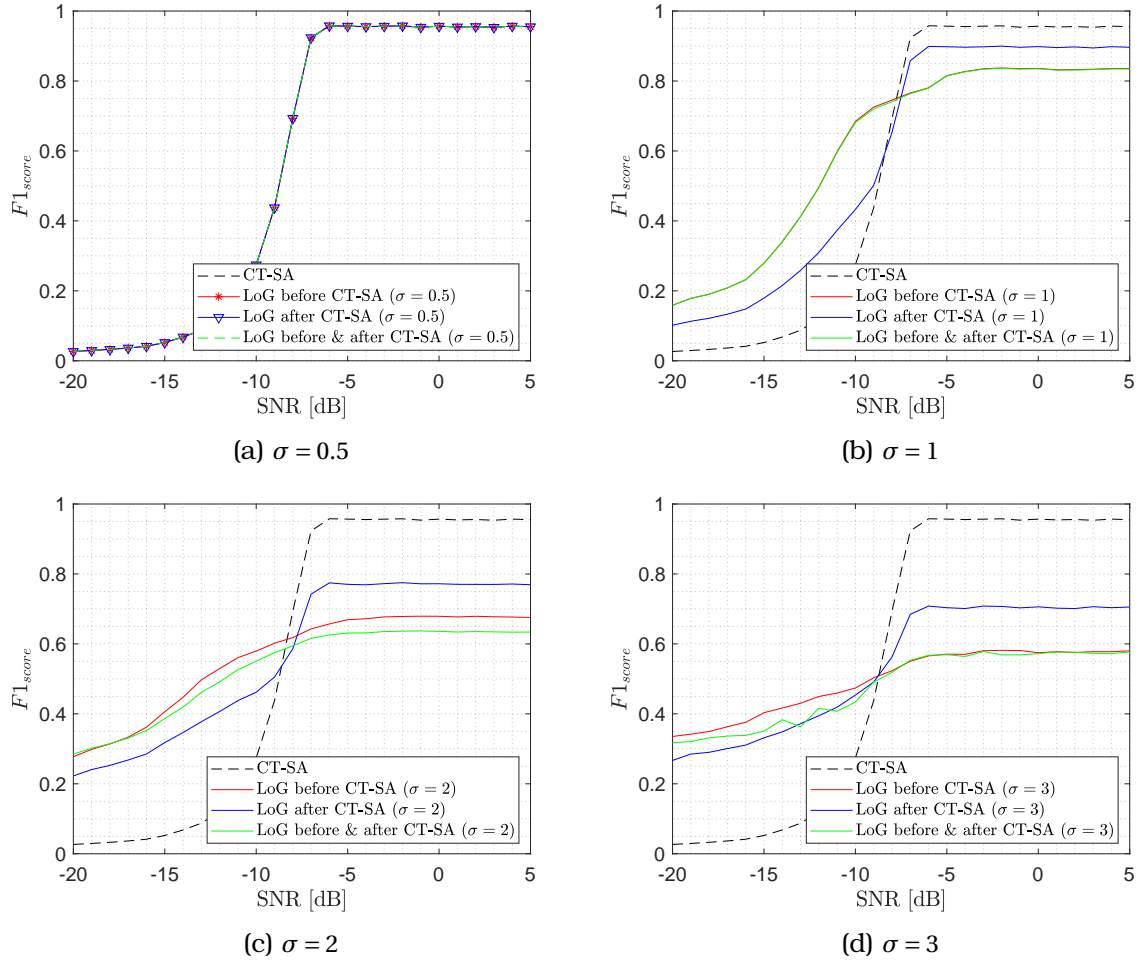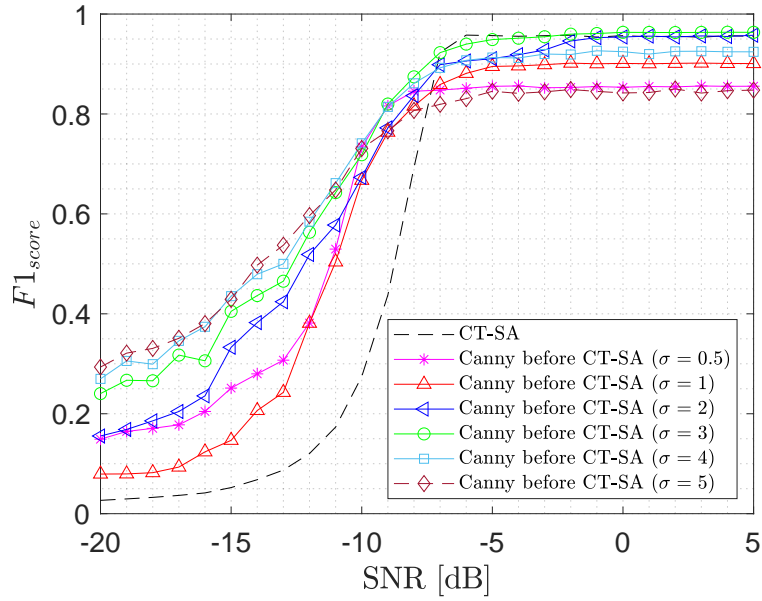
Figure 5.13: Performance of SAE based on CT-SA combined with Canny edge detection as a pre-processing technique only for several values of the filter's standard deviation (parameter σ).

in an overall reduction of gradient values. Based on the obtained histograms, the two threshold values identified in Section 5.3.1 were slightly reduced for the Canny method to $\lambda_{low} = 0.05$ (to isolate pixels with zero-gradient belonging to the image background) and $\lambda_{high} = 0.7$ (corresponding to the gradient magnitude of strong edge pixels after the initial Gaussian blurring step).

Once the thresholds $(\lambda_{low}, \lambda_{high})$ are configured, the performance of the Canny method as a SAE method depends on σ in a largely similar manner as the LoG edge detector and the same main conclusions are reached (all figures are not shown to avoid repetitive results, however the main conclusions are summarised here). In particular, the optimum value of σ that yields the best attainable accuracy increases when the SNR decreases, both when used as a standalone SAE method and in combination with other SAE methods such as CT-SA and SSA; moreover, the latter achieves better accuracy than the former, also when the Canny edge detection plus flood fill are used as a pre-processing stage to other SAE method. The main difference between the Canny and LoG edge detectors when used for SAE, as it can seen by comparing Fig. 5.13 with Fig. 5.10, is that larger standard deviations need to be used for the filter with the Canny method ($\sigma_{opt} \in [3, 6.5]$), which can also be explained based on the blurring effect of its initial Gaussian filtering step. This is corroborated in Fig. 5.14, which shows the optimum standard deviation (σ_{opt}) that maximises the F1 score for each SNR with the Canny edge detector (this figure is the counterpart to Fig. 5.12 and has been obtained following the same procedure; the corresponding fitting coefficients for the model in (5.6) are provided in Table 5.4). Another relevant difference is that with the Canny method it is not possible to cover the whole SNR range with a small set of σ_{opt} values (the optimum value is different for each SNR).
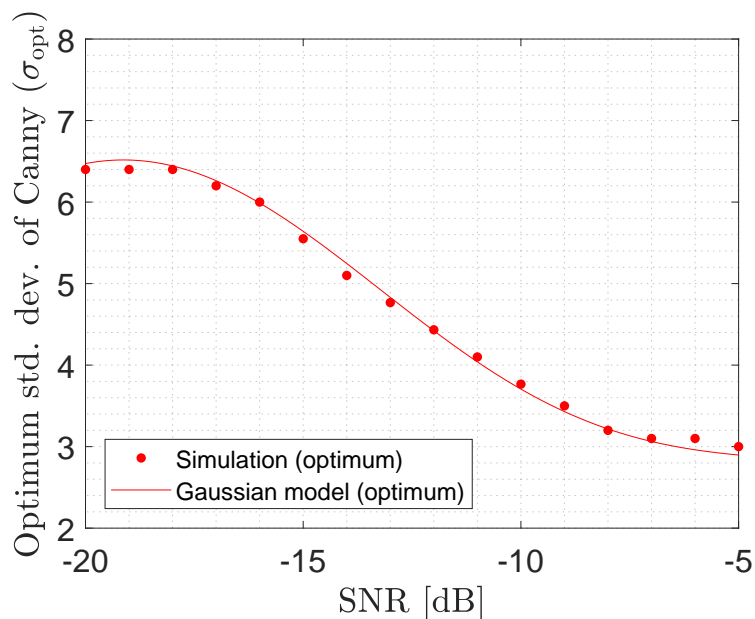
Figure 5.14: Optimum value of the Canny filter's standard deviation as a function of the experienced SNR.

Table 5.4: Fitting coefficients of the model in (5.6) for the Canny edge detection method.

Parameter	Value	95% confidence interval
x	SNR [dB]	N/A
N	2	N/A
a_1	–838.9	$(-6.66 \cdot 10^7, 6.66 \cdot 10^7)$
b_1	–11.15	(–1129, 1106)
c_1	11.69	(–1985, 2009)
a_2	843	$(-6.66 \cdot 10^7, 6.66 \cdot 10^7)$
b_2	–11.18	(–1146, 1124)
c_2	11.74	(–1987, 2010)
RMSE of fit	0.0609	N/A

Based on the results above, the optimum configuration for the Canny edge detector as a SAE method is similar to that of the LoG edge detector. At low SNR, the best accuracy is obtained when combined with another SAE method as a pre-processing step, adjusting the filter standard deviation according to the experienced SNR based on the model in (5.6) with the fitting coefficients shown in Table 5.4. At high SNR (above –5 dB according to Figs. 5.13 and 5.14) the best accuracy is obtained by using only the other SAE method alone.

5.3.4 Comparison of Different Edge Detection Methods

The previous subsections have explored the performance of the three main edge detection algorithms when used along with flood fill as SAE methods. In all cases it has been observed that they lead to an overall accuracy degradation at high SNR but can provide significant improvements at low SNR. Moreover, the best accuracy improvement at low SNR is obtained when combined with other SAE methods (such as CT-SA and SSA) as a pre/post-processing stage. The optimum configurations at low SNR have been determined for each edge detection method. In particular, the use of gradient-magnitude methods is controlled by a set of three SNR switching thresholds (γ_l, γ_m, γ_h), while for the LoG and Canny methods the standard deviation of the corresponding filters is adjusted according to the experienced SNR. Based on these optimum configurations, the three methods are compared in Fig. 5.15. This figure shows the best accuracy that can be attained by each method when the optimum configuration is employed in each case (the results correspond to the combination with CT-SA but similar results are obtained when combined with SSA). The obtained results show that the considered SAE approach can provide significant accuracy improvements in the lower SNR regime compared to the application of the CT-SA method alone, thus effectively extending the SNR sensitivity of existing SAE methods. Concretely, it can be observed that the performance is very similar for SNR values above a certain threshold (above –6 dB in this case). However, for SNR values below this threshold, the performance of the CT-SA method degrades abruptly, providing accuracy levels of ≈30% at –10 dB SNR, ≈8% at –15 dB SNR and ≈5% at –20 dB SNR. On the other hand, the proposed approach is more robust under degraded SNR conditions, providing a significantly better performance. In the best case, which corresponds to the use of the Canny edge detector, the SAE detection accuracy can reach up to ≈75% at –10 dB SNR, ≈50% at –15 dB SNR and ≈43% at –20 dB SNR, which represent absolute performance improvements of 45%, 42% and 38%, respectively. This improvement is obtained at the expense of an increased computation time as illustrated in Fig. 5.16. The largest increase in the computation time is observed at low SNR, which increases from a minimum of ≈2 ms for the CT-SA method alone to a worst-case maximum below 5 ms for the Prewitt and LoG edge detectors and below 6 ms for the Canny edge detector. The higher computation time observed at low SNR for the proposed approach can be partly attributed to the additional calculations required by the edge detection and flood fill operations but also to the detection of a higher number of SA components, which also increases the computational workload for the CT-SA method applied afterwards. It is also worth noting that these computation times were obtained with a general purpose processor in an off-the-shelf desktop computer and using code that was not specifically optimised for performance. A commercial system implementation would be expected to rely on specific purpose hardware, such as Application-Specific Integrated Circuits (ASICs) or System-on-Chip (SoC) implementations based on micro-controllers, micro-processors or Digital Signal Processors (DSPs), and run code specifically optimised for performance under that underlying hardware platform, which should lead to even shorter computation times (without sacrificing accuracy). As it can be appreciated in Figs. Fig. 5.15 and 5.16, the Canny method provides a slightly higher accuracy than the other two edge detection methods, which could be explained by its ability to reconnect edge fragments that
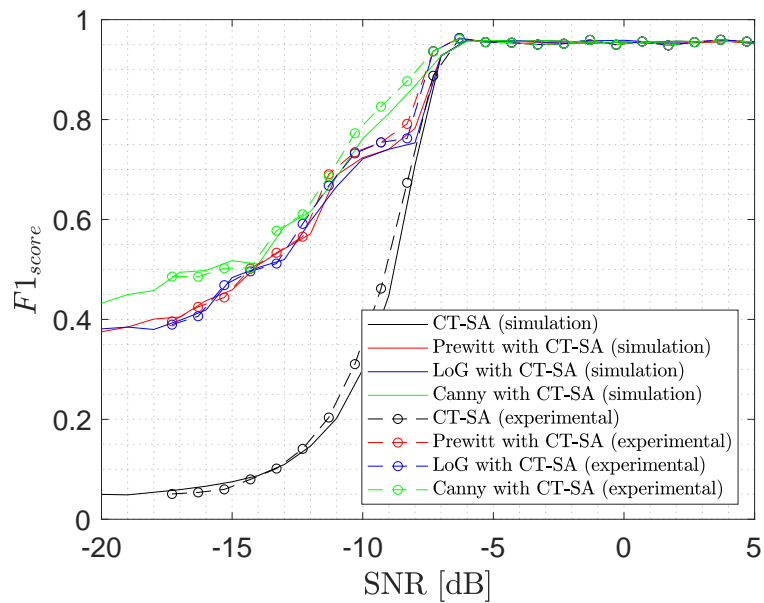
Figure 5.15: Comparison of the three considered edge detection methods and validation of simulation results with hardware experiments.
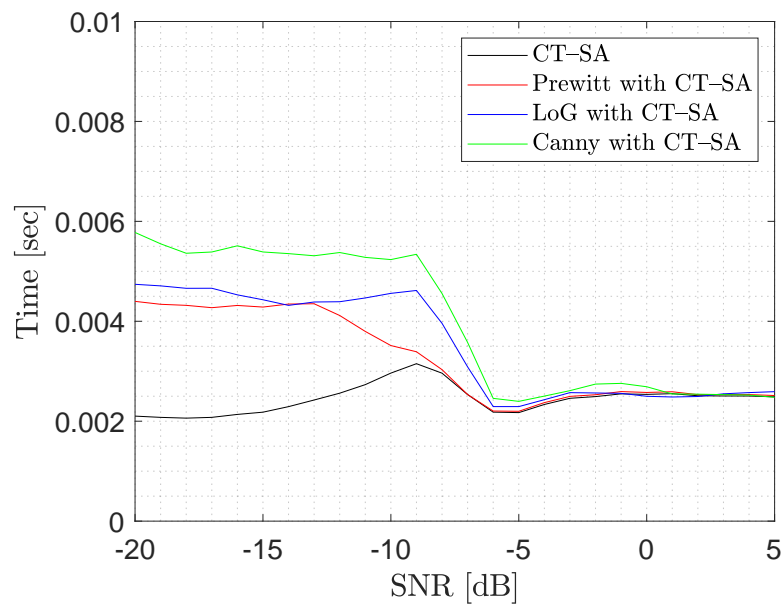
Figure 5.16: Comparison of the computation time for the three considered edge detection methods.

have been disconnected due to noise degradation, and this is also associated with a slightly higher computation time. Fig. 5.15 also validates the obtained simulation results by comparing with their counterparts based on hardware experiments, which demonstrates the ability of the proposed SAE strategy to actually achieve significant accuracy improvements in practical system implementations.

5.4 Summary

Several methods have been proposed in the literature for SAE in radio spectrograms, however their performance degrades significantly in the low SNR regime. In this context, the chapter has proposed a novel approach for SAE based on the use of two well-known techniques from the field of image processing, namely edge detection (to identify the edges of potential SAs) and flood fill (to fill the area inside the estimated edges). The performance of three popular edge detection methods (gradient magnitude, Laplacian of Gaussian and Canny) has been assessed under a broad range of configuration parameters and a suitable SAE strategy has been formulated for each edge detection method. The obtained simulation results have shown that the proposed SAE approach based on edge detection plus flood fill can improve significantly the performance of existing SAE methods in the lower SNR range when used as a pre/post-processing step, thus effectively extending their operational SNR range. The accuracy improvements observed in simulations have been corroborated by experimental results.

Chapter 6

Signal Area Estimation based on the Hough Transform

6.1 Introduction

The use of image processing methods to the problem of SAE is motivated by the fact that the problem of estimating a SA in a noisy spectrogram is similar to the problem or recognising a rectangle in a noisy image. By interpreting each radio spectrogram point (indicating a binary occupied/empty state) as a pixel in a binary (black-and-white) image, spectrograms can be seen as images, which enables the application of several powerful image processing techniques to the problem of SAE, concretely, the estimation of solid rectangular shapes degraded by the presence of noise and radio propagation impairments. Several image processing techniques can be used to identify shapes after separating them from their background (noise) [63]. Chapters 4 and 5 have explored the suitability of morphological operations as well as edge detection and flood fill techniques, respectively. Another image processing technique that is particularly suited to the problem of SAE is the Hough transform (HT). The HT can be employed to recognise lines and rectangular shapes and is, therefore, an appropriate tool to identify SAs in a radio spectrogram. This chapter explores the usability of the HT in the context of SAE and proposes two approaches that exploit the HT to estimate SAs in a spectrogram. The main interest of the proposed methods, and a distinguishing feature with respect to most other methods proposed in the literature, is their ability to automatically extract the parameters of each SA (i.e., the coordinates of the vertical and horizontal lines containing each SA). Most of the previously proposed SAE methods produce enhanced spectrograms where the present SAs can be appreciated more accurately, however have not typically been designed to automatically provide the coordinates and dimensions of each SA. On the other hand, the HT-based methods proposed in this chapter can provide not only an enhanced spectrogram but also the coordinates and dimensions for each of the SAs detected in such spectrogram. This feature can be extremely useful in the automatic processing of radio spectrograms, for instance in the context of autonomous spectrum-aware wireless and mobile communication systems.

The remainder of this chapter is structured into two main parts. First, Section 6.2 provides an overview of the basic principles of the HT and presents the two new methods proposed in this chapter. Then, the obtained results are presented and analysed in Section 6.3. Finally, Section 6.4 summarises and concludes the study.

6.2   Signal Area Estimation based on the Hough Transform

6.2.1   Motivation

The problem of SAE in a time-frequency grid of discrete occupied/empty elements (obtained by appropriately thresholding a spectrogram of continuous-power values) is similar to the problem or recognising a rectangular shape in a noisy binary image. By interpreting each radio spectrogram point (indicating a binary occupied/empty state) as a pixel in a binary (black-and-white) image, spectrograms can be seen as images, which enables the application of several powerful image processing techniques to the problem of SAE, concretely, the estimation of solid rectangular shapes degraded by the presence of noise and radio propagation impairments. This point of view motivates the exploration of powerful tools from the field of Image Processing in the context of SAE. Image Processing is a well-developed field that counts with advanced and sophisticated techniques to detect shapes in noisy images. One such technique that is particularly suited to the problem of SAE considered in this work is the Hough transform (HT). The HT can be employed to recognise lines and rectangular shapes and is therefore an appropriate tool to identify SAs in a radio spectrogram [80]. This chapter explores the usability of the HT in the context of SAE and proposes two approaches that exploit the HT to estimate SAs in a spectrogram.

6.2.2   Overview of the Hough Transform

The HT is a feature extraction technique whose purpose is to identify imperfect instances of objects in an image. The HT originated from the basic need to detect certain shapes inside arbitrary images corrupted by noise and other artefacts. In its most basic definition, the classical HT was concerned with the identification of lines in an image, while the generalised HT was later on introduced to enable the detection of more complex arbitrary shapes such as circles or ellipses and their positions within images. Notice that SAs are by definition rectangularly shaped and therefore are delimited by four lines corresponding to the edges of the SA. Such straight lines can be detected with a classical HT and therefore the interest of this work lies on the classical HT [81, 82].

The HT detects imperfect instances of a certain shape (in the case concerned in this work, straight lines) based on a voting procedure carried out over parametised image objects. Basically, each possible candidate shape (line) is represented according to a given parameter space and then all possible candidates are tested by assessing how closely they match with the pixels of the image. The best fitting candidate is then selected by means of a voting procedure. Lines are typically represented in a Cartesian x-y space in the form $y = mx + n$, where m is the slope of the line and n its displacement with respect to the origin. Thus, in a Cartesian space each line can be represented as a point (m, n) in the parameter space. This parameter space, however, has the inconvenience that vertical lines would give rise to unbounded values of the slope parameter ($m \rightarrow \infty$), which would pose computational problems. For this reason, the HT is carried out over a Hessian normal form $\rho = x \cos\theta + y \sin\theta$, where ρ is the distance from the origin to the closest point on the straight line and θ is the angle between the abscissas axis and the line connecting the origin with that closest point, as illustrated in Fig. 6.1. In this parameter space, each line is represented as a point
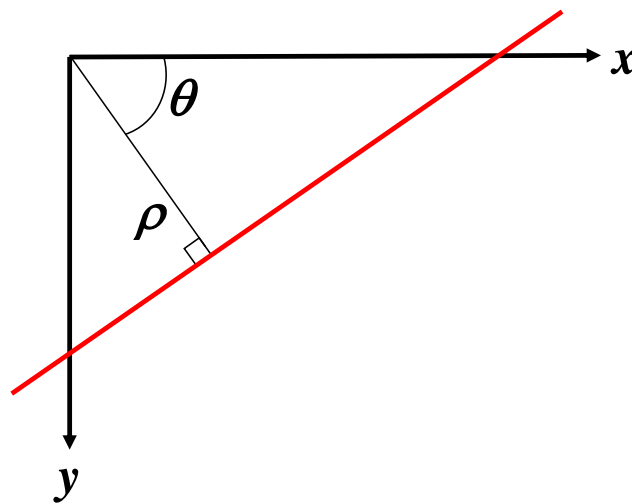
Figure 6.1: Parameter space for the Hough transform.

(ρ, θ). The result of the HT is a matrix whose elements are used as accumulators indicating the frequency of occurrence of the potential lines observed for each pair (ρ, θ). In the context of SAE, the SAs can be assumed to be aligned with the x-y axes of the Cartesian space and therefore each SA can be assumed to be delimited by two pairs of mutually parallel lines, a pair of vertical lines ($\theta = 0$) and another pair of horizontal lines ($\theta = \pi/2$). The abscissas (x) coordinates of vertical lines are then obtained as the value of ρ in the HT for $\theta = 0$, while the ordinates (y) coordinates of horizontal lines are obtained as the value of ρ in the HT for $\theta = \pi/2$ as illustrated in Figs. 6.2 and 6.3. Figs. 6.2a and 6.3a show spectrograms with one and three SAs, respectively, while Figs. 6.2b and 6.3b show their corresponding HTs, respectively. In order to infer from the HTs the SAs present in the spectrograms, one should look for the coordinates of the edges of each SA. As stated above, this information can be obtained from the HT by looking at the coordinates of the vertical lines ($\theta = 0$) and the horizontal lines ($\theta = \pi/2$) detected in the HT. The values of ρ observed in Figs. 6.2b and 6.3b for $\theta = 0$ and $\theta = \pi/2$ provide the coordinates of such SA edges in the spectrograms of Figs. 6.2a and 6.3a, respectively. Thus, the HT can automatically provide the coordinates of the lines that correspond to the edges of each SA. Having the coordinates of the lines that delimit the SAs in a radio spectrogram, it is possible to extract the coordinates and dimensions for each individual SA in a radio spectrogram. This is a significant advantage of HT-based SAE compared to most existing SAE methods, many of which have not been specifically designed to obtain this information (despite of its importance in practical applications) in an automated manner (i.e., without human manual intervention).

6.2.3   Proposed HT-based SAE Methods

The proposed SAE methods, similar to many other SAE methods, are based on the processing of binary spectrograms where each spectrogram point contains a binary value indicating whether a signal component is believed to be present or not. Such

(a)   (b)
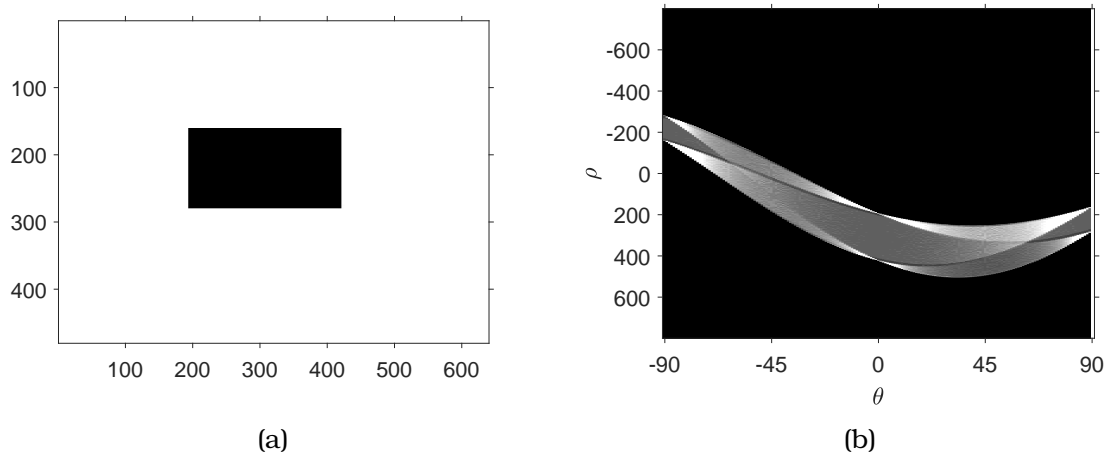
Figure 6.2: HT example with 1 SA: (a) spectrogram, (b) HT.

(a)   (b)
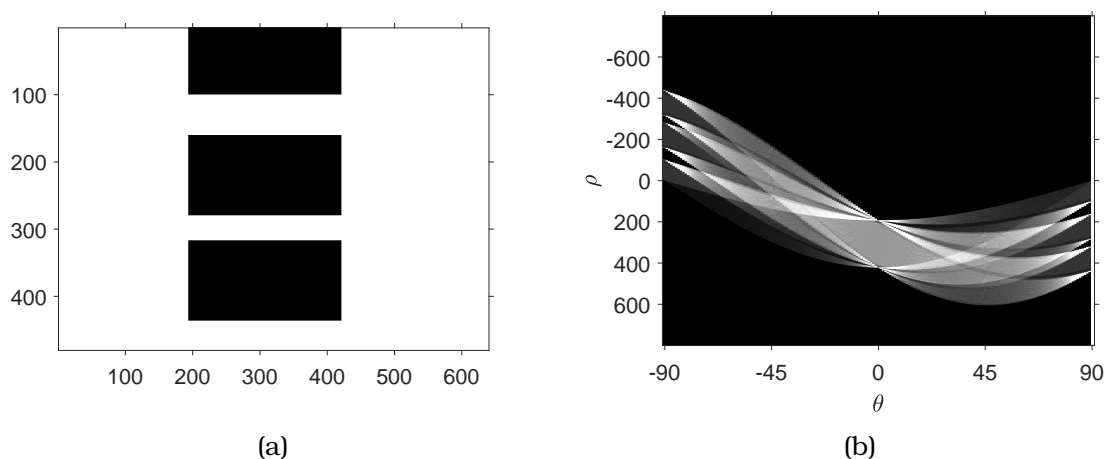
Figure 6.3: HT example with 3 SAs: (a) spectrogram, (b) HT.

spectrogram can be obtained by thresholding a continuous-domain power spectrogram. The configuration of such threshold as well as the resolution of the spectrogram can have a significant impact on the performance of SAE methods. These aspects are out of the scope of this work but a detailed analysis and discussion can be found in [40].

The examples shown in Figs. 6.2 and 6.3 correspond to ideal cases where a perfect SA is observed without any degradation. In a real radio spectrogram obtained from actual empirical measurements there will be artefacts in the image in the form of false alarms (introduced by the noise present at the radio receiver) and missed detections (caused by radio propagation impairments). Missed detections will in general not be a source of major concerns since they will often occur inside SAs and therefore will be surrounded by other points in occupied/busy state that will help detect the SA. However, false alarms can lead to significant detection performance degradation (the same effect was also observed and discussed in [11] in the context of SAE). False alarms are particularly problematic in the application of the HT because each false

alarm point will be processed by the HT algorithm by trying to identify lines that pass through that point. A large number of false alarms may therefore have a significant impact on the HT output. To address this problem, a false alarm reduction step is first applied by convolving the input binary image with a 3×3 box blur filter whose template is composed of all ones. This filtering helps to isolate and remove false alarms due to its smoothing effect. The busy points with an output value lower than or equal to two (i.e., isolated points not surrounded by a significant number of other busy points) are deemed to be false alarms rather than true SA points and therefore discarded (their value is inverted to the free/empty state). This process is similar to that employed by the MA method described in Chapter 3 (see Section 3.2.1) and [43].

After the input spectrogram has been filtered to reduce the incidence of false alarms, the resulting cleaner image can be more accurately processed with a HT. However, the HT is rarely directly applied to an image. It is often a common practice to first apply an edge detection method in order to extract the edges of those objects present in the image. In the case of a radio spectrogram, this edge detection step will highlight and show more clearly the potential lines (edges of the SAs) present in the image. In this work, the Canny edge detector [78] is selected due to its ability to account for image noise [83] and its higher detection performance compared to other conventional edge detectors. Notice that an edge detector will provide a more clear visualisation of the lines delimiting the SAs in a spectrogram, however such edges will be imperfect in the sense that they will usually not be a clear and well-defined single straing line at a unique coordinate. Instead, due to the presence of noise and radio propagation degradation, each side of a SA will appear, not as a single edge/line, but instead as a concatenation of several much smaller lines randomly distributed along the true original edge/line, with slightly different coordinates. The application of the HT can in this case provide a more clear identification of the single coordinate of that edge/line around which the small fragments are detected by the edge detector, thus helping find a unique coordinate for each edge/line delimiting each SA. After the edge detection step, the HT is applied to extract the coordinates of the lines delimiting the SAs in a spectrogram.

The output of the HT will contain peaks at the coordinates that are more often observed and therefore the most likely candidates to be the true edges of the SA. These peaks can be extracted by setting an appropriate threshold. In this work, this threshold is set as a percentage of the maximum value of the HT (several thresholds will be tested in order to find the most convenient configuration). Following the extraction of the peaks in the HT, a clear indication of the coordinates of the lines in the spectrogram will be obtained. However, notice that these lines will only determine a grid of vertical and horizontal lines over the spectrogram but will not indicate in which of those rectangles in the grid a SA is actually contained. To resolve this problem, the pixel density in each rectangular region of the grid is calculated and if it is above a properly defined threshold then a SA will be assumed to be present. Notice that in those rectangles of the grid where a SA is actually present, the density of busy/occupied pixels will be higher than in those other rectangles placed within SAs, where no signal components should be present (except for some random false alarms). Following this procedure, it is possible to identify the rectangles where a SA is present and therefore extract the coordinates and dimensions of each SA in the spectrogram.

(a)   (b)
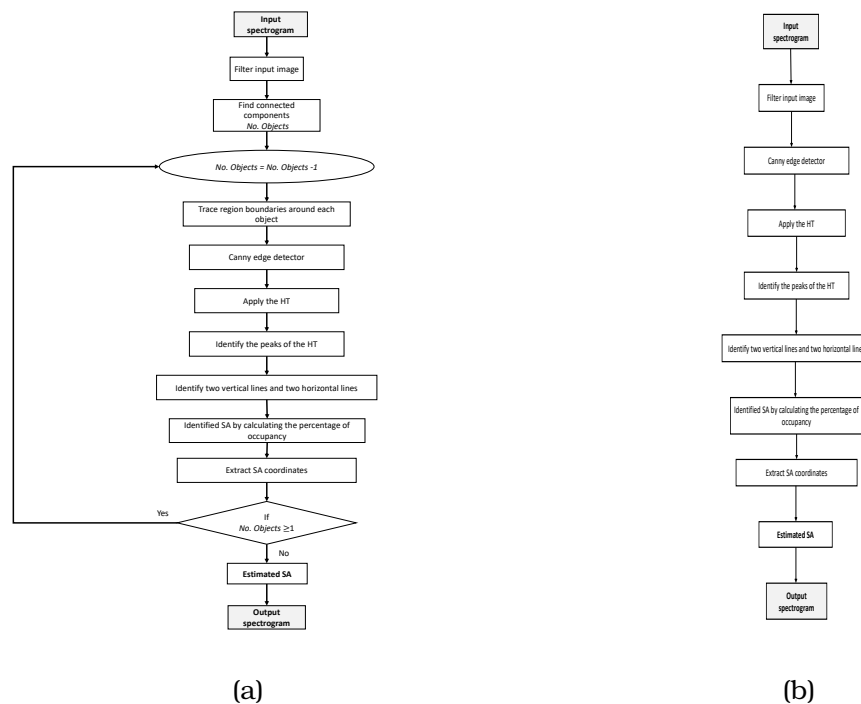
Figure 6.4: Flowcharts of the proposed HT-based SAE methods: (a) Approach 1 (b) Approach 2.

The proposed method is applied following two different approaches. The first approach attempts to isolate each SA component from the spectrogram before applying the procedure above. As a result, the procedure above will be applied individually to a set of subimages, each of which contains a single SA, which should presumably (but not necessarily) be located in the central rectangle of the subimage. The second approach applies the procedure above to the whole spectrogram, without attempting to isolate individual SA components. As a result, the procedure above will provide together the coordinates of all the SAs found in the spectrogram. The complete set of steps for both approaches are detailed below and shown in Fig. 6.4.

Approach 1:

1. Filter input image to reduce incidence of false alarms.

2. Find connected components in the binary image in order to calculate the number of objects (blobs) in the image.

3. Trace region boundaries around each object/blob obtained above. These boundaries will divide the original image/spectrogram into a number of non-overlapping subimages/components. Each of such components will contain a single SA that will be processed individually repeating the steps below for each detected component.

4. In each component detected above:

    (a) Find edges with a Canny edge detector.

    (b) Apply the HT to the output of the edge detector.

    (c) Identify the peaks of the HT by applying a threshold to the HT, which is calculated as a fraction/percentage of the maximum value of the HT.

    (d) Identify *two* vertical lines and *two* horizontal lines. This assumes that a single SA will be present in the current component (assuming that region boundaries have been properly traced in Step 3).

    (e) The four lines identified above will define a grid with 9 rectangular regions, where in principle only one of them should contain a SA. Such region can be identified by calculating the percentage of occupancy (i.e., percentage of busy pixels) and comparing to a properly set occupancy threshold.

    (f) In the rectangular region where a SA is deemed to be present, extract its coordinates (for its delimiting vertical and horizontal lines) and add it to the final output image/spectrogram.

Approach 2:

1. Filter input image to reduce incidence of false alarms.

2. Find edges with a Canny edge detector.

3. Apply the HT to the output of the edge detector.

4. Identify the peaks of the HT by applying a threshold to the HT, which is calculated as a fraction/percentage of the maximum value of the HT.

5. Identify *all* vertical lines and *all* horizontal lines. This does not make any assumption on the number of SAs present since the complete spectrogram/image is being processed as a whole in this case.

6. The lines identified above will define a grid with an arbitrary number of rectangular regions, any of them can potentially contain a SA. Such regions containing a SA can be identified by calculating the percentage of occupancy (i.e., percentage of busy pixels) and comparing to a properly set occupancy threshold.

7. In the rectangular region where a SA is deemed to be present, extract its coordinates (for its delimiting vertical and horizontal lines) and add it to the final output image/spectrogram.

Both approaches are considered to determine whether the individual processing of each region of the spectrogram can provide any performance improvements over the whole processing of the complete spectrogram as a single image.

6.3   Performance Evaluation

The evaluation methodology followed in this chapter is identical to the one presented in Chapter 3 (please refer to Section 3.3 for details). To illustrate the operation of the HT-based SAE methods proposed in this work, Figs. 6.5 and 6.6 show examples of the SA edges estimated by the proposed method based on Approaches 1 and 2, respectively. These figures represent the outcome of Step 4c for Approach 1 (aggregating the detections for each individual SA together in the same figure) and the outcome of Step 4 for Approach 2. The figures show for reference the edges detected by the Canny edge detector (Step 4a in Approach 1 and Step 2 in Approach 2) as thick white lines (notice that these SA edges are not perfectly rectangular due to the corruption produced by false alarms and missed detections). These figures also plot the detected peaks of the HT joined by straight lines for a more clear visualiation. These peaks are identified based on the maximum value of the HT, denoted as $\max(\mathcal{H})$, using different thresholds equal to $0.1\cdot\max(\mathcal{H})$, $0.3\cdot\max(\mathcal{H})$, $0.5\cdot\max(\mathcal{H})$ and $0.7\cdot\max(\mathcal{H})$. By carefully inspecting these figures, one can notice that Approach 1 will only work with a threshold equal to $0.1\cdot\max(\mathcal{H})$; selecting a threshold greater than this will lead to some of the edge components of the SAs being missed (in particular in some of the vertical edges). On the other hand, Approach 2 can detect relevant edges with thresholds equal to $0.1\cdot\max(\mathcal{H})$ and $0.3\cdot\max(\mathcal{H})$, however it will miss relevant edge components of the SAs if the threshold is set to $0.5\cdot\max(\mathcal{H})$ or $0.7\cdot\max(\mathcal{H})$. These results indicate that relevant peaks of the HT are observed at relatively low values and therefore the threshold to identify the peaks of the HT needs to be selected to an equally low value accordingly.

Another interesting observation that can be made from the comparison of Figs. 6.5 and 6.6 is that Approach 1 seems to misinterpret the edges of some small artefacts as edges of SA components. This can be clearly appreciated in the bottom-left corner of the top SA of Fig. 6.5, where a large number of lines/edges are detected. These are not edges of a genuine SA but simply the edges of small objects, possible fragments of the original SA or a relatively large number of false alarms that could not be removed in the false alarm removal step. Such small objects can potentially be classified as independent regions containing SAs in Step 3 of Approach 1 and each of them will be processed individually with the aim to detect a SA component in each of them, which leads to errors.

The observation above can be verified in Fig. 6.7, where it can be noticed that a small SA is attached to the bottom-left corner of the top SA detected in the final output of Approach 1. This seems to suggest that the principle of Approach 1, according to which each region in a spectrogram where a SA component is believed to be present is processed individually, may be counterproductive since certain artefacts may mislead the boundary tracing process of Step 3 and make it believe that there are potential SAs where none are actually present.

To confirm this observation, Figs. 6.8 and 6.9 show the equivalent result with Approach 2 for HT peak thresholds of $0.1\cdot\max(\mathcal{H})$ and $0.3\cdot\max(\mathcal{H})$ (which were observed above to provide good SA edge detection performance). In this case it can be observed that Approach 2 does not misinterpret small objects or artefacts in the input spectro-gram as individual SAs due to its global processing of the whole spectrogram, which confirms the observation above regardling the limitations of Approach 1. However, it

Figure 6.5: Examples of the SA edges estimated by the proposed HT method based on **Approach 1**. The peaks of the HT are identified based on the maximum value of the HT, $\max(\mathcal{H})$, using different thresholds equal to: (a) $0.1 \cdot \max(\mathcal{H})$, (b) $0.3 \cdot \max(\mathcal{H})$, (c) $0.5 \cdot \max(\mathcal{H})$, and (d) $0.7 \cdot \max(\mathcal{H})$ [SNR = –5 dB].

Figure 6.6: Examples of the SA edges estimated by the proposed HT method based on **Approach 2**. The peaks of the HT are identified based on the maximum value of the HT, $\max(\mathscr{H})$, using different thresholds equal to: (a) $0.1 \cdot \max(\mathscr{H})$, (b) $0.3 \cdot \max(\mathscr{H})$, (c) $0.5 \cdot \max(\mathscr{H})$, and (d) $0.7 \cdot \max(\mathscr{H})$ [SNR = –5 dB].

(a)   (b)

(c)   (d)

Figure 6.7: Examples of the SAs estimated by the proposed HT method based on **Approach 1**. The peaks of the HT are identified based on the maximum value of the HT, $\max(\mathcal{H})$, using a threshold equal to $0.1 \cdot \max(\mathcal{H})$. The presence of SAs in the grid is detected with a percentage occupancy threshold of: (a) 10%, (b) 20%, (c) 30%, (d) Clean test grid (for reference) [SNR = –5 dB].

can be noticed in Figs. 6.8 and 6.9 that Approach 2 can detect SAs in some regions where no SAs are present. These erroneous regions seem to occur between regions where genuine SAs are present and the error may be due to some false alarms, which would be difficult to remove following the employed filtering process when they are present in small narrow gaps between SAs. However, as it can be seen in Figs. 6.8 and 6.9, this problem can be easily resolved by increasing the minimum percentage of busy tiles that are required in a region for it to be considered as a true SA. Configuring such threshold to 10% or 20% of the tiles in the rectangular region does not seem to be sufficient since the percentage of busy tiles present in those regions after applying the HT-based procedure is higher than these thresholds. However, increasing the value of the threshold to 30% is finally able to discriminate correctly between true SAs and regions containing small objects/artefacts. These results indicate that Approach 2 constitutes a preferred option compared to Approach 1 and that, with an adequate configuration of its parameters, Approach 2 can provide an accurate identification of the SAs present in a spectrogram.

Fig. 6.10 compares the performance of the proposed HT-based SAE method with that attained by the ED, CT-SA and SSA methods in terms of the F1 score, representing how accurately the detected SAs describe the original SAs generated by the transmitter. As it can be observed, Approach 2 provides a higher accuracy than Approach 1 at high SNR and slightly lower performance (with an almost negligible difference) at lower SNRs;
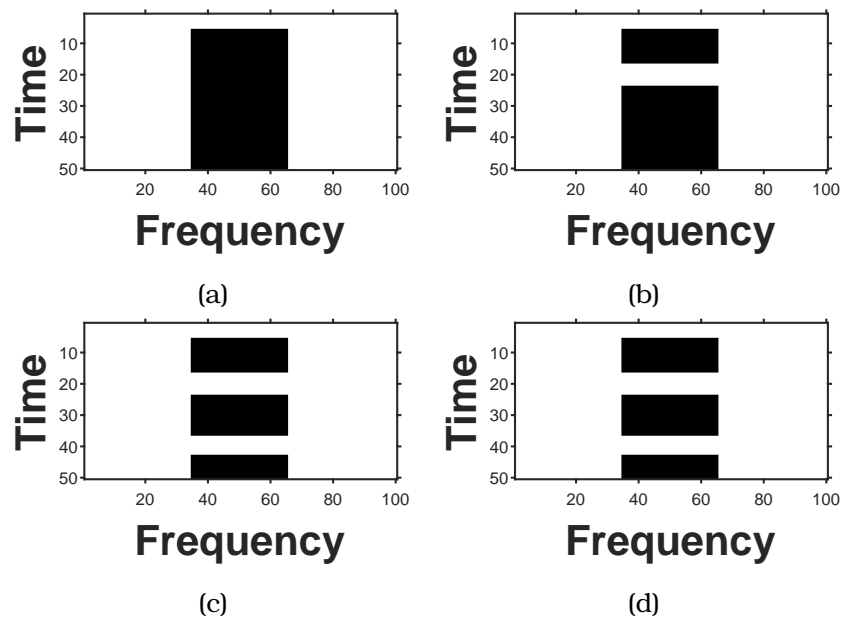
Figure 6.8: Examples of the SAs estimated by the proposed HT method based on **Approach 2**. The peaks of the HT are identified based on the maximum value of the HT, $\max(\mathcal{H})$, using a threshold equal to $0.1 \cdot \max(\mathcal{H})$. The presence of SAs in the grid is detected with a percentage occupancy threshold of: (a) 10%, (b) 20%, (c) 30%, (d) Clean test grid (for reference) [SNR = –5 dB].

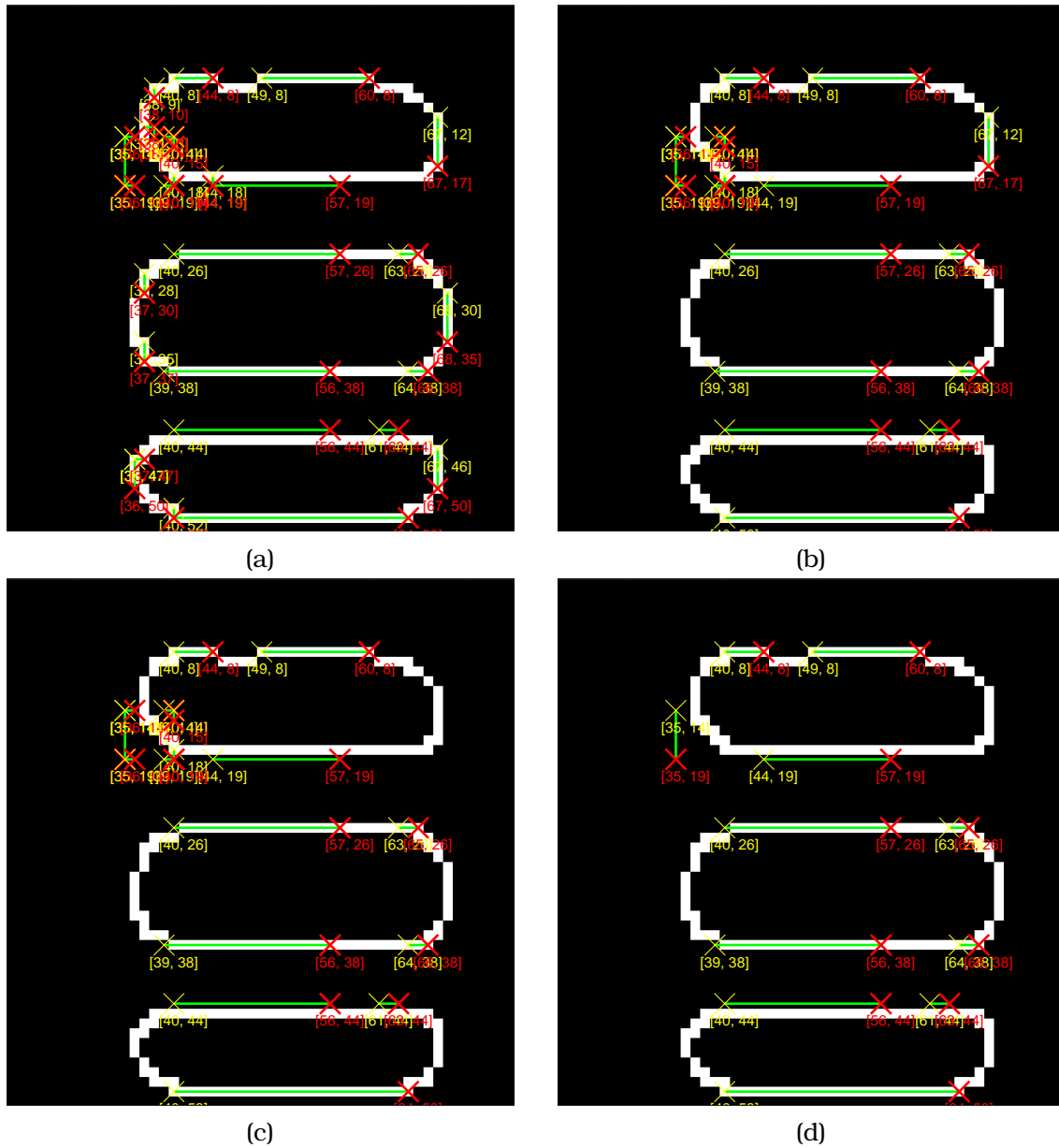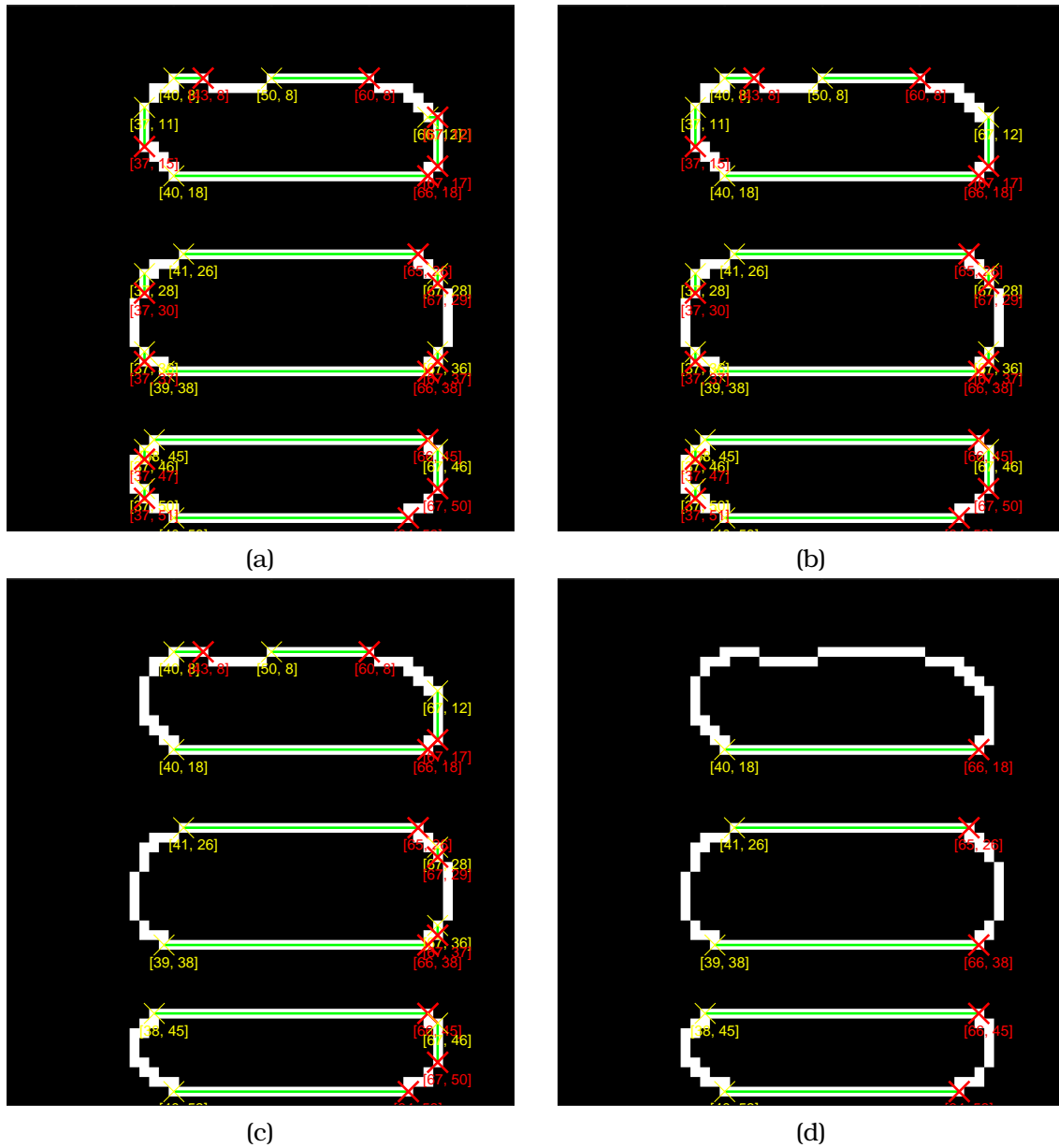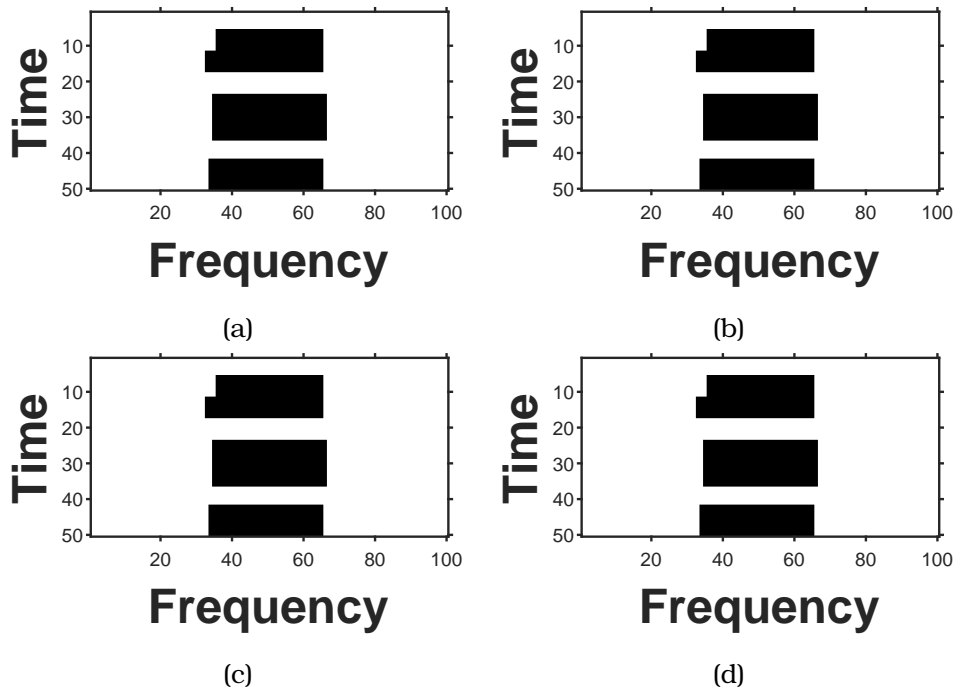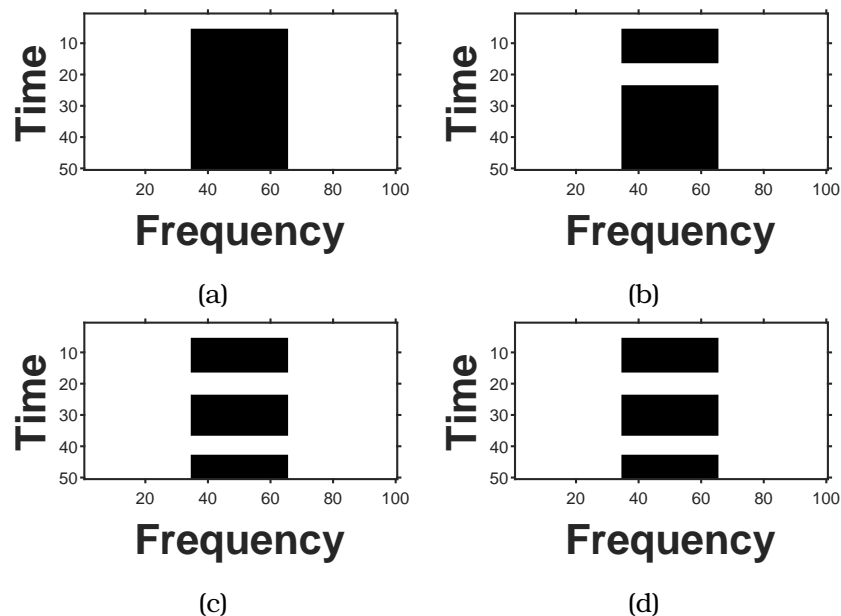Figure 6.9: Examples of the SAs estimated by the proposed HT method based on **Approach 2**. The peaks of the HT are identified based on the maximum value of the HT, $\max(\mathcal{H})$, using a threshold equal to $0.3 \cdot \max(\mathcal{H})$. The presence of SAs in the grid is detected with a percentage occupancy threshold of: (a) 10%, (b) 20%, (c) 30%, (d) Clean test grid (for reference) [SNR = –5 dB].

these results also confirm that Approach 2 is a preferred option compared to Approach 1. When compared with the other SAE methods used as a reference, Approach 2 can achieve the best performance attained by the other methods in the region of higher SNR down to a minimum SNR of about –6 dB or –7 dB, which can be identified as the sensitivity of this SAE method. Above this SNR value, the accuracy obtained in terms of the F1 score is noticeably higher than that attained by the CT-SA and SSA methods and is only matched by the ED method. However, it is worth reminding that the ED method cannot extract automatically the coordinates and dimensions of the SA in the spectrogram and, in fact, it is unable to identify rectangularly shaped SAs. Only the CT-SA and SSA methods are able to do so, both of which provide an accuracy below that of the proposed HT-based method. This better accuracy obtained in the region of high SNR is obtained at the expense of a lower accuracy in the region of low SNR. However, it is worth noting that once the F1 score decreases below a relatively high value (close to one) the detected SAs start to diverge noticeably from the original ones, both in numbers and dimensions. Therefore, a good detection accuracy in practical implementations requires an F1 score very close to one, around 0.9 and above, which can be obtained only under relatively high SNR conditions. Under such conditions, the proposed HT-based method can provide a more accurate detection of the SAs present in a radio spectrogram. It is also worth noting from Fig. 6.10 that the results obtained from software simulations provide a very close match with (and are therefore corroborated by) those obtained from hardware experiments.

Finally, Fig. 6.11 compares the computational costs of the different SAE methods considered in this work. As it can be observed, Approach 1 involves the highest computational load over most of the considered SNR interval due to its more complex procedure, which requires first isolating non-overlapping regions of the original spectrogram and then applying the proposed procedure to each region individually. This results in a significantly higher computational cost that, as seen in Fig. 6.10, cannot be justified based on the obtained accuracy performance. On the other hand, Approach 2 requires a significantly lower computational cost than Approach 1 in the SNR range of interest (i.e., higher SNR values), which can be explained by its more simple formulation where the whole spectrogram is processed as a single image; this not only reduces the computational burden of the proposed SAE method compared to Approach 1 but also, as seen in Fig. 6.10, provides more accurate results in the SNR range of interest. The computation time of Approach 2 is comparable to that of the reference methods. ED is the most lightweight method, as it could be expected, with CT-SA requiring a slightly higher computational cost (but lower than Approach 2) and SSA requiring a higher computational cost than the proposed method with Approach 2. Therefore, the proposed method (with Approach 2) not only can provide significantly accurate performance levels but can also do so at comparable costs than other existing SAE methods (and even lower in some cases).

6.4   Summary

An accurate estimation of the SA for each radio transmission contained in a spectrogram can provide valuable information in many practical application scenarios, such as autonomous spectrum-aware wireless communication systems. In this context, the
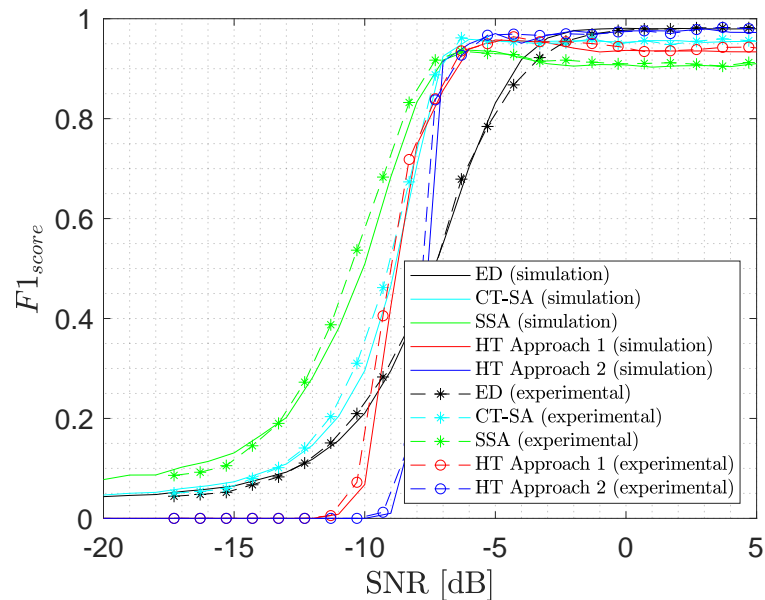
Figure 6.10: F1 score as a function of the SNR for the different reference SAE methods (ED, CT-SA, SSA) and the proposed HT-based SAE method (Approaches 1 and 2, using in both cases the best configuration for each approach).
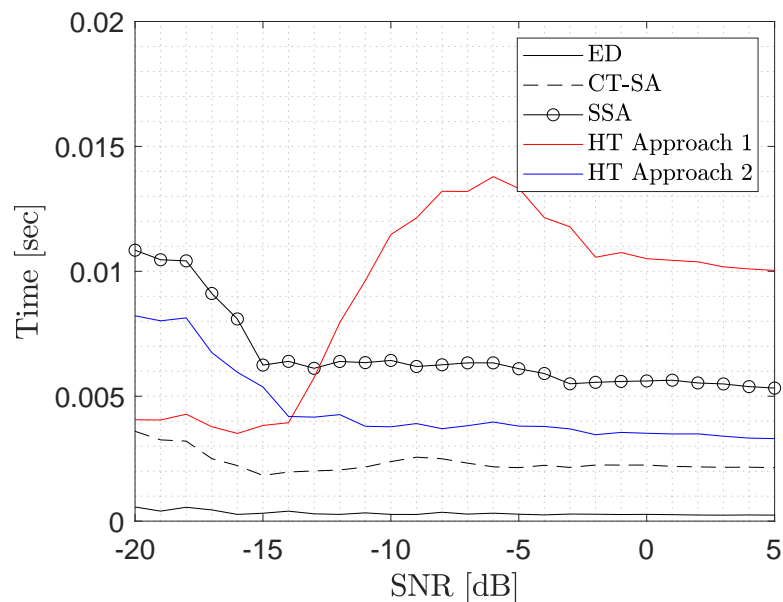
Figure 6.11: Computational cost as a function of the SNR for the different reference SAE methods (ED, CT-SA, SSA) and the proposed HT-based SAE method (Approaches 1 and 2, using in both cases the best configuration for each approach).

chapter has proposed new methods for an accurate estimation based on the application of the Hough Transform (HT) combined with other techniques from the field of image processing. The performance of the proposed methods has been evaluated by means of simulations and the obtained results have shown that they can achieve a high level of SAE accuracy. An interesting feature of the proposed methods is their ability to extract automatically the coordinates and dimensions of each SA detected in a radio spectrogram. This feature can be useful in the automatic processing of radio spectrograms, e.g. in the context of autonomous spectrum-aware wireless systems.

Chapter 7

Signal Area Estimation based on Deep Learning

7.1 Introduction

The interest of this thesis is on how to accurately determine the SAs present in a radio spectrogram obtained from radio spectrum measurements and extract the information about the coordinates of each SA automatically. Several methods have been proposed in the literature in order to achieve this end, however many of such methods have some limitations, which include one or more of the following issues: are based on heuristic principles, involve a number of configuration parameters that need to be tunned individually for each operation scenario, offer a poor performance when the Signal-to-Noise Ratio (SNR) is low, or are unable to extract automatically the coordinates of each SA present in a spectrogram (which is useful for automatic spectrogram processing is autonomous spectrum-aware wireless systems). To address these issues, this chapter proposes a novel approach for SAE based on the use of widely known and well-developed deep learning techniques.

The field of Artificial Intelligence (AI) has experienced a dramatic development associated with past and recent advances in the areas of Machine Learning (ML) methods in general and Deep Learning (DL) techniques in particular. DL is a group of ML techniques that allows computers to learn and discover complex patterns in large datasets automatically, taking inspiration from the human brain [84]. DL relies on Artificial Neural Networks (ANNs), which consist of layers of nodes (neurons) and synapses inspired by the human brain. A typical ANN is a simplified computation model with multiple interconnected layers of neurons [84]. The network is trained to produce useful predictions based on identification of patterns in training data. One area were DL techniques based on ANNs have gained widespread application is in communication systems [84–86]. However, the application of DL techniques to the particular problem of SAE has received very limited attention in the existing literature. In this context, this chapter proposes a novel approach for SAE that relies on the use of Deep Learning based on Artificial Neural Network (DL-ANN). The proposed method addresses the limitations of existing SAE methods in the literature as mentioned above. The performance of the proposed DL-ANN method for SAE is assessed both with software simulations and hardware experiments, showing that the proposed

method provides an accurate SAE performance – with significant improvements in the low SNR regime – and offers the interesting feature of automatically extracting the coordinates of each SA detected in a radio spectrogram obtained from spectrum measurements. A key feature of the proposed method is the improvement in the SAE accuracy compared to other existing methods (in particular in the low SNR regime) and the capability to extract the location of the detected SAs automatically. Overall, the proposed technique is a promising solution for the automatic processing of radio spectrograms in spectrum-aware wireless systems.

7.2 Proposed DL-ANN Method for SAE

7.2.1 Motivation

The basic problem in SAE is how to detect and estimate a rectangular grid representing a solid SA in a time-frequency matrix (spectrogram) of degraded power values (affected by noise and impaired by the propagation channel). To facilitate the problem, the continuous-domain power levels are thresholded in order to produce a binary matrix with zero/one values indicating the idle/busy state of each point in the power spectrogram (i.e., absent/present signal component). The problem of estimating a solid SA in such binary matrix has some analogies with the problem of recognition of patterns in a noisy black-and-white image. Therefore, image processing principles aimed at detecting objects in images can be employed to address the problem considered in this chapter by treating the spectrogram of power values as a greyscale image or its binary version as a black-and-white image (the latter case is the one considered in this chapter), where each spectrogram time-frequency point represents an image pixel. The problem of SAE then becomes the problem of detecting rectangular shapes (i.e., SAs) in a binary noisy image. This viewpoint offers a new perspective for SAE that enables the application of a broad range of tools from the field of image processing [87] to the problem of SAE, which has been investigated in previous chapters. While traditional image processing techniques can provide an interesting approach to the problem of SAE, more recent approaches from the field of computer vision and pattern recognition [88], many of which make use of AI/ML/DL techniques, provide more advanced methods to address the problem considered in this chapter from the point of view of object detection and recognition. This motivates this chapter to explore the suitability of using DL techniques to address the problem of SAE.

It is worth noting that, even though the use of DL techniques for object detection, and in particular for the detection of rectangular objects in an image, is not new (e.g., see [89]) the problem of detecting rectangular SAs in a radio spectrogram in the context of SAE has some particular characteristics that require special consideration and hence a tailored study as the one presented in this chapter. Concretely, the problem of SAE has some specific properties, including the fact that the rectangular objects to be detected (i.e., the SAs) are aligned with the horizontal and vertical axes of the spectrogram (in other words, the SAs do not have any rotation) and moreover the SAs do not overlap among them (overlapping SAs would mean harmful interference between radio transmissions and most radio communication systems are explicitly engineered to avoid this). In general, these two features would mean that the problem of SAE

might be seen as a simplified version of the general problem of detecting rectangular objects in a noisy image. However, the detection of SAs in a spectrogram is particularly challenging due to the degrading effects introduced by the radio propagation channel and the receiver noise. These two degrading effects will lead to the appearance of random false alarms (i.e., time-frequency points where a signal component is not present but its power level is observed above the detection threshold due to increased noise) and random missed detections (i.e., time-frequency points inside SAs that are observed below the detection threshold due to a power reduction caused by the radio propagation channel). These two types of degradations, as it will be shown, can distort significantly the SAs present in a radio spectrogram and their rectangular shapes to the extent that they may become undistinguishable from the background noise of the receiver and therefore unrecongnisable, in particular when the radio signals are received at very low SNR (where SAE becomes extraordinarily challenging). This implies that addressing the problem of SAE from the point of view of detecting rectangular objects in an image requires a specific and tailored analysis, which motivates the study presented in this chapter.

7.2.2   Proposed SAE Approach with DL based on ANN

DL represents a category of ML methods that use a number of deep layers to transform and process raw input data in order to extract relevant features. DL models are commonly based on ANNs, in which model learning can be supervised, unsupervised, or semi-supervised [90]. ANNs are inspired by the working of the human brain to process information. With the advances in DL techniques, ANNs have gained widespread application in digital image processing [90, 91]. However, the application of DL techniques in general, and ANNs in particular, to the specific problem of object detection in the context of SAE has received little attention. In this context, this chapter proposes a novel approach for SAE that relies on the use of a DL-ANN approach for SAE. The proposed approach relies on a standard Multi-Layer Perceptron (MLP) network for SAE, which is a class of feedforward ANN composed of multiple layers of perceptrons (neurons that use non-linear activation functions), including an input layer, one or more hidden layers, and a final output layer. MLPs utilise a supervised learning technique called backpropagation for training, where the network is trained using labelled input data to help recognise the corresponding correct output. This is among the simplest types of DL networks and, given the lack of previous work considering the use of DL techniques to the problem of SAE, the study of this type of network seems a natural first step in the investigation of DL in the context of SAE. This motivates the consideration of a standard MLP ANN in this chapter.

The proposed DL-ANN model is depicted in Fig. 7.1. As discussed earlier, the main input information is a binary spectrogram, which is composed of zero/one values indicating where a signal component is observed above a given power threshold. This binary spectrogram is obtained by thresholding a power spectrogram (obtained by the receiver from spectrum measurements) with a properly set decision threshold. Several methods to set such threshold in the context of SAE were investigated in Chapter 2, where it was concluded that a threshold set for a low Constant False Alarm Rate (CFAR), such as 0.01, provides a good performance in SAE. Two different scenarios are
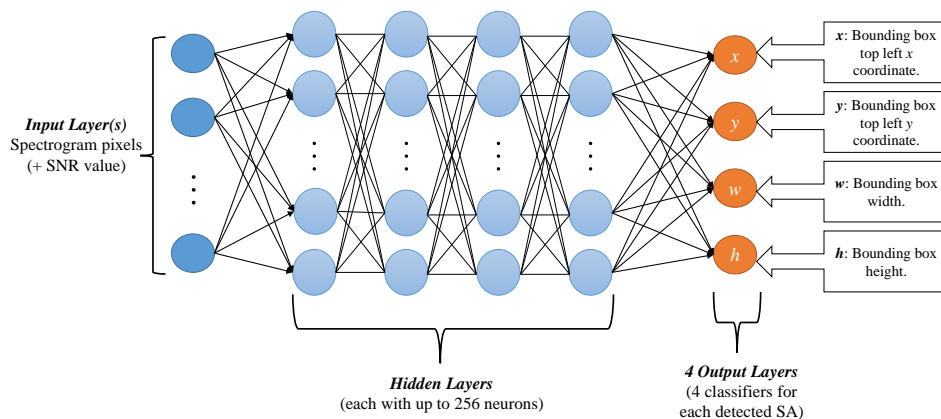
Figure 7.1: DL-ANN network architecture for SAE.

considered regarding the input information provided to the DL-ANN. In the first scenario only the binary spectrogram obtained from spectrum measurements is provided, while in the second scenario the SNR value at which the provided spectrogram was measured is also fed to the network as a second input parameter. It is well-known that ANNs can learn better when additional input information is provided (assuming that the input parameters are independent), therefore the approach considered in this second scenario is investigated to determine whether it can provide better performance than the more simple approach proposed in the first scenario. The main drawback of this second approach in a practical system implementation is that the SNR needs to be estimated and any inaccuracies in such estimation may also affect the accuracy of the SAE process. However, this extra cost may be worth if it enables a more accurate SAE, which makes the consideration of this second approach interesting.

The output information provided by the DL-ANN needs to identify unambiguously the location and dimensions of each SA detected in the input spectrogram. To this end, four output parameters are considered for each SA as illustrated in Fig. 7.1:

- x: Abscissa of the SA's top-left corner.

- y: Ordinate of the SA's top-left corner.

- w: SA's width.

- h: SA's height.

The tuple (x, y, w, h) univocally identifies the bounding box within which each SA is contained and therefore provides sufficient information to unambiguously characterise each detected SA. Notice that this output information means that the DL-ANN is able to automatically extract the relevant information related to each detected SA.

The complete definition of the proposed DL-ANN involves the specification of the network architecture (number of hidden layers and neurons per layer), the tuning/optimisation of the network hyperparameters and the used training procedure. These aspects are discussed in more detail in the following section as part of the methodology followed in this study.
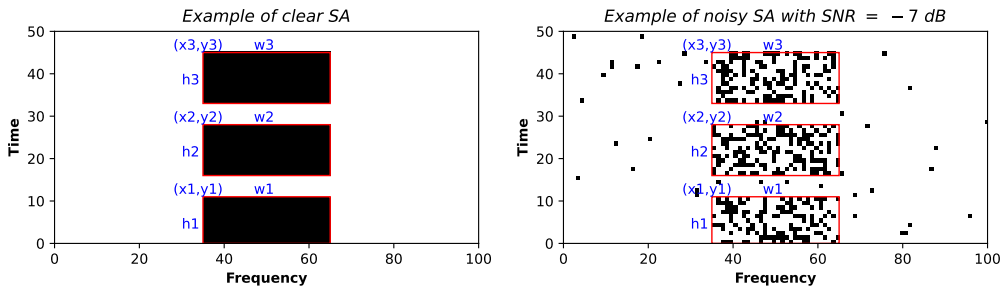
Figure 7.2: Example of a randomly generated time/frequency test grid: (a) Clean test grid, (b) Test grid with noise (SNR = –7 dB).

7.3 Development of the DL-ANN Model

In order to train, validate and test the proposed DL-ANN method, spectrum occupancy data were generated by means of both software simulations and hardware experiments. The simulation and experimental evaluation methodology followed in this chapter is similar to the one presented in Chapter 3 (please refer to Section 3.3 for details). The main difference in this study is that the generated spectrum data were also processed in order to extract appropriate features and their corresponding labels for training as depicted in Fig. 7.2, which shows a sample test grid containing three SAs and their corresponding bounding boxes (Fig. 7.2a) along with an illustration of how the same spectrogram would be observed at the receiver (Fig. 7.2b) according to the employed simulation procedure when the SNR at the receiver is –7 dB (at which $P_{md} \approx 0.61$), which would be the input spectrogram available for SAE. This section will provide details on those methodological aspects that are specific to this study, namely the set of employed performance metrics (which includes some additional metrics) and how the proposed DL-ANN was optimised, trained, validated and tested.

7.3.1 Performance Metrics

Several performance metrics, which includes the metrics in previous chapters (see details in Section 2.3) and some additional metrics, are used in this chapter both for DL-ANN training and optimisation as well as for evaluation of the final SAE accuracy. Concretely, in addition to the F1 score employed in previous chapters, the Mean Squared Error (MSE) and Intersection over Union (IOU) metrics are also considered in this chapter given their popularity in the context of deep learning, in general, and in the context of object detection in images, in particular.

In this study, the MSE and IOU metrics are mainly used for model training and configuration (along with the F1 score as well), while the F1 score and the computation times are mainly used for assessment of the final SAE accuracy. As it will be shown, the F1 score provides a suitable metric that follows a similar trend as the MSE and IOU metrics while providing a more complete characterisation of the output spectrogram generated by SAE methods.

Mean Squared Error (MSE)

The average squared difference between estimated and actual values is a popular metric commonly employed to assess the training of ANNs [92] and is also employed in this chapter. The MSE metric here employed is calculated based on the four output parameters of the proposed DL-ANN model shown in Fig. 7.1 as follows:

$$\text{MSE} = \frac{1}{4}\left((x - \tilde{x})^2 + (y - \tilde{y})^2 + (w - \tilde{w})^2 + (h - \tilde{h})^2\right)$$

where $m \in \{x, y, w, h\}$ denotes the true value of parameter m and $\tilde{m}$ represents its estimated value. The closer to zero the value of this metric, the more accurate the SAE.

Intersection over Union (IOU)

This metric is commonly used to measure the accuracy of a model on a given dataset, especially in the context of object detection [93]. For each estimated SA, this metric is calculated based on the areas of the ground-truth and the estimated bounding boxes. In the particular case of SAE, the bounding box of each SA coincides with the SA edges and therefore the area of the bounding box equals the area of the SA itself. The IOU metric is defined as the quotient between I (the area of intersection of the actual and estimated bounding boxes) and U (the area of the union of the actual and estimated bounding boxes), as illustrated in Fig. 7.3. Mathematically, it can be calculated as $\text{IOU} = I/U$, where $I = I_w \cdot I_h$, with the width I_w and height I_h of the intersection area obtained as:

$$I_w = \min(x + w, \tilde{x} + \tilde{w}) - \max(x, \tilde{x}) \tag{7.1}$$

$$I_h = \min(y + h, \tilde{y} + \tilde{h}) - \max(y, \tilde{y}) \tag{7.2}$$

and the union area is obtained as $U = w \cdot h + \tilde{w} \cdot \tilde{h} - I$. The IOU metric takes values within the interval $[0, 1]$, with zero indicating the worst possible accuracy and one indicating a perfect SAE accuracy. The closer to one the value of this metric, the more accurate the SAE.

F1 score

The MSE and IOU metrics described above place the focus on the location and dimension of the estimated SAs with respect to the true SAs, but do not pay attention to what occurs outside those regions. It is worth noting that some SAE methods can *detect* SAs in regions where no true SA is present, in particular at low SNR, where a large number of missed detections and false alarms can be expected. To include the impact of these artefacts in the performance of SAE methods, the F1 score metric is also evaluated, which compares the output spectrogram to the ground-truth spectrogram on a point-by-point basis, thus taking into account the behaviour of the SAE method not only in the regions where SAs are present but also in the rest of the spectrogram (see Section 2.3.2 for details).
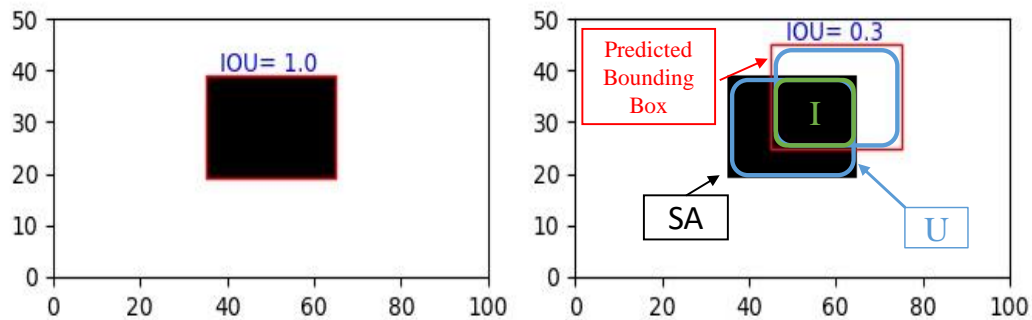
Figure 7.3: Illustration of the IOU concept.

Computation time

The computation time of each SAE method is also evaluated in this study. This measure is important because it affects the overall performance of the SAE method when it is practically implemented. For the proposed DL-ANN method, the computation time refers to the time required to execute the DL-ANN model once it has been trained. The training time, which is significantly longer than the execution time, is not included since in a practical system implementation the model would normally be trained only once and offline before it is deployed in a real implementation.

7.3.2 DL-ANN Model Training and Configuration

Raw Dataset Construction

Raw datasets were generated based on software simulations and hardware experiments separately as explained in Section 3.3. The construction of data-driven models such as those based on deep learning is typically characterized by demanding data requirements in terms of the quantity of data necessary for training, validation and testing. In general, deep learning algorithms frequently perform badly when the amount of data available is minimal [94]. In this chapter, the employed amount of data was set empirically to the largest size allowed by the computational resources available in terms of processor (GPU) and memory. As a result, for each individual SNR value considered in this study, a total of 60,000 independent test grids (i.e., original spectrograms) were generated and the corresponding features and labels were extracted in order to construct the required dataset, which was divided into separate subsets used for training (60%), validation (20%) and testing (20%). As explained in Section 7.2.2, two different scenarios are considered regarding the input information provided to the DL-ANN model. In the first scenario only the binary spectrogram obtained from spectrum measurements is provided, while in the second scenario the SNR value at which the provided spectrogram was generated is also fed to the network as a second input parameter. The raw data generation process for both scenarios is illustrated in Figs. 7.4 and 7.5, respectively. The only difference is that the SNR value at which each test grid (original spectrogram) is generated is not considered as an input feature in scenario 1 (Fig. 7.4) while it is considered as an input feature in scenario 2 (Fig. 7.5).
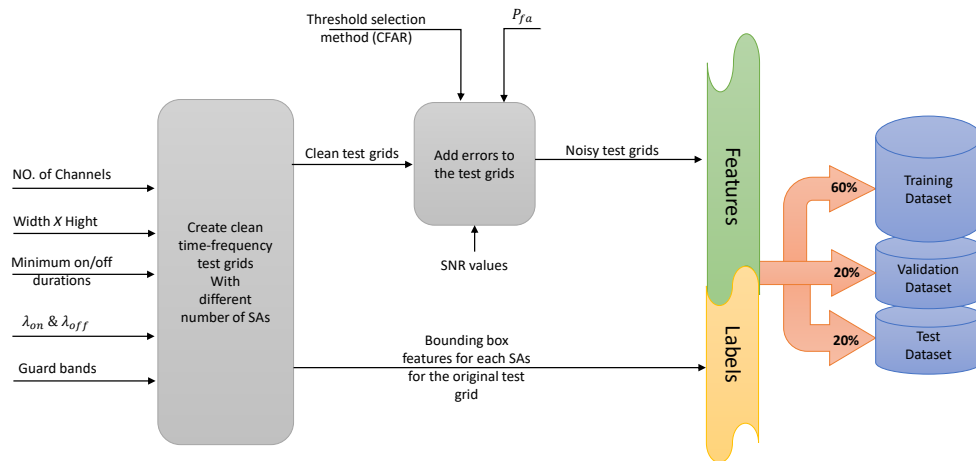
Figure 7.4: Construction of DL-ANN raw dataset for scenario 1.
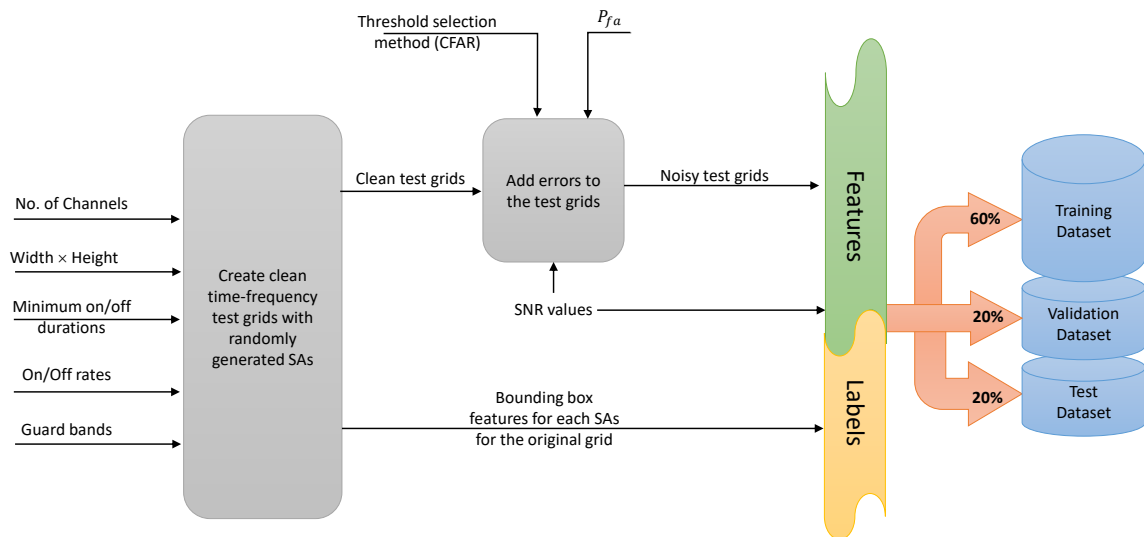
Figure 7.5: Construction of DL-ANN raw dataset for scenario 2.

Table 7.1: Hyperparameter tuning settings

Hyperparameter	Settings
Number of hidden layers	[1, 2, 3, **4**]
Number of neurons	[16, 32, 64, 128, **256**]
Batch size	[5, 10, 15, 20, **25**]
Epoch	100
Optimiser	Adam
Learning rate	0.001
Dropout regularisation	0.4
Activation function	ReLU, Sigmoid (output)

Before using the datasets for training, validation or testing, they must be preprocessed in order to extract the relevant features and corresponding labels. Python is utilised to this end because of the availability of several tools and advanced DL libraries (e.g., TensorFlow [95], Keras [96] and PyTorch [97])[1] that help not just with the dataset preparation, but also with the construction, training and testing of the DL model. After this, the prepared dataset is ready for training of the DL-ANN model and its validation (which is important to ensure that the ANN can generalise to new data and avoid the overfitting problem) before the final testing is carried out. Notice that the amount of data used for training makes it more difficult that the model is overfitted.

Hyperparameter Tuning and DL-ANN Optimisation

After the data preparation process, the DL-ANN model is trained to help it learn the optimum hyperparameter values. Table 7.1 shows a summary of the main hyperparameters considered and their selected values. Among the numerous hyperparameters that are amenable to optimisation, several hyperparameter settings were tested for the number of hidden layers, number of neurons per layer and batch size (with the selected values shown in bold font), while other relevant parameters were set to standard and commonly used values [98]. The approach used in this study was to optimise the first three hyperparameters shown in Table 7.1 based on the MSE as the performance metric as a function of the number of epochs. The hyperparameter optimisation was carried out based on a manual grid search method and the Adaptive Experimentation Platform (Ax). This approach was chosen because it allows an intelligent selection of properties in the search space when there is no opportunity for explicit choice of properties [99]. The results of the optimisation process are shown in Fig. 7.6 and the corresponding optimised DL-ANN models for scenarios 1 and 2 are shown in Figs. 7.7 and 7.8, respectively.

---

[1]In this chapter, all three tools are employed. Concretely, TensorFlow and Keras are used to define the objective for optimisation metrics on the training data while PyTorch is used on the Adaptive Experimentation (Ax) platform for the hyperparameter optimisation. After the hyperparameter optimisation, Keras is used in all cases to the end of the DL-ANN model design and evaluation.

(a)   (b)

(c)   (d)
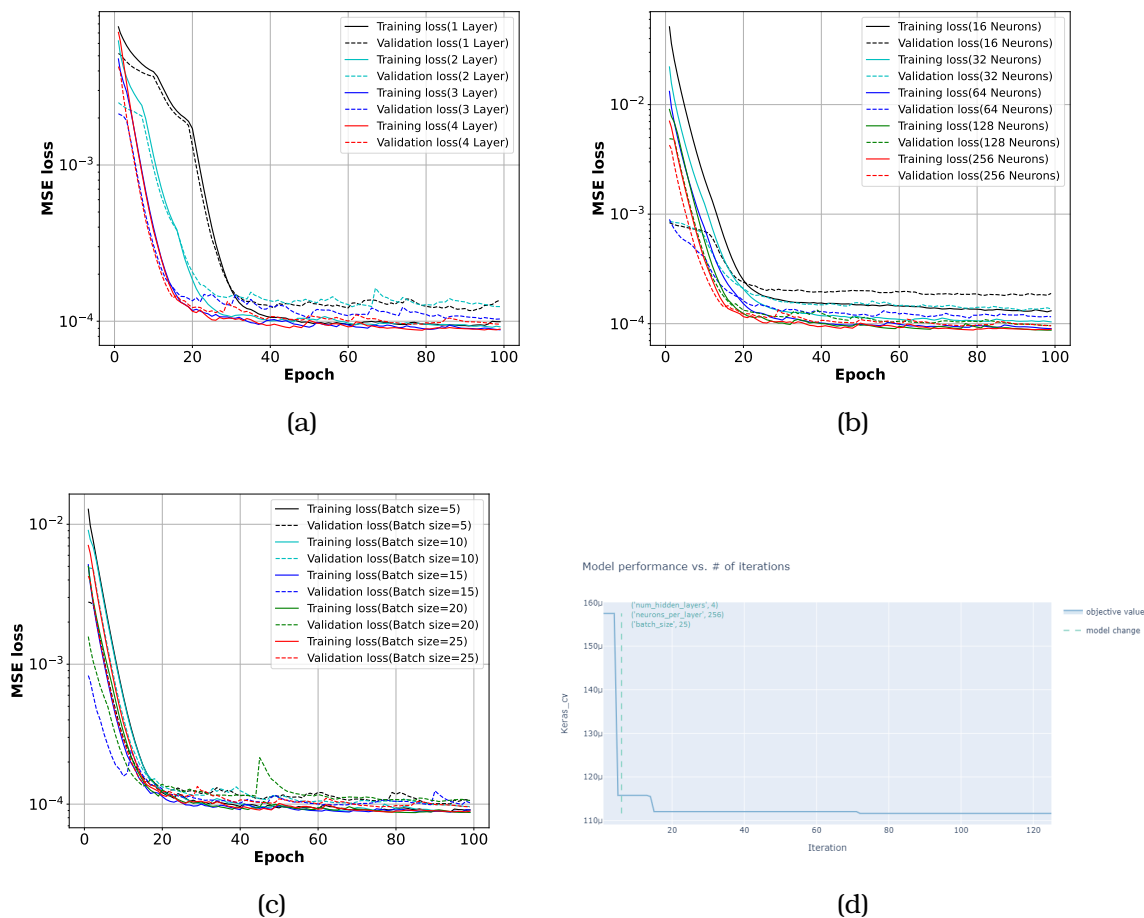
Figure 7.6: DL-ANN hyperparameter optimisation based on MSE: (a) using different numbers of hidden layers (with 256 neurons per layer and 25 batch size), (b) using different numbers of neurons per layer (with 4 hidden layers and 25 batch size), (c) using different batch sizes (with 4 hidden layers and 256 neurons per layer), and (d) using the Adaptive Experimentation Platform (Ax).

Training, Validation and Testing Options

For the DL-ANN model training and validation, four options were considered in order to obtain more detailed insights into the operation and performance of the proposed DL-ANN model: the first three options are related to scenario 1 (one input layer for the input spectrogram) and the last option is related to scenario 2 (with two input layers including the estimated SNR at the receiver):

- Option 1: Single input layer for input spectrograms generated at –5 dB SNR.

- Option 2: Single input layer for input spectrograms generated at –10 dB, –7 dB and –5 dB SNR.

- Option 3: Single input layer for input spectrograms generated at SNR values from –20 dB to +5 dB in 1-dB increments.

input_1	InputLayer	input:	[(None, 5000)]
		output:	[(None, 5000)]

dropout	Dropout	input:	(None, 5000)
		output:	(None, 5000)

dense	Dense	input:	(None, 5000)
		output:	(None, 256)

dense_1	Dense	input:	(None, 256)
		output:	(None, 256)

dense_2	Dense	input:	(None, 256)
		output:	(None, 256)

dense_3	Dense	input:	(None, 256)
		output:	(None, 256)

dense_4	Dense	input:	(None, 256)
		output:	(None, 80)
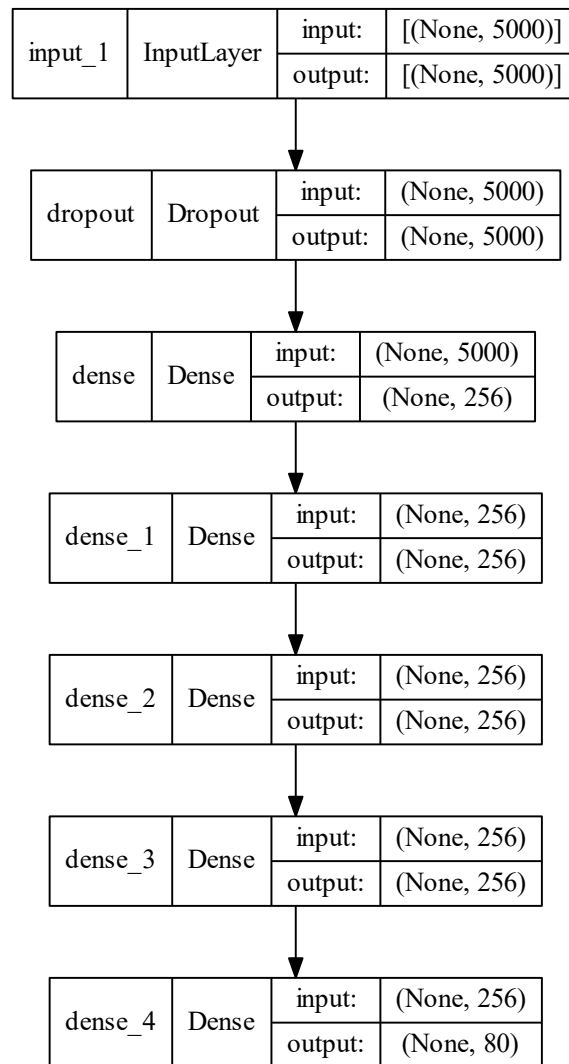
Figure 7.7: Optimised DL-ANN model for scenario 1.
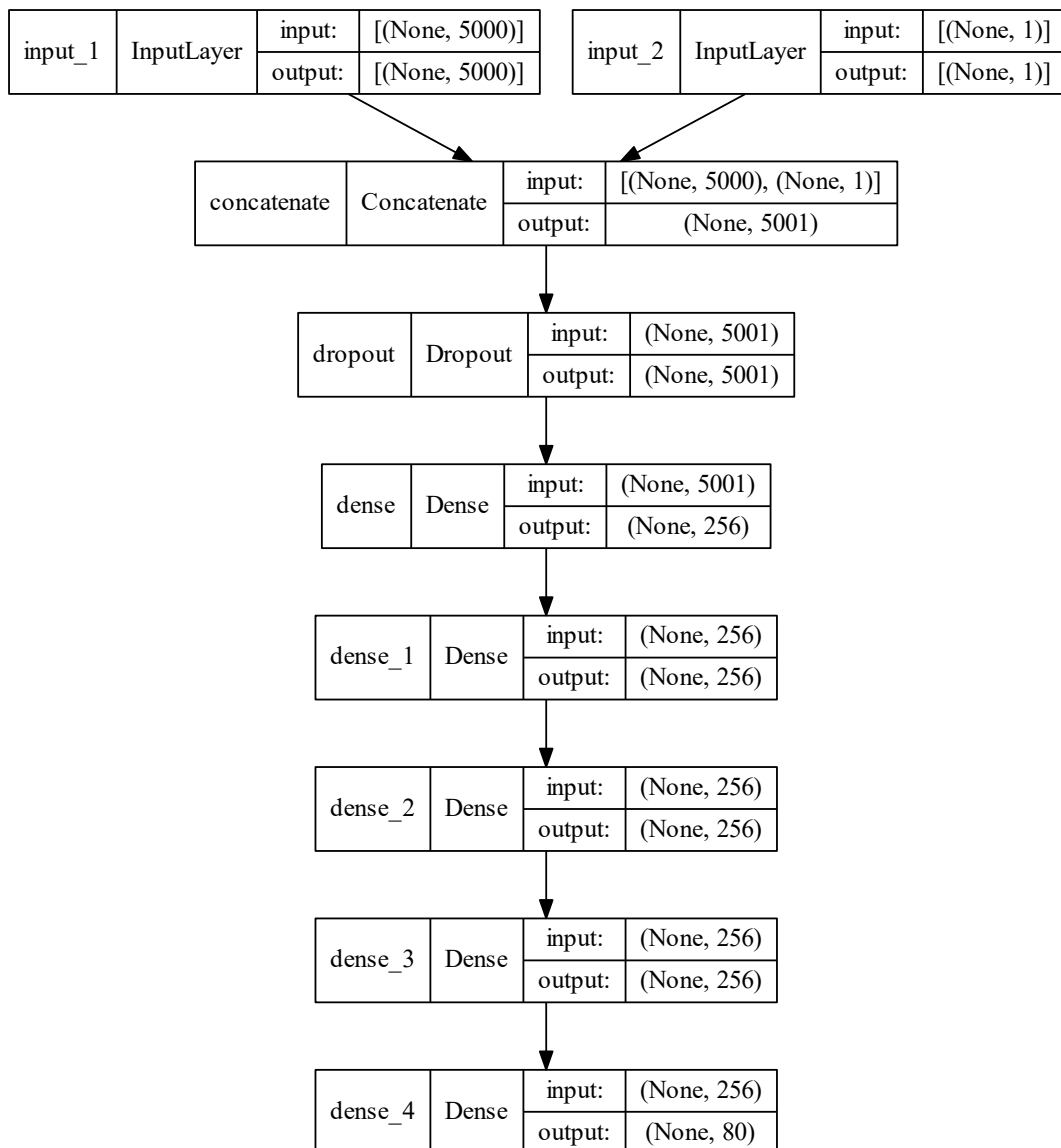
Figure 7.8: Optimised DL-ANN model for scenario 2.

- Option 4: Same as Option 3 with a second input layer that provides the SNR at which the input spectrogram provided in the first input layer was obtained.

In training option 1, the DL-ANN model was trained based on input spectrograms generated at –5 dB SNR (which represents a case of low SNR), while in option 2 the model was trained using input spectrograms generated at three different SNR values, namely –10 dB, –7 dB and –5 dB (which represents a larger training data set but still a limited one compared to the full SNR operational range from –20 dB to +5 dB). Option 3 trains the model with data generated at all possible SNR values from –20 dB to +5 dB in 1-dB increments. These three options were considered to determine the degree to which the amount of data available for training can help the DL-ANN model produce accurate SAE outputs and is motivated by the fact that in some practical application scenarios it may not be possible to acquire data for training at all the SNR levels that may be experienced once the model is deployed in regular working conditions. Finally, option 4 is considered to determine the degree to which providing additional input information to the model (namely, the SNR value at which the input spectrogram was obtained) can help produce more accurate outputs. The results of the DL-ANN training for these four options can be seen in Fig. 7.9 in terms of the IOU and F1 score metrics. As it can be observed, the trends are similar for the IOU and F1 score. For simplicity, the remainder of the performance analysis will focus on the F1 score only, which is in line with previous work in [40, 43, 100].

Once trained and validated, the DL-ANN model was tested using the same kind of data (i.e., new matrices of noisy test grids with the same kind of spectrograms but not previously used for training nor validation). However, in the testing stage only the input features (spectrogram only in options 1–3 and also the receiving SNR in option 4) were fed to the DL-ANN to predict its output, while labels were used to quantify the accuracy of the SAE result. It is worth noting that in all cases the input spectrograms employed in the testing stage were generated for all SNR values from –20 dB to +5 dB regardless of what data were used in the training/validation stage (including the testing of options 1 and 2). The results of this testing are presented and discussed in Section 7.4.

7.4 Performance Evaluation

7.4.1 Performance of DL-ANN

In order to illustrate the output produced by the proposed DL-ANN model under the four different training options described in Section 7.3.2, Figs. 7.10–7.13 show some examples of the estimated SAs for various spectrograms under three different SNR values, namely –5 dB, –7 dB and –10 dB (notice that all these cases correspond to a low SNR regime, where SAE becomes more challenging). The figures show the spectrograms observed at the receiver along with the estimated SAs, which are depicted as red rectangles. Even though the original (ground truth) spectrograms are not shown, the original SAs can be easily guessed from these figures and thus they can be used for an initial qualitative assessment of the SAE performance.

The results shown in Fig. 7.10 for option 1, where the DL-ANN model is trained using only spectrograms observed at –5 dB SNR, suggest that the SAs in the received
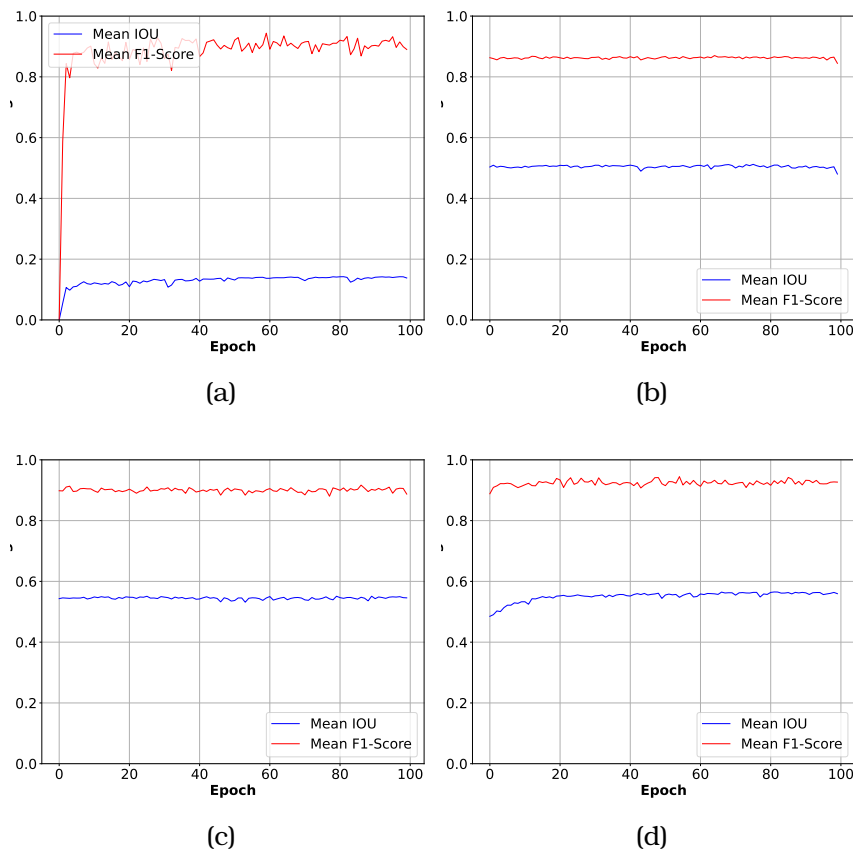
Figure 7.9: DL-ANN training performance for different training options: (a) option 1, (b) option 2, (c) option 3, and (d) option 4.

spectrogram can be detected with a reasonable degree of accuracy at the SNR level at which the model is trained (i.e., – 5 dB) and also at slightly lower SNRs (i.e., –7 dB), but fails to produce satisfactory results at a much lower SNRs (i.e., –10 dB). This suggests that the network can perform well when operating at the same SNR at which it was trained and also at slightly different SNR values[2], but fails to deliver satisfactory results when it operates at SNR values that are substantially different from those at which it was trained. To confirm this, the DL-ANN model was also trained at the three tested SNR values in option 2 and, as it can be appreciated in Fig. 7.11, in this case the model also provides a reasonable detection performance at lower SNR values (–10 dB) once it has been trained for those particular operating conditions. It is interesting to note that, even though the presence of SAs at –10 dB SNR is hardly recognisable for the human eye, the DL-ANN model can identify correctly the number of SAs and their locations with a remarkable level of accuracy once it has been trained with data observed at such low SNR level (see Fig. 7.11a). Moreover, it is also worth noting that training the network with additional data at lower SNR values such as –10 dB also makes the network perform better at higher SNR values such as –7 and –5 dB, as it

---

[2]This suggests that the model can be generalised to some extent and therefore was not overfitted.
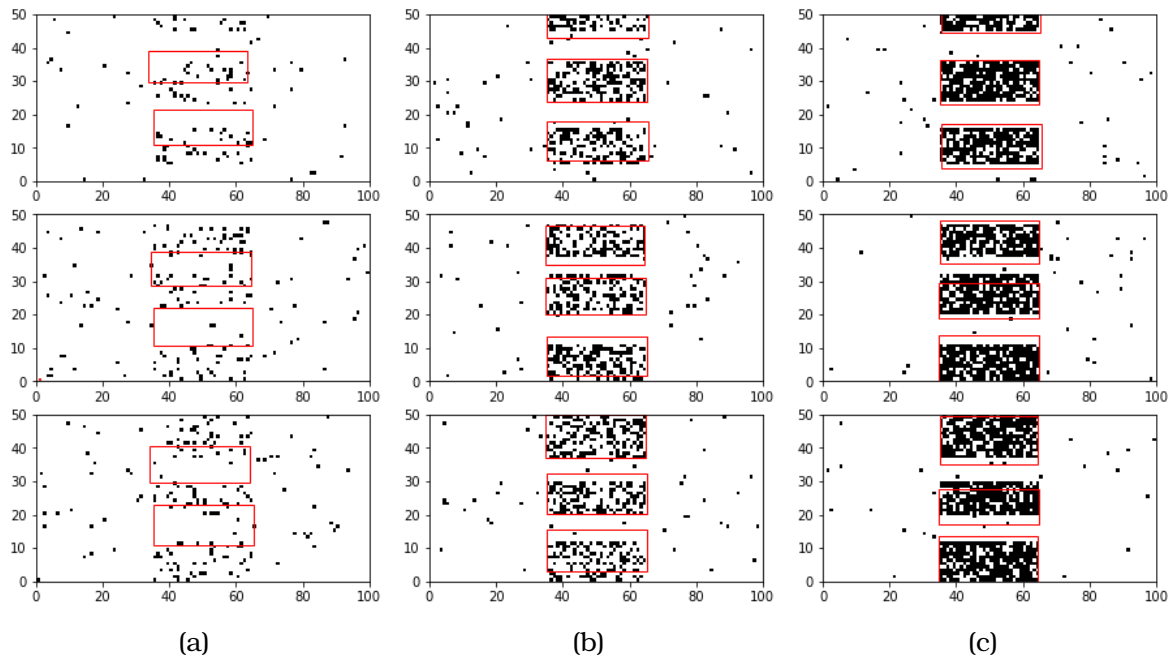
Figure 7.10: Three different examples of SAE (one per row) for Option 1: (a) SNR = −10dB, (b) SNR = −7dB, and (c) SNR = −5dB.
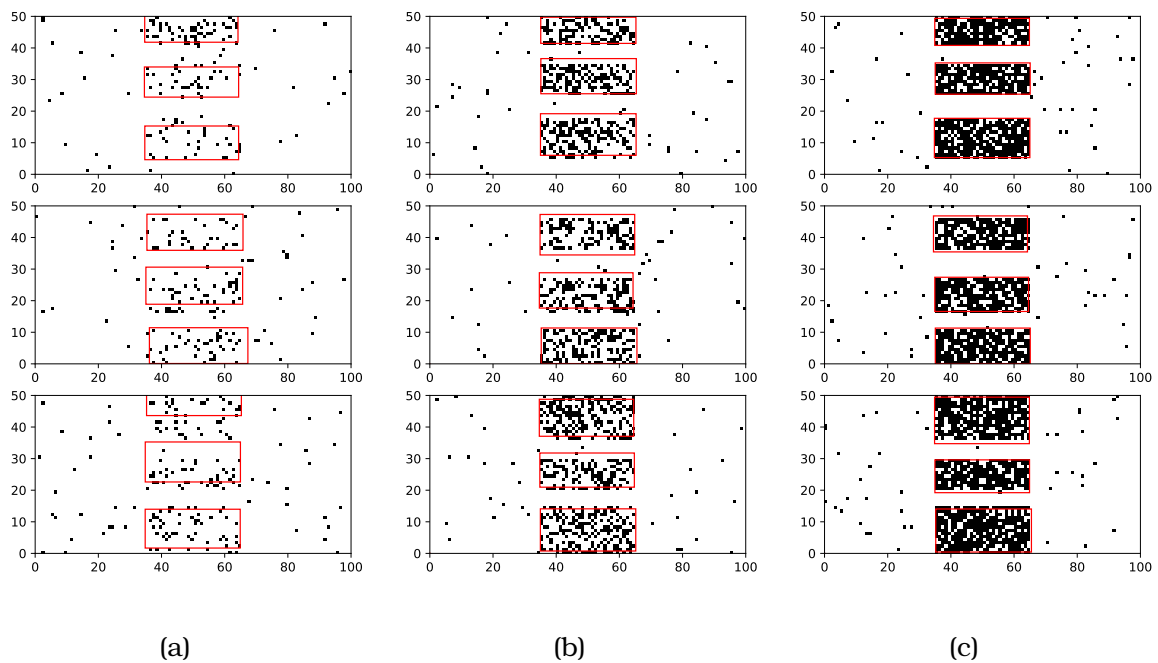
Figure 7.11: Three different examples of SAE (one per row) for Option 2: (a) SNR = −10dB, (b) SNR = −7dB, and (c) SNR = −5dB.
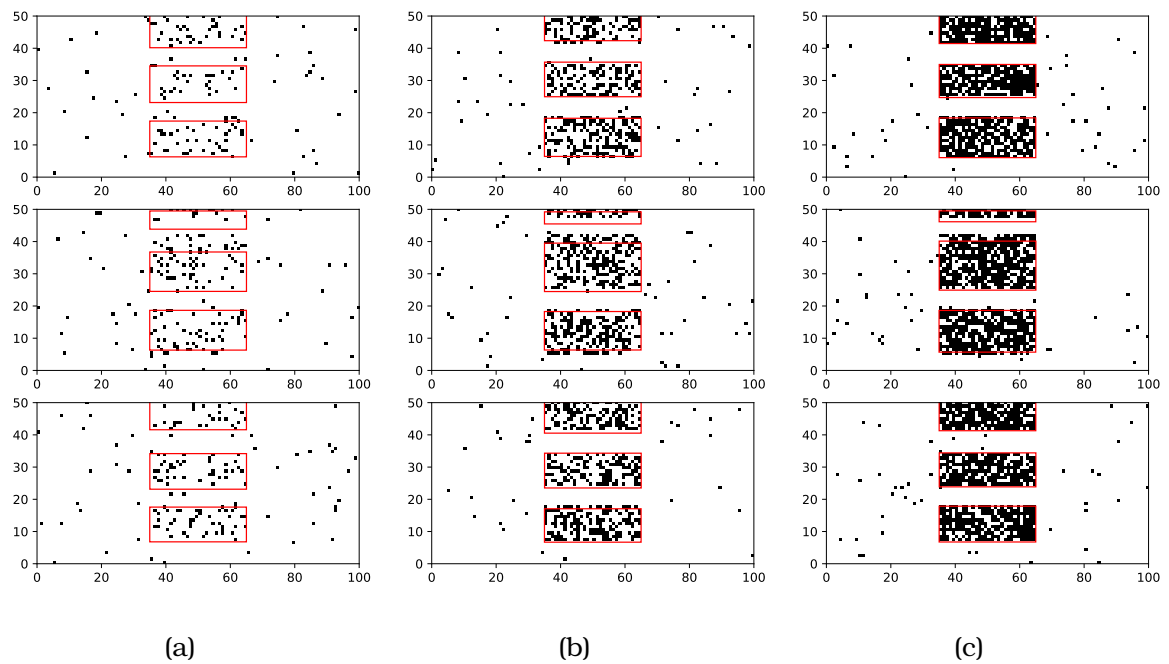
Figure 7.12: Three different examples of SAE (one per row) for Option 3: (a) SNR = −10dB, (b) SNR = −7dB, and (c) SNR = −5dB.
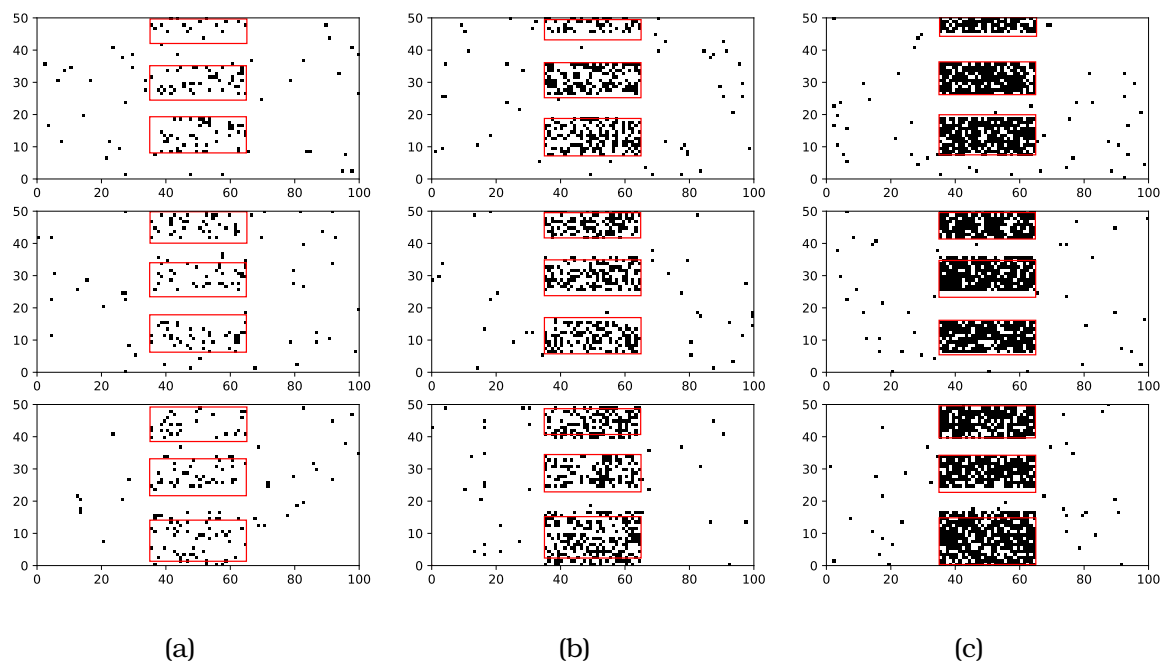
Figure 7.13: Three different examples of SAE (one per row) for Option 4: (a) SNR = −10dB, (b) SNR = −7dB, and (c) SNR = −5dB.

can be appreciated by comparing Figs. 7.11b and 7.11c with Figs. 7.10b and 7.10c, respectively, which suggests that the network will experience an improved learning process from any training data even when operating at other SNR levels[2]. The results in Fig. 7.12 correspond to option 3, where the model is trained with data generated at all the possible SNR values considered in this study (from –20 dB to +5 dB in 1-dB increments); in this particular case, there is no significant difference with respect to Fig. 7.11[2], since in both cases the network has been trained with data generated at the three SNR values shown in these examples. In Fig. 7.13, the network is also trained with spectrogram data generated at all the possible SNR values and, in addition to that, is also trained with a second input feature which is the actual SNR value at which the spectrogram is generated. This additional input information would in principle be expected to produce a more accurate detection of the SAs present in the spectrogram. However, as it can be observed by comparing Figs. 7.12 and 7.13, there does not seem to be a significant difference, which suggests that providing the SNR as a second input feature may not have a relevant impact on the model performance.

To verify the above statements and assess the performance of the DL-ANN model in a more quantitative manner, Fig. 7.14 shows the performance of the four considered training options in terms of the F1 score as a function of the SNR along with the corresponding computation time. The figure also includes the performance of the two selected benchmark methods (namely CT-SA and SSA) and the performance of a simple energy detector (ED), which cannot be considered as a SAE method in strict sense but provides an interesting baseline for comparison purposes (ED is the step needed to generate the spectrogram previous to the SAE process). Fig. 7.14a corroborates the observations made above based on Figs. 7.10–7.13. It can be noticed that the performance of the DL-ANN model when trained as in option 1 starts to degrade significantly for SNR values below –5 dB, which is the SNR at which the employed trained data was generated. Similarly, when trained as in option 2, the performance starts to degrade significantly when the operating SNR falls below the lowest SNR used for training (i.e., –10 dB). When the DL-ANN model is trained as in option 3 with spectrogram data generated at all the SNR values at which the model operates, the performance is significantly improved over the whole SNR range and, even though the performance experiences a natural degradation as the SNR decreases, the degradation in this case is significantly less accentuated than in the other two training options. It is also worth noting that the training considered in option 4, where also the actual SNR value is provided as an input feature, provides only a marginal performance improvement with respect to the training based on option 3, where only spectrogram data (without actual SNR information) are used. Therefore, this suggests that the training in option 3 can be considered as a preferred option[3] since it does not require the estimation of the receiving SNR, which would imply additional complexity in a practical system implementation. When the DL-ANN model is trained based on spectrograms generated at all the possible SNR values as in option 3, the proposed system provides an excellent performance over the whole SNR range, comparable to that attained with

---

[3]Notice that the trained DL-ANN model is unable to reach a perfect F1 score even at high SNR. This is caused by the presence of false alarms in the spectrogram, whose probability is independent of the SNR, and is in itself an indication that the DL-ANN model has not learnt and memorised the noise in the training data and therefore it has not been overfitted.

129

(a)

(b)
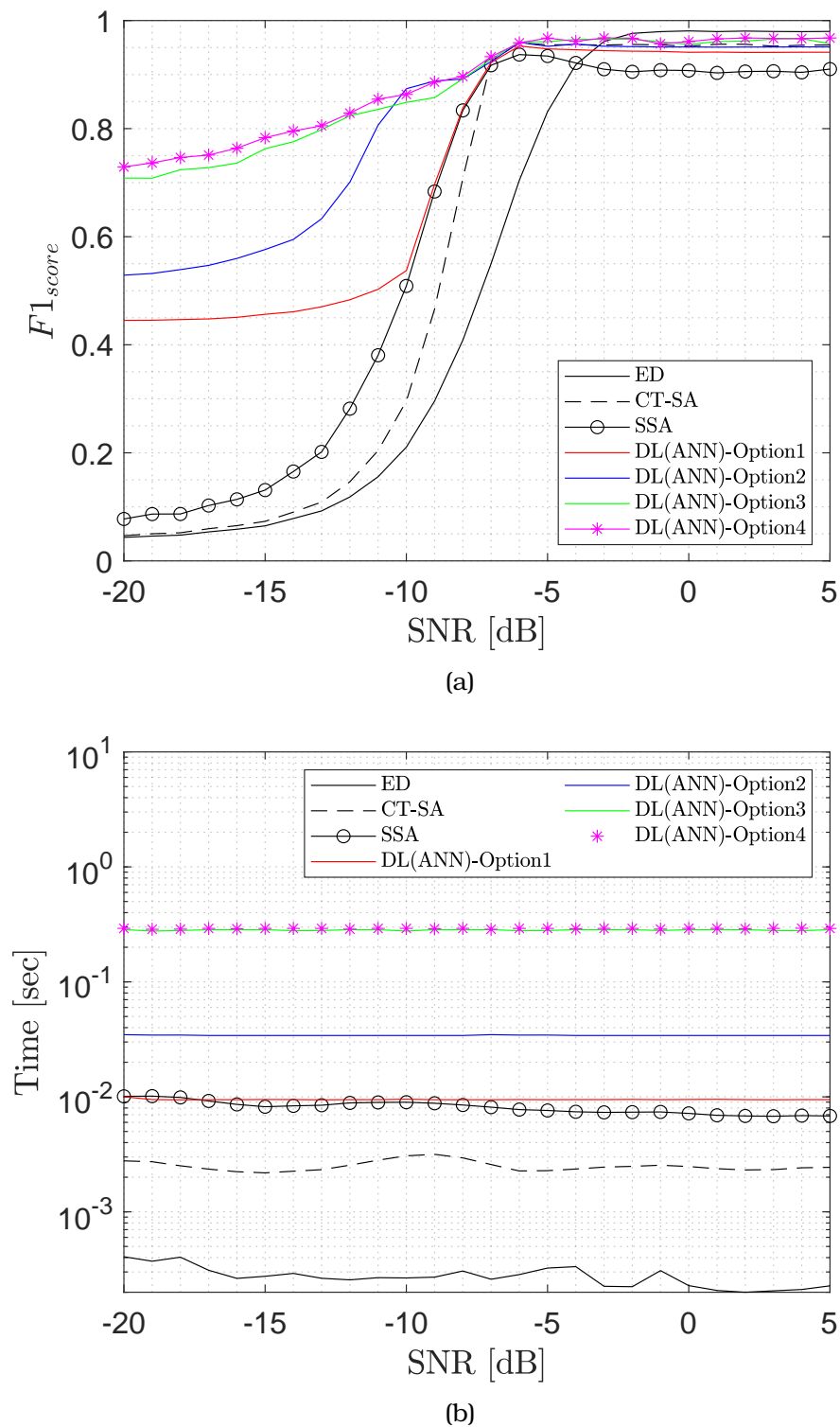
Figure 7.14: Performance comparison of options 1–4 in terms of: (a) F1 score, and (b) computation time.

option 4, but with a much simpler system implementation (where the receiving SNR does not need to be estimated). Moreover, it is worth noting that the DL-ANN model trained as in option 3 outperforms both SAE benchmark methods (i.e., CT-SA and SSA) over the whole SNR range. While the SAE accuracy is similar at relatively high SNR values (at around –7 dB and above), there is a significant performance improvement attained with the DL-ANN method at lower SNR values. In particular, at SNR values as low as –20 dB, the DL-ANN model can provide an estimation accuracy (based on the F1 score) of about 73% (for option 3) while the benchmark methods would provide an estimation accuracy of 5–7% for the same SNR level. This significant performance improvement results in a noticeable extension of the SAE detection sensitivity (i.e., the ability to accurately detect SAs at lower SNR values). The price to be paid for this significant performance improvement, as observed in Fig. 7.14b, is a higher computational cost in terms of the computation time required to run the DL-ANN SAE method. Fig. 7.14b indeed shows the existence of a trade-off between SAE accuracy and required computation time, with the two benchmark methods (CT-SA and SSA) requiring the lowest computation time but also providing the lowest SAE accuracy, and the proposed DL-ANN method (training options 3 and 4) providing the best SAE accuracy at the expense of a higher computation time. However, with the availability of powerful processors nowadays (and pressumably more powerful ones in the future), this is an affordable cost that is worth paying for the significant performance improvements that can be attained with the DL-ANN model, in particular in the low SNR regime.

7.4.2   Performance with Image Processing Techniques

As discussed in Section 7.2.1, the problem of SAE can be addressed from the point of view of image processing by looking at binary spectrograms as binary images where each time-frequency point represents an image pixel, which allows the application of image processing techniques. This section explores the performance of the proposed DL-ANN method when combined with some popular image processing techniques. In particular, two image processing techniques are considered here, namely morphological operations (explored in detail in Chapter 4) and a combination of edge detection and flood fill (explored in detail in Chapter 5). These image processing techniques are combined with the proposed DL-ANN method by using them as pre/post-processing stages, where they can be applied only before (pre-processing), only after (post-processing) or both before and after (pre- and post-processing) the DL-ANN model is run.

Morphological Operations (MO) are carried out by moving a small (typically squared or rectangular) filter template referred to as *Structuring Element* (SE) over the binary image by centering it at every image pixel (based on the defined SE's origin, which is usually its geometric centre) and performing some logical operation between the SE pixels and the image pixels that fall within the SE template. The basic MOs include erosion, dilation, opening and closing [45, 79]. In morphological erosion (dilation) the image pixel at the centre of the SE is set to one if all (any) of the neighbouring pixels within the SE have the value one, and zero otherwise. Morphological erosion removes islands and small objects in the input image, so that only substantive objects remain and can be useful to remove false alarms in the input spectrogram, while morphological dilation has the opposite effect to erosion, it adds more pixels to the boundaries of
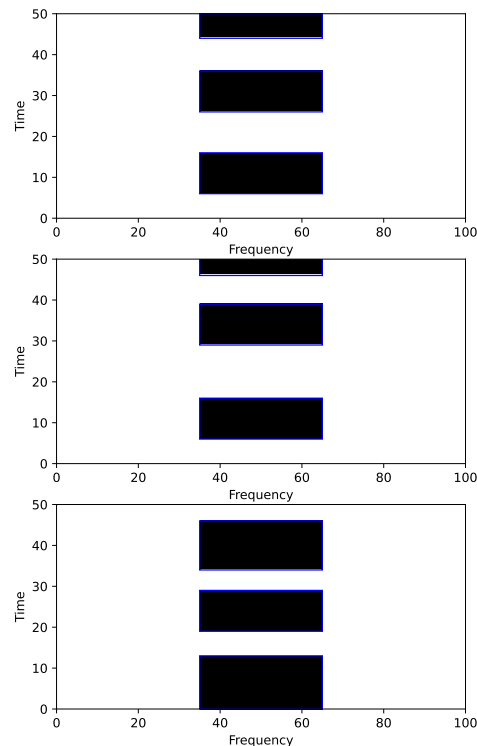
Figure 7.15: Ground truth SAs in Figs. 7.16–7.23.

existing regions, making objects more visible and reducing gaps between them, which can be useful to fill in missed detections within SAs. The other two morphological operations are obtained as a combination, where morphological opening (closing) is obtained by first eroding (dilating) and then dilating (eroding) an image using the same SE for both operations. Morphological opening can remove small entities from an image while conserving the dimensions and proportions of larger objects almost unaltered, while morphological closing enlarges an image and then corrodes the expanded image, with the visual effect being the repletion of gaps in the image. The performance of the DL-ANN model is here shown when combined with dilation and opening, which are the two operations that can help fill gaps within SAs due to signal missed detections and therefore provide a more clear visualisation of the SAs in a spectrogram. Without loss of generality, the other two MOs (erosion and closing) are not shown here to avoid an excessively long analysis but similar conclusions can be reached.

For reference, Fig. 7.15 shows the ground truth SAs for the subsequent examples. The performance of the DL-ANN model when combined with the morphological dilation operation as a pre-, post, and both pre/post-processing technique is illustrated in Figs. 7.16, 7.17 and 7.18, respectively. Notice that the application of a MO after the DL-ANN model means that the information about the location and dimensions of the
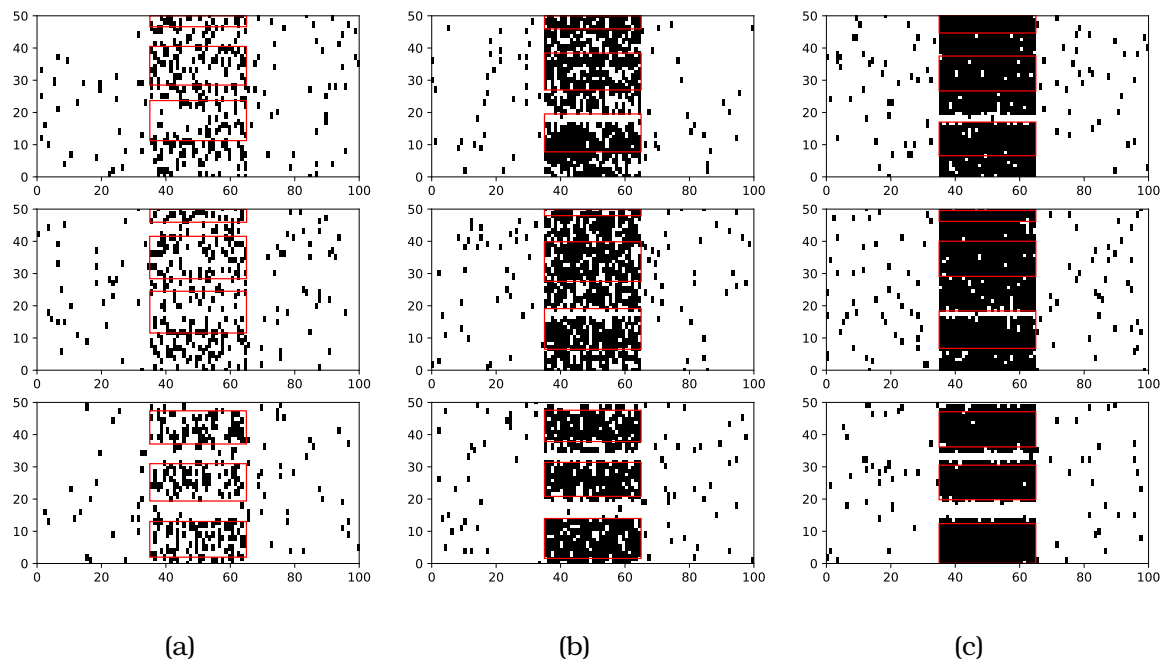
Figure 7.16: Performance of dilation before DL-ANN: (a) SNR = −10dB, (b) SNR = −7dB, and (c) SNR = −5dB.
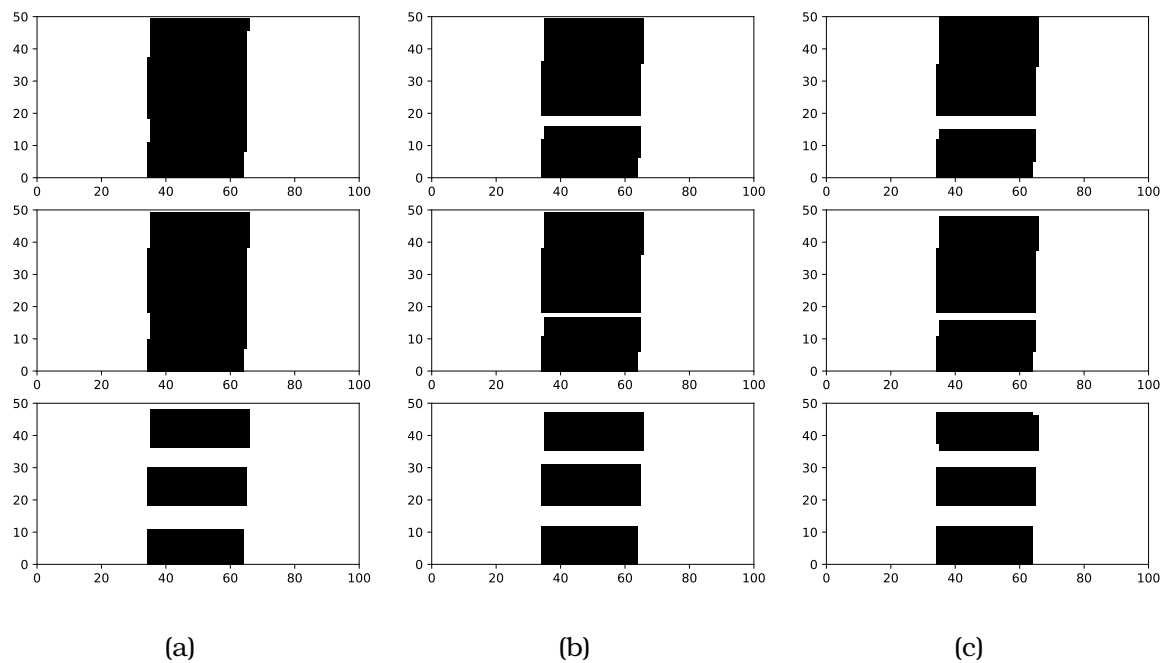
Figure 7.17: Performance of dilation after DL-ANN: (a) SNR = −10dB, (b) SNR = −7dB, and (c) SNR = −5dB.
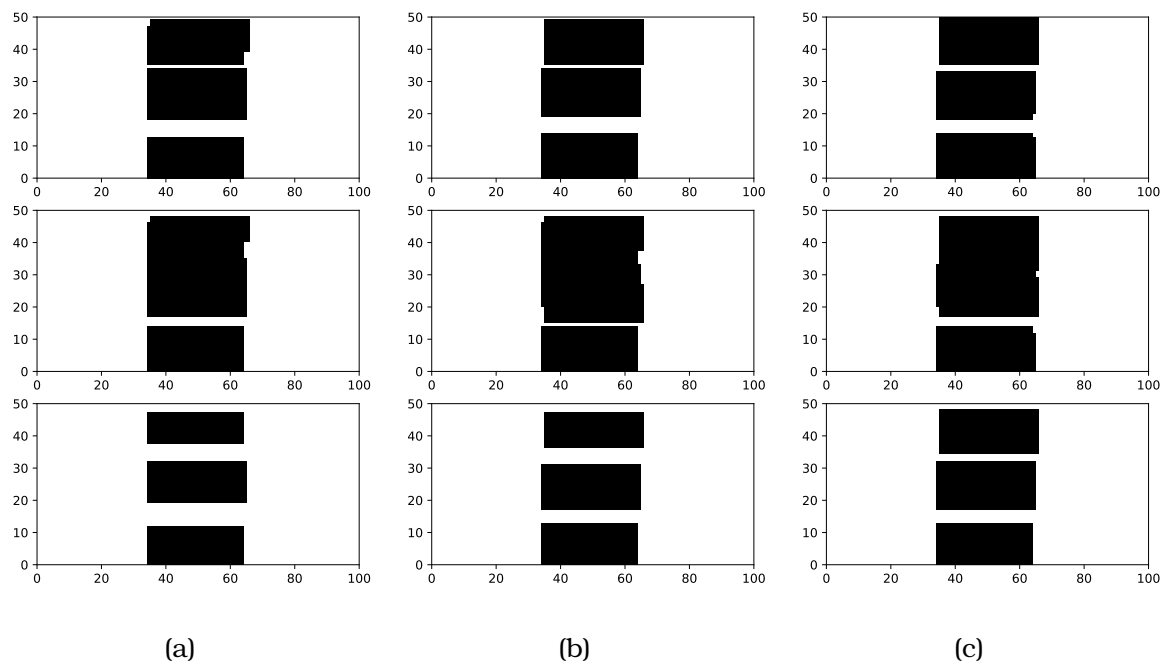
Figure 7.18: Performance of dilation both before and after DL-ANN: (a) SNR = −10dB, (b) SNR = −7dB, and (c) SNR = −5dB.

SAs detected by the DL-ANN (represented by red rectangles) is lost, hence such red rectangles are not shown in Figs. 7.17 and 7.18 (however these cases are also included in the study for completeness). As it can be appreciated, the overall effect of the dilation operation is to expand the regions where the presence of signal components is detected. This effectively fills gaps within genuine SAs created by signal missed detections, however it also magnifies these regions to the extent that the DL-ANN model overestimates the true dimensions of the SAs. The overall result, as shown in Fig. 7.19a, is an overall degradation of the detection accuracy. Notice that the introduction of the dilation step does not affect significantly the overall computation cost as indicated by Fig. 7.19b, which is due to a negligible computation time with respect to that required by the DL-ANN model. However, despite this negligible computational load, the introduction of this particular MO does not provide any performance improvement and therefore is of little utility. On the other hand, the performance of the DL-ANN model when combined with the morphological opening operation as a pre-, post, and both pre/post-processing technique is illustrated in Figs. 7.20, 7.21 and 7.22, respectively. The performance can be appreciated in more detail in Fig. 7.23. In this other case, it can be noted that the use of morphological opening as a pre-processing technique provides a very similar detection performance as the DL-ANN model alone without a noticeable variation in the required computational cost. The introduction of dilation as a pre-processing step can indeed result in a slightly better SAE accuracy at high SNR values (above around −7 dB) and in that SNR regime can be of some utility, even though the DL-ANN model on its own can achieve a very similar performance.
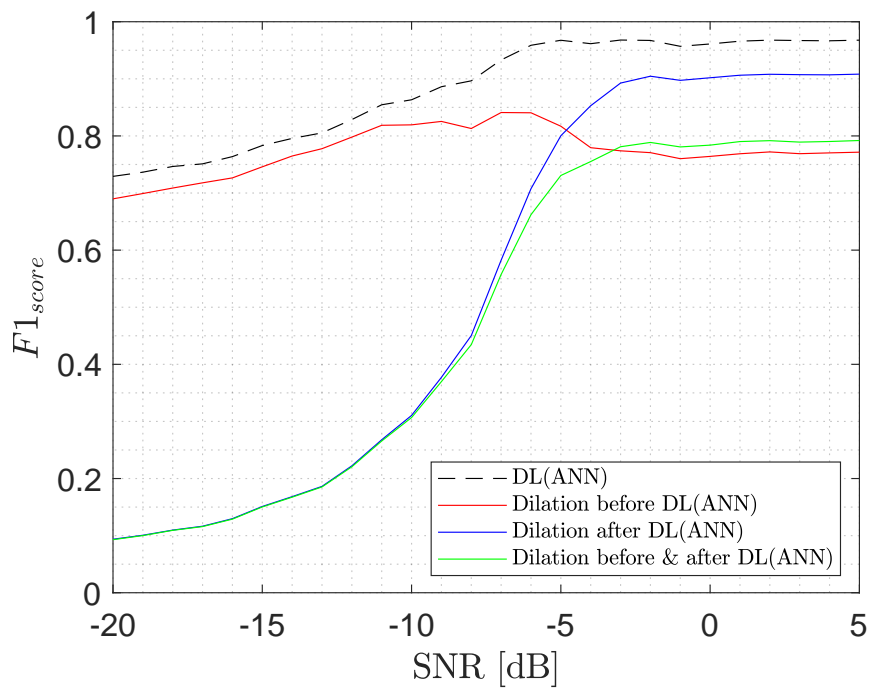
(a)
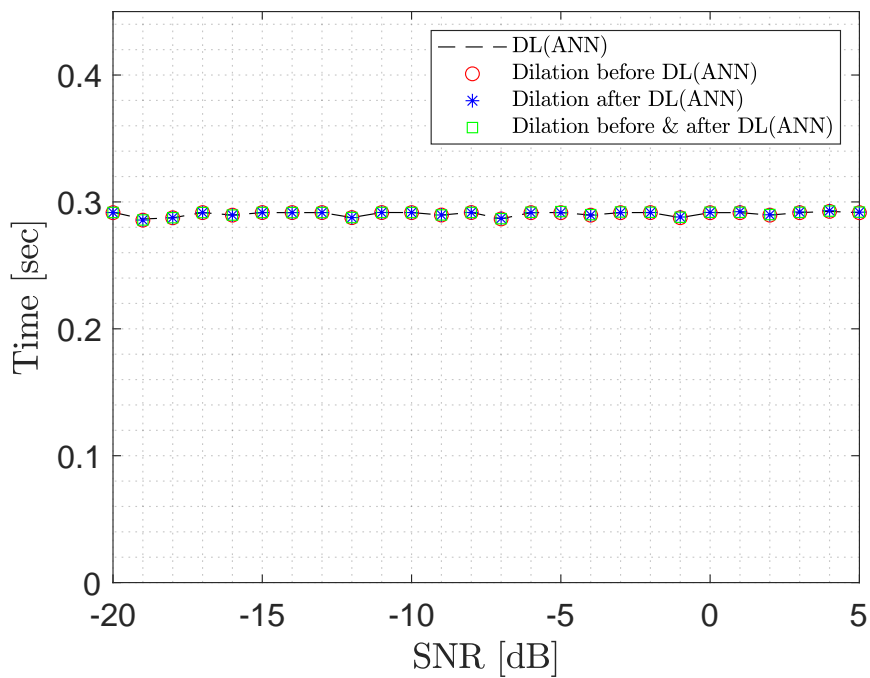
(b)

Figure 7.19: Performance of DL-ANN combined with morphological dilation in terms of: (a) F1 score, and (b) computation time.
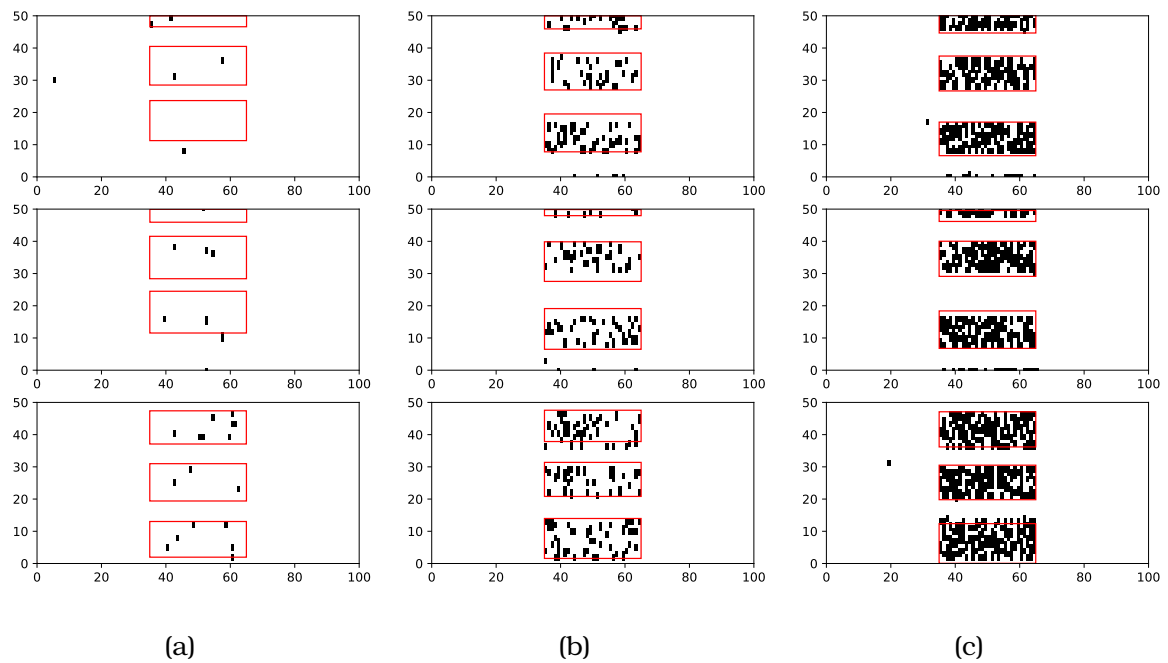
Figure 7.20: Performance of opening before DL-ANN: (a) SNR = −10dB, (b) SNR = −7dB, and (c) SNR = −5dB.
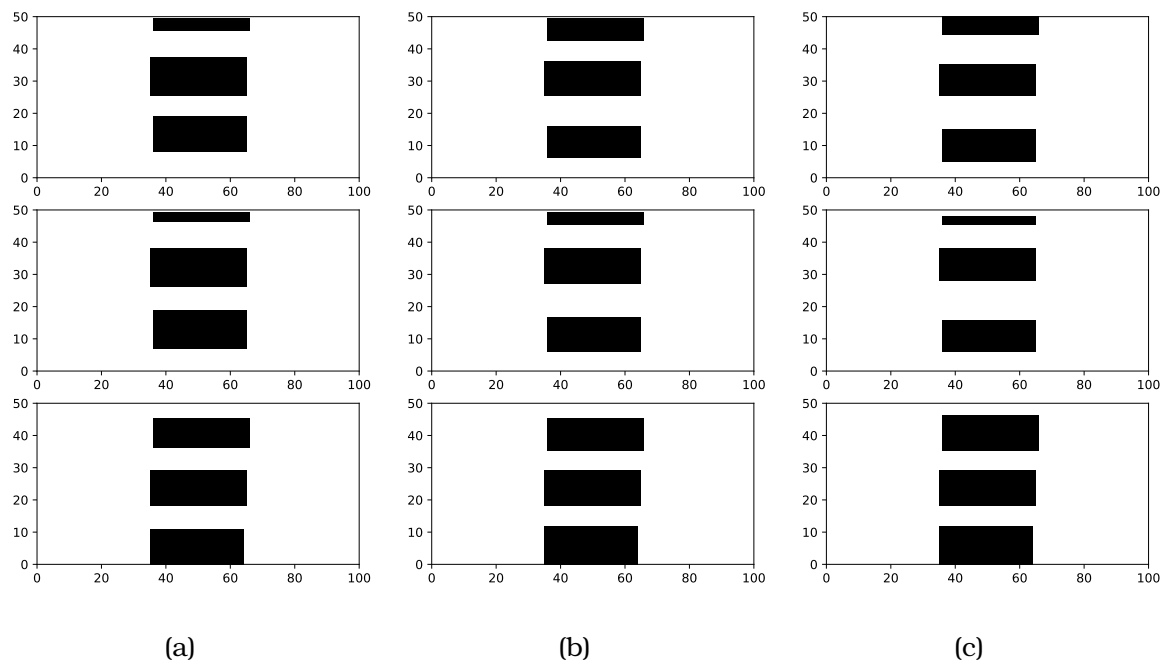
Figure 7.21: Performance of opening after DL-ANN: (a) SNR = −10dB, (b) SNR = −7dB, and (c) SNR = −5dB.

(a)   (b)   (c)
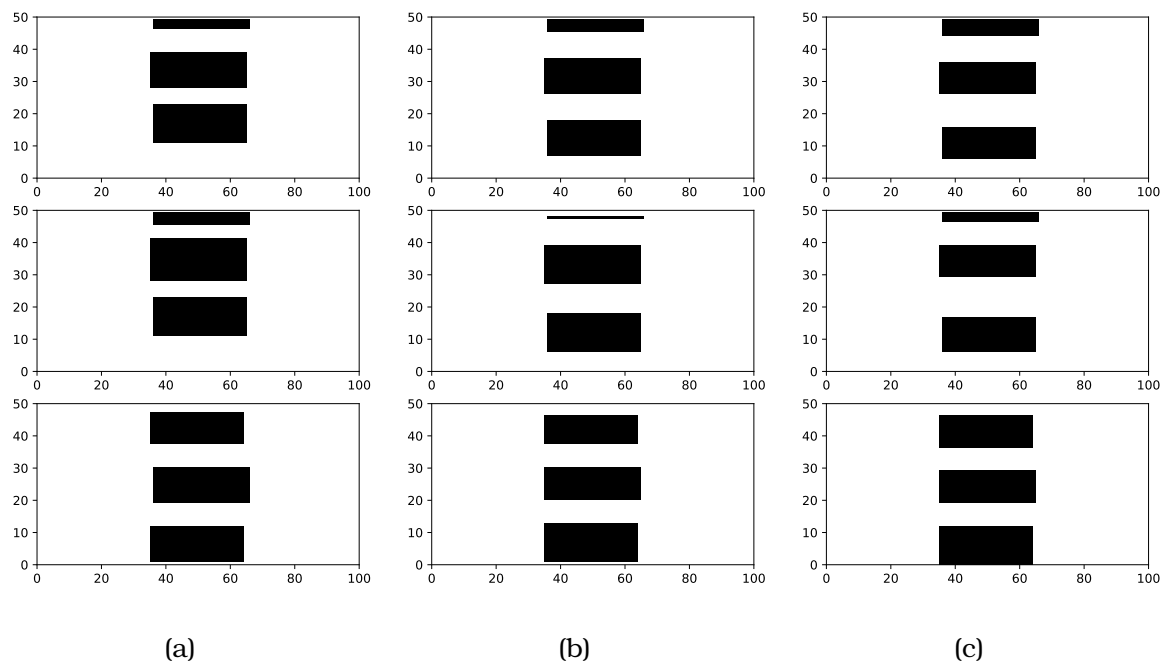
Figure 7.22: Performance of opening both before and after DL-ANN: (a) SNR = −10dB, (b) SNR = −7dB, and (c) SNR = −5dB.

The second image processing technique explored here is a combination of edge detection (used to estimate the edges of the potential SAs in a spectrogram) and flood fill (used to fill the area inside the detected edges). In this approach, the Canny edge detector is used followed by a standard flood fill method [62, 63]. The motivation for using these image processing techniques is to attempt to enhance the recognisability of SAs (or fragments thereof) to help the DL-ANN recognise the SAs in the spectrogram. However, in this case, as observed in Figs. 7.24–7.27, the introduction of this image processing approach cannot improve the SAE accuracy already attained by the DL-ANN model itself, while resulting in slightly increased computation times.

In summary, the results obtained in this subsection suggest that image processing techniques, which may be suitable for their application to the SAE problem, do not improve the performance attained by the proposed DL-ANN method. The use of image processing techniques in the context of SAE has provided noticeable benefits and performance improvements in some previous studies [43, 100]. However, the use of more advanced techniques such as DL can achieve by itself excellent levels of SAE estimation accuracy over the whole range of SNR values without the need of combining them with image processing techniques, which in this subsection have been shown to be of limited utility or, at best, provide very slight performance improvements in some cases.
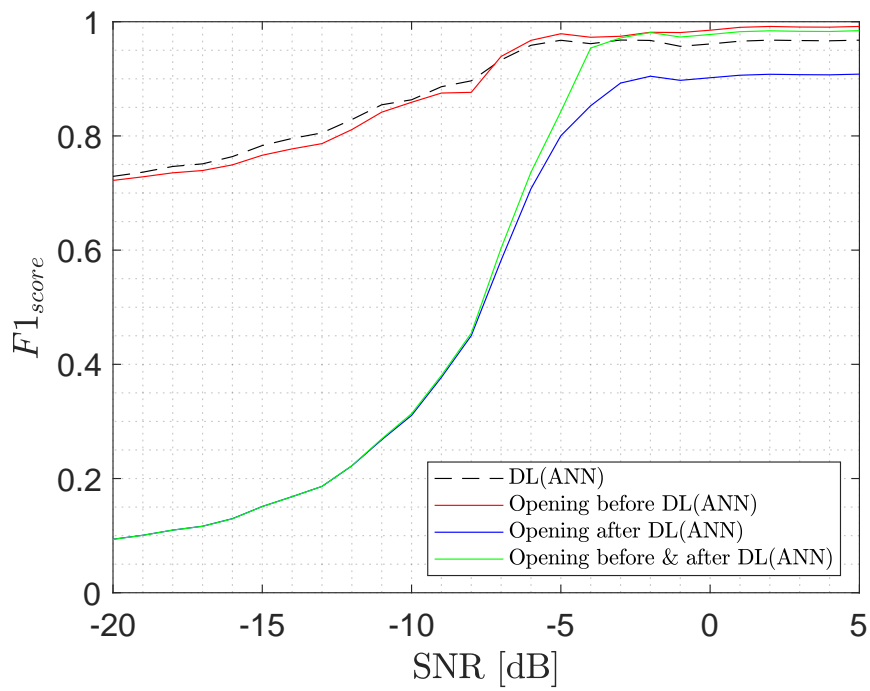
(a)
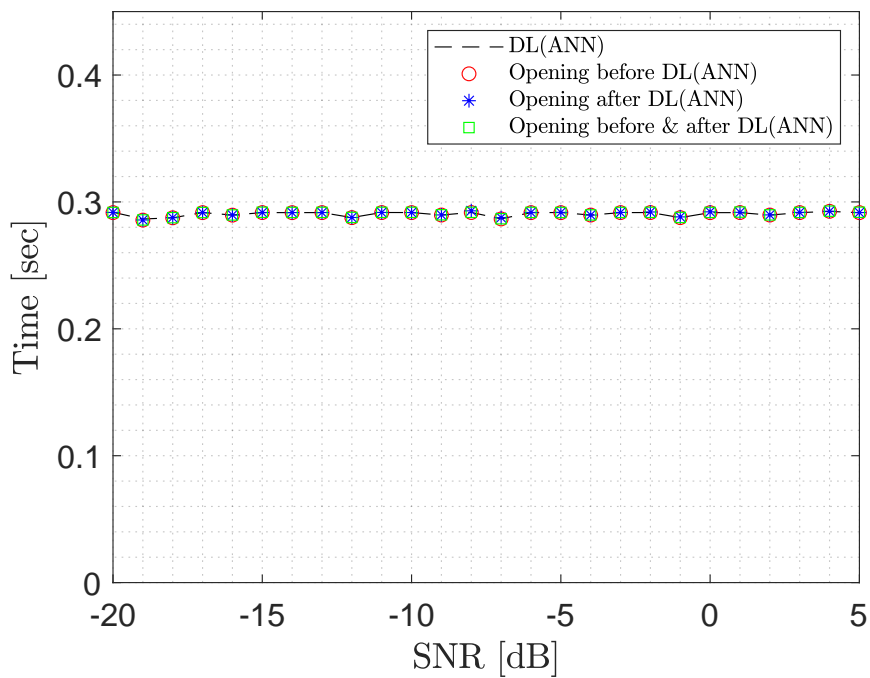
(b)

Figure 7.23: Performance of DL-ANN combined with morphological opening in terms of: (a) F1 score, and (b) computation time.
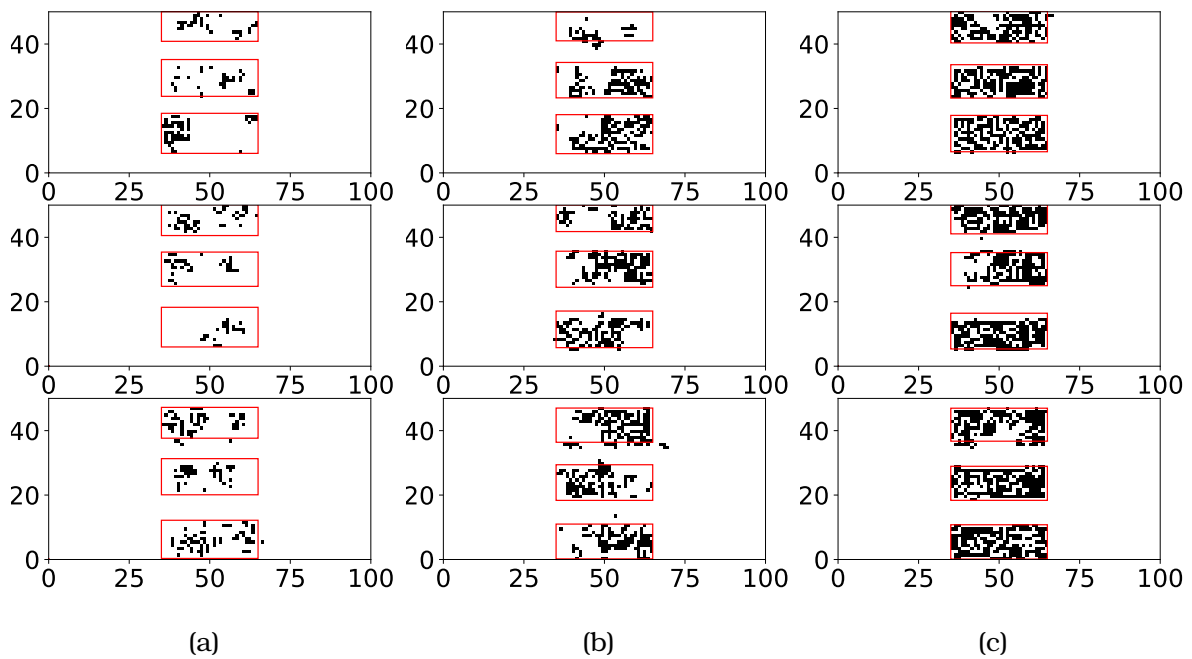
Figure 7.24: Performance of edge detection and flood fill before DL-ANN: (a) SNR = −10dB, (b) SNR = −7dB, and (c) SNR = −5dB.
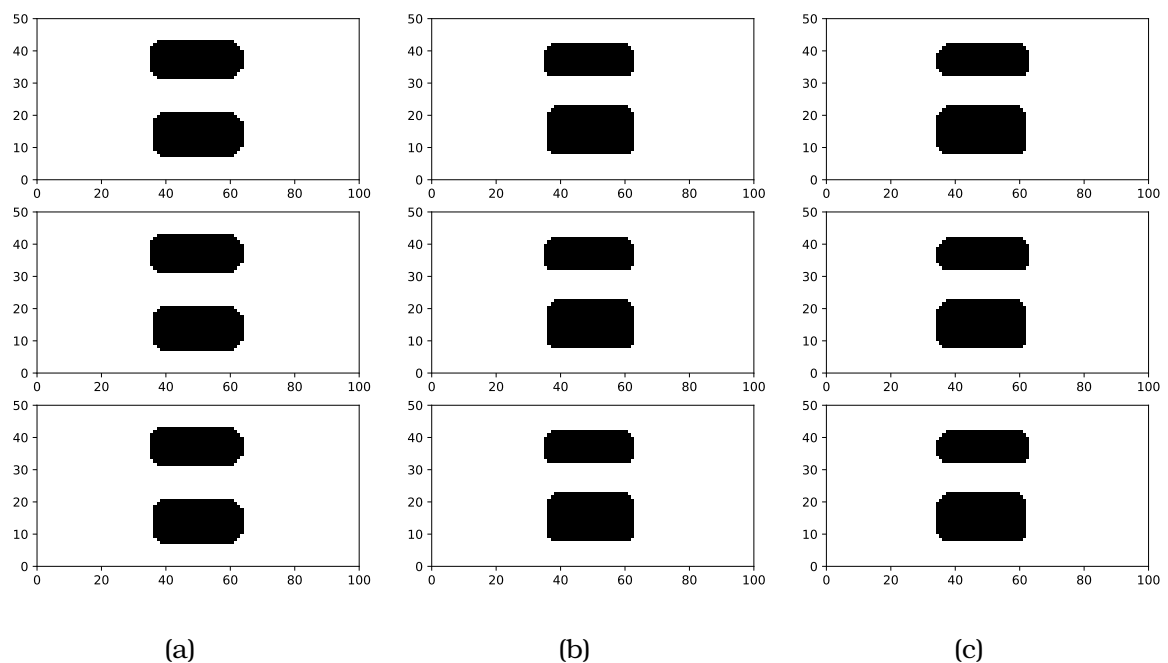
Figure 7.25: Performance of edge detection and flood fill after DL-ANN: (a) SNR = −10dB, (b) SNR = −7dB, and (c) SNR = −5dB.

(a)   (b)   (c)
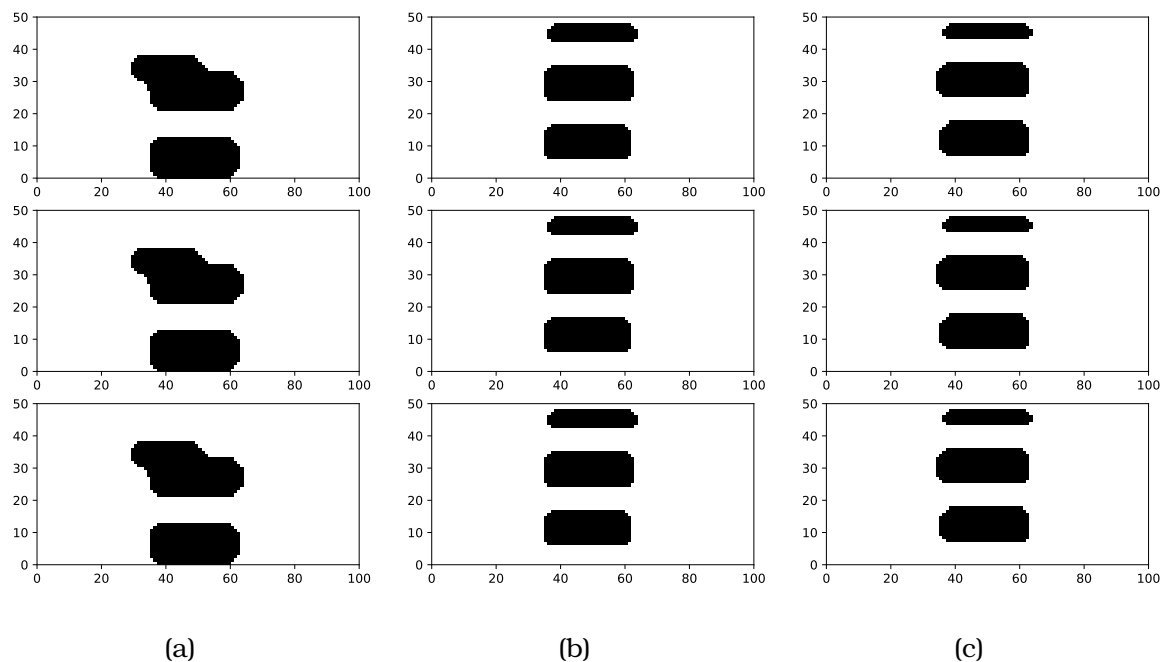
Figure 7.26: Performance of edge detection and flood fill both before and after DL-ANN: (a) SNR = −10dB, (b) SNR = −7dB, and (c) SNR = −5dB.

7.4.3 Experimental Validation

The results presented so far have been obtained based on software simulations. Simulations are a convenient and efficient way to explore the performance of the SAE approaches considered in this study under a broad range of operating conditions, however an experimental validation is required to provide a more convincing case showing the potential benefits that the proposed DL-ANN method can bring in a practical system implementation. Fig. 7.28 presents a comparison of the simulation and experimental performance results obtained for the DL-ANN model under the four considered training options, while Fig. 7.29 also includes the variants based on the combination with image processing techniques. As it can be appreciated, the obtained simulation results match very closely with their experimental counterparts, thus confirming the conclusions derived from the analysis presented above and corroborating the performance improvements that the proposed DL-ANN method for SAE can achieve in a practical system implementation. As it can be noticed, the proposed DL-ANN approach can provide significant SAE accuracy improvements compared to other SAE methods from the literature, in particular when considering the low SNR regime.
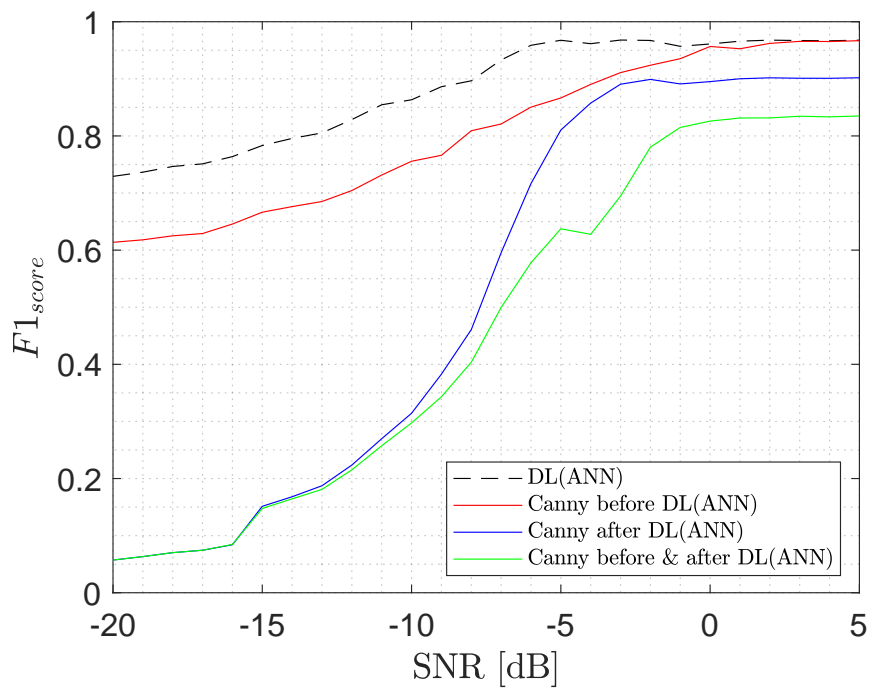
(a)
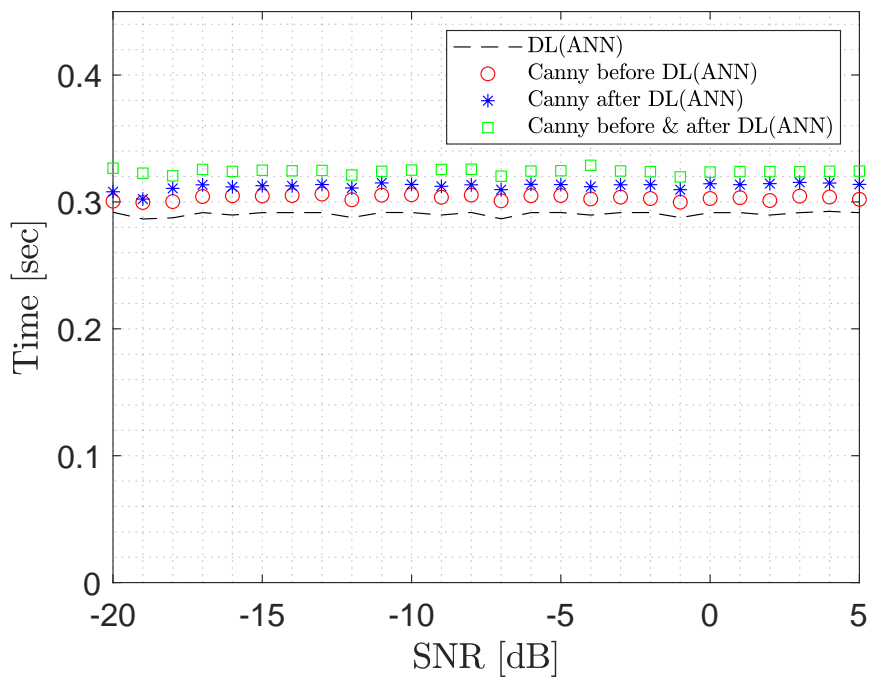
(b)

Figure 7.27: Performance of DL-ANN combined with edge detection and flood fill in terms of: (a) F1 score, and (b) computation time.

141

(a) Option 1

(b) Option 2
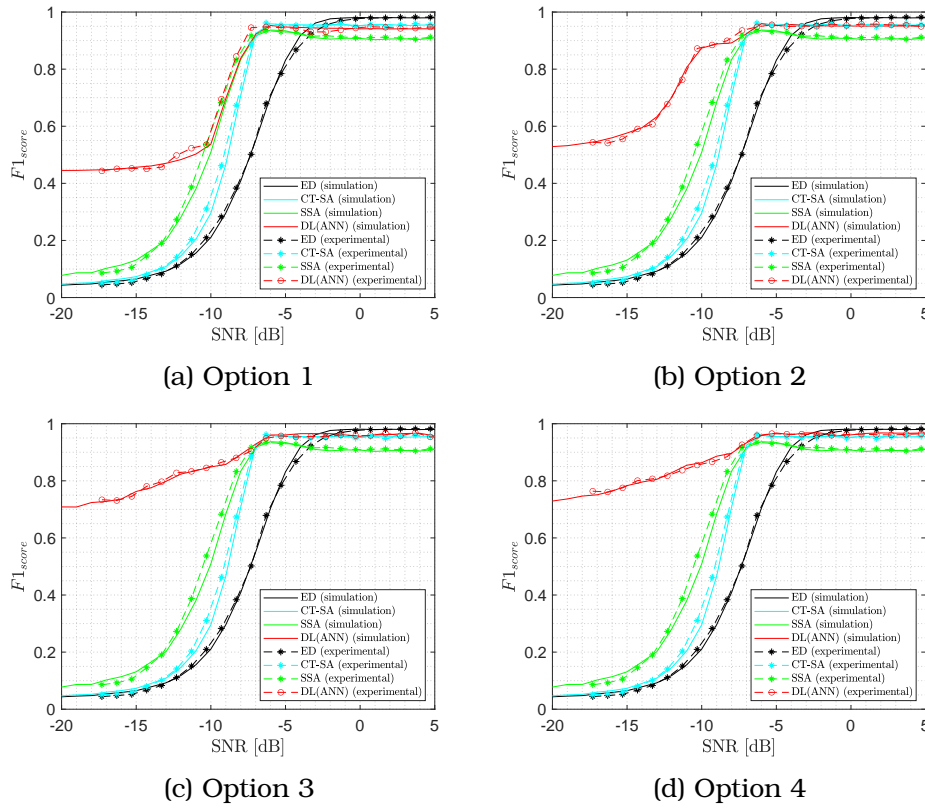
(c) Option 3

(d) Option 4

Figure 7.28: Experimental validation of the performance of the proposed DL-ANN method and the reference benchmark methods (ED, CT-SA, SSA) in terms of the F1 score as a function of the SNR for the four different training options considered in this chapter.
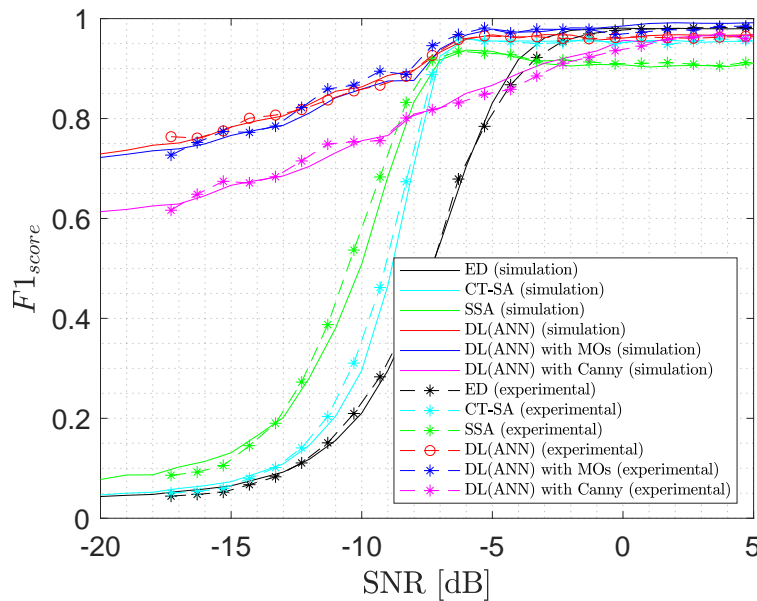
Figure 7.29: Experimental validation of the performance of the proposed DL-ANN method (including the variants based on image processing techniques) and the reference benchmark methods (ED, CT-SA, SSA) in terms of the F1 score as a function of the SNR (for option 3).

7.4.4   Comparison of All the Proposed SAE Methods

Before concluding this last technical chapter of the thesis, it is worth noting that the different SAE methods developed in this thesis have been compared to the same reference SAE methods (i.e., ED, CT-SA and SSA) in their respective chapters but they have not been compared among them. Such comparison is provided in this section.

Fig. 7.30 provides a comparison (in terms of the F1 score and computation time, as usual) of the best-performing configuration for each of the strategies developed in each chapter, including the MA algorithm proposed in Chapter 3, the MO-based SAE method proposed in Chapter 4, the SAE method based on Canny edge detection plus flood fill presented in Chapter 5, the HT-based SAE method developed in Chapter 6 and the DL-ANN model presented in this chapter. All methods are compared with the reference methods (ED, CT-SA and SSA), which are shown in the figure as well. The results in Fig. 7.30a show that the different SAE methods developed in this thesis based on image processing techniques can provide significant performance improvements in terms of SAE accuracy compared to the reference SAE methods available in the literature (ED, CT-SA and SSA), which confirms that image processing techniques are a promising approach to enhance the performance of SAE methods. The performance improvements are more noticeable in the low SNR regime, where most methods clearly outperform the reference methods, even though some of the proposed SAE strategies can effectively achieve a virtually perfect SAE accuracy (i.e., 100% F1 score) in the high SNR regime as well, something that none of the reference SAE methods is able to achieve. The general exception to this statement is the HT-based method, which performs well at high SNR (providing a similar accuracy as the existing methods) but performs poorly in the low SNR regime. However, notice that the HT-method was designed with the aim to automatically extract and provide the coordinates of each SA in the spectrogram (something for which SAE methods have usually not been designed) rather than to improve the overall SAE accuracy. It is particularly remarkable the extent to which DL-ANN method can dramatically increase the SAE accuracy in the low SNR regime comapred to any of the other SAE methods investigated in this research, which, as it can be appreciated in Fig. 7.30b, is obtained at the expense of a higher computational cost. This observation highlights the promising potential of DL techniques in the context of SAE methods and motivates further investigation towards this direction (a more detailed discussion of future research suggestions is provided in Chapter 8).

7.5   Summary

In this chapter, a technique for SAE has been proposed using Deep Learning based on Artificial Neural Network (DL-ANN) for enhanced extraction of SA information from radio spectrograms. The proposed DL-ANN method has shown overall an excellent performance over the whole range of SNR levels, with significant improvements in particular in the low SNR regime (e.g., 73% estimation accuracy at –20 dB SNR compared to 5–7% for reference methods from the literature). The performance when combined with image processing techniques has been explored as well. The obtained results have shown that the use of DL techniques in the context of SAE, such as the proposed DL-ANN model, can achieve excellent levels of SAE accuracy without the need

143
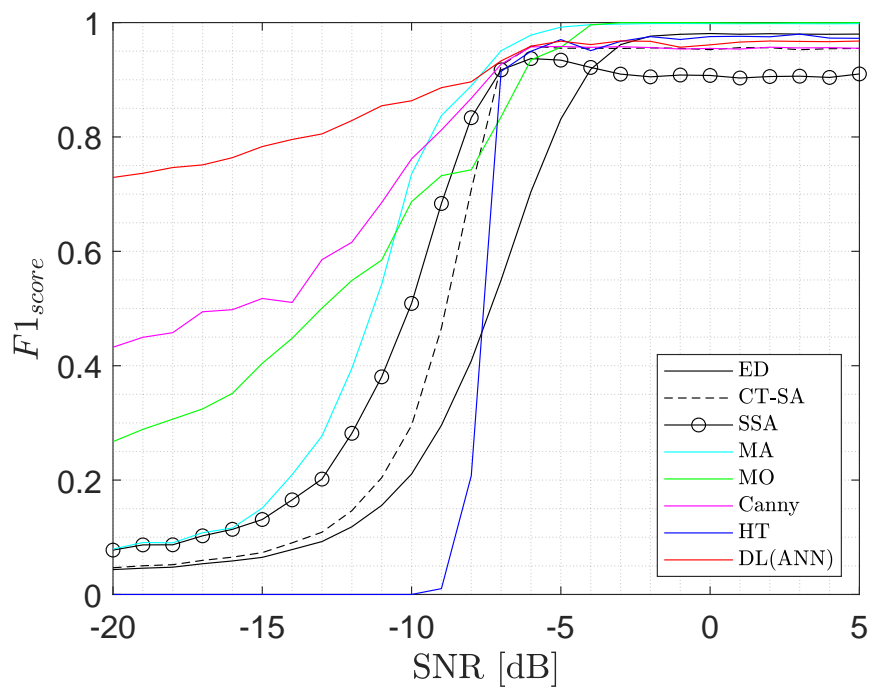
(a)
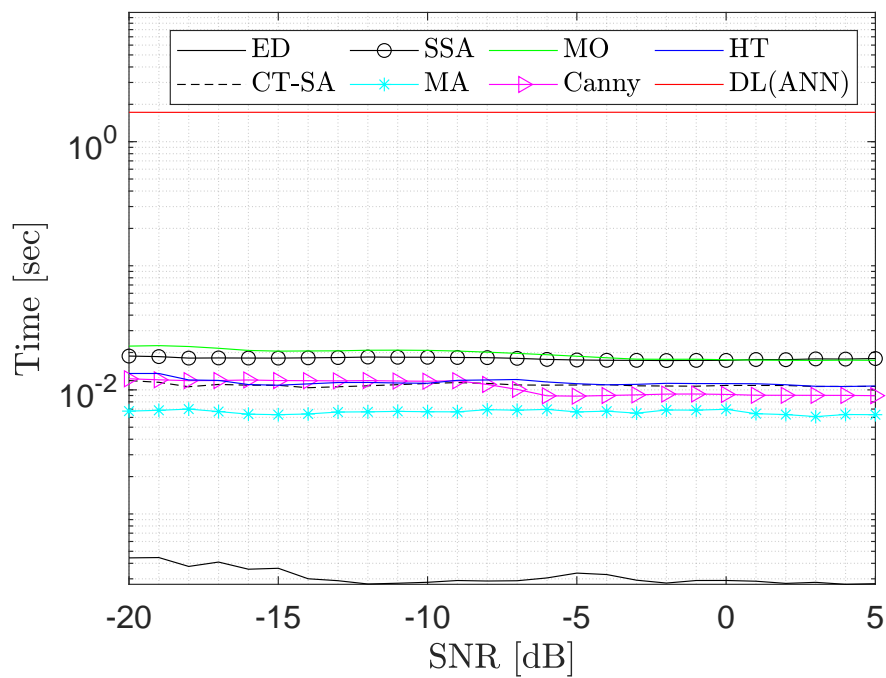
(b)

Figure 7.30: Performance comparison of the SAE methods developed in this thesis in terms of: (a) F1 score, and (b) computation time.

of assistance from image processing techniques, which in this particular case are of rather limited utility or, at best, provide very slight performance improvements in some cases. The obtained simulation results have been compared with experimental results obtained with a hardware platform specifically designed and implemented to this end, thus corroborating the performance improvements that the proposed DL-ANN method for SAE can achieve in a practical system implementation. It is also worth noting that, in addition to the significant SAE accuracy improvements compared to other SAE methods from the literature (in particular in the low SNR regime), a key feature of the proposed method is the capability to extract the location and dimensions of the detected SAs automatically. Overall, the proposed technique is a promising solution for SAE and the automatic processing of radio spectrograms in spectrum-aware systems.

Chapter 8

Conclusions and Future Work

8.1 Conclusions

In many practical application scenarios, radio communication signals are very frequently represented as spectrograms, which represent the received signal strength measured at multiple discrete time instants and frequency points within a specific time interval and frequency band, respectively. Radio spectrograms have been used for time-frequency signal analysis in spectrum-aware systems for many purposes. An important aspect in the processing of radio spectrograms is the region that each individual radio transmission or signal component occupies in the time-frequency domain within the spectrogram, which in this research is referred to as Signal Area (SA). The concept of SA precisely determines the occupied bandwidth and the start/end times of each individual radio transmission. The capability to obtain this information accurately from a radio spectrogram can be useful in many practical applications, including spectrum surveillance (both for enforcement of spectrum regulations and gathering of signal intelligence in military applications), radio signal interception and identification, electronic warfare and radio environment spectral awareness (for instance, in databases for spectrum sharing systems). Consequently, the process of Signal Area Estimation (SAE), which entails determining the subsets of spectrogram points that belong to one or more SAs, is an important function is spectrum-aware wireless communication systems. The process, however, is not trivial since the spectrum data observed by monitoring spectrum-aware systems is a degraded version of the transmitted signals after having suffered impairments introduced by radio propagation, the receiver's own noise and other external sources of unwanted noise and interference (e.g., out-of-band transmissions, ambient noise or man-made noise).

The interest of this research is on how to accurately determine the SAs present in a radio spectrogram obtained from empirical spectrum measurements based on the application of techniques from the field of image processing. Image processing techniques can be employed to this end by treating spectrograms as images, where each time-frequency point in the spectrogram is seen as an image pixel. This point of view converts the problem of SAE in a noisy spectrogram into the problem of recognising rectangular shapes in a noisy image, for which several image processing techniques can be employed. The unique characteristics of the SAE problem in radio spectrograms require a tailored research study. In this context, the main aim of this thesis has been to

explore the feasibility of using image processing techniques to enhance the accuracy of SAE, and to propose novel SAE methods based on image processing techniques. To this end, a broad range of relevant techniques from the field of image processing have been explored, including morphologic operations, edge detection and flood fill techniques, the Hough transform along with other heuristic methods and solutions based on deep learning techniques for the processing of images. The proposed methods have been evaluated both with software simulations and using an experimental hardware platform specifically built to this end. The obtained simulation and experimental results have shown that the methods proposed in this thesis can provide significant accuracy improvements compared to other SAE methods in the existing literature.

The outcomes and main findings of the comprehensive study presented in this thesis can be summarised as follows:

- Chapter 2 has presented a comparative study of the performance of existing SAE methods under different configuration parameters. The investigated SAE methods have included ED, CT-SA, and SSA. These methods have been investigated under different threshold selection methods that include CFAR, CSDR and MSER, and the performance under different time/frequency resolutions has been studied as well. The most appropriate configuration has been determined accordingly. The obtained results have indicated that the three considered SAE methods achieve their best accuracy when the decision threshold is selected according to the CFAR method (i.e., set for a fixed probability of false alarm), which also has the practical advantage that it only requires the noise power (and not the signal power or SNR) to be known. The best accuracy over the whole range of SNR values has been provided by the SSA method with a decision threshold set based on the CFAR criterion. It has also been observed that the accuracy of the ED and CT-SA methods is mainly affected by the SNR and remains unaffected by the employed grid resolution. However, in the case of the SSA method, the accuracy is also affected by the spectrogram resolution. Interestingly, for the SSA method, a degradation in the accuracy of the estimated SA as a result of a reduced SNR can be compensated (at least to some extent) by selecting the optimum spectrogram resolution for each SNR value, which provides an additional degree of freedom in the configuration and optimisation of the SSA method. This study has filled the gap created by the lack of comparative research to show how the configuration of different methods affects their relative performance, and has provided useful insights into the optimum design and configuration of SAE methods.

- Chapter 3 has proposed a novel SAE technique based on a minesweeper algorithm (MA), which can be seen as a kind of morphological operation and therefore as a first attempt to apply image processing principles to SAE. The proposed method processes each tile in the time-frequency matrix (spectrogram) where the SA is to be detected to determine the most likely state (busy/idle) based on the number of busy tiles around it. Two variants have been proposed, one based on a simple thresholding principle where the number of busy tiles around a central tile is compared to a threshold to decide the central tile state, and a more sophisticated one where the actual pattern of idle/busy states around the central tile (and not only the number of busy tiles) is taken into account to make the final decision

148

based on the matching of some templates/patterns with the input spectrogram. The obtained results have shown that the second variant does not produce significant alterations to the input spectrogram and therefore its application provides no benefit. However, the first proposed variant based on thresholding can provide noticeable performance improvements at a low computational cost. The impact of introducing several iterations has also been investigated, showing that a single iteration is enough to provide the achievable performance improvement without introducing unnecessarily increased computational cost. The proposed method can be employed both as a standalone SAE method as well as a pre/post-processing technique for other SAE methods (to correct sensing errors or errors introduced by the other method itself). When used as a standalone SAE method it can provide similar or even slightly better accuracy than other methods at a much lower computational cost. However, the best performance improvement is obtained when used as a pre/post-processing technique in combination with other existing methods (such as CT-SA and SSA), without increasing significantly the computation cost. The proposed MA method has a low complexity and therefore does not increase significantly the computational cost of existing SAE methods while providing noticeable accuracy improvements when combined with them.

- Chapter 4 has explored the applicability of morphological opeations (MOs) from the field of image processing in the context of SAE, analysing their individual impacts when applied both as standalone SAE methods and as pre/post-processing techniques to other existing SAE methods (such as CT-SA and SSA). Based on the outcomes of this study, a suitable MO-based SAE method has been formulated, which employs MOs as pre/post-processing techniques to other existing SAE methods. The obtained results have demonstrated that the application of carefully selected and properly configured MOs for each SNR regime can provide significant accuracy improvements both at low SNR (with gains of up to 40%) and high SNR (reaching 100% accuracy levels). These operations, when used properly, can reduce false alarms and fill gaps within the original SAs, which facilitates and simplifies the task of detecting SAs for both CT-SA and SSA. As a result, the proposed MO-based SAE method can help existing SAE methods provide a significantly more accurate estimation of the existing SAs without increasing, and in some cases even reducing, their computational cost.

- Chapter 5 has provided an exhaustive analysis on the suitability of common edge detection techniques to the problem of SAE, including gradient-based methods, the Laplacian of Gaussian method, and the Canny method. Edge detection has been used to find the most likely edges of SAs. Once these boundaries are determined, a flood fill algorithm has been employed to fill the space within the detects edges in order to produce solid objects (i.e., final detected SAs). By means of simulations, the consequence of applying different edge detectors to SAE have been investigated under a broad range of configuration parameters for each edge detector, and the accuracy of edge detection plus flood fill has been explored when used both as a standalone SAE method and as a pre/post-processing stage combined with other existing SAE methods from the literature. Moreover, a suitable SAE strategy has been formulated for each edge detection method. The

obtained results have shown that the proposed SAE approach based on edge detection plus flood fill can improve significantly the performance of existing SAE methods in the lower SNR range when used as a pre/post-processing step (with respect to the case where the other SAE methods are used alone), thus effectively extending their operational SNR range, and without having a significant impact on the overall computational cost.

- Chapter 6 has explored the usability of the Hough transform (HT) in the context of SAE and has proposed two approaches that exploit the HT to estimate SAs in a spectrogram. The main interest of the proposed methods, and a distinguishing feature with respect to most other methods proposed in the literature, is their ability to automatically extract the parameters of each SA (i.e., the coordinates of the vertical and horizontal lines containing each SA). Most of the previously proposed SAE methods produce enhanced spectrograms where the present SAs can be appreciated more accurately, however have not typically been designed to automatically provide the coordinates and dimensions of each SA. On the other hand, the HT-based methods proposed in this chapter can provide not only an enhanced spectrogram but also the coordinates and dimensions for each of the SAs detected in such spectrogram. This feature can be extremely useful in the automatic processing of radio spectrograms, for instance in the context of autonomous spectrum-aware wireless and mobile communication systems.

- Chapter 7 has proposed a technique for SAE using Deep Learning based on Artificial Neural Network (DL-ANN). The proposed DL-ANN method has shown overall an excellent performance over the whole range of SNR levels, with significant improvements in particular in the low SNR regime (e.g., 73% estimation accuracy at –20 dB SNR compared to 5–7% for reference methods from the literature). The performance when combined with image processing techniques has been explored as well. The obtained results have shown that the use of DL techniques in the context of SAE, such as the proposed DL-ANN model, can achieve excellent levels of SAE accuracy without the need of assistance from image processing techniques, which in this particular case are of rather limited utility or, at best, provide very slight performance improvements in some cases. It is also worth noting that, in addition to the significant SAE accuracy improvements compared to other SAE methods from the literature (in particular in the low SNR regime), a key feature of the proposed method is the capability to extract the location and dimensions of the detected SAs automatically. Overall, the proposed technique is a promising solution for SAE and the automatic processing of radio spectrograms in spectrum-aware systems.

It is worth noting that some of the SAE methods developed in this thesis decide the optimum procedure to be followed based on the SNR of the signal whose area is to be detected and estimated. In practical system implementations, this information may or may not be available depending on a broad range of technical and practical aspects. Several options can be proposed when the SNR information is not available and cannot be estimated directly by the spectrum monitoring receiver. In some cases it may be possible to make an educated guess of the expected SNR; for instance, if

the transmitter location is known and its transmission power is constant and known (or can be estimated), then the use of a suitable path loss model can give a good approximation to the expected SNR (or expected range of SNR values if the transmission power is variable). Note that, in general, the SNR does not need to be known or estimated to a great level of accuracy since the relevant aspect is whether the SNR is greater or lower than certain SNR thresholds. In a worst-case scenario where nothing is known about the signals that may be present, the solution would be to apply the procedures proposed for each individual SNR range and select the output with the highest response. This approach increases the chances of a more accurate result for completely unknown signals at the expense of an increased computational cost.

8.2   Future Work

The research undertaken as part of this dissertation offers up new ideas for future works and generates novel concepts for prospective future studies. The discussion that follows indicates some potential areas for furthering the research conducted in this dissertation along with some of the lessons learned in this work and how it can be exploited and applied to generate further knowledge.

The main motivation of this research has been to explore the use of image processing techniques to address the problem of SAE. A broad range of different techniques have been considered and their applicability has been explored. However, there are still other image processing techniques that can be considered for enhanced SAE in spectrum-aware systems, mainly concentrating on refining the suggested solutions through additional image processing techniques. For instance, blob detection methods can be very promising techniques. A blob is in general defined as a region in a digital image that differs from surrounding regions in properties such as their size, shape, brightness or colour. In images, to generalise, a blob is a collection of pixel values that form a relative colony or a large object that is distinct from its background. Blob detection methods can potentially be exploited for SAE. By altering the scale parameter, blobs (i.e., SAs) of any size may be extracted. By using blob detection methods, a number of properties are retrieved in addition to the blob's centre point and boundaries. These go into further depth about the unique blob features, allowing for a future categorisation of blobs [101]. Moreover, it may be interesting to investigate many techniques for rectangular blob (i.e., SA) identification, including the Laplacian of Gaussian (LoG), Difference of Gaussian (DOG), and Determinant of Hessian (DOH), which are able to observe how related components may make blob recognition much easier and separate the blobs visible in the image using area props [102]. Future work should materialise this concept into a specific algorithm and evaluate its performance.

Additionally, other advanced image processing techniques may be explored as well. Future work should investigate the integration of multiple image processing methods in light of the wide variety of signal types and characteristics as well as the increasing complexity of wireless communication systems. The blend of morphologic tasks, edge locations, flood fill strategies, and profound learning approaches investigated in the postulation can be additionally improved and tweaked for explicit signal sorts and situations. It should be possible to develop SAE methods that are more robust and adaptable by combining the strengths of various methods and developing hybrid approaches. An

important lesson learned in this research is that image processing techniques that are known for certain performance characteristics when applied to general digital images may not perform in the same way when applied to spectrograms (interpreted as images). This should also be carefully taken into account when considering the integration of multiple image processing techniques into hybrid approaches, in particular possible interactions between different techniques when combined together.

It is also important to remember that this thesis has assumed a rectangular shape for the signal areas and a binary image representation. Nonetheless, in common situations, there might be cases where the signal area region does not adjust to a rectangular shape. Some wireless technologies will not operate at a constant carrier frequency and/or with a constant signal bandwidth and, as a result, the resulting signal area in a spectrogram will not be perfectly rectangular. Some examples of this case include analogue signals based on frequency modulation (where the carrier frequency is constant but the signal bandwidth is variable) and wireless systems based on frequency hopping (where the signal bandwidth is usually constant but the carrier frequency changes over time according to a predefined hopping pattern). Chirped spread spectrum signals such as those generated by LoRa systems represent another example of such kind. Even though the rectangular signal area model considered in this work is believed to work in these cases (with some specific considerations discussed in the thesis), future examinations should focus on investigating strategies that can successfully deal with non-rectangular signal regions. It would be beneficial for future research to develop techniques that precisely identify and estimate these irregular areas. Additionally, the subtleties of the signal's power levels may not be captured using a binary image representation (black and white) to distinguish between the busy and idle states as considered in this research. Understanding the intensity and more subtle characteristics of the signal area requires power level information. Future research should investigate methods that incorporate power-level information into the estimation process to overcome this limitation. This might necessitate the creation of image-processing algorithms capable of analysing and representing signal areas in response to various power levels or gradients. The estimation accuracy and granularity can be significantly enhanced by incorporating power-level information.

A promising tool to tackle the above challenges is deep learning, which in this work has been shown to provide a high potential for very accurate signal area estimations, even though this work has considered a simple Multi-Layer Perceptron (MLP) network, which is one of the most basic and often used variants of Artificial Neural Networks (ANNs). Other more sophisticated neural network models, such as Convolution Neural Network (CNN), Recurrent Neural Network (RNN), Long-Short Term Memory (LSTM) networks offer additional capabilities that would be interesting to explore in order to determine whether a better performance can be proven when using such ANNs for SAE. In this context, this thesis has taken a first step towards this direction by exploring for the first time the application of neural networks to resolve the problem of signal area estimation. The obtained results are promising and this should motivate a much more detailed exploration of other deep learning networks (e.g., deep morphological neural networks) and associated techniques.

Moreover, a wider variety of real-world scenarios and radio propagation environments should be included in the evaluation of the proposed methods. Experiments

and simulations based on a variety of wireless communication scenarios, including various signal types, varying signal strengths, interference conditions, and environmental factors, would be required for this. By assessing the strategies under these different circumstances, a more far-reaching comprehension of their exhibition and limits can be accomplished, upgrading the viable relevance of the exploration results. The evaluation of signal area estimation methods in a more realistic scenario where the experimental radio receiver (e.g., a spectrum analyser or software-defined radio) is fetched measurements from actual radio signals generated by commercial radio communication systems and received through a real radio propagation channel would be highly desirable for a more practical and realistic implementation and demonstration of the investigated SAE techniques. However, this also introduces the challenging problem of requiring some form of control (or at least, information) on the actual signals transmitted by the wireless transmitters so that the received/detected information can be compared to some ground truth information for assessment of the SAE accuracy. Having this kind of access in a commercial system faces many important challenges (not only technical, but also administrative and regulatory) which may not be possible to overcome in reality but that will be considered for future work and explored if and where possible. Some spectrum regulators (including the United Kingdom) provide temporary and relatively inexpensive spectrum licenses to access specific bands for wireless experimentation, which could be a possible way to further test the proposed SAE methods investigated in this thesis. The use of already available online databases of empirical radio communication signals that provide the required information could also be another feasible alternative. These options for further experimental evaluation will be considered in the future. In any case, there is no doubt that it is crucial to assess the success of the suggested solutions in more realistic circumstances in order to further increase their applicability and realism. In order to better understand how the SAE approaches function in real-world settings, studies may be carried out utilising commercial equipment and authentic radio propagation channels. It is equally crucial to realise the difficulties in gaining access to the actual wireless transmitter signals itself as well as the legal considerations that control this access. It may be possible to test and evaluate the suggested SAE methodologies using alternative means, such as getting temporary spectrum licenses for wireless experimentation or using internet databases of empirical radio communication signals.

Reflecting on this research experience, there are a number of things that, if done over, may be tackled differently. To find further viable strategies for improving SAE accuracy, for instance, more investigation of various image processing techniques might be made. To create more reliable and thorough SAE approaches, it may also be thought to investigate more relevant deep learning techniques and combine several methodologies. Additionally, broadening the examination of the suggested approaches in a variety of real-world situations and radio propagation conditions may offer insightful information about how well they function. The generalisability and robustness of the suggested SAE methodologies might be further tested by including a wider variety of measurement situations.

Along with these technological developments, it is essential to investigate the practical applications of these solutions in particular use cases in order to close the gap between theoretical developments and actual implementations. The capability to obtain

signal area information accurately from a radio spectrogram can be useful in many practical applications, including spectrum surveillance (both for enforcement of spectrum regulations and gathering of signal intelligence in military applications), radio signal interception and identification, electronic warfare and radio environment spectral awareness (for instance, in databases for spectrum sharing systems). Spectrum management and enforcement are one possible use case that might tremendously benefit from spectrum surveillance. Effective use of the available spectrum is essential given the rising demand for wireless communication services. Regulatory agencies and spectrum managers may learn a great deal about the patterns of usage, occupant density and interference levels across the spectrum by using spectrum surveillance techniques like the proposed spectrum-aware approaches. This information can help with more efficient spectrum allocation, interference mitigation, and regulatory policy enforcement, which will lead to enhanced quality of service and optimised spectrum utilisation for a variety of wireless applications. Furthermore, in cognitive radio networks, radio environment spectral awareness, made possible by cutting-edge image processing methods and artificial neural networks (ANNs), might be extremely important for spectrum sharing. Cognitive radios are designed to opportunistically employ underutilised spectrum bands without interfering with other users. Cognitive radios may learn about the spectral environment in real-time, detecting possibilities for available spectrum, and dynamically modifying their broadcast settings in response. This adaptive behaviour boosts the effectiveness of spectrum sharing, reduces interference, and maximises total spectrum utilisation, providing enhanced performance and flexibility in cognitive radio networks. All this can be enabled by spectrum-aware image processing-based algorithms and ANNs.

The challenges associated with non-rectangular signal areas, the incorporation of power level information, the integration of multiple image processing techniques, and the execution of evaluations in a variety of real-world scenarios ought to be the primary areas of focus for future work in the area of enhanced signal area estimation for spectrum-aware systems based on image processing techniques. The research can make significant progress in accurately estimating signal areas by focusing on these aspects. This will make it possible for wireless communication systems to manage and use spectrum more efficiently. Nonetheless, the current research is a significant addition to the body of knowledge on this subject. This research presents novel approaches that make use of image-processing techniques to improve the precision and efficacy of signal area estimation in radio spectrograms. While previous research has looked into a variety of approaches for estimating signal area, this study introduces new ones. By regarding spectrograms as pictures and applying customised picture handling calculations, this exploration gives important experiences into perceiving and removing signal regions from noisy spectrograms. The proposed strategies are assessed utilising both programming recreations and a trial equipment stage, showing critical precision enhancements contrasted with existing methods. This examination fills a significant hole by offering reasonable and successful answers for signal region assessment, giving an establishment to additional headways in a range of mindful frameworks along with their applications.

In conclusion, future works based on this research should further explore the practical implementations of the suggested solutions in particular use cases rather than just

concentrating on technical developments like additional image processing techniques and realistic assessments. Spectrum monitoring may boost spectrum management and enforcement, and radio environment spectral awareness can boost spectrum sharing in cognitive radio networks, resulting in enhanced wireless communication services and optimised spectrum utilisation.

Finding the answers to these questions still requires a substantial research effort.

Appendix A

Evaluation of the Computational Cost and Complexity

The main aspect considered in the performance evaluation of Signal Area Estimation (SAE) methods in this thesis is the accuracy of the estimated Signal Areas (SAs). However while estimation accuracy is the main and most relevant performance parameter to consider, the computational cost of each SAE method is also a relevant aspect to take into account that cannot be ignored. This is because SAE methods that provide a better accuracy will usually do so at the expense of an increased computational cost. Moreover, the computational cost is also important because it affects the overall performance of the SAE method when it is implemented in a practical system.

In this thesis, the computational cost of SAE methods has been evaluated in terms of the computation time required to run each SAE method on a computer processor. The performance of different SAE methods is therefore compared in terms of their absolute computation times, averaged over a sufficiently large number of repetitions in order to remove any random fluctuations in the resulting computation time (such random fluctuations may be caused by the operating system and other platform-specific aspects). After having considered various metrics to evaluate computational cost, evaluating the computation time following this approach is deemed to be the most convenient and appropriate (and probably the only viable) approach to compare the computational cost of various SAE methods. Evaluating complexity by means of other metrics faces several important problems and limitations, which are discussed below to justify the choice of the computation time as a metric of computational cost.

First, the heterogeneity of SAE methods available in the literature and considered in this research makes it difficult to adopt a common definition of computational cost or complexity that is applicable in all cases for a fair comparison. This is indeed a challenge for neural networks alone since, in general, there is no single, well-established and agreed way to quantify the computational complexity of a neural network (this is in fact an active area of discussion and research, see for example [103]). The big-O mathematical notation has become a very popular tool to analyse and characterise the computational complexity of algorithms in Computer Science, however even such metric has important disadvantages in this case. In feed forward neural networks with backpropagation as the one considered in this work, the asymptotic complexity of the forward/back-propagation procedures could be found by analysing the dimensions of

the network and the operations performed at each layer (e.g., matrix multiplication and evaluation of activation function, etc.). The learning phase (backpropagation) is in general slower than the inference phase (forward propagation), and this is even more pronounced by the fact that gradient descent often has to be repeated many times. This results in a large constant factor that has real world consequences, but which big-O notation (i.e., the traditional notation used to represent computational complexity) does not show. However, it can be captured by the actual computation time when timed in an actual processor. For other SAE methods (based on any principle, not necessarily neural networks), the determination of the computational complexity may not always be possible, or at least not in a straightforward manner. An example of this is the SSA method that this work uses as a reference. Such method performs an iterative process to estimate the width of each individual signal area, followed by another iterative process to provide a coarse estimation of the height of each signal area and a final iterative process to provide a fine estimation of the height of each signal area. The number of iterations required in each of these three processes depends on the signal area itself and its dimensions, which makes the total number of iterations dependent on the actual signal area properties. Therefore, for the same spectrogram size, different computation times can be obtained depending on the number of signal areas present in the spectrogram and the properties of each of them. Trying to represent this with big-O notation would be difficult without making significant assumptions and simplifications of the actual algorithm and the input data as well, while it is straightforwardly and more accurately quantified by means of actual processor time required for its evaluation (if appropriately measured and averaged over a sufficiently large number of Monte Carlo snapshots as it has been done in this work).

It is also worth noting that the big-O notation is, by definition, a description of how the time complexity of an algorithm increases with the size of its input data. In the context of SAE methods, big-O notation would effectively describe how the total computation time of a SAE method increases as the size of the input spectrogram is made larger. In other words, big-O notation is a measure of *scalability*, which may not be appropriate in practical scenarios, where the actual size of empirical spectrograms will usually be fixed for a specific application scenario. This description of computational cost or complexity, while very common and suitable to many problems in Computer Science (where such notation originated) with variable input data sizes, may not necessarily be the most suitable one for the practical evaluation of SAE methods. Moreover, there are practical aspects in a real system implementation that affect the total time complexity (computation time) that this theoretical metric cannot capture, but that are implicitly included in any experimental measurement of the computation time as considered in this research. When looking at other options that could be suitable to evaluate the computational cost of SAE methods, it becomes apparent that other alternatives are limited to metrics that are part of the family of mathematical notations that is collectivelly known as *Bachmann–Landau notation* or *asymptotic notation* (to which big-O notation belongs). However, such alternatives are based on similar fundamental principles as the big-O notation and therefore suffer from the same drawbacks and limitations. As a result, it is difficult to find other suitable metrics, besides the experimental computation time, that can be used to evaluate and compare the performance of different SAE methods in a fair and meaningful manner.

The discussion above explains why the evaluation of computational complexity in traditional sense (represented in big-O notation or other similar related notations) would be difficult and would hardly provide a fair comparison at all when evaluating and comparing different SAE methods. In fact, as it can be confirmed from previous work available in the literature, such type of quantification of the computational complexity is extremely unusual in the context of SAE (if used at all – in fact, no precedent of using big-O notation or similar complexity analysis tools can be found in the literature of SAE methods). To the best of the author's knowledge, previous work has relied on absolute computation time (i.e., the execution time as measured in a real processor) as a way to quantify and compare the computational cost of various SAE methods and this is the approach that has been followed in this research as well. It is therefore believed that the computation time, despite its potential practical limitations, provides overall a representative, realistic and fair comparison of the real computational cost of different SAE methods and it is the most convenient (and perhaps the only feasible) metric for comparison of the computational cost of SAE methods.

Bibliography

[1] F. R. P. Cavalcanti and S. Andersson, *Optimizing wireless communication systems*. Springer, Boston, MA, Jan. 2009, vol. 386.

[2] T. Seymour, A. Shaheen *et al.*, "History of wireless communication," *Review of Business Information Systems (RBIS)*, vol. 15, no. 2, pp. 37–42, Apr. 2011.

[3] J. Zander, "Trends in resource management future wireless networks," in *2000 IEEE Wireless Communications and Networking Conference. Conference Record (Cat. No.00TH8540)*, vol. 1, Aug. 2000, pp. 159–163.

[4] I. Selinis, K. Katsaros, M. Allayioti, S. Vahid, and R. Tafazolli, "The race to 5G Era; LTE and Wi-Fi," *IEEE Access*, vol. 6, pp. 56 598–56 636, Oct. 2018.

[5] P. Leaves, K. Moessner, R. Tafazolli, D. Grandblaise, D. Bourse, R. Tonjes, and M. Breveglieri, "Dynamic spectrum allocation in composite reconfigurable wireless networks," *IEEE Communications Magazine*, vol. 42, no. 5, pp. 72–81, Jun. 2004.

[6] S. M. Baby and M. James, "A comparative study on various spectrum sharing techniques," *Procedia Technology*, vol. 25, pp. 613–620, Dec. 2016.

[7] C. Xin, P. Paul, M. Song, and Q. Gu, "On dynamic spectrum allocation in geo-location spectrum sharing systems," *IEEE Transactions on Mobile Computing*, vol. 18, no. 4, pp. 923–933, Apr. 2019.

[8] S. Chatzinotas, B. Ottersten, and R. De Gaudenzi, *Cooperative and cognitive satellite systems*. Academic Press, Mar. 2015.

[9] H. Arslan and T. Yücek, "Spectrum sensing for cognitive radio applications," in *Cognitive radio, software defined radio, and adaptive wireless systems*, H. Arslan, Ed. Dordrecht: Springer, 2007, pp. 263–289. [Online]. Available: https://doi.org/10.1007/978-1-4020-5542-3_9

[10] M. Subhedar and G. Birajdar, "Spectrum sensing techniques in cognitive radio networks: A survey," *International Journal of Next-Generation Networks*, vol. 3, no. 2, pp. 37–51, Jul. 2011.

[11] R. Mizuchi, K. Umebayashi, J. J. Lehtomaki, and M. López-Benítez, "A study on false alarm cancellation for spectrum usage measurements," in *Proc. IEEE Wireless Commun. and Networking Conf. (WCNC 2017), 3rd Int'l. Works. Smart Spectrum (IWSS 2017)*. IEEE, Mar. 2017, pp. 1–6.

[12] K. Umebayashi, H. Iwata, J. J. Lehtomäki, and M. López-Benítez, "Study on simple signal area estimation for efficient spectrum measurements," in *2017 European Conference on Networks and Communications (EuCNC 2017)*. IEEE, Jun. 2017, pp. 1–5.

[13] M. López Benítez and F. J. Casadevall Palacio, "Spectrum occupancy in realistic scenarios and duty cycle model for cognitive radio," *Advances in Electronics and Telecommunications, Special Issue on Radio Communication Series: Recent Advances and Future Trends in Wireless Communication*, vol. 1, no. 1, pp. 1–9, Apr. 2010. [Online]. Available: http://hdl.handle.net/2117/8139

[14] A. Garhwal and P. P. Bhattacharya, "A survey on dynamic spectrum access techniques for cognitive radio," *arXiv preprint arXiv:1201.1964*, vol. 3, no. 4, Dec. 2011.

[15] H. Rohling, "Radar cfar thresholding in clutter and multiple target situations," *IEEE Transactions on Aerospace and Electronic Systems*, vol. AES-19, no. 4, pp. 608–621, 1983.

[16] K. Y. Sohn and Y. O. Park, "Method for transmitting and receiving random access channel signal in wireless communication system," Jun. 30 2016, uS Patent App. 14/949,168.

[17] E. N. Skomal, *Man-made radio noise*. Van Nostrand Reinhold, 1978.

[18] R. J. Matheson, "Measurements of electromagnetic noise radiated from automotive ignition systems," National Telecommunications and Information Administration (NTIA), Tech. Rep. 80–54, Nov. 1980.

[19] A. D. Spaulding and R. T. Disney, "Man-made radio noise, part 1: Estimates for business, residential, and rural areas," Office of Telecommunications (OT), Tech. Rep. 74–38, Jun. 1974.

[20] R. J. Achatz and R. A. Dalke, "Man-made noise power measurements at VHF and UHF frequencies," National Telecommunications and Information Administration (NTIA), Tech. Rep. 02-390, Dec. 2001.

[21] R. Dalke, R. Achatz, Y. Lo, P. Papazian, and G. Hufford, "Measurement and analysis of man-made noise in VHF and UHF bands," in *Proceedings of 1997 Wireless Communications Conference*. IEEE, Aug. 1997, pp. 229–233.

[22] P. Constantinou, D. Apostolakis, and M. Katsikis, "Man made noise measurements," in *Proc. 41st IEEE Vehicular Technology Conf. (VTC 1991)*. IEEE, May 1991, pp. 475–476.

[23] A. Krishnakumar and P. Krishnan, "On the accuracy of signal strength-based estimation techniques," in *Proceedings IEEE 24th Annual Joint Conference of the IEEE Computer and Communications Societies.*, vol. 1. IEEE, Mar. 2005, pp. 642–650.

[24] C. Hory, N. Martin, and A. Chehikian, "Spectrogram segmentation by means of statistical features for non-stationary signal interpretation," *IEEE Transactions on Signal Processing*, vol. 50, no. 12, pp. 2915–2925, Dec. 2002.

[25] C. Smith, Q. R. Black, and M. Magee, "Computer vision for improved single-sensor spectrum sensing," in *Proc. Sensor Signal Processing for Defence (SSPD 2012)*. IET, Sep. 2012, pp. 1–5.

[26] S. Phonsri, S. S. Mukherjee, and M. Sellathurai, "Computer vision and bi-directional neural network for extraction of communications signal from noisy spectrogram," in *Proc. IEEE Conf. Antenna Measurements and Applications (CAMA 2015)*. IEEE, Dec. 2015, pp. 1–4.

[27] X. Zha, H. Peng, X. Qin, G. Li, and S. Yang, "A deep learning framework for signal detection and modulation classification," *Sensors*, vol. 19, no. 18, pp. 1–21, Sep. 2019.

[28] W. Liu, D. Anguelov, D. Erhan, C. Szegedy, S. Reed, C.-Y. Fu, and A. C. Berg, "SSD: single shot multibox detector," in *Proc. 14th European Conf. Computer Vision (ECCV 2016)*. Springer, Oct. 2016, pp. 21–37.

[29] W. Li, K. Wang, and L. You, "A deep convolutional network for multitype signal detection and classification in spectrogram," *Mathematical Problems in Engineering*, vol. 2020, pp. 1–16, Sep. 2020.

[30] Y. Zhou, Y. Feng, V. Tarokh, V. Gintautas, J. McClelland, and D. Garagic, "Multi-level mean-shift clustering for single-channel radio frequency signal separation," in *Proc. IEEE 29th Int'l. Works. Machine Learning for Signal Processing (MLSP 2019)*. IEEE, Oct. 2019, pp. 1–6.

[31] J. Kokkoniemi and J. Lehtomäki, "Spectrum occupancy measurements and analysis methods on the 2.45 GHz ISM band," in *2012 7th international ICST conference on cognitive radio oriented wireless networks and communications (CROWNCOM)*. IEEE, Jun. 2012, pp. 285–290.

[32] K. Umebayashi, K. Moriwaki, R. Mizuchi, H. Iwata, S. Tiiro, J. J. Lehtomäki, M. López-Benítez, and Y. Suzuki, "Simple primary user signal area estimation for spectrum measurement," *IEICE Transactions on Communications*, vol. E99-B, no. 2, pp. 523–532, Feb. 2016.

[33] R. Mizuchi, K. Umebayashi, J. J. Lehtomaki, and M. López-Benítez, "A study on FFT-ED based signal area estimation for spectrum awareness (short range wireless communications)," *IEICE technical report*, vol. 116, no. 29, SR2016-9, pp. 27–34, May 2016. [Online]. Available: https://ci.nii.ac.jp/naid/40020849217/en

[34] M. López-Benítez and J. Lehtomäki, "Energy detection based estimation of primary channel occupancy rate in cognitive radio," in *2016 IEEE Wireless Communications and Networking Conference Workshops (WCNCW)*. IEEE, Aug. 2016, pp. 355–360.

[35] L. D. Stefano and A. Bulgarelli, "A simple and efficient connected components labeling algorithm," in *Proc. 10th Int'l. Conf. Image Analysis and Processing (ICIAP 1999)*. IEEE, Sep. 1999, pp. 1–6.

[36] D. W. Capson, "Performance comparisons of contour extraction algorithms," *IEEE Trans. Instrum. and Measurement*, vol. IM-35, no. 4, pp. 409–417, Dec. 1986.

[37] F. Cao, Y. Gousseau, P. Muse, F. Sur, and J.-M. Morel, "Accurate estimates of false alarm number in shape recognition," *Cachan, France (http://www. cmla. ens-cachan. fr/Cmla/), Tech. Rep*, Jan. 2004.

[38] X. Han, L. Xue, F. Shao, and Y. Xu, "A power spectrum maps estimation algorithm based on generative adversarial networks for underlay cognitive radio networks," *Sensors*, vol. 20, no. 1, p. 311, Jan. 2020. [Online]. Available: https://www.mdpi.com/1424-8220/20/1/311

[39] J. Li, X. Cui, H. Song, Z. Li, and J. Liu, "Threshold selection method for UWB TOA estimation based on wavelet decomposition and kurtosis analysis," *EURASIP Journal on Wireless Communications and Networking*, vol. 2017, no. 1, pp. 1–10, Nov. 2017. [Online]. Available: https://doi.org/10.1186/s13638-017-0990-4

[40] M. M. Alammar and M. López-Benítez, "Evaluation of the impact of thresholding and frequency/time resolution on signal area estimation methods," in *2021 IEEE 93rd Vehicular Technology Conference (VTC 2021-Spring), 7th IEEE International Workshop on Smart Spectrum (IWSS 2021)*. IEEE, 2021, pp. 1–7.

[41] M. Abramowitz, I. A. Stegun, and R. H. Romer, "Handbook of mathematical functions with formulas, graphs, and mathematical tables," *American Journal of Physics*, vol. 56, no. 10, pp. 958–958, 1988. [Online]. Available: https://doi.org/10.1119/1.15378

[42] D. Powers, "Evaluation: From precision, recall and F-measure to ROC, informedness, markedness and correlation," *Journal of Machine Learning Technologies*, vol. 2, pp. 37–63, Jan. 2011.

[43] M. M. Alammar and M. López-Benítez, "A minesweeper algorithm for improved signal area estimation in spectrum aware systems," in *IEEE 28th International Conference on Telecommunications (ICT 2021)*. IEEE, Jun. 2021, pp. 1–6.

[44] R. Kaye, "Minesweeper is NP-complete," *Mathematical Intelligencer*, vol. 22, no. 2, pp. 9–15, 2000.

[45] H. J. Heijmans, "Mathematical morphology: A modern approach in image processing based on algebra and geometry," *Society for Industrial and Applied Mathematics (SIAM) review*, vol. 37, no. 1, pp. 1–36, Mar. 1995.

[46] M. J. Ready, M. L. Downey, and L. J. Corbalis, "Automatic noise floor spectrum estimation in the presence of signals," in *Conference Record of the Thirty-First Asilomar Conference on Signals, Systems and Computers (Cat. No.97CB36136)*, vol. 1. IEEE, Nov. 1997, pp. 877–881.

[47] K. F. Tom, "An automated energy detection algorithm based on morphological filter processing with a semi-disk structure," US Army Research Laboratory Aberdeen Proving Ground United States, Tech. Rep. ARL-TR-8271, Jan. 2018.

[48] J. Rivest, "Mathematical morphology and short-term fourier transforms," Defence Research and Development Canada - Ottawa, Tech. Rep. TM 2011-103, Sep. 2011.

[49] X. Mankun, P. Xijian, L. Tianyun, and X. Mantian, "A new time-frequency spectrogram analysis of fh signals by image enhancement and mathematical morphology," in *Fourth International Conference on Image and Graphics (ICIG 2007)*. IEEE, Aug. 2007, pp. 610–615.

[50] A. Offringa, J. van de Gronde, and J. Roerdink, "A morphological algorithm for improving radio-frequency interference detection," *Astronomy and Astrophysics*, vol. 539, no. A95, pp. 1–11, Mar. 2012.

[51] V. Sharma, M. Choubisa, and S. S. Shekhawat, "Analysis of proposed hybrid approaches for laplacian edge based image segmentation using morphological image processing," in *Proceedings of International Conference on Sustainable Computing in Science, Technology and Management (SUSCOM), Amity University Rajasthan, Jaipur-India*, Feb. 2019, pp. 1471–1479.

[52] M. Roy, S. Chakraborty, K. Mali, S. Chatterjee, S. Banerjee, S. Mitra, R. Naskar, and A. Bhattacharjee, "Cellular image processing using morphological analysis," in *2017 IEEE 8th Annual Ubiquitous Computing, Electronics and Mobile Communication Conference (UEMCON)*, Oct. 2017, pp. 237–241.

[53] H. S. Lee, Y. Baek, Q. Lin, J. Minsu Chen, M. Park, D. Lee, S. Kim, and K. Lee, "Efficient defect identification via oxide memristive crossbar array based morphological image processing," *Advanced Intelligent Systems*, vol. 3, no. 2, p. 2000202, Nov. 2021.

[54] M. Mishra, R. R. Panigrahi, and P. K. Rout, "A combined mathematical morphology and extreme learning machine techniques based approach to micro-grid protection," *Ain Shams Engineering Journal*, vol. 10, no. 2, pp. 307–318, Jun. 2019.

[55] S. E. Juliet, V. Sadasivam, and D. J. Florinabel, "Effective layer-based segmentation of compound images using morphology," *Journal of real-time image processing*, vol. 9, no. 2, pp. 299–314, Jun. 2014.

[56] C. Shan, B. Huang, and M. Li, "Binary morphological filtering of dominant scattering area residues for sar target recognition," *Computational intelligence and neuroscience*, vol. 2018, pp. 1–15, Dec. 2018.

[57] W. Huang, R. Wang, Y. Zhou, and X. Chen, "Simultaneous coherent and random noise attenuation by morphological filtering with dual-directional structuring element," *IEEE Geoscience and Remote Sensing Letters*, vol. 14, no. 10, pp. 1720–1724, Aug. 2017.

[58] S. Datta and C. Sturtivant, "Dolphin whistle classification for determining group identities," *Signal Processing*, vol. 82, no. 2, pp. 251–258, Feb. 2002.

[59] D. M. Gillespie, "Detection and classification of right whale calls using an 'edge' detector operating on a smoothed spectrogram," *Canadian Acoustics*, vol. 32, no. 2, pp. 39–47, Jun. 2004.

[60] W. B. Hussein, M. A. Hussein, and T. Becker, "Spectrogram enhancement by edge detection approach applied to bioacoustics calls classification," *Signal and Image Processing: An International Journal*, vol. 3, no. 2, pp. 1–20, Apr. 2012.

[61] H. Ou, W. W. Au, L. M. Zurk, and M. O. Lammers, "Automated extraction and classification of time-frequency contours in humpback vocalizations," *J. Acoust. Soc. Am.*, vol. 133, no. 1, pp. 301–310, Jan. 2013.

[62] J. R. Parker, *Algorithms for Image Processing and Computer Vision*, 2nd ed.   John Wiley & Sons, 2011.

[63] R. C. González and R. E. Woods, *Digital Image Processing*.   Prentice Hall, 2002.

[64] J. M. S. Prewitt, "Object enhancement and extraction," in *Picture processing and Psychopictorics*, B. Lipkin and A. Rosenfeld, Eds.   New York: Academic Press, 1970, pp. 75–149.

[65] R. O. Duda and P. E. Hart, *Pattern Classification and Scene Analysis*.   New York: John Wiley & Sons, 1973, pp. 271–272.

[66] P. E. Danielsson and O. Seger, "Generalized and separable Sobel operators," in *Machine vision for three-dimensional scenes*, H. Freeman, Ed.   Academic Press, 1990, pp. 347–379.

[67] B. Jähne, H. Scharr, and S. Körkel, "Principles of filter design," in *Handbook of Computer Vision and Applications*, B. Jähne, H. Haußecker, and P. Geißler, Eds.   Academic Press, 1999, vol. 2, ch. 6, pp. 125–151.

[68] D. Kroon, "Numerical optimization of kernel based image derivatives," in *Short Paper University Twente*, 2009, pp. 1–3.

[69] H. Farid and E. P. Simoncelli, "Optimally rotation-equivariant directional derivative kernels," in *International Conference on Computer Analysis of Images and Patterns*, Sep. 1997, pp. 207–214.

[70] ——, "Differentiation of discrete multidimensional signals," *IEEE Transactions on image processing*, vol. 13, no. 4, pp. 496–508, Apr. 2004.

[71] A. Hast, "Simple filter design for first and second order derivatives by a double filtering approach," *Pattern Recognition Letters*, vol. 42, no. 1, pp. 65–71, Jun. 2014.

[72] L. G. Roberts, "Machine perception of three-dimensional solids," Ph.D. dissertation, Massachusetts Institute of Technology, Jun. 1963.

[73] E. Kawalec-Latala, "Edge detection on images of pseudoimpedance section supported by context and adaptive transformation model images," *Studia Geotechnica et Mechanica*, vol. 36, no. 1, pp. 29–36, Jun. 2014.

[74] R. Kirsch, "Computer determination of the constituent structure of biological images," *Computers and Biomedical Research*, vol. 4, no. 3, pp. 315–328, Jun. 1971.

[75] R. A. R. Lateef, "Expansion and implementation of a 3x3 Sobel and Prewitt edge detection filter to a 5x5 dimension filter," *Journal of Baghdad College of Economic sciences University*, no. 18, pp. 336–348, 2008.

[76] V. Bogdan, C. Bonchis, and C. Orhei, "Custom dilated edge detection filters," *Journal of the World Society for Computer Graphics*, vol. 28, no. 1-2, pp. 161–168, Jan. 2020.

[77] C. Orhei, V. Bogdan, and C. Bonchis, "Edge map response of dilated and reconstructed classical filters," in *22nd International Symposium on Symbolic and Numeric Algorithms for Scientific Computing (SYNASC 2020)*, Sep. 2020, pp. 187–194.

[78] J. Canny, "A computational approach to edge detection," *IEEE Transactions on Pattern Analysis and Machine Intelligence*, vol. PAMI-8, no. 6, pp. 679–698, Nov. 1986.

[79] P. Soille, *Morphological Image Analysis: Principles and Applications*, 2nd ed. Springer-Verlag, 1999.

[80] L. Cirillo, A. Zoubir, and M. Amin, "Parameter estimation for locally linear fm signals using a time-frequency hough transform," *IEEE Transactions on Signal Processing*, vol. 56, no. 9, pp. 4162–4175, Aug. 2008.

[81] N. Aggarwal and W. Karl, "Line detection in images through regularized hough transform," *IEEE Transactions on Image Processing*, vol. 15, no. 3, pp. 582–591, Mar. 2006.

[82] K. Zhao, Q. Han, C.-B. Zhang, J. Xu, and M.-M. Cheng, "Deep hough transform for semantic line detection," *IEEE Transactions on Pattern Analysis and Machine Intelligence*, pp. 1–1, May 2021.

[83] B. Govindarajan, K. A. Panetta, and S. Agaian, "Image reconstruction for quality assessment of edge detectors," in *2008 IEEE International Conference on Systems, Man and Cybernetics*, Oct. 2008, pp. 691–696.

[84] K. Igwe, O. Oyedum, A. Aibinu, M. Ajewole, and A. Moses, "Application of artificial neural network modeling techniques to signal strength computation," *Heliyon*, vol. 7, no. 3, p. e06047, Mar. 2021.

[85] K. Yang, Z. Huang, X. Wang, and F. Wang, "An SNR estimation technique based on deep learning," *Electronics*, vol. 8, no. 10, p. 1139, Oct. 2019.

[86] O. H. Toma and M. López-Benítez, "Traffic learning: A deep learning approach for obtaining accurate statistical information of the channel traffic in spectrum sharing systems," *IEEE Access*, vol. 9, pp. 124 324–124 336, Sep. 2021.

[87] H. Zhou, J. Wu, and J. Zhang, *Digital image processing: part I*.   Bookboon, 2010.

[88] S. E. Umbaugh, *Digital image processing and analysis: human and computer vision applications with CVIPtools*.   CRC press, 2010.

[89] M.-C. Su and C.-H. Hung, "A neural-network-based approach to detecting rectangular objects," *Neurocomputing*, vol. 71, no. 1-3, pp. 270–283, Dec. 2007.

[90] Y. H. Hu and J.-N. Hwang, *Handbook of Neural Network Signal Processing*, 1st ed. CRC Press, oct 2018.

[91] P. Alapuranen and J. Schroeder, "Complex artificial neural network with applications to wireless communications," *Digital Signal Processing*, vol. 119, p. 103194, Dec. 2021.

[92] K.-L. Du and M. N. S. Swamy, *Recurrent Neural Networks*.   London: Springer London, Sep. 2019, pp. 351–371.

[93] X. Tong, B. Sun, J. Wei, Z. Zuo, and S. Su, "Eaau-net: Enhanced asymmetric attention u-net for infrared small target detection," *Remote Sensing*, vol. 13, no. 16, p. 3200, Aug. 2021.

[94] Y. LeCun, Y. Bengio, and G. Hinton, "Deep learning," *Nature*, vol. 521, no. 7553, pp. 436–444, 2015.

[95] M. Abadi, A. Agarwal, P. Barham, E. Brevdo, Z. Chen, C. Citro, G. S. Corrado, A. Davis, J. Dean, M. Devin, S. Ghemawat, I. J. Goodfellow, A. Harp, G. Irving, M. Isard, Y. Jia, R. Józefowicz, L. Kaiser, M. Kudlur, J. Levenberg, D. Mané, R. Monga, S. Moore, D. G. Murray, C. Olah, M. Schuster, J. Shlens, B. Steiner, I. Sutskever, K. Talwar, P. A. Tucker, V. Vanhoucke, V. Vasudevan, F. B. Viégas, O. Vinyals, P. Warden, M. Wattenberg, M. Wicke, Y. Yu, and X. Zheng, "Tensorflow: Large-scale machine learning on heterogeneous distributedm systems," *CoRR*, vol. abs/1603.04467, 2016. [Online]. Available: http://arxiv.org/abs/1603.04467

[96] F. Chollet, "Keras, github," 2015. [Online]. Available: https://github.com/fchollet/keras

[97] A. Paszke, S. Gross, F. Massa, A. Lerer, J. Bradbury, G. Chanan, T. Killeen, Z. Lin, N. Gimelshein, L. Antiga, A. Desmaison, A. Kopf, E. Yang, Z. DeVito, M. Raison, A. Tejani, S. Chilamkurthy, B. Steiner, L. Fang, J. Bai, and S. Chintala, "Pytorch: An imperative style, high-performance deep learning library," in *Advances in Neural Information Processing Systems*, H. Wallach, H. Larochelle, A. Beygelzimer, F. d'Alché-Buc, E. Fox, and R. Garnett, Eds., vol. 32.   Curran Associates, Inc., 2019, pp. 8026–8037.

[98] S. F. M. Radzi, M. K. A. Karim, M. I. Saripan, M. A. A. Rahman, I. N. C. Isa, and M. J. Ibahim, "Hyperparameter tuning and pipeline optimization via grid search method and tree-based automl in breast cancer prediction," *Journal of Personalized Medicine*, vol. 11, no. 10, p. 978, Sep. 2021.

[99] E. Bakshy, L. Dworkin, B. Karrer, K. Kashin, B. Letham, A. Murthy, and S. Singh, "AE: A domain-agnostic platform for adaptive experimentation," in *Conference on Neural Information Processing Systems*, 2018, pp. 1–8.

[100] M. M. Alammar and M. López-Benítez, "Automatic extraction of signal areas from radio spectrograms based on the Hough transform," in *Proc. IEEE Int. Symp. on a World of Wireless, Mobile and Multimedia Networks (WoWMoM 2022)*, Jun. 2022, pp. 1–10.

[101] S. Hinz, "Fast and subpixel precise blob detection and attribution," in *IEEE International Conference on Image Processing 2005*, vol. 3.   IEEE, Sep. 2005, pp. III–457.

[102] H. Kong, H. C. Akakin, and S. E. Sarma, "A generalized laplacian of gaussian filter for blob detection and its applications," *IEEE transactions on cybernetics*, vol. 43, no. 6, pp. 1719–1733, Dec. 2013.

[103] P. J. Freire, S. Srivallapanondh, A. Napoli, J. E. Prilepsky, and S. K. Turitsyn, "Computational complexity evaluation of neural network applications in signal processing," 2022, DOI: https://doi.org/10.48550/arXiv.2206.12191.